The relationship between galaxy environment and the quenching of star formation

Miguel Socolovsky

Thesis submitted to the University of Nottingham
for the degree of Doctor of Philosophy

October 2018

"*La potenza è nulla senza controllo*"

– Adele Nasti

Supervisors: Prof. Omar Almaini
Dr. Nina A. Hatch

Examiners: Prof. Bianca M. Poggianti *(Osservatorio Astronomico di Padova)*
Dr. Steven P. Bamford *(University of Nottingham)*

Submitted: 10 October 2018

Examined: 27 November 2018

Final version: 18 December 2018

Contents

List of Figures

List of Tables

Abstract

In this thesis, we explore the impact of environment on the star formation properties of galaxies across 6.5 Gyrs of cosmic time, corresponding to the redshift range $0.5 < z < 3.0$. In order to accomplish this task, we study the dependence of various galaxy properties, such as the stellar mass function, galaxy structure, star formation rate and passive fraction, as a function of environmental density and galaxy type. The work presented here is entirely based on the deep photometric data of the 8th and 11th data releases (DR8 and DR11 respectively) of the UKIDSS Ultra Deep Survey (UDS). The galaxy classification we use is based on a Principal Component Analysis (PCA) technique which allows us to identify star-forming and passive galaxies, and also post-starburst galaxies (PSBs), using only broad-band photometry. Both the UDS catalogues and the PCA technique are described in Chapter 2 of this thesis.

We characterise galaxy environment using two different methods. The first method is used at low redshift ($z < 1.0$) and is based of a friends-of-friends algorithm, which allows us to identify overdensities (galaxy clusters and groups) in the UDS field. This method was thoroughly optimised to run on the UDS data, and the output tested using the extensive spectroscopic redshifts that are available in the UDS field, and by comparing to previous overlapping cluster studies. The method also generates a field sample with the same redshift distribution as the cluster sample, allowing for the comparison between these two environments. A second method, based on fixed apertures, was also implemented in order to study the environmental trends in a more self-consistent way across the broad redshift range $0.5 < z < 3.0$.

Our first study focuses on the redshift range $0.5 < z < 1.0$ using the UDS DR8 data and the cluster finder described above. The study of the stellar mass function reveals clear differences between the cluster and field environments, with a strong excess of low-mass PSB galaxies in clusters compared to the field. Cluster environments also show a corresponding deficit of young, low-mass star-forming galaxies, which also show a sharp radial decline towards the cluster centres. By comparing mass functions and radial distributions, we conclude that young star-forming galaxies are rapidly quenched as they enter overdense environments, becoming PSBs before joining the red sequence. Our results also point to the existence of two environmental quenching pathways operating in galaxy clusters, on different timescales. Fast quenching acts on galaxies with high specific star formation rates (SSFRs), operating on timescales shorter than the cluster dynamical time ($\lesssim 1$ Gyr). In contrast, slow quenching affects galaxies with moderate SSFRs, regardless of their stellar mass, and acts on longer timescales ($\gtrsim 1$ Gyr). Of the cluster galaxies in the stellar mass range $9.0 < \log(M/\mathrm{M}_{\odot}) < 10.5$ that were quenched during this epoch, we find that 73% were transformed through fast quenching, while the remaining 27% followed the slow quenching route.

We extend our analysis through the usage of effective radii and Sérsic indices as tracers for galaxy structure, determined using the deep K-band imaging from DR11.

We find that the high-SSFR galaxies that survive into the cluster environment have, on average, larger effective radii than those in the field. We suggest that this trend is driven by the most compact star-forming galaxies being preferentially quenched in dense environments. We also find that PSBs in clusters have stellar masses and effective radii that are similar to the missing compact star-forming population, suggesting that these PSBs are the result of size-dependent quenching. We propose that both strong stellar feedback and the stripping of the extended halo act together to preferentially and rapidly quench the compact and low-mass star-forming systems in clusters to produce PSBs. We test this scenario using the stacked spectra of 124 high-SSFR galaxies showing that more compact galaxies are more likely to host outflows. From these results we conclude that a combination of environmental and secular processes is the most likely explanation for the appearance of PSBs in galaxy clusters.

Finally, we study the evolution of environmental quenching across a wider redshift range ($0.5 < z < 3.0$) by using the deeper data of the UDS DR11. We find that galaxy star-formation properties (passive fraction, SFR and SSFR) strongly correlate with environment until $z = 2.0$. Furthermore, we find evidence suggesting that the quenching effects of environment and stellar mass are not independent from each other, as galaxies with $M_* < 10^{10.3}\mathrm{M}_\odot$ and $M_* > 10^{10.3}\mathrm{M}_\odot$ show slightly different environmental trends. At low stellar masses there is an enhancement of both star-forming galaxies with low SSFRs and PSBs in dense environments at $z < 1.5$. In contrast, at higher masses the low-SSFR galaxies are strongly depleted in dense environments since $z \sim 1.75$. We also find that massive galaxies are more sensitive to environment, i.e. their star-forming properties are more affected than those of low-mass galaxies at the same environmental overdensity level. From this we conclude that the action of secular processes in massive galaxies might be aiding the environmental effects, leading to faster quenching. In other words, secular and environmental processes may join forces to drive the evolution of the most massive galaxies in the distant Universe.

Acknowledgements

The realisation of this thesis has been possible thanks to the help and moral support of a large number of people, including my family, friends and colleagues. Without them it would have been impossible to walk this path, I am immensely grateful to them. Some of them have directly contributed to the production of this thesis whereas others have granted me their support throughout. All of them have been essential.

First and foremost, I wish to thank my PhD supervisors, Omar and Nina. For your exceptional guidance and patience throughout the past four years. Special thanks to Dave for being a third supervisor and a good friend, I will miss your invaluable help and our endless science discussions in the office. I also wish to thank the rest of the UDS team, Charutha, Aaron, Rachel and Lizzie for those exciting weekly round-ups. I feel very honoured to have worked with such great scientists and better people. Also thanks to all my amazing officemates, Aaron, Dave, Cristina, Florian, Silvia, Pete, Tom, Paul, James and Ben for creating such a great work environment. I would also like to thank everyone in the Centre for Astronomy and Particle Theory (CAPT), for creating such a welcoming atmosphere, where I could always feel at home.

A huge thanks to all the good friends and travel companions that have walked by my side in this long journey. Thanks Charutha, Jake, Finlay and Fahad for having me in your office so often to discuss so many important issues (and not so important ones too); Amelia, Tom and Martha for our regular hikes in the Peak District; Ulli, Felipe, Rachel and the rest of the coffee club (special mention to Lizzie, the best barista to set foot in CAPT) for the much needed breaks from work; Berta and Kshitija for sharing with us your amazing baking skills and for the parties at your place; and thanks Anand for never saying 'no' to a plan, no matter how ridiculous they were, your positivity and willingness will be missed. Thanks Adele and Felipe for so much fun, in particular for our never-ending tennis sessions, the *futbolín*, the spa evenings in Derby and so many more. I think I am right when I say that we lived with great intensity every minute we spent together. I would also like to thank Rach, Eugenio, Mehdi, Ismael, Bruno, Lyndsay and Cristina for your company and support, as well as for all the experiences we have shared and those still to come. I also wish to thank the rest of my Nottingham family: Fabio, Nephtalí, Elisa, Julie, Jorge and Chris. Thanks for bearing with me in my both my good and bad moments.

Thank you Laura, my counterpart in Madrid, for sharing the joys and sufferings of the PhD life with me and not letting me lose contact during the last four years. Thanks to all those friends back in Spain that always believed in me, in particular to Ivan, Alvaro and Lucia for facing the British weather in order to visit me.

Last but not least, I want to thank my parents and sister for their unconditional encouragement and understanding. Thanks for always supporting me in every decision I have made. I am certain I would not be here if it was not for you.

Published work

The majority of the work in this thesis has been presented in the papers listed below. The work presented in Paper I has been split into Chapters 3 (method) and 4 (results). The work presented in Chapter 5 corresponds to Paper II, which has been submitted to MNRAS. Finally, most of the work in Chapter 6 will appear in a forthcoming paper (Paper III), in preparation.

I **Miguel Socolovsky**, Omar Almaini, Nina A. Hatch, Vivienne Wild, David T. Maltby, William G. Hartley, Chris Simpson, MNRAS, 476, 1242: *'The enhancement of rapidly quenched galaxies in distant clusters at* $0.5 < z < 1.0$*'*.

II **Miguel Socolovsky**, David T. Maltby, Nina A. Hatch, Omar Almaini, Vivienne Wild, William G. Hartley, Chris Simpson, MNRAS, 482, 1640: *'Compact star-forming galaxies being preferentially quenched to become PSBs in* $z < 1$ *clusters'*.

III **Miguel Socolovsky**, Omar Almaini, Nina A. Hatch, Vivienne Wild, David T. Maltby, William G. Hartley, Chris Simpson: *'Galaxy environment since* $z = 3$*: the evolution of environmental quenching'*, in preparation.

IV David T. Maltby, Omar Almaini, Vivienne Wild, Nina A. Hatch, William G. Hartley, Chris Simpson, **Miguel Socolovsky**, MNRAS, 480, 381: *'The structure of post-starburst galaxies at* $0.5 < z < 2$*: evidence for two distinct quenching routes at different epochs'*.

The vast majority of the work presented in this thesis was carried out by the author, with advice from the paper coauthors listed above. Where the material presented is the result of more collaborative work, this is mentioned in the relevant chapter.

Chapter 1

Introduction

It is now well established that the Milky Way, the galaxy we live in, is only one of many. However, for a long time galaxies had been considered objects contained within our own. It was Immanuel Kant, and others, who started the "Great Debate" in the mid-1700's by suggesting that nebulae may be external galaxies or "island universes". It was not until less than 100 years ago when astronomers finally settled this down with the first observational evidence that 'spiral nebulae' lay far beyond the boundaries of our home Galaxy, and were galaxies in their own right (Hubble 1925). Consequently, the Universe we inhabit is much larger than it was previously believed. This discovery opened a myriad of fundamental questions regarding the formation and evolution of these extra-galactic objects. The field of extra-galactic astronomy had been born.

In the following years, Hubble realised that galaxies had a range of morphologies and classified them in different types according to their complexity (Hubble 1936). This classification is still used today and is commonly known as the "Hubble tuning fork", illustrated in Figure 1.1. Smooth and featureless galaxies are located on the left side of the diagram and are classified as "early-type" galaxies. On the other side we find spirals, which are "late-type" galaxies. Late-types are also subdivided into barred or un-barred according to whether their central regions have this feature. Finally, lenticular or S0 galaxies are an interesting subset of early-types. They are thought to be transition objects between the two classes (Spitzer & Baade 1951; Moore et al. 1996; Dressler et al. 1997). They have a disc, which is more common amongst late-type galaxies, but a smooth stellar distribution.

1.1 Cosmology and galaxy evolution

The current paradigm for structure formation is the so-called ΛCDM cosmological model. Also referred to as the standard cosmological model, it describes a Universe dominated by a cosmological constant (Λ) and cold dark matter (CDM). The approximate contributions to the Universe total energy density today are: 69% dark energy, 26% cold dark matter and 5% baryonic matter (as measured by the Planck Collaboration; Ade et al. 2016). The ΛCDM model reproduces accurately most of the observed properties of the Cosmos, e.g. the large-scale structure of the Universe, the power spectrum of the cosmic microwave background (CMB) and the abundances of the most common elements. However, it also highlights the magnitude of our ignorance, given that 95% of the composition of the Universe, which does not correspond to ordinary matter, is still very poorly understood.

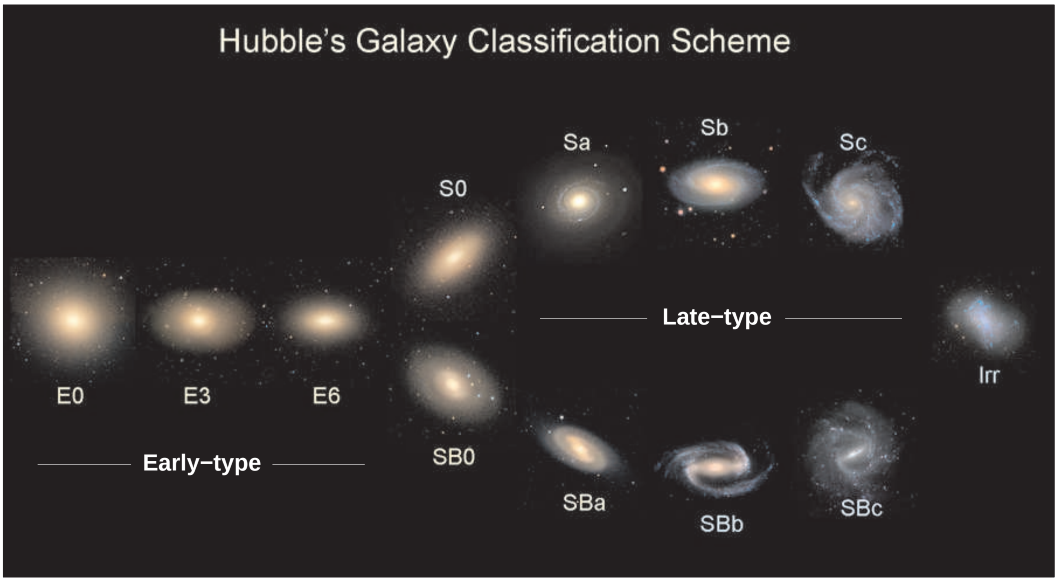

Figure 1.1. The Hubble sequence. This image was produced using galaxies from the Sloan Digital Sky Survey (SDSS; York 2000) classified by members of the GalaxyZoo project (Lintott et al. 2008).

Although we do not know what dark energy and dark matter are, there is indirect evidence indicating they exist. For example, Λ is expected to be the driver of the accelerated expansion of the Universe (Riess et al. 1998; Perlmutter et al. 1999), while dark matter is invoked to explain the velocity dispersions of galaxies in clusters and the flat galaxy rotation curves of disc galaxies (Zwicky 1933; Rubin et al. 1978). The main reason why dark matter has remained so elusive until the present day could be that, until recently, we had been confined to the small fraction of the composition of the Universe which interacts with light and can, thus, be directly observed with a telescope. However, with the first direct detections of gravitational waves in 2015 (Abbott et al. 2016), a new window might open in the near future allowing us to observe phenomena that were previously beyond our reach.

The standard cosmological model also governs the formation and evolution of galaxies. The seeds to structure formation were the primordial density fluctuations observed in the CMB. These primordial fluctuations, amplified during the epoch of cosmic inflation, kept growing through the accretion of dark matter to form dark matter haloes. In the standard model, dark matter is non-relativistic (CDM), so structures can collapse, first at smaller scales, giving rise to a bottom-up growth of structure in the Universe. Low-mass haloes formed first, from the largest perturbations, and increased in size and mass via merging with each other to produce more massive ones (White & Rees 1978; Lacey & Cole 1993). This process is known as the hierarchical growth of structure, and is used in cosmological simulations to successfully reproduce the observed distribution of dark matter haloes (e.g. Springel et al. 2005). Alternatively, 'top-down' models have also been tested, which involve hot dark matter (HDM). However, if most of the dark matter is relativistic the small-scale structure is completely wiped out, under-predicting the number of dwarf satellite galaxies observed in the Universe.

The distribution and growth of galaxies is assumed to be a strongly biased tracer

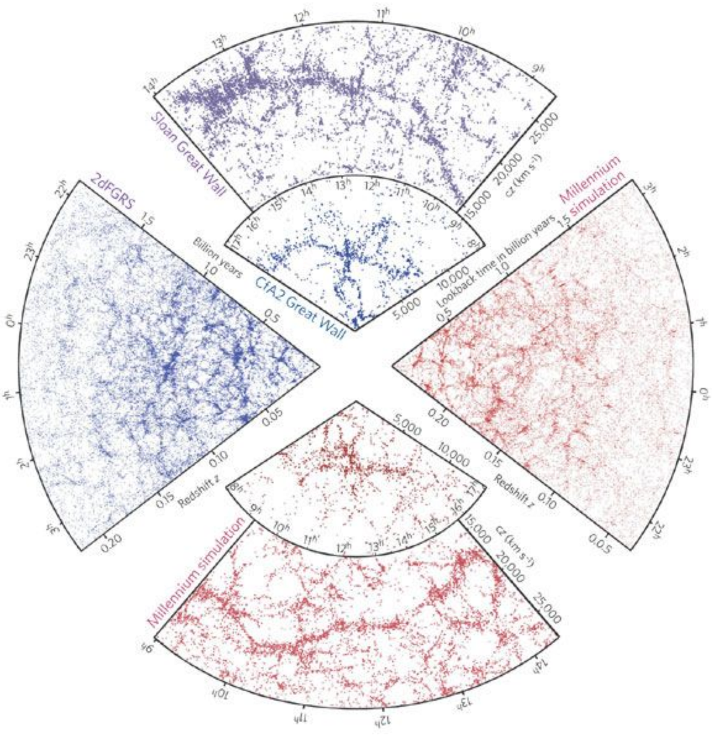

Figure 1.2. The large-scale structure of the Universe. In the top and left cones (in blue and purple) the redshift distributions in some large spectroscopic surveys, including CfA2, 2dFGRS and SDSS is presented. In the bottom and right cones (in red) the distribution from mock galaxy catalogues constructed using semi-analytic prescriptions based on the 'Millenium' simulation is shown. The figure shows that the observed large-scale structure of the Universe is remarkably similar to the predictions from dark-matter-only simulations.

of dark matter, typically inhabiting the central regions of dark matter haloes. This is suggested by the remarkable similarity between the observed large-scale structure of galaxies and that predicted by dark matter N-body simulations (see Figure 1.2). More recently, full hydrodynamical simulations which include gas physics have also shown that gas particles follow the same filamentary structure as galaxies and dark matter (e.g. EAGLE; Schaye et al. 2015 or Illustris; Vogelsberger et al. 2014). Galaxies are assumed to form in the centre of collapsed dark matter haloes. When two haloes merge, the respective galaxies associated with them tend to eventually do the same. However, this can take a long time. In massive haloes, the velocity dispersion of the galaxies is so high that galaxy mergers are rare and galaxies accumulate forming groups and clusters of galaxies.

The galaxy luminosity function (related to the mass function through the mass-to-light ratio) is one of the most fundamental characteristics of the galaxy population. It represents the number of galaxies of a given luminosity per unit volume. It has been shown that the mass function of dark matter haloes does not match the shape of the galaxy luminosity function (Figure 1.3). While the halo mass function resembles a power law, the galaxy mass function presents a 'knee' shape (Cole et al. 2001; Kochanek et al. 2001; Huang et al. 2003). It is broadly accepted nowadays that the galaxy luminosity function is well parametrised by a Schechter function (Schechter 1976). A Schechter function (1.1) consists of a power law (at low masses) with slope α, which turns into an exponentially decaying profile above a 'characteristic luminosity' (L^*); it also has a normalisation constant ϕ^*.

$$\phi(L)dL = \phi^* \left(\frac{L}{L^*}\right) \exp\left(\frac{-L}{L^*}\right) d\left(\frac{L}{L^*}\right) \tag{1.1}$$

If the mass-to-light ratio is chosen so that the halo mass function matches the knee of the galaxy luminosity function, a deficit of galaxies is found at both the high and low-mass ends. This discrepancy is usually associated with feedback processes dictated by baryon dynamics. The abrupt change in the slope of the galaxy luminosity function at high masses can be successfully reproduced by including AGN feedback to the models (Bower et al. 2006; Croton et al. 2006). Powerful AGN are more frequent in massive galaxies and their strong feedback is modelled to heat up the gas and prevent further star formation. Similarly, the detriment of low-mass galaxies can be matched if stellar feedback, i.e. supernova and super-winds, regulates star formation in low-mass systems (Larson 1974; White & Frenk 1991).

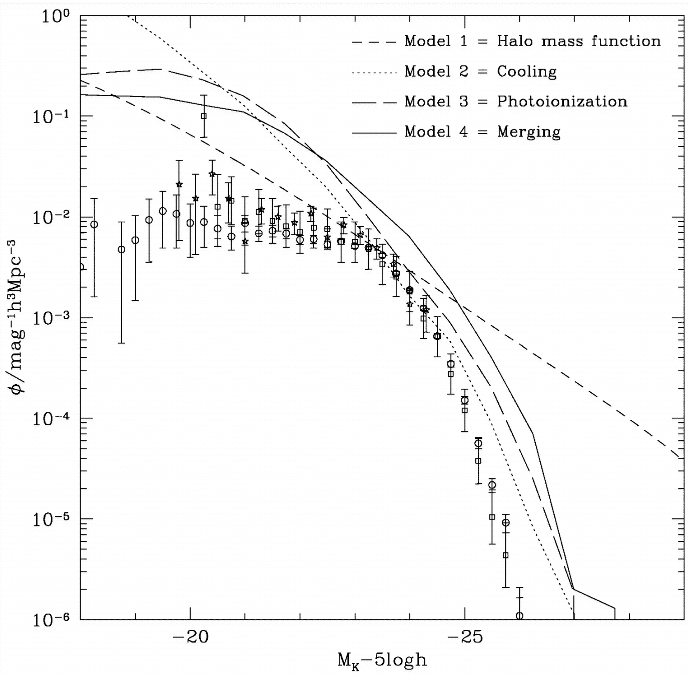

Figure 1.3. K-band galaxy luminosity function. The data-points correspond to a collection of observations (circles from Cole et al. 2001; squares from Kochanek et al. 2001; and stars from Huang et al. 2003). The lines show different theoretical predictions. The short dashed line corresponds to a model assuming a fixed mass-to-light ratio such that the halo mass function matches the knee of the galaxy luminosity function. It can be appreciated that extra mechanisms are needed in the simulation in order to reproduce the low star-formation efficiencies at high and low halo masses. Credit: Benson et al. (2003).

The shape of the galaxy luminosity functions demonstrates that, although we have a good understanding of the mass assembly in the Universe to a first order approximation (dark matter), the formation and evolution of galaxies is a much more complex process. To explain galaxy evolution requires the understanding of the complex physics of star formation, stellar evolution, feedback processes, gas cooling and so on; which are overlaid on top of the dark matter distribution. The complexity of baryonic physics gives galaxies a broad range of morphologies, sizes and colours.

1.2 Galaxy bimodality

Broadly speaking, the distribution of galaxy properties is bimodal. In the local Universe, almost all galaxies fall in one of two classes. The most numerous of these two groups includes star-forming galaxies. These tend to have low stellar masses, late-type morphologies, high SFRs and they tend to be blue in the optical, which gives this subset of galaxies its name, the "blue cloud". The other peak of the distribution corresponds to passively evolving galaxies, which tend be massive, have early-type morphologies, low SFRs and red optical colours, therefore they are commonly known as the "red sequence". Although, this characteristic distribution of galaxy properties has been thoroughly studied at low redshifts, the underlying physical mechanisms responsible for shaping it are still under debate. Galaxies are generally assumed to form in the blue cloud, however, in order to explain the bimodal nature of the distribution, they must quickly evolve onto the red sequence (e.g. Muzzin et al. 2012; Wetzel et al. 2012), through a process known as galaxy "quenching". Furthermore, the evolution of the galaxy bimodality at $z > 1$ is even less understood. Some studies have found evidence for the bimodality being in place at redshifts as high as $z = 2$ (Muzzin et al. 2012; Foltz et al. 2015; Balogh et al. 2016) but it becomes less clear at higher redshifts. In this section we review the existence of this bimodality in some of the most studied galaxy properties, our current understanding and the redshift evolution of the bimodality.

1.2.1 Morphology and structure

Generally, most galaxies in the local Universe are either disc-dominated or elliptical. This strong morphological bimodality is characterised by massive galaxies ($M_* > 10^{10.5}M_\odot$) being typically spheroidal while lower mass galaxies tend to be discs (Strateva et al. 2001; Hogg et al. 2002). Another frequently used visual morphology classification scheme is the one introduced by Hubble, which divides the total population in two according to the complexity of their morphology. The simplest morphologies, i.e. smooth and featureless, are called early-type galaxies; while the more complex ones are called late-type galaxies. Early-type galaxies include elliptical and lenticular galaxies, whilst late-type galaxies include spiral, irregular and peculiar galaxies.

In order to systematically study the morphology of large numbers of galaxies, it is common practise to quantify morphology using structural parameters. The most widely used method consists of parametrising galaxy structure by fitting a Sérsic function to the surface brightness profile of the galaxy (Sérsic 1968):

$$\Sigma(R) = \Sigma_e \exp\left\{-\kappa_n \left[\left(\frac{R}{R_e}\right)^{1/n} - 1\right]\right\} \tag{1.2}$$

where R is the distance from the centre of the galaxy, R_e is the effective radius, such that half of the total flux is within this radius. Σ_e represents the surface brightness at R_e. The parameter n is the Sérsic index. Finally, κ_n is a positive parameter whose value varies with n. R_e is a good proxy for galaxy size, while n describes how centrally concentrated the galaxy light is. High n values represent profiles that are strongly peaked at their centres, whilst low-n profiles tend to be more extended. Two cases are of particular interest; $n = 4$ (also called de Vaucouleurs profile; de Vaucouleurs 1959) represents the typical profile of a massive elliptical galaxy, and $n = 1$ (exponential profile) has traditionally been used to describe the light profile of a pure disc.

Multiple studies have shown that n correlates well with visual morphology and galaxies with $n > 2.5$ tend to be ellipticals while those with $n < 2.5$ are often disc-dominated systems (Ravindranath et al. 2004; Bell et al. 2004; Nair & Abraham 2010; Buitrago et al. 2013; Mortlock et al. 2013). The structural bimodality has been observed until $z \sim 2$. The fraction of disc-dominated galaxies decreases with cosmic time, while the fraction of spheroids increases (see Figure 1.4). However, the number of irregular and peculiar galaxies rises with redshift. For example, at $z \sim 1.5$ approximately half of the galaxies have irregular morphologies while the other half corresponds to traditional Hubble types (Conselice et al. 2005; Mortlock et al. 2013; Huertas-Company et al. 2016). At $z > 2$ the majority of galaxies are peculiar with some spheroidal galaxies and very few discs (Mortlock et al. 2013; Huertas-Company et al. 2016). However, although using Sérsic profiles is less biased than visual morphological classification, this method is also less reliable at high redshift due to the lower resolution of the images. Furthermore, the quality required to study precise morphologies for individual objects can only be reached with space-based imaging. Nevertheless, ground-based imaging can be used for measurements of structural parameters if the point spread function (PSF) is well characterised (e.g. Almaini et al. 2017), which can allow robust studies for populations of galaxies even if the individual measurements are uncertain. The considerable advantage of measuring structural parameters from the ground is that it allows us to study much larger samples.

1.2.2 Colour

Galaxy colour is defined as the difference between the magnitude of a galaxy in two wavelength bands. The distribution of galaxy optical colours is again bimodal (Strateva et al. 2001; Blanton et al. 2003; Kauffmann et al. 2003; Baldry et al. 2004). Massive galaxies tend to be optically red in colour and have elliptical morphologies, while lower mass galaxies tend to be optically blue and disc-dominated (this is well illustrated in the colour–stellar mass plots in Figure 1.5). Red galaxies follow a tight relation between the rest-frame colour and stellar mass (or absolute magnitude), known as the *red sequence*. In contrast, blue galaxies present a weaker correlation between colour and magnitude, therefore the region populated by these galaxies is usually referred to as the *blue cloud*. Finally, a handful of objects are found in between these two populations, in a region commonly known as the *green valley*. This third group is believed to be inhabited by transitional galaxies making their way between the blue cloud and the red sequence (Bell et al. 2004; Faber et al. 2007; Martin et al. 2007; Mendez et al. 2011; Gonçalves et al. 2012), however, a fraction of them might be simply scattered from either side.

Galaxy colour is related to the luminosity weighted mean age of the stellar population present in the galaxy. For example, galaxies that are blue in the optical have their spectra dominated by extremely luminous hot and massive O and B stars. These star types are short-lived and finish their lives as supernovae within tens of Myrs from their formation. Hence, these galaxies must have experienced star for-

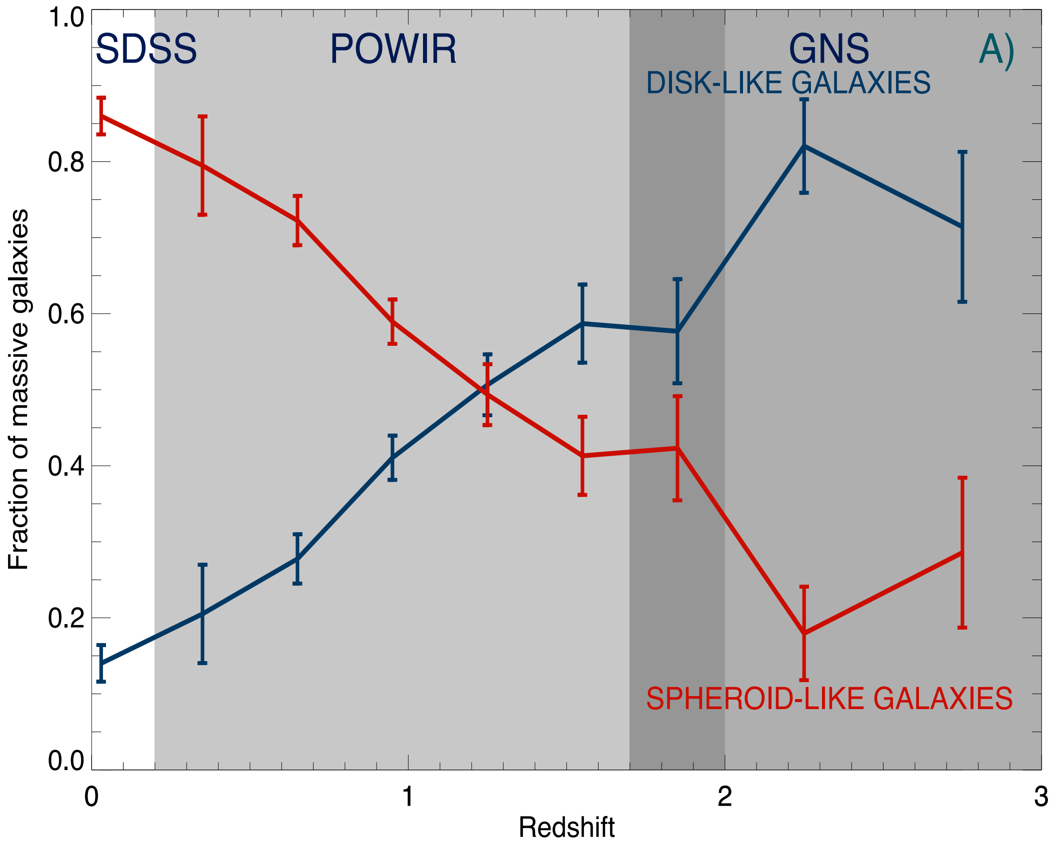

Figure 1.4. Fraction of massive ($M_* > 10^{11} M_\odot$) galaxies with disc-like ($n < 2.5$) and spheroid-like ($n > 2.5$) light profiles as a function of redshift. In the figure, from Buitrago et al. (2013), the different background colours represent the redshift ranges covered by three different surveys: SDSS, POWIR/DEEP2, and GNS.

mation recently. In the case of red galaxies, most stars are cold and evolved, with few young stars remaining. Furthermore, the radiation from old galaxies tends to be dominated by luminous evolved red giants, which contribute much more to the total light output. However, a fraction of red galaxies may actually be star-forming with strong dust extinction, which absorbs most of the blue light, making them look redder than they would otherwise.

Although this colour bimodality is well established at $z = 0$ (e.g. Strateva et al. 2001; Blanton et al. 2003; Kauffmann et al. 2003; Baldry et al. 2004), its strength is inversely proportional to redshift. There is evidence suggesting that the bimodality already exists at $z \sim 2$ but weakens beyond (e.g. Cucciati et al. 2006; Willmer et al. 2006; Cirasuolo et al. 2007; Cassata et al. 2008; Kriek et al. 2008; Brammer et al. 2009; Williams et al. 2009). Nevertheless, some studies find red galaxies at $z > 2$, implying that their assembly must have taken place at $z > 3$ (Cassata et al. 2008).

1.2.3 Star formation activity

The rate at which a galaxy forms stars is one of its most fundamental properties. For most galaxies the star formation rate is found to be directly proportional to their stellar mass (e.g. Brinchmann et al. 2004; Salim et al. 2007; Daddi et al. 2007; Whitaker et al. 2012). Galaxies that follow this trend are said to lie on the star-

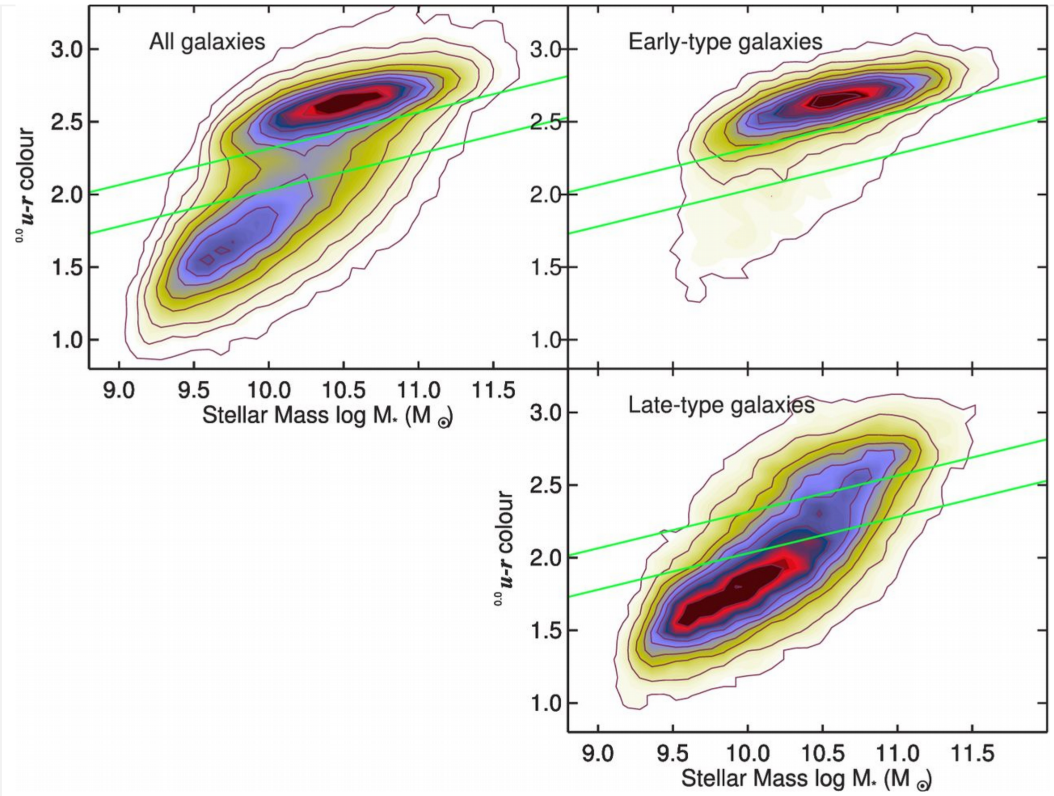

Figure 1.5. The u–r colour–mass diagram for SDSS at $z \sim 0$ (Schawinski et al. 2014). The panel on the top-left shows the strong colour bimodality of the total galaxy population. The distribution presents two peaks, corresponding to the red sequence and the blue cloud. The region located in between these two maxima (region between the green lines) is the green valley, inhabited by galaxies with intermediate properties which are believed to be caught in transition between the two main groups. The panels on the right show how the morphology and colour bimodalities are closely interrelated. The top panel shows the colour–mass distribution for early-type galaxies only, demonstrating that most of these galaxies reside in the red sequence. In contrast, late-type galaxies (bottom) tend to populate the blue cloud.

forming main sequence. However, some galaxies are forming stars at a too low rate, typically one order of magnitude below the expected SFR for their stellar mass (Bluck et al. 2016). These galaxies that lie below the main sequence are commonly known as passively evolving or quenched galaxies. This bimodality has been observed to build up since $z \sim 1$ (see Figure 1.6), being well established in the present-day Universe.

This bimodality in the star formation properties of galaxies is closely related to other galaxy properties. Star-forming galaxies are blue in colour due to the presence of young and hot O, B stars. In contrast, quiescent galaxies are red because their stars formed a long time ago and only old low-mass stars remain. Furthermore, star-forming galaxies tend to be late-type while passive galaxies tend to be early-type (Schawinski et al. 2014). This suggests that when galaxies evolve from the blue cloud to the red sequence, all three properties are affected, although we do not know whether this co-evolution occurs simultaneously or the properties change one after another. Thus, this problem is only partially solved and the link between these

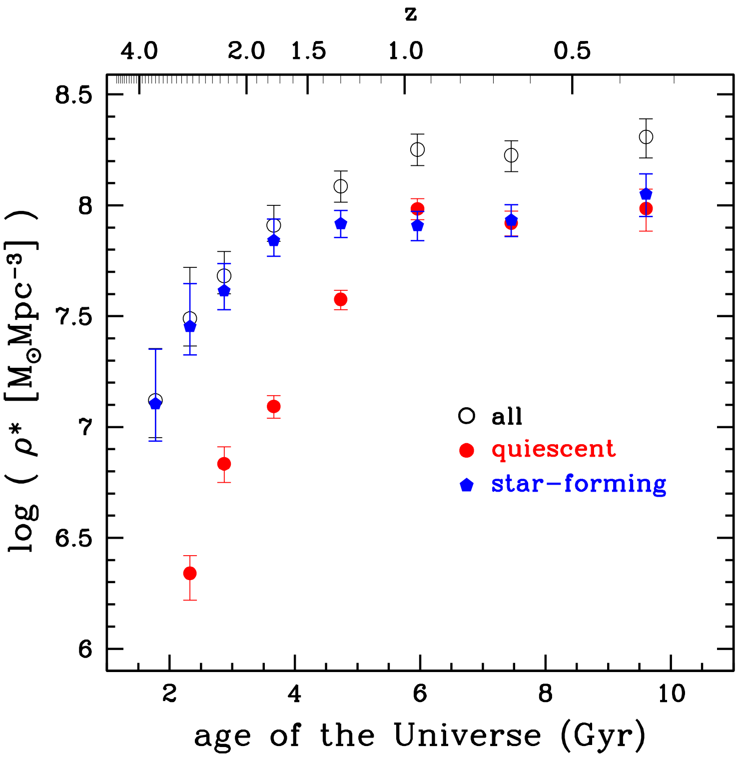

Figure 1.6. Stellar mass density as a function of cosmic time from Ilbert et al. (2013). Blue pentagons and red circles represent the star-forming and passive galaxy populations, respectively. The open black circles correspond to the full galaxy sample. The graph shows the build-up of the red sequence, at $z \sim 1$ the quiescent stellar mass density matches the one of star-forming galaxies.

properties remains unproven.

1.2.4 Correlations between galaxy properties and their environment

The environment represents the surroundings of a galaxy. It can vary from a crowded environment, such as a massive cluster core, to the isolation of the cosmic void, passing through intermediate environments like galaxy groups and the field. There are several galaxy properties that show strong correlations with galaxy environment, e.g. morphology, colour, SFR and the fraction of AGN.

(i) *Morphology–density relation.* The first environmental trend to be reported was the morphology–density relation. It has long been known that galaxies in high-density environments, such as cluster cores, have predominantly early-type morphologies (ellipticals and lenticulars), while in low-density regions of the Universe late-type morphologies (spirals) vastly dominate (Hubble & Humason 1931; Abell 1965; Oemler 1974). Dressler (1980) quantified this relationship as a function of local density at $z = 0$. Figure 1.7 shows the main result of this study. They found a steady increase in the fraction of elliptical and S0 galaxies towards the dense cluster core. In contrast, the fraction of spirals and irregulars smoothly decreases with increasing galaxy density.

The study of the redshift evolution of the morphology–density relation is a key

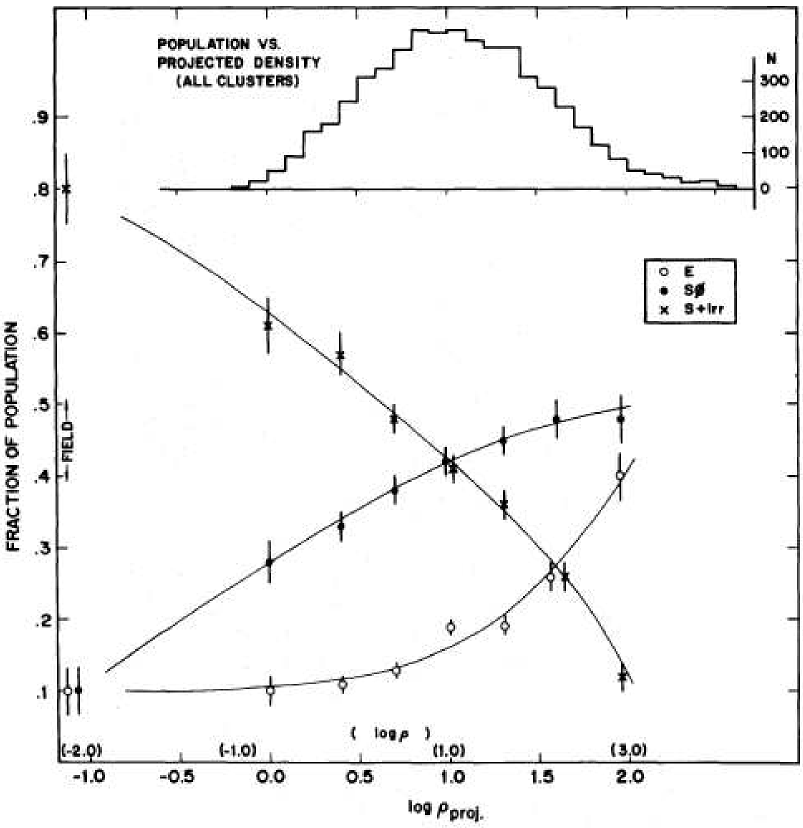

Figure 1.7. The morphology–density relation taken from Dressler (1980). The observed fractions of elliptical (E), lenticular (S0) and spiral+irregular (S+Irr) galaxies in the local Universe as a function of projected local density. These galaxies are drawn from a sample of 55 rich clusters at $z \sim 0$. The fraction of elliptical and S0 galaxies steadily increases with environmental density, whilst the fraction of spirals and irregulars decreases.

element to understanding the physics of morphological transformation. Although Dressler et al. (1997) found that the fraction of elliptical galaxies in cluster environments is unchanged at $z \sim 0.5$, the fraction of cluster S0 galaxies declines by a factor 2-3 with respect to the observations in the local Universe. This evolution is accompanied by a significant increase in the fraction of spiral galaxies in dense environments at $z \sim 0.5$ (e.g. Andreon 1998; Couch et al. 1998; Fasano et al. 2000).

At even higher redshifts, differentiating between elliptical and lenticular morphologies becomes increasingly difficult (Smail et al. 1997; Fabricant et al. 2000). Nevertheless, the total early-type fraction as a function of local environment has been measured up to $z \sim 1$ (van Dokkum et al. 2000, 2001; Lubin et al. 2002). These studies find that the fraction of early-type galaxies in dense environments has experienced a steady increase with cosmic time from $f_{\mathrm{E+S0}} = 0.5 - 0.7$ at $z = 1$ to $f_{\mathrm{E+S0}} = 0.9$ in the local Universe. In contrast, the late-type fraction remains approximately constant at all epochs since $z = 1$ (Smith et al. 2005).

(ii) *Colour–density relation.* Galaxy colour is strongly correlated with environment (e.g. Kodama et al. 2001; Blanton et al. 2005; Baldry et al. 2006). Galaxies in dense environments tend to be redder in optical colours than galaxies of similar luminosity or mass in the field. This relationship is most prominent in the local

Universe, nevertheless, it has been observed at redshifts as high as $z \sim 1.5$ (Cooper et al. 2007; Chuter et al. 2011).

(iii) *Star formation rate.* In the present-day Universe, star formation rate is a strong function of galaxy environment, with galaxies in dense environments tending to have lower star formation rates than galaxies in the field (Lewis et al. 2002; Gómez et al. 2003). Interestingly, some studies have found that this trend disappears or even reverses at $z \sim 1$ (Elbaz et al. 2007; Cooper et al. 2008) suggesting that star formation is enhanced in dense environments. However, more recent studies seem to contradict this reversal of the star formation–density relation. For example, Brammer et al. (2009); Williams et al. (2009); Ilbert et al. (2010); Chuter et al. (2011) all show that the local star formation–density relation was already in place at $z \sim 1 - 1.5$. Similarly, a number of studies have found that passive galaxies are more strongly clustered at $z \gtrsim 1.5$ (Grazian et al. 2006; McCarthy et al. 2007; Quadri et al. 2007; Wilson et al. 2009; Strazzullo et al. 2010; Hartley et al. 2010).

(iv) *AGN fraction.* There is also a relationship between the local environment and the fraction of galaxies hosting AGN. It is well established that AGN activity is suppressed in galaxy clusters in the local Universe (Dressler et al. 1985; Kauffmann et al. 2004). This trend might be driven by the fact that AGN trace the presence of gas, which is known to be scarce in galaxy clusters. However, the link between AGN and environment at higher redshift is a topic of much debate. Some authors have found that this anticorrelation reverses at higher redshifts, and the AGN fraction might increase with local density at $z \gtrsim 1$ (Martini et al. 2009; Miyaji et al. 2007; Bradshaw et al. 2011; Kocevski et al. 2009; Krishnan et al. 2017)

The existence of these trends with environment suggests that, as galaxies become satellites of a galaxy cluster, they undergo significant transformations. Consequently, galaxies in dense environments, such as galaxy clusters, tend to have a more passive population, dominated by early-type galaxies. In contrast, field galaxies tend to be star-forming spirals. This scenario suggests that field spiral galaxies are quenched via some environmental process that takes place in the cluster environment, potentially giving rise to the S0 population we see in the local Universe.

1.3 Galaxy quenching: Nature vs Nurture

Despite the unprecedented wealth of data that has become available in the last few years, the physical nature of the bimodality in the properties of galaxies remains poorly understood. The most accepted theory of galaxy formation proposes that galaxies form from the gravitational collapse of primordial gas clouds. Conservation of angular momentum causes these gas to form a rotating disc which is unstable and, therefore, allows for star formation to take place (Eggen et al. 1962). The assembly of mass is thought to be hierarchical, which means that small galaxies merge in order to produce larger ones (White & Rees 1978). Alternatively, galaxies also grow by building up stellar mass through star formation. Disc instabilities may take place in gas-rich high-redshift galaxies, leading to the collapse of the disc (Dekel & Burkert 2014; Zolotov et al. 2015). How these mergers and disc collapse events are capable of dynamically disrupting the galaxy disc and forming ellipticals is reasonably well understood (Toomre & Toomre 1972; Mihos & Hernquist 1996). However, the origin of the transformation in colour and star-formation rate is less clear.

The star formation rate density of the Universe peaked at $z \sim 2$ (see Figure 1.8), and it has been decreasing ever since. At this epoch the Universe was intensely star forming, with stars being formed at a rate an order of magnitude higher than observed today. Roughly 50% of the stellar mass observed today formed at $z > 1$ (Madau & Dickinson 2014). Although the stellar mass in star forming galaxies has barely changed, the total mass in red and dead galaxies has grown by a factor of 2 since $z = 1$ (Bell et al. 2004; Faber et al. 2007).

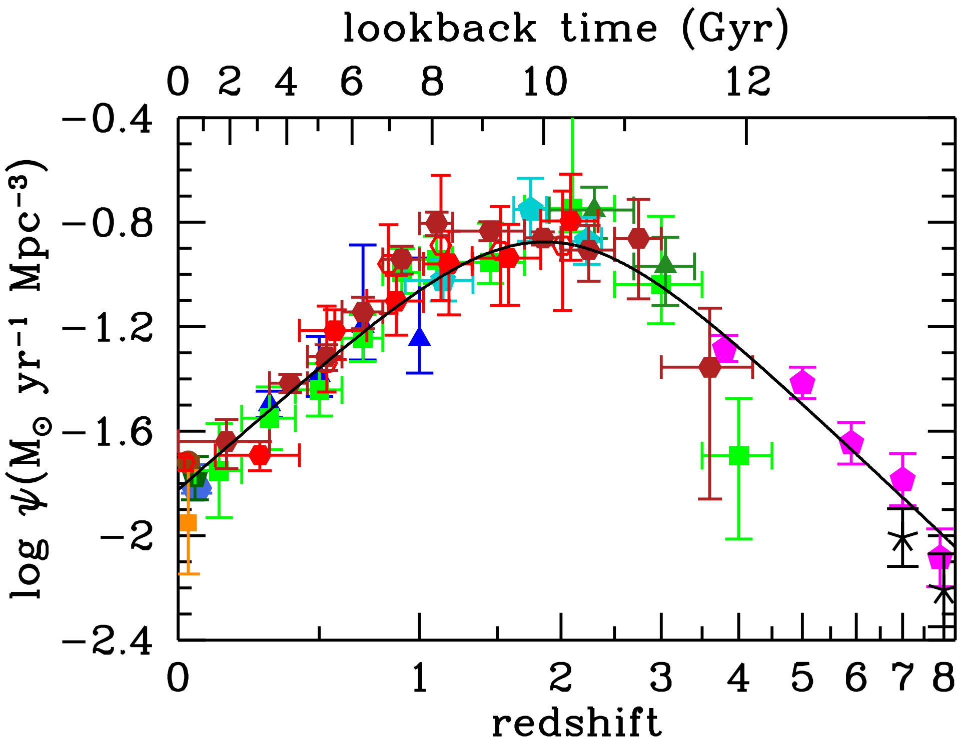

Figure 1.8. Evolution of SFR density as a function of cosmic time. This figure shows a collection of results from different studies, showing that the cosmic SFR density peaked at $z \sim 2$ (*'Cosmic noon'*). Figure and references therein from Madau & Dickinson (2014).

This scenario requires a 'quenching' mechanism that causes galaxies to cease forming stars, evolving from the blue cloud to the red sequence. The simplest case, in which galaxies use up all their fuel through star formation is highly unlikely. The dense central regions in hot haloes are efficient at cooling down gas, which falls into galaxies in the so-called cooling flows. Additionally, simulations show that the gas filaments are able to feed fresh gas from the intergalactic medium on to galaxies (Brooks et al. 2009; Kereš et al. 2009). This means that galaxies simply do not run out of gas unless some additional processes act on them to quench them.

Furthermore, given that star formation is strongly correlated with other galaxy properties (see Section 1.2), it is natural to think that the quenching mechanisms are also responsible for the morphological evolution. However, even though these properties are strongly correlated, this does not imply there is any causal link. There could be a third variable which correlates with star formation activity and morphology, without the later two being connected. This leads to the so-called 'nature' versus 'nurture' problem.

In hierarchical models of galaxy formation (e.g. De Lucia et al. 2006), those galaxies in denser environments formed earlier than their counterparts in low-density environments. Therefore, it is not surprising to find that galaxies in clusters are more evolved with older stellar populations than analogous field galaxies. Consequently, purely secular processes could account for the environmental correlations we observe in the local Universe, while environment itself has little or no direct effect on galaxy evolution.

We now introduce the main properties of both the *nature* and *nurture* scenarios:

1. Nature: galaxies are unaffected by their local environment. The observed correlations with galaxy density are driven by the fact that cluster galaxies are older than galaxies of the same mass in the field. The key parameter governing the evolution of the star formation rate is some intrinsic property to the galaxy, with the galaxy's mass often invoked as the main driver. Galaxies evolve though internal processes (such as AGN or stellar feedback).

2. Nurture: environment directly affects galaxies, which results in the observed trends with local density. Environmental processes are responsible for the evolution in galaxy properties such as the star formation rate, morphology and colour.

However, *nature* and *nurture* are not mutually exclusive. It is much more likely that quenching is triggered via a combination of both secular and environmental processes. Peng et al. (2010) conducted a fully empirical approach in order to study the dependence of star formation rates on galaxy stellar mass and environmental density. They conclude that there are two independent quenching processes that halt star formation in galaxies. Their main finding can be summarised as follows: (see Figure 1.9) massive galaxies are likely to be quenched regardless of their environment ('mass quenching') and galaxies in high-density environments are also likely to be quenched independently of their stellar mass ('environmental quenching').

1.3.1 Mass quenching

According to the model of Peng et al. (2010), the more massive a galaxy is the more likely it is to be quenched. Here we present a list of possible mechanisms that can cause mass quenching.

1. *Hot halo.* When intergalactic gas falls towards the centre of a galaxy its gravitational energy turns into heat. For haloes with masses above $\sim 10^{12} M_{\odot}$ the infalling gas cannot cool down quick enough and forms a halo of hot gas embedded in the dark matter halo (Birnboim & Dekel 2003; Kereš et al. 2005; Dekel & Birnboim 2006). Any further accretion of cold gas by the system is rapidly shock-heated and, therefore, prevented from forming stars. However, virial shock heating on its own is not enough to explain quenching. The gas in the centre of these hot haloes eventually cools down (on timescales of $\sim$ 2 Gyrs) through radiative cooling, which would trigger star formation in the centre. Therefore, some additional heating mechanisms might be required.

2. *AGN feedback.* When the super massive black hole in the centre of a galaxy accretes matter it injects large amounts of energy into its surroundings. The energetic jets of gas that originate near the black hole have the potential to heat up or even eject part of the interstellar medium, which may lead to premature quenching (Silk & Rees 1998; Hopkins et al. 2005). However, the role of AGN on galaxy evolution is still unclear. Some authors suggest that AGN feedback

may not be the main mechanism responsible for quenching galaxies but it might play an essential role in keeping them quenched (Best et al. 2005; Croton et al. 2006; Best et al. 2006; McNamara & Nulsen 2007). Croton et al. (2006) suggested that the slow cooling of gas in massive haloes may trigger low-luminosity AGN (also called 'radio mode' feedback), which transfers energy to the surroundings preventing further cooling and star formation.

However, more recent studies point in the direction of positive feedback. It has been found that in certain cases both radio and quasar modes can create shock waves that compress gas and facilitate star formation (Gaibler et al. 2011; Zubovas et al. 2013).

3. *Stellar feedback.* In starburst galaxies, the energy and momentum generated by supernova explosions and stellar winds can produce significant outflows (Chevalier & Clegg 1985; Leitherer et al. 1992; Diamond-Stanic et al. 2012). This could have a similar effect to AGN feedback. Strong stellar feedback is vital in current galaxy formation models to suppress the formation of low-mass galaxies.

4. *Disc instability.* Another proposed mechanism consists of the catastrophic collapse of a galactic disc that has become unstable. If a disc grows above a certain mass threshold it becomes unstable (Dekel et al. 2009). Additionally, clumpy accretion or gravitational interactions can have the same effect. The collapse of the disc is likely to produce a starburst that rapidly depletes the gas in the galaxy, leading to quenching.

1.3.2 Environmental quenching

There is a multitude of proposed quenching mechanisms linked to galaxy environment (see Figure 1.10), trying to explain the observed correlation between galaxy properties and environment. Most of these mechanisms fall in two groups: galaxy-galaxy interactions and interactions with the intra-cluster medium (ICM). In dense environments, a large number of galaxies share a relative small space, therefore, interactions between them are frequent. Additionally, galaxy clusters develop an ICM of hot diffuse gas, which can interact with newly accreted satellites, as we describe in the following sections. There are a number of review papers on the topic of environmental dependence of galaxy evolution (see Treu et al. 2003; Poggianti 2006; Boselli & Gavazzi 2006).

The processes that refer to gravitational interactions between two or more galaxies are the following:

(a) *Mergers.* This is the strongest kind of interaction galaxies can undergo and it results in the merging of the respective stellar distributions (Icke 1985; Bekki 1998). The merger cross section is inversely proportional to the galaxy velocity dispersion. Therefore, galaxy mergers are more frequent in small groups than in massive cluster cores, where the relative velocities of the galaxies are too high (Ostriker 1980; Makino & Hut 1997).

There are two main classification schemes for galaxy mergers. One is based on the mass ratio of the merging galaxies:

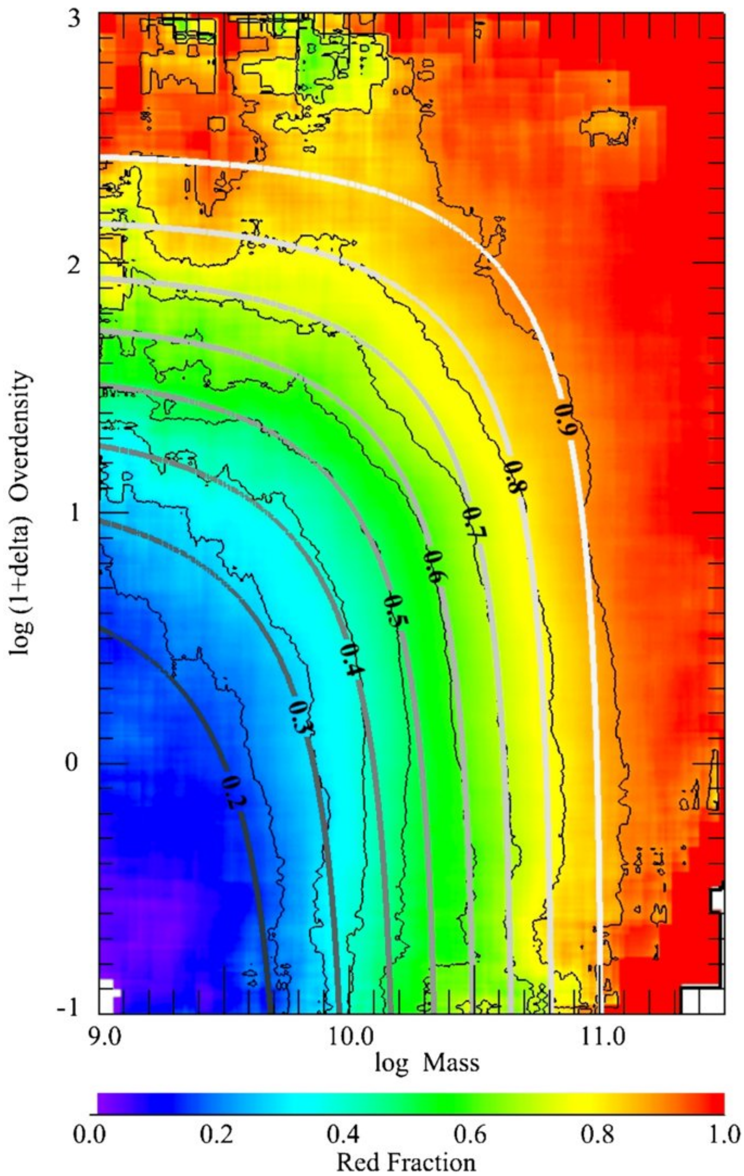

Figure 1.9. Fraction of red galaxies in SDSS as a function of stellar mass and environment. The red fraction is independently proportional to both stellar mass and environmental density. This suggests that there are two quenching processes responsible for ceasing star formation in galaxies: mass quenching and environmental quenching (Peng et al. 2010)

(i) *Major mergers:* the two merging galaxies have similar masses. Such events lead to strong structural changes in the stellar distribution of the galaxies involved (Toomre & Toomre 1972; González-García & Balcells 2005).

(ii) *Minor mergers:* when a low-mass galaxy is 'accreted' by a more massive one. The typical mass ratio for this kind of merger is 4:1 or larger. The smaller companion is completely disrupted as a result of the interaction and may produce a stellar envelope or outer disc around the more massive galaxy (Younger et al. 2007; Naab et al. 2009).

The second scheme is based on the gas content of the merging galaxies:

(ii) *'Wet' mergers:* merging of gas-rich galaxies. The interaction and compression of the gas dissipates a significant fraction of the kinetic energy. Furthermore, the gas is funnelled into the galactic centre leading to a nuclear starburst and, therefore, the galaxy remnant tends to be compact (Mihos & Hernquist 1996; Barton et al. 2000).

(i) *'Dry' mergers:* merger of gas-poor galaxies (van Dokkum 2005; Bell et al. 2006). These mergers are also known as *dissipationless*, since given the lack of gas, little energy is lost in triggering star formation. Hence, these events lead to the expansion of the stellar distribution of the remnant galaxy.

(b) *Tidal interactions.* Long distance gravitational interactions between two or more galaxies. These encounters can occur at high and low velocities, which affects the likely outcome of the interaction.

(ii) *High-speed interaction (galaxy harassment):* repeated quick encounters between galaxies with high relative velocities (like those found in galaxy cluster cores; Moore et al. 1996). The impact of a single encounter is reduced as they are short-lived, however, multiple interactions of this kind are thought to gradually build a bulge component and potentially disturb the gas component.

(i) *Low-speed interaction:* low-speed encounters that do not result in a merger. These events are thought to be more prevalent in group-like environments. Due to the low-speed nature of these events, galaxies have more time to interact, producing more dramatic effects, such as tidal stripping.

The second kind of environmental interactions are those between infalling galaxies (satellites) and global cluster properties, such as the ICM or the potential well.

(c) *Ram-pressure stripping:* the removal of the cold gas reservoir as a result of ram pressure exerted by the ICM (Gunn & Gott 1972). Since the galaxy is deprived of the fuel for star formation, its star formation rate falls quickly (on timescales of hundreds of Myrs; Steinhauser et al. 2016). However, in the initial stages of the stripping process, the gas may be partially compressed triggering some star formation (Dressler & Gunn 1983; Evrard 1991).

(d) *Strangulation:* The ram pressure exerted by the ICM is not always strong enough to remove the interstellar medium (ISM). Nonetheless, in most cases it is enough to sweep the diffuse circumgalactic medium (CGM) away. The galaxy remains star forming as there is still cold gas available. However, the absence of CGM means that the ISM will not be replenished and the galaxy quenches once it has used up the remaining gas (Larson et al. 1980). This process operates on timescales > 1 Gyr.

(e) *Thermal evaporation:* The interaction of the hot ICM heats up the ISM (Cowie & Songaila 1977), preventing the gas from collapsing into stars.

(f) *Tidal interactions:* The interaction between an infalling galaxy and the gravitational potential of the cluster can disturb the distribution of gas and/or stars in the galaxy. For example, it could lead to tidal compression of the galactic gas (Byrd & Valtonen 1990; Henriksen & Byrd 1996), which would potentially enhance star formation. Another effect this kind of interaction could have is the tidal truncation of the outer galactic regions (Merritt 1983, 1984), causing the removal of the outer hot gas reservoir (strangulation).

Figure 1.10. Cartoon illustrating the main environmental processes that are believed to have an impact on the star formation rate of a galaxy. These include interactions between individual galaxies (such as harassment or merging), interactions between the galaxy and the intra-cluster medium (ram-pressure stripping, starvation or thermal evporation) and interaction with the cluster potential well (tidal truncation). Credit: Aeree Chung.

1.4 Transition galaxies: Post-starburst galaxies

A popular approach to understand what drives the galaxy bimodality is to identify transitioning objects. Some of these galaxies may not obey the bimodality and have intermediate properties between the red sequence and the blue cloud (known as 'green valley' galaxies). Such galaxies may be in the process of terminating their star formation and they could show traces of the mechanisms that caused it. Another example of transiting galaxies consists of galaxies that have very recently reached the 'red sequence'. These look like passive galaxies in some aspects (colour or SFR), however, having been quenched so recently they may retain features directly related to the quenching event. One such example is post-starburst galaxies.

Post-starburst galaxies (PSBs; often referred to as "k+a" galaxies) are characterised by the presence of strong Balmer absorption lines in their spectra (Dressler & Gunn 1983; Wild et al. 2009). This Balmer absorption is produced by a residual population of A stars overlaid on a rather passive-looking spectrum (see Figure 1.11). The typical lifespan of this type of star is short (~ 1 Gyr), meaning that the visual signatures of PSBs are also short-lived. Consequently, PSBs are a rare population at all epochs, accounting for less than 5% of the entire galaxy population (Goto et al. 2003; Wild et al. 2009; Alatalo et al. 2016). Nevertheless, one of the most interesting properties of PSB galaxies is that they are transition objects. The lack of bright O and B stars indicates that the galaxy is no longer forming new stars. In contrast, the presence of A stars implies that PSBs had been star forming and formed a significant fraction of their stellar mass during the last Gyr (Norton et al. 2001; Yang et al. 2004; Kaviraj et al. 2007). Therefore, this type of galaxy must have had its star formation rapidly and recently truncated. This makes PSBs the ideal subjects to study the mechanisms responsible for galaxy quenching.

Although PSBs present, by definition, the same spectral features across all redshifts, their formation mechanisms are thought to differ across redshift and environment. At low redshift ($z < 0.5$), most of the studied PSBs are typically massive and found in field-like environments (Zabludoff et al. 1996; Tran et al. 2004; Quintero et al. 2004) and exhibit disturbed morphologies suggesting they could be the remnants of gas-rich mergers, which trigger a starburst followed by an abrupt quenching (Yang et al. 2004; Goto et al. 2004; Wild et al. 2009; Cales et al. 2011; Cales & Brotherton 2015). In contrast, at intermediate redshifts ($0.5 < z < 1.0$) PSBs are ubiquitous in cluster environments (e.g. Poggianti et al. 2009) and tend to have lower stellar masses (Wild et al. 2016; Maltby et al. 2016; Socolovsky et al. 2018). At high redshift ($z > 1$) they seem to be the massive remnants of major starbursts (Almaini et al. 2017), potentially driven by mergers and the vast amount of gas available at this redshifts.

Active galactic nuclei (AGN) feedback is often invoked as a quenching agent in simulations (Narayanan et al. 2008), removing the residual gas and dust after the starburst. However, from the observational point of view there is conflicting evidence showing either a prevalence of AGN in low-redshift field PSBs (e.g. Schawinski et al. 2009; Alatalo et al. 2011; Cicone et al. 2014) or a lack of AGN activity altogether (e.g. Fabello et al. 2011; French et al. 2015; Geréb et al. 2015; Rowlands et al. 2015). On top of this, some studies have found that field PSBs host substantial gas reservoirs, even up to 1 Gyr after the starburst event, suggesting that these galaxies may not be deprived of their residual gas and have the potential to form new stars (Zwaan et al. 2013; Rowlands et al. 2015; French et al. 2015; Alatalo et al. 2016).

These contradicting results are likely to be a consequence of their different selection techniques. For example, the wealth of good quality spectra sampling the 4000 Å at low redshift enables the robust identification of PSBs, however, it is likely to be biased towards massive galaxies. On the other hand, very few spectroscopically identified PSBs exist at $z > 1$ (Vergani et al. 2010). In order to study PSBs in a consistent way across redshift and mass it is necessary to resort to photometric classification methods. Two techniques that have proved successful at this task are the one described in Whitaker et al. (2012), which consists in identifying the youngest component of the red sequence using the widely accepted rest-frame UVJ diagram; and the more recently developed one by Wild et al. (2014), using a principal component analysis of the spectral energy distribution (SED). The latter is the one used in this thesis and we provide more details in the next chapter, Section 2.2.

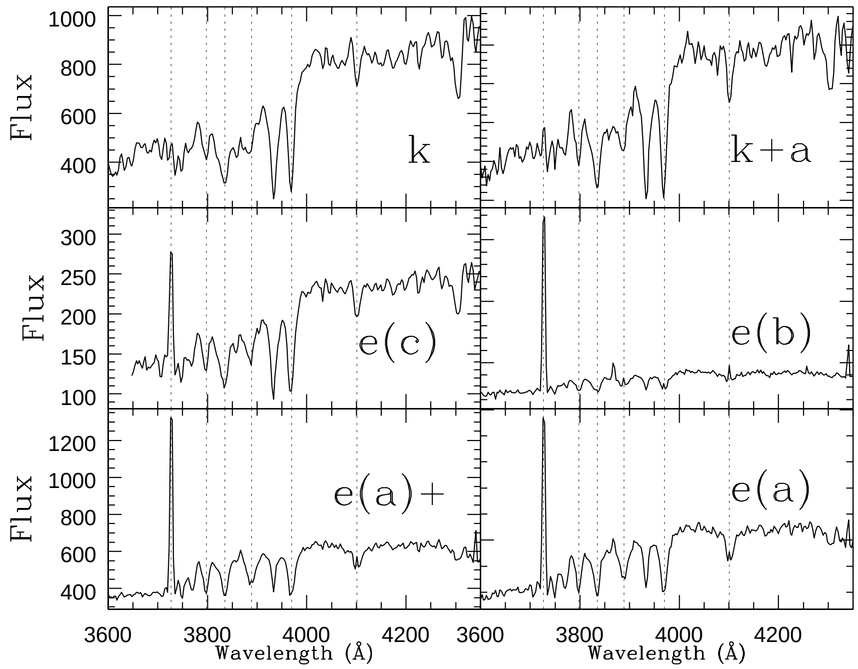

Figure 1.11. Characteristic spectrum of PSB galaxies ("k+a" galaxies in this figure) compared to the spectrum of a typical passive ("k"), star-forming ("e(c)"), starbursting ("e(b)") and dust-obscured starbursting ("e(a)" and "e(a)+") galaxy. The figure is obtained from Poggianti et al. (2009).

1.5 Aim and structure of this thesis

The aim of this Thesis is to investigate the effects of environment on galaxy evolution at $z > 0.5$. In particular, we study the effect of galaxy environment on different galaxy populations (passive, star-forming and post-starburst) by investigating the stellar mass function and galaxy structure. The galaxy classification is based on a Principal Component Analysis (PCA) of model SEDs applied to the photometric data from the UKIDSS Ultra Deep Survey (UDS). For our environmental measure we identify a sample of galaxy clusters at $0.5 < z < 1.0$ using a friends-of-friends algorithm, which we complement with a measurement of the local density at $z > 1.0$. These methods allow us to compare the above-mentioned galaxy properties across environments. We now break these goals down into the separate chapters of this Thesis.

In Chapter 2 we describe the data we use in this Thesis, which corresponds mostly to the work carried out by third parties. These include the galaxy catalogues (photometry, photometric redshifts and stellar masses) derived from the 8th and 11th data releases of the UDS. I will also describe the galaxy classification method, which is based on the application of a PCA to the photometric data of the UDS.

In Chapter 3 we review the most used methods to measure galaxy environment in deep photometric surveys. We then provide a description of our own cluster-finding method, published in Socolovsky et al. (2018). Here we show how the algorithm's parameters are optimised using simulations of mock clusters and the tests we run to reject the spurious detections. After this we use spectroscopic redshifts to confirm some of our structures. Finally, we compare our cluster sample with previous studies carried out in the same field using different methods.

In Chapter 4 we focus on the effects of environment on the stellar mass function at $0.5 < z < 1.0$. This work was published in Socolovsky et al. (2018). We also study the distribution of star-forming, passive and PSB galaxies in clusters as a function of cluster-centric distance. These tools allow us to investigate the potential quenching pathways that galaxies can take after they are accreted into a cluster and the corresponding timescales.

Chapter 5 is the continuation of the work initiated in the previous chapter. Here, we study the relationship between environment and the structure of star-forming and PSB galaxies at $0.5 < z < 1.0$, which will be presented in Socolovsky et al. (submitted). Adding structural information to the previous analysis helps us to better constrain the environmental quenching mechanisms.

In Chapter 6 we extend the analysis of the stellar mass function to $z = 3$. In addition, we use a fixed-aperture method to determine galaxy number densities and trace galaxy environment between $0.5 < z < 3.0$. This allows us to study the redshift evolution of environmental quenching and, potentially, estimate the epoch when environmental effects become significant.

We summarise our results and conclusions in Chapter 7 and also discuss future work.

Throughout this thesis, we use AB magnitudes and adopt a ΛCDM cosmology with the following parameters: $\Omega_M = 0.3$, $\Omega_\Lambda = 0.7$ and $H_0 = 70$ kms^{-1}Mpc^{-1}.

Chapter 2

The UDS and galaxy classification

The work presented in this thesis is predominantly based on the data obtained from the UKIDSS Ultra Deep Survey (UDS). In Section 2.1 of this chapter we describe the survey and the galaxy catalogues used throughout this thesis. In Section 2.2 we outline the photometric classification method we use to separate our galaxy sample into passive, star-forming and post-starburst galaxies. This classification method (developed in Wild et al. 2014) is based on a Principal Component Analysis (PCA) which is applied to the photometry of the UDS. The work presented in Chapters 3 and 4 uses solely the data derived from the 8th UDS data release. The final UDS data release (DR11) was made public in July 2016, and has allowed us to use significantly deeper images to estimate the structural parameters used in Chapter 5. However, for the work in Chapter 5, photometric redshifts, stellar masses and galaxy classification are still derived from DR8 data. In Chapter 6, photometric redshifts, galaxy properties and PCA classifications were derived using the deeper DR11.

This chapter presents the data used throughout this thesis. Although most of the work presented in this chapter was not carried out by me, it is highly relevant for this thesis, as it describes the origin and nature of our data. Only the comparison between the PCA and the classic UVJ methods (Section 2.2.3) and the determination of the stellar mass limits (Section 2.3) are part of my own work. Credit is given to the authors who did the relevant work in the corresponding sections.

2.1 The Ultra Deep Survey and photometric catalogues

2.1.1 The Ultra Deep Survey

This work is based on the Ultra Deep Survey (UDS; Almaini et al. in preparation). The UDS is centred at RA $= 02:17:48.1$ and Dec $= -05:05:44.9$, and covers an area of ~ 0.77 deg^2 on the sky, and is the deepest component of the UKIRT (United Kingdom Infra-Red Telescope) Infrared Deep Sky Survey (UKIDSS; Lawrence et al. 2007). The UDS consists of deep near-infrared imaging in the JHK photometric bands, and is the deepest near-infrared survey to date over such a large area.

The total integration time is over $\sim$1,000 hours (480 in K, 210 in H and 330 in J); taken over an 8-year period from 2005 to 2013. The UDS is made up of 10-second exposures with 3×3 microstepping (to sample the PSF) and 9-point dither pattern. This leads to a basic exposure unit of $81 \times 10 = 810$ seconds. These are the minimum blocks that are processed and stacked together to produce the UDS images. A summation stack is used with a conservative 5σ clipping to remove the most extreme artefacts, satellite trails and cosmic rays. Other artefacts are masked out in the final image or removed at the earlier quality control stage.

The instrument used to take the images is the UKIRT infrared Wide-Field Camera (WFCAM; Casali et al. 2007, for details), which consists of four 2k $\times$ 2k HgCdTe Rockwell Hawaii-2 infrared detectors. These detectors are separated by 90% of the size of one detector from each other; therefore, in order to map the entire 0.8 square degree region, four separate pointings were needed.

2.1.2 The UDS DR8

The UDS DR8 catalogue reaches 5σ depths of $J = 24.9$, $H = 24.2$ and $K = 24.6$ (all AB and 2 arcsec apertures).

Masks were applied to the optical and JHK images in order to remove artefacts. Masked features include bright stars, stellar haloes, diffraction spikes, cross talk, CCD bleeds and faulty pixels. Finally, stars are identified and removed from the source catalogue according to the method described in Simpson et al. (2013)

The UDS is complemented with imaging from other multiwavelength deep photometric surveys (see Figure 2.1). Deep optical imaging is available from the Subaru *XMM–Newton* Deep Survey (SXDS; Furusawa et al. 2008; Ueda et al. 2008), with 5σ depths of $B = 27.6$, $V = 27.2$, $R = 27.0$, $i' = 27.0$ and $z' = 26.0$. Deep U-band imaging is provided by the Canada-France-Hawaii Telescope (CFHT), to a depth of $U = 26.75$ to 5σ and the *Spitzer* Legacy Program (SpUDS, PI: Dunlop) provides $[3.6] = 24.2$ and $[4.5] = 24.0$ at 5σ. This wealth of multiwavelength data is crucial for the derivation of well-defined SEDs, and therefore, accurate photometric redshifts and stellar masses. The combined area, after masking, covers ~ 0.62 square degrees.

The source catalogue we use is K-band selected. Hence, the catalogue was extracted by running SExtractor on the K-band. 3 arcsec apertures are then placed in order to measure fluxes and determine magnitudes. After this, a magnitude cut of $K = 24.3$ was applied to ensure a detection completeness of at least 95%. This magnitude limit was determined from simulations. Fake galaxies were inserted into an image and SExtractor was re-run in order to measure what fraction of mock sources was recovered (for more details see Hartley et al. 2013).

The K band was chosen as the detection band because it provides the best selection by stellar mass for high-redshift galaxies. Therefore, observations in K were conducted in the best seeing and with the longest exposure time. Consequently the K-band presents the smallest PSF, ~ 0.76 arcsec (FWHM), in contrast with the J and H bands, $\gtrsim 0.8$ arcsec. Since the UDS is a mosaic constituted by 16 sub-regions, corresponding to four pointings of the four detectors that make up the WFCAM, with a small overlap for the contiguous tiles, the PSF was analysed independently for each region. The procedure to measure the small variation of the PSF across the field is outlined in Lani et al. (2013). The PSF was calculated using the stacked light profiles of approximately 100 stars within each sub-region.

The DR8 catalogues are used in Chapters 3, 4 and 5, where we investigate environmental quenching in the redshift interval $0.5 < z < 1.0$.

2.1.3 The UDS DR11

The DR11 is the final data release of the UDS. It benefits from the same multiwavelength coverage as DR8, with the addition of a Y filter from the Visible and Infrared Survey Telescope for Astronomy (VISTA) Deep Extragalactic Observations

(VIDEO; Jarvis et al. 2013). In this section we describe the main improvements of the new DR11 catalogue with respect to DR8 (see Table 2.2 for a comparison summary of these two catalogues). The improvements made for DR11, including the background subtraction and the determination of photometric redshifts, will be described in Almaini et al. (in preparation).

First of all, the new JHK images, which were made public in July 2016, are significantly deeper than the previous DR8, with depths of $J = 25.6$, $H = 25.1$ and $K = 25.3$ (AB and 2 arcsec). In addition to the multiwavelength coverage in 11 broad-band filters, outlined in the previous section, DR11 benefits from deep imaging in the Y band from VIDEO ($Y = 24.4$; AB and 2 arcsec). The addition of this filter is key for determining accurate photometric redshifts at $z \gtrsim 1$, as it probes the Balmer break part of the spectrum at this redshift.

The masking was also improved. The JHK masks were re-made, while the IRAC images were masked for the first time. The rest of the optical masks remained the same, with the addition of the Y-band mask. As a result of the additional masking, the effective area of the survey is slightly reduced to 0.59 square degrees.

The background subtraction is possibly the most significant improvement with DR11. In previous releases the sky was slightly over-subtracted, which was driven by faint undetected sources and residuals from the outer parts of detected bright sources. For DR11, the faintest objects were identified and removed by stacking the JHK images, which allows us to reach as deep as possible. Furthermore, residuals from brighter objects were removed by artificially expanding the segmentation maps for these sources. The new sky background subtraction was tested by ensuring that the outer parts of stellar light profiles remain constant as a function of magnitude. This meticulous determination of the background level was applied to all photometric bands, which significantly improves the quality of the catalogues derived from them. The effect of over-subtracting the sky light can lead to an underestimation of the flux of faint objects (at $K = 25.0$) of approximately 25%.

Another important improvement is the recalibration of the WFCAM zero-point. Small ($1 - 2\%$) systematic differences were detected and corrected between the four detectors of the infrared camera. In previous releases this effect was not accounted for, meaning that the zero-point varied slightly across the field.

Finally, the source catalogues were extracted by running SExtractor on the K-band image and magnitudes were measured by placing 2 arcsec apertures around the detected sources in all photometric bands. The images are previously corrected for PSF effects, i.e. all the input optical/IR images were convolved to ensure they had the same PSF. The K-band limit to ensure a 95% detection completeness was estimated to be $K = 25.0$ (Hartley et al. in preparation).

2.1.4 The UDSz

The UDS field is almost entirely covered by the UDSz (180.A-0776; PI: Almaini), a spectroscopic survey which combines optical spectra obtained using the VIsible MultiObject Spectrograph (VIMOS) and FORS2 instruments from the European Southern Observatory Very Large Telescope. In order to exploit the strengths of both instruments, VIMOS was used to target optically bright galaxies ($i' < 24$ or $V < 25$) while FORS2 was used for fainter and redder objects ($i' < 24$ and $V > 24$).

The UDSz programme was awarded a total of 235 hours of observing time. Of this time, 93 hours (8 pointings) were allocated to the VIMOS spectrograph, covering and area of 0.5 square degrees across the UDS field. The multi-object mode was

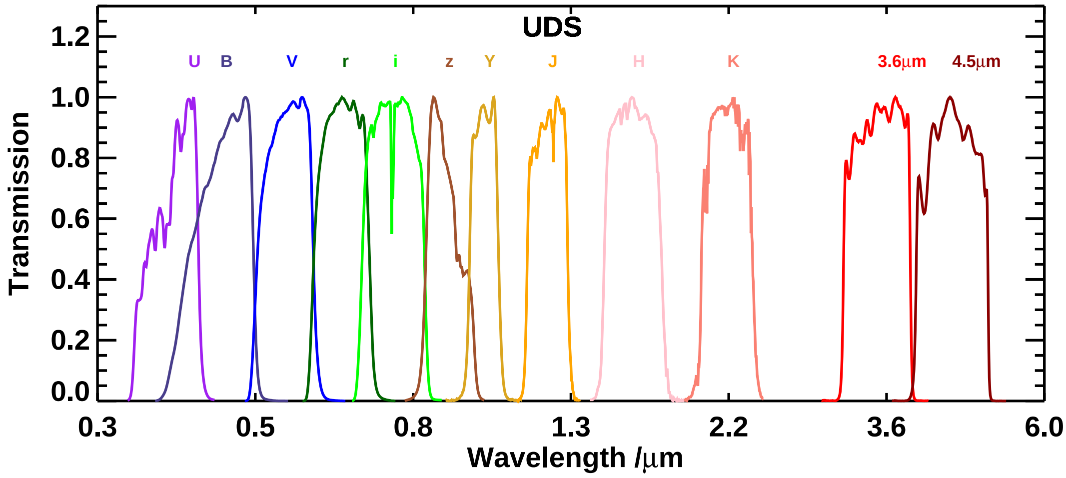

Figure 2.1. Transmission response curves as a function of wavelength for each of the UDS filters. Note that the Y-band is only available for the DR11.

employed, typically observing over 300 objects per pointing. The LR blue and LR red grisms were used, with resolving powers of $R = 180$ and 210, respectively. The usage of both grisms together offered a wavelength coverage of $3700 < \lambda < 9500$ Å. The remaining 142 hours (20 pointings) were allocated for the FORS2 instrument, which observed roughly 40 galaxies per pointing using the medium-resolution GRT-300I grism ($R = 660$) with coverage $6000 < \lambda < 10000$ Å. In total, 2881 galaxies were targeted with VIMOS and 802 with FORS2.

The main goal of UDSz was to target $K < 23$ galaxies in order to provide a representative spectroscopic sample of the K-band selected galaxies in the UDS. These targets were photometrically pre-selected to lie at redshift $z_{\rm phot} \geq 1$, with a control sample at $z_{\rm phot} < 1$. In this thesis, these spectra are used for the spectroscopic confirmation of our galaxy cluster sample in Chapter 3, and in Chapter 5 where we look for outflow signatures in star-forming galaxies.

2.1.5 Photometric redshifts and stellar masses

In this section I summarise how the photometric redshifts and stellar masses are determined for the galaxies in our catalogue; the full description of the process can be found in Simpson et al. (2013).

Photometric redshifts were obtained by fitting template spectra to the spectral energy distributions (SEDs) constructed using all 11 photometric bands : U, B, V, R, i', z', J, H, K, 3.6μm and 4.5μm (DR11 also uses Y). The SED-fitting software used was the EAZY photometric redshift code (Brammer et al. 2008). The photometric redshift determination was performed by fitting linear combinations of six solar metallicity simple stellar population templates (Bruzual & Charlot 2003) with a Chabrier (2003) initial mass function (IMF), with ages logarithmically spaced from 30 Myr to 10 Gyr. Dust absorption was taken care of by including three dust-reddened templates using a Small Magellanic Cloud extinction law.

In addition to the deep multiwavelength photometry, the UDS field benefits from approximately 1500 spectroscopic redshifts from the UDSz (described in Section 2.1.4) and 3500 from the literature (Simpson et al. 2012). These were used to test the reliability of the photometric redshifts. The measured median absolute deviation on $\Delta z/(1+z)$ is $\sigma_{\mathrm{NMAD}} \sim 0.023$ for DR8 and $\sigma_{\mathrm{NMAD}} \sim 0.0183$ for DR11. Galaxy redshifts were fixed to the spectroscopic values, where available, otherwise photometric redshifts were assumed.

The stellar masses are also calculated in Simpson et al. (2013) by fitting a much finer grid of synthetic SEDs covering the same age range, and including a larger number of young reddened templates, using a Chabrier (2003) IMF. The redshift was fixed to the spectroscopic, when available, otherwise the best-fitting photometric redshift was used. Furthermore, only those templates whose age was less than the age of the Universe at the given redshift were fitted, to ensure the estimated star-formation histories were valid.

2.2 PCA method

Although galaxy classification would ideally be performed spectroscopically, it is practically impossible to obtain spectra for all the objects in large-area deep surveys, like the UDS. Not only it is extremely costly in terms of time and resources, but measuring the spectrum of the faintest objects is nearly impossible. Therefore, we need to resort to photometric methods (i.e. SED fitting) in order to determine the properties of large numbers of galaxies (da Cunha et al. 2008; Noll et al. 2009; Acquaviva et al. 2011). However, SED fitting is strongly dependent on the accuracy of spectral synthesis models and it is subjected to numerous degeneracies between redshift and physical properties. The traditional colour–colour diagrams are probably the most widely used method to classify galaxies photometrically. However, the determination of rest-frame colours requires the use of spectral synthesis models.

One alternative to the previous methods is the application of Principal Component Analysis (PCA). The PCA is a technique very widespread in the field of statistics. It is used to reduce the number of parameters required to describe a system. This is done by identifying the optimal set of variables that effectively describe the properties of the system. In the particular case of classifying galaxy SEDs, the PCA determines which features of the SED vary the most between modelled galaxies of different types. Then it derives the principal components (or eigenvectors) that produce the variance of these features.

The application of the PCA to the photometric data of the UDS (described in Wild et al. 2014) provides the optimal combination of colours (i.e. the eigenspectra) that best reproduce the full shape of the galaxy SEDs. In order to do this it is crucial to sample in detail the full range of SEDs. This is done by finely sampling model SEDs using all the photometric bands available in the UDS and at the targeted redshift range. A grid of 44,000 stochastic burst model SEDs from Bruzual & Charlot (2003) was used. These models assumed an exponentially decaying star formation rate superposed with stochastic bursts of star formation of varying strength. Star formation rates and metallicities were randomly sampled using a flat prior. The dust attenuation prescription was taken from Charlot & Fall (2000). The model SEDs are then convolved with the filter responses corresponding to the photometry in the UDS field and shifted in intervals of $\Delta z = 0.01$ in the redshift range $0.5 < z < 2.0$ (DR8; Wild et al. 2014, 2016) and $0.5 < z < 3.0$ (DR11; Wilkinson in prep.).

As outlined in Wild et al. (2014), the PCA is applied to the differences of each model SED from the median spectrum (m_λ), all SEDs are normalised at 1 μm. It is found that linear combinations of only three eigenvectors ($e_{i\lambda}$; presented in Figure 2.2) are enough to account for 99.98% of the variance in the modelled SEDs.

Therefore, linear combinations of these three eigenvectors can accurately reproduce a galaxy normalised SED $\left(\frac{f_\lambda}{n}\right)$:

$$\frac{f_\lambda}{n} = m_\lambda + \sum_{i=1}^{3} a_i e_{i\lambda}, \tag{2.1}$$

where a_i are the principal component amplitudes (supercolours; SC) associated with each of the eigenvectors. The first supercolour, $SC1$, modifies the red-blue slope and is strongly correlated with the R-band weighted mean stellar age or specific star formation rate (SSFR). Supercolour $SC2$ alters the strength of the Balmer break and correlates with the fraction of the stellar mass formed in bursts during the last billion years, and also traces metallicity. Supercolour $SC3$ affects the shape of the SED around 4000 Å and is used to break the degeneracy between metallicity and the fraction of the stellar mass formed in bursts during the last Gyr (these correlations can be seen in Figures 2.3 and 2.4).

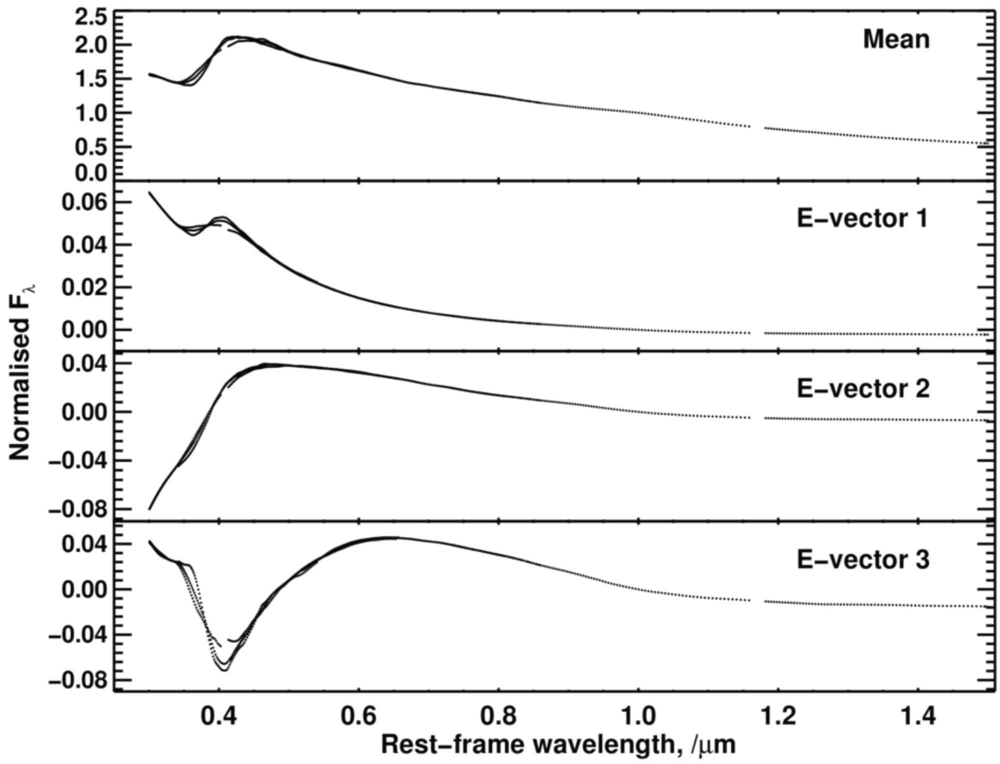

Figure 2.2. The mean normalised SED and the first 3 eigenvectors from the PCA of a library of Bruzual & Charlot (2003) model SEDs. The addition of the mean and combinations of the eigenvectors builds the shapes of the different SEDs of the galaxies in the UDS DR8. The first eigenvector modifies the red-blue slope, while the remaining two parametrise the strength and shape of the 4000 Å/Balmer break region. This plot is taken from Wild et al. (2014).

In order to determine the nature of our galaxies, the classification is based on the position of galaxies in SC-SC diagrams (typically SC1-SC2 and SC1-SC3; see Figures 2.3 and 2.4, respectively) and the boundaries between populations are determined empirically using the model SEDs adopted to obtain the SCs and spectroscopy (see Wild et al. 2014). Figures 2.3 and 2.4 show how the three supercolours correlate with the physical properties of the models (r-band light-weighted mean stellar age, metallicity, total effective dust attenuation and fraction of the mass formed during the last Gyr). It is clear that $SC1$ correlates with mean stellar age, while $SC2$ shows strong trends with metallicity and burst fraction. Additionally, the most dust-reddened objects are localised at low values of both $SC1$ and $SC2$. The third supercolour, $SC3$, also correlates with metallicity and burst fraction, nonetheless, the former is a negative correlation while the second is positive, allowing us to break the degeneracy between these two properties. Therefore, based on these trends boundaries across the SC-space are placed dividing the galaxy sample according to their physical properties. This method divides the population into star-forming (SF), passive (PAS), post-starburst (PSB), metal-poor and dusty galaxies. Additionally, the SF population is also divided into three subpopulations of decreasing SSFR: SF1, SF2 and SF3.

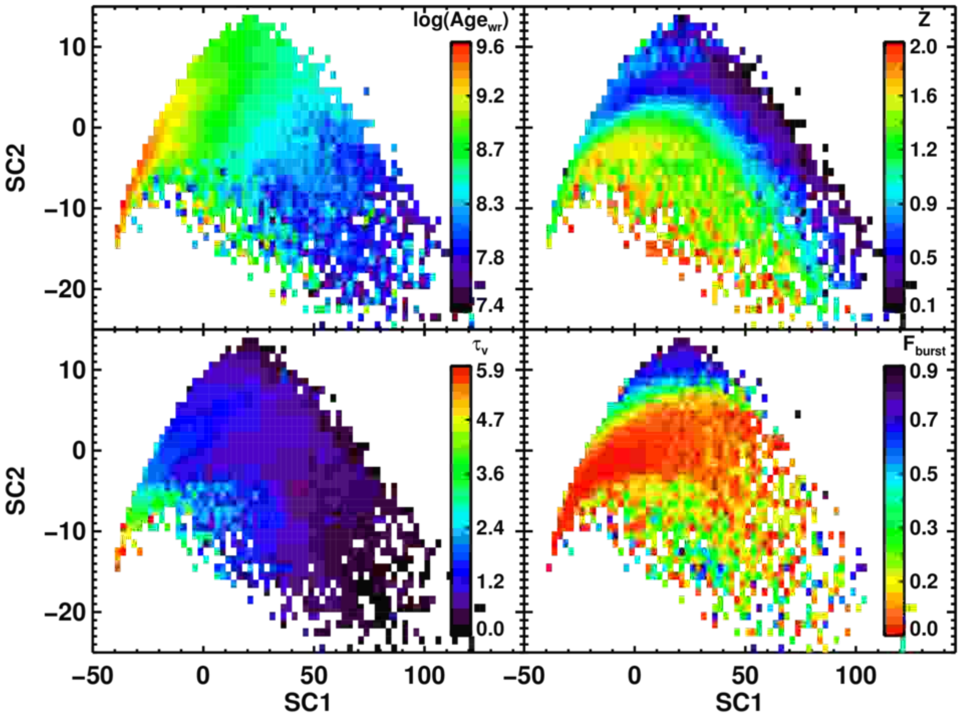

Figure 2.3. Super colour diagrams (SC1-SC2) for model SEDs in the UDS DR8, from Wild et al. (2014). The diagrams are colour-coded with the mean value of different physical properties from the models. From left to right, and top to bottom: log of the r-band weighted mean stellar age (yr), metallicity (relative to solar), total effective V-band optical depth affecting stars younger than 10^7 yr ($= 0.92A_V$, where A is attenuation in magnitudes) and fraction of stellar mass formed in bursts in the last Gyr.

2.2.1 Spectral confirmation of the PCA classification

Several studies have made use of the large number of spectra available in the UDS to test the robustness of the PCA classification method. The sample of galaxy spectra

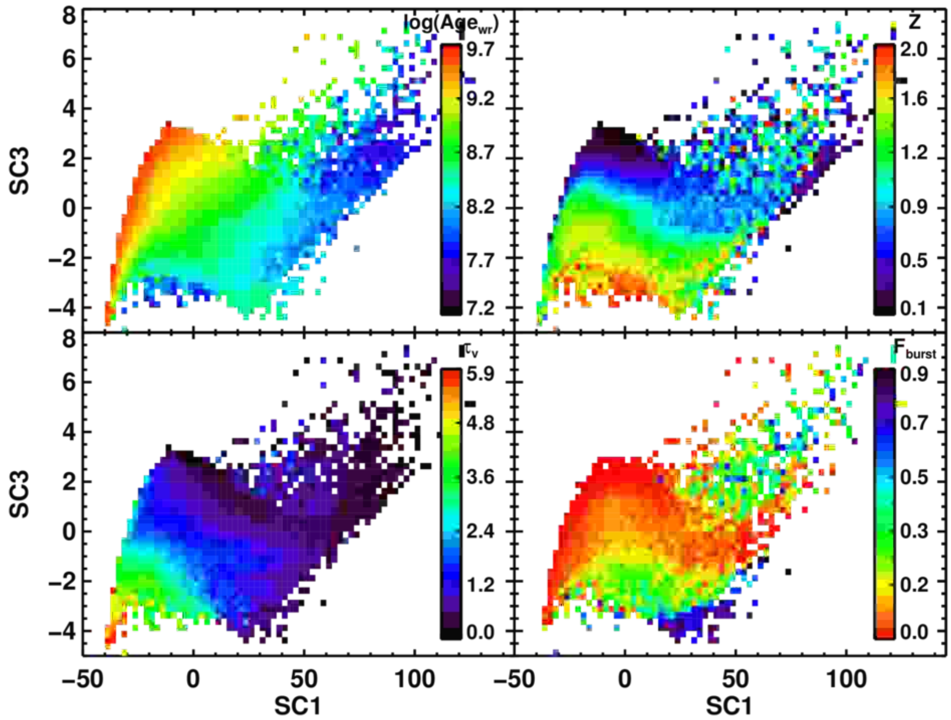

Figure 2.4. Super colour diagrams (SC1-SC3) for model SEDs in the UDS DR8, from Wild et al. (2014). The diagrams are colour-coded with the mean value of different physical properties from the models. From left to right, and top to bottom: log of the r-band weighted mean stellar age (yr), metallicity (relative to solar), total effective V-band optical depth affecting stars younger than 10^7 yr ($= 0.92A_V$, where A is attenuation in magnitudes) and fraction of stellar mass formed in bursts in the last Gyr.

comes from a combination of different projects: the UDSz, which combines data from the VIMOS and FORS2 instruments (ESO Large Programme 180.A-0776, PI: Almaini); and more recent VIMOS observations (ESO programme 094.A-0410, PI: Almaini), which were specifically designed to target PSB candidates and test their nature. Together these make a total of ~ 3700 spectra in the UDS field.

Wild et al. (2014) used the spectroscopy from UDSz to confirm the PCA method. A sample of 282 spectra with moderate quality around the 4000 Å break region was selected in the redshift range $0.9 < z < 1.2$. They stacked these spectra by PCA-class and looked at the typical spectrum of each population. They found that red sequence galaxies have strong 4000 Å breaks and CaII H & K lines, which is a sign of an old mean stellar age and low SSFR. SF galaxies show characteristic [OII] emission implying recent star formation. Although the subdivisions of the SF population into SF1, SF2 and SF3 was arbitrary, following the $SC1$ axis, they find that the strength of the [OII] decreases from the SF1 to the SF3 populations. A weak 4000 Å break appears in the oldest of the SF populations (SF3). However, when it comes to the confirmation to the PSB population, Wild et al. (2014) only had 5 galaxies in the corresponding PCA region with sufficient signal-to-noise ratio. These numbers were recently increased through the acquisition of tens of spectra for PSB candidates in the UDS region. Maltby et al. (2016) used these spectra to carry out a follow-up study to confirm the nature of photometrically selected

PSB galaxies. They built a sample of 24 PSB candidates with good quality spectra ($S/N > 7$), from UDSz and the more recent spectroscopy. Using a Hδ equivalent width $W_{\mathrm{H}_\delta} > 5$ Å to spectroscopically define PSB galaxies (Goto 2007), they find that 19 of these candidates show strong PSB features ($\sim$ 80%). Using a more conservative prescription and rejecting those PSB candidates with $W_{[\mathrm{OII}]} < -10$ Å in order to get rid of possible residual star formation (Yan et al. 2006), the success rate drops to $\sim$ 60%. However this last constraint may bias the classification against PSB galaxies that host AGN. Furthermore, some residual star formation is expected since star formation will not shut down instantly. In conclusion, the PCA photometric classification is consistent with the results from spectra, with between 60–80% of the PSBs candidates showing the expected spectral features from the PSB population (see Figure 2.5 for some examples).

2.2.2 Post-starburst galaxies from the PCA

In this section we acknowledge that supercolour-selected PSB galaxies are not strictly classic post-starburst galaxies. The majority (60–80%) of galaxies located in the PSB region of the SC-diagram show spectroscopic "k+a" properties (Maltby et al. 2016). This indicates that they have undergone an abrupt termination of their star formation within the last Gyr, which followed a period of significant star formation. As noted in Wild et al. (2016), however, this does not necessarily imply that they all underwent a "starburst" phase before quenching. Very rapid quenching following a more extended period (< 3 Gyr) of star formation may also produce these spectral features. Consequently, we use the term "PSB" to refer to a population that potentially includes these two scenarios, classic post-starburst galaxies (rapidly quenched following an episode of enhanced star formation) and galaxies that experienced a rapid truncation of their star formation activity. In both cases the "k+a" spectral features are not expected to last longer than 1 Gyr, hence, quenching must have taken place recently.

As a further caveat, we note that spectroscopic confirmation is so far confined to brighter galaxies ($K < 23$). However, a large fraction of our PSBs lie at slightly fainter limits ($23 < K < 24$). Based on their SEDs, however, we have no reason to believe that the fainter PSB candidates show different characteristics, and they populate the PSB region of the SC diagram in the same way as the brighter counterparts. Additionally, we note that Maltby et al. (2016) exclude galaxies with $W_{[\mathrm{OII}]} < -5$ Å to rule out PSB candidates with significant ongoing star formation. We acknowledge that galaxies with no significant [OII] have been found with residual H_α emission (Yan et al. 2006), but the lack of [OII] together with strong higher order Balmer absorption lines (i.e. H_β, H_γ and H_δ) is considered sufficient to rule out significant ongoing star formation (Goto et al. 2003; Tran et al. 2003; Blake et al. 2004).

Finally, the PCA method remains untested for PSB galaxies at $z > 1.5$, where the key spectral features move into the IR. This will be tested soon for a few bright PSB galaxies using deep spectroscopy from the K-band Multi-Object Spectrograph (KMOS; ESO programme 0100.A-0545 and 0102.A-0300 ; PI: Maltby), but a good statistical test to faint limits will require James Webb Space Telescope (JWST) observations.

Regarding the presence of further contaminants in our PSB sample coming from other galaxy populations, dusty star-forming galaxies need to be mentioned. Dusty galaxies may have heavily obscured star formation activity, so that the light from O and B stars is absorbed by dust particles, while A stars have had time to escape

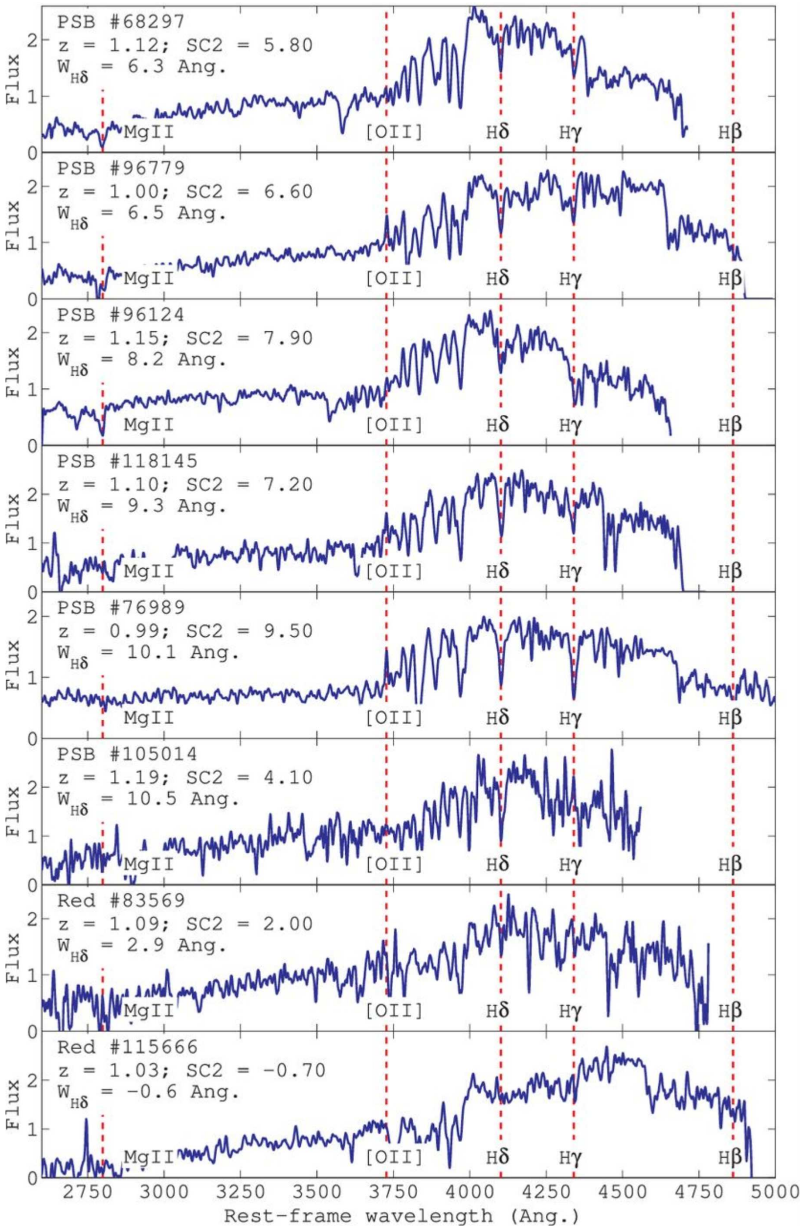

Figure 2.5. Eight examples of VIMOS spectra corresponding to photometrically selected PCA PSB galaxies (first six panels) and two passive galaxies (last two panels) from Maltby et al. (2016). Most of these galaxies show strong Balmer absorption lines and Balmer breaks.

their dusty cocoons (Poggianti et al. 1999). Consequently, these galaxies could show the characteristic 'k+a' features. In order to classify these type of galaxies robustly, optical spectra is needed in order to observe the presence of weak to strong emission lines (Poggianti et al. 2009), which cannot be detected using broadband photometry. Nevertheless, the typical overall SED shape across the optical to the IR differs significantly between dusty and PSB galaxies, and the eigenvectors are able to detect these differences. Therefore, the contamination of the PSB sample due to dusty star-forming galaxies is not a major concern.

2.2.3 Comparison with the traditional UVJ method

In this section, we compare the supercolour method with the most widely-used photometric method to separate passive and star-forming galaxies, the UVJ colour–colour classification (Williams et al. 2009; Ilbert et al. 2013). We include the method designed by Whitaker et al. (2012) to identify PSB galaxies using UVJ, which consists of selecting the galaxies at the blue end of the red sequence.

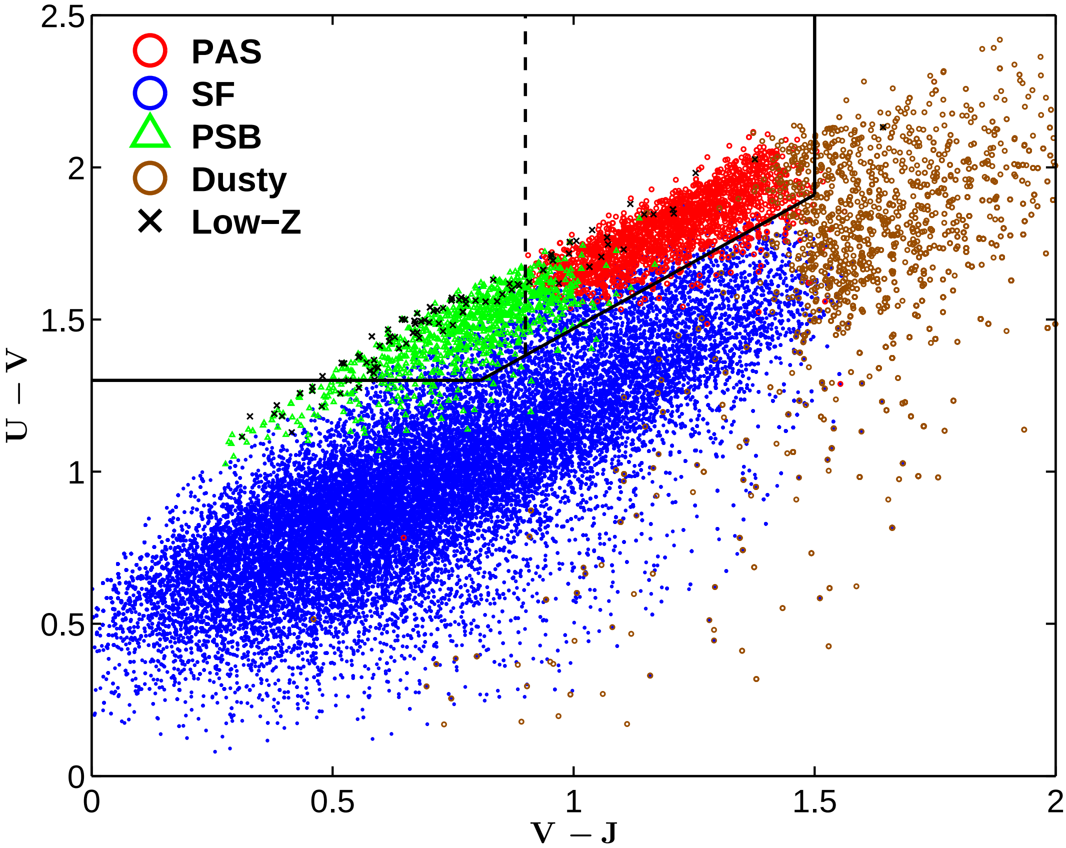

Figure 2.6. Comparison between the supercolour populations and those obtained using a traditional UVJ diagram for the UDS DR11 galaxies at $0.5 < z < 2.0$. The supercolour populations include: passive (red), star-forming (blue), PSB (green), dusty (brown) and metal-poor (black). The black solid line corresponds to the UVJ demarcation between star-forming and passive galaxies. The dotted line is used to select PSB galaxies (Whitaker et al. 2012).

We find good agreement between the classifications from each method (compared in Figure 2.6). However, it is obvious that the boundaries do not match perfectly. Given that the PCA utilises all the photometric bands available, and therefore uses more information for the classification, we expect the supercolour method to identify higher order variations with respect to the UVJ classification. Additionally, we observe that low-metallicity galaxies are found across the entire red sequence, hence, they would not be identifiable using only UVJ diagrams. The extra information provided by $SC3$ is essential to identify these type of galaxies photometrically.

Another significant discrepancy concerns the PSB population. Although the degree of agreement between the two methods is good, we see that a significant fraction of the PCA PSB galaxies lie within the UVJ star-forming region. These

PSB galaxies are likely to be recently quenched SF galaxies that are just entering the PSB phase. They tend to be less massive and fainter than their older counterparts. Given that they are so faint, we are lacking their spectroscopic confirmation so far. Nevertheless, given the success of the PCA classification at $K < 23$, there is no reason to believe the method is less successful for less massive galaxies.

Let us now discuss the advantages and disadvantages of these two methods with respect to each other. The main advantage of the PCA is that it it only uses models to optimise the eigenvectors derived. Hence, it is potentially more robust as it does not require assuming a model by fitting synthetic SEDs to the photometric data. In contrast, UVJ uses K-corrections which rely SED fitting. In addition to this, by combining all filters in an optimal configuration, the PCA achieves a higher signal-to-noise. Furthermore, it contains more information in a very compact format. Only three principal components can identify galaxy properties that would require several colour–colour diagrams, e.g. the selection of low-metallicity galaxies. Finally, the method provides an easy way to derive galaxy physical properties, as this information is directly extracted from the models that occupy the same location on the SC-diagrams. However, there are disadvantages as well. Although the SC space is well sampled by the models, there is a non-negligible fraction of galaxies in the UDS that lie beyond the sampled area. The PCA method does not provide accurate information about these outliers that are not traced by models. Nonetheless, the UVJ selection is also affected by this, as it relies on models to derive certain properties. Another, shortcoming is that the PCA is only effective if a broad wavelength coverage is available. In particular, the method needs to be able to characterise the 4000 Å region. This can be particularly tricky to study broad redshift ranges, as many bands may be required to sample the break at all redshifts. Luckily, the UDS provides this wealth of multiwavelength photometry, allowing us to use this method in the redshift range $0.5 < z < 3.0$ (with UDS DR11).

In conclusion, we have shown that the supercolour method, which uses a PCA of the photometry from the UDS, is a suitable method to classify galaxy types and derive a range of physical properties, given the nature of our data.

2.3 Stellar mass completeness limit estimation

Our photometric sample is magnitude limited (in the K band). The magnitude limit applied to the UDS corresponds to the minimum flux in the K filter, below which the probability of detecting an object is lower than 95%. It is essential to remove galaxies below this limit in order to avoid biases. However, this magnitude cut is equivalent to a stellar mass at a given redshift and mass-to-light ratio. Given that the mass-to-light ratio varies between different galaxy types, it is required to estimate this stellar mass completeness limit for each of our galaxy populations.

The method we use in order to calculate the 90% stellar mass completeness limits is described in Pozzetti et al. (2010). We only describe the main features here. This method estimates a distribution of limiting masses ($M_{\rm lim}$) for a galaxy sample. The limiting mass at a given redshift is defined as the stellar mass a galaxy would have if it had the limiting magnitude of the survey ($K_{\rm lim}$), and it is calculated using the following equation,

$$\log(M_{\rm lim}) = \log(M_*) + 0.4(K - K_{\rm lim}), \tag{2.2}$$

Table 2.1. The 90% stellar mass completeness limits $\log(M_{\text{lim}}/M_{\odot})$ as a function of redshift for DR11 and DR8 (the latter values are shown in parentheses). Mass limits are for the total sample, with star-forming, passive and PSB galaxies presented independently.

z	0.5	1.0	2.0	3.0
Total	8.40 (8.8)	8.80 (9.4)	9.35 (9.9)	9.80
SF	8.35 (8.5)	8.71 (9.0)	9.25 (10.0)	9.62
PAS	8.50 (8.9)	9.00 (9.5)	9.75 (10.2)	10.0
PSB	8.45 (8.9)	8.95 (9.3)	9.55 (10.1)	9.84

where M_* and K are the stellar mass and K-band magnitude of the galaxy, respectively. The resulting distribution of M_{lim} represents the distribution of stellar mass-to-light ratios at each redshift in our sample. As described in Pozzetti et al. (2010), we use the M_{lim} of the 20% faintest galaxies in order to produce a representative limit for our sample. This takes into account the colour-luminosity relation and avoids including very bright, red galaxies with the highest mass-to-light ratios, which do not significantly contribute to the magnitude limit. Instead, the method only includes galaxies with typical mass-to-light ratios close to the magnitude limit. The stellar mass limit is then defined as the 90th percentile of this M_{lim} distribution at each redshift. This stellar mass limit corresponds to the 90% mass completeness limit.

The method is applied independently to both UDS data releases (see Table 2.1 for some M_{lim} values at given redshifts). The DR8 catalogue, with a limiting magnitude in the detection band of $K_{\text{lim}} = 24.3$, leads to an overall stellar mass limit of $\log(M_*) \geq -0.41z^2 + 1.76z + 8.00$. We express the mass limit dependence with redshift as the result of fitting a second-order polynomial to the estimated $M_{\text{lim}}(z)$, which is a good approximation. In Chapters 4 and 5, the PCA was applied to the DR8 data, to a K-band magnitude $K < 24$ and $z \leq 2$. For Chapter 6 the PCA is done on the DR11 data, which allows us to extend the analysis to $K < 24.5$ and $z \leq 3$ (even though the 5σ survey limit is $K = 25.0$). This slightly more conservative K-magnitude cut is used in order to reduce the scatter when the PCA method was applied. The mass limits for the main galaxy populations for the DR8 sample are shown in the top panel of Figure 2.7. We see that passive galaxies (in red) have a higher mass completeness limit than the star-forming ones (blue), as expected given that the former have the highest mass-to-light ratios. In contrast, the PSB population's mass limit (green) lies in between the previous two, this is in agreement with the idea of PSBs being transitional objects from the star-forming to the passive populations.

The results are similar for the DR11 catalogue (see bottom panel of Figure 2.7), with a limiting magnitude of $K_{\text{lim}} = 25.0$. The overall stellar mass completeness limit as a function of redshift is well described by a polynomial of the form $\log(M_*) \geq -0.10\ z^2 + 0.88\ z + 7.90$.

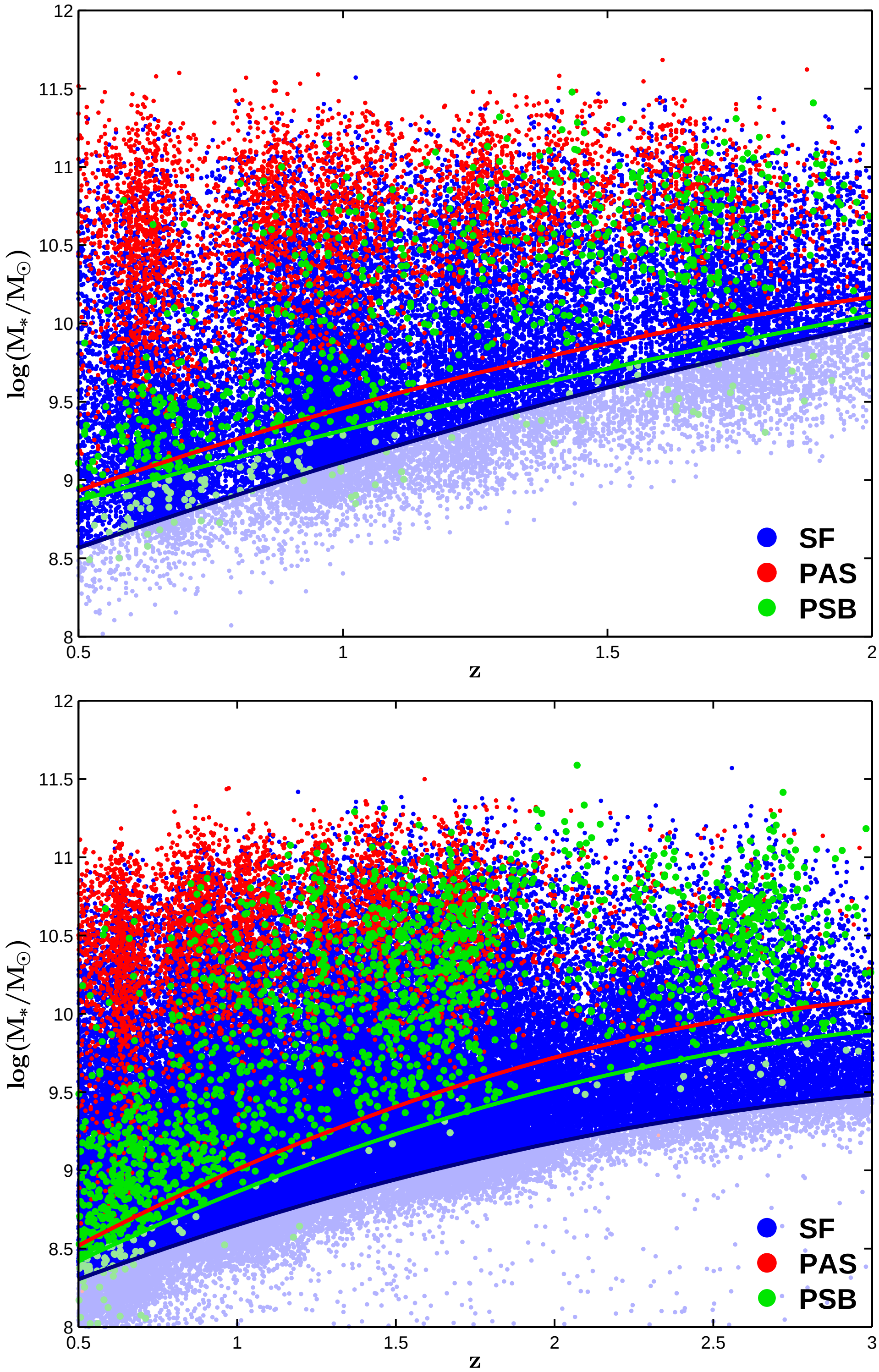

Figure 2.7. Stellar mass function as a function of redshift for the UDS DR8 (top panel) and DR11 (bottom panel) galaxy samples at $0.5 < z < 2.0$ and $0.5 < z < 3.0$, respectively. The solid lines represent the 90% stellar mass limits for the star-forming (blue), passive (red) and PSB (green) galaxy populations. These limits are calculated using the method presented in Pozzetti et al. (2010).

Table 2.2. Comparison between the UDS DR8 and DR11 catalogues. The number of galaxies are given for the samples with the stellar mass and magnitude completeness limits already applied.

	DR8	**DR11**
$\boldsymbol{H}$	24.2	25.1
$\boldsymbol{J}$	24.9	25.6
$\boldsymbol{K}$	24.6	25.3
Filters	11	12 ($Y = 24.4$)
$\boldsymbol{\sigma_z/(1+z)}$	0.023	0.0183
$\boldsymbol{K_{\mathrm{lim}}}$	24.3	25.0
$\boldsymbol{M_{\mathrm{lim}}\ (z = 1.0)}$	$10^{9.4} M_\odot$	$10^{8.8} M_\odot$
# of galaxies		
$\boldsymbol{0.5 < z < 1.0}$	$23,398$	$29,821$
$\boldsymbol{1.0 < z < 2.0}$	$31,948$	$46,155$
$\boldsymbol{2.0 < z < 3.0}$	$14,921$	$15,354$
PCA galaxies		
$\boldsymbol{0.5 < z < 1.0}$	$20,535$	$29,684$
$\boldsymbol{1.0 < z < 2.0}$	$28,010$	$45,447$
$\boldsymbol{2.0 < z < 3.0}$	-	$14,533$

Chapter 3

Identifying groups and clusters in the UDS

In this chapter we review the most widespread methods for measuring environments in photometric surveys and discuss their advantages and disadvantages. After which we detail the "friends-of-friends" algorithm we constructed to find clusters in the UDS, which is the main method we employ to define galaxy environment in this thesis (Chapters 4 and 5). In Section 3.3 we also compare our method with previous work to show that our findings are consistent.

The work presented in this chapter corresponds to the methodology section of Socolovsky et al. (2018). Although the majority of the analysis is done by me, I did not take part in the derivation of the underlying galaxy catalogue, photometric redshifts and stellar masses (see Chapter 2) which are described in Simpson et al. (2013).

3.1 Ways to measure galaxy environments

Nowadays there is a wide variety of methods for measuring galaxy environment. Although most of them have proven successful in recovering the expected environmental trends, there is no standard method to-date. Different studies use different techniques, which sometimes makes the comparison between them difficult or impossible. The choice of environmental indicator is important, since different methods trace different physical properties (Muldrew et al. 2012). For example, some techniques may trace the large-scale density, while others provide a measurement of the density within the local galaxy halo. Furthermore, some techniques may be more suitable than others depending on the nature of the data.

We are in the era of large and deep photometric surveys. This means that we have access to an unprecedented wealth of data. We have been compiling photometry of many hundreds of thousands of galaxies in recent years and the potential of these data is yet to be fully exploited. However, this abundance of data comes with some difficulties. In order to measure galaxy number densities, knowing the position of each galaxy with accuracy is essential. The main disadvantage of photometric surveys with respect to spectroscopic surveys is the large uncertainties associated with redshift determination. In photometric surveys, redshifts are determined by reconstructing a "low-resolution" spectrum using the flux in the available filters, the so-called spectral energy distribution (SED). Such methods are much weaker at constraining the redshift of the galaxies than any low-signal-to-noise spectrum, leading to large uncertainties and degeneracies. This loss of information along the line-of-sight impedes calculating accurate spatial densities. Nonetheless, the strength of photometric surveys lies in their ability to detect large and deep galaxy samples. Such large samples generally make up for the lack of accurate positions, allowing for the environment to be robustly measured in a statistical manner. This means although we cannot measure the environment of a single galaxy, the typical environment of a galaxy population can be robustly recovered.

The most frequently used techniques to probe environment in photometric surveys usually consist of measuring the local density field of neighbouring galaxies around a target galaxy. Typically, the inaccurate photometric redshift information is used to avoid the contamination of obvious interlopers. Most methods split the sample into redshift slices and then use the much more precise astrometric position on the sky to define the density. Apertures or similar methods are applied in order to isolate the neighbourhood of the target galaxy, and count the number of nearby companions. There are two main types of environmental measurements: continuous and discrete, each of them with different advantages and disadvantages as we describe in the following sections.

3.1.1 Continuous environmental measurements

As their name suggests, these methods provide a continuous measurement of galaxy environment, usually based on a galaxy number density or stellar mass density. The methods that are more commonly used in the literature are fixed apertures, nth nearest neighbour and Voronoi tessellation. We describe them briefly in this section.

(i) Fixed aperture method: This technique consists of counting the number of galaxies within a fixed volume, which can be centred around galaxies or randomly placed across the field. These volumes are usually constructed with an aperture on the sky, and a depth along the line-of-sight, usually corresponding to a redshift slice. A variety of aperture shapes have been used including spheres (Croton et al. 2005), cylinders (Gallazzi et al. 2009) and annuli (Wilman et al. 2010). Given that, in photometric surveys, the accuracy in the position along the line-of-sight is significantly lower than the angular position on the sky, cylinders tend to be the preferred choice. Alternatively, some studies prefer to use spheres or other volume shapes.

If the apertures are centred around galaxies, it is common practice to subtract the central galaxy from the number count. Otherwise, the number count would always be one or higher, which introduces a bias, especially when using small apertures. Furthermore, since the method is probing the environment of the galaxy, including the target in the count is meaningless.

The main advantage of this method is that it can account for edges and holes in the field to a first order approximation. One can correct the galaxy number counts by weighting using the number of good (unmasked) pixels per aperture using the following equation,

$$1 + \delta_{\rm aper} = \frac{N_{\rm aper}}{N_z} \frac{N_{\rm tot}^{\rm Mask}}{N_{\rm aper}^{\rm Mask}}, \tag{3.1}$$

where $\delta_{\rm aper}$ is the relative density increment in the aperture with respect to the mean density at the same redshift. $N_{\rm aper}$ is the galaxy number count within the aperture once the target galaxy is subtracted, while N_z is the number of galaxies in a redshift slice covering the entire field with the same depth as the cylinder. $N_{\rm tot}^{\rm Mask}$ and $N_{\rm aper}^{\rm Mask}$ represent the number of good pixels within the aperture and within the entire survey field, respectively.

The downside is that, given its discrete nature, this method tends to have poor resolution at low densities. Therefore, the use of a small aperture will perform well in high-density environments while in low-density regimes only the target galaxy is found within the aperture, resulting in a density measure of zero. Consequently, large apertures are better at measuring the densities in the field or underdense regions. However, large apertures tend to smooth out the density field over the scale of the aperture size. This means that the bigger the aperture is, the larger the fraction of field galaxies included within the aperture. Due to this effect any peaks in density are brought down towards the mean (field) value.

(ii) Nth nearest neighbour: In this method the volume varies and is chosen to enclose the n nearest neighbours of the target galaxy. This is in contrast to the fixed aperture method, which uses a fixed volume and changing n. Then a redshift cut is also applied to avoid background and foreground contamination. This method keeps the signal-to-noise roughly constant as the number of neighbours is fixed, which ensures the method does not perform better in high or low-density regimes. However, the choice of n is critical. If the nth nearest neighbour lies in a different structure to the target's, the selected volume will correspond to the inter-group distance. For this reason, the number of neighbours is chosen to be low to reduce the risk of facing this problem. Therefore, the scales at which environment is probed depends on the choice of n. Another issue is that dealing with masked regions is not as straight-forward as in the fixed aperture method. Often galaxies whose distance to the nth nearest neighbour is larger than the distance to a masked pixel are discarded, which can lead to a significant loss of information due to holes and field edges.

(iii) Voronoi tessellation: The volume of the survey is once more broken down into redshift slices, then cells are constructed around each of the galaxies in the redshift slice. The cell corresponding to one galaxy is made of all the points that are closer to that galaxy than to any other. The inverse of the area of these polyhedra is a proxy for environmental density (Marinoni et al. 2002; Cooper et al. 2005). Galaxies in dense environments yield smaller Voronoi areas than those in the field. This method provides a good measurement of the galaxy local density, with stable signal-to-noise. It is fully adaptive since the sizes and shape of the polyhedra are not fixed but depends on the number and distance to the neighbours. Furthermore, it does not require arbitrarily chosen parameters, such as the size of the aperture or n as in the previous methods. However, Voronoi tessellation is more difficult to implement and requires more computational power. Furthermore, the presence of masked pixels tend to produce abnormally low densities, an effect that is difficult to correct given the irregular shape of the Voronoi cells. Consequently, dealing with holes and edges in the field of view is a complication of this method.

These are the most basic and widely used methods to measure local environmental density. More sophisticated variations exist but, nevertheless, most of them are based on the above mentioned principles. An example is the so-called "variable aperture" method, which is a combination of the fixed aperture and the nth nearest neighbour methods. The size of the aperture is selected based on the distance to the nth nearest neighbour, while the correction for edges and holes is performed in the same way as in the fixed aperture method. Another improvement which can account for photometric redshift uncertainties is to combine any of the above-mentioned methods with a Monte-Carlo technique. This involves running the environmental indicator a large number of times on samples with varying simulated redshifts, which are randomly generated sampling the photometric redshift errors. This provides uncertainties for each galaxy density, giving an estimate of how robust the measurements are.

3.1.2 Discrete environmental measurements

This family of techniques classify galaxies into two or more classes: isolated galaxies or galaxies in clusters (in some cases galaxies in groups may be included as a separate category). The main advantage of these methods is the addition of spatial information, i.e. the position of the galaxies with respect to the structure they inhabit, which allows for the estimation of other properties regarding the quenching processes, e.g. timescales. Furthermore, a galaxy cluster usually spans across different density regimes (cluster cores are very dense while the outskirts are less so), which gives a more complete view of the environmental dependence. On the other hand, determining cluster membership accurately is a known, but as yet unsolved, problem. There is no consensus on which is the optimal way to select cluster member galaxies. In this context, optimal means complete, i.e. the ability to detect a large fraction of the cluster members, and contamination-free, which means that the fraction of interloper galaxies (contaminants) is low. These two metrics tend to be degenerate so that it is usually necessary to choose between high completeness but high contamination or low contamination and also low completeness.

There are several families of cluster finders. The first class is purely geometrical, and identifies structures based on their positions (including redshift if available). One of the most popular algorithms is the so-called "Friends-of-friends" (FoF) method (Huchra & Geller 1982; Geller & Huchra 1983; Botzler et al. 2004; Merchán & Zandivarez 2005; Trevese et al. 2007; Wen et al. 2012). The algorithm links galaxies that are within a certain distance (linking parameter) from each other. All groups of galaxies linked in this way are classed as galaxy cluster candidates. When a galaxy cannot be linked to any other it is classified as an isolated galaxy. One of the downsides of this simple method is that it is heavily dependent on the linking parameters, so that these have to be carefully chosen. Furthermore, in the absence of spectroscopic data, this method requires good-quality photometric redshifts, therefore, good multiwavelength coverage is required.

The second type of structure finder combines galaxy position with other properties (e.g. magnitude or colour). These methods typically rely on well known environmental trends. Red sequence finders are one of the most popular methods (e.g. Gladders & Yee 2000; Rykoff et al. 2014, 2016; Licitra et al. 2016). Galaxies in clusters tend to be quiescent and red. Therefore, these algorithms look for overdensities of red galaxies, which gets rid of a large fraction of spurious galaxy cluster detections from using geometry alone. However, it is strongly biased towards locating only evolved and virialised structures with an established red sequence. It is most likely to miss young overdensities of star-forming galaxies. Thus, it is not well suited for locating structures in the high-redshift Universe, where clusters are in early stages of assembly.

Other methods use independent observational features, such as extended X-ray emission (e.g. Piffaretti et al. 2011; Willis et al. 2013), SZ-effect on the CMB photons (e.g. Vanderlinde et al. 2010; Planck Collaboration et al. 2011) or the presence of AGN (e.g. Pentericci et al. 2000; Venemans et al. 2007). However, we do not describe these as they are not relevant for the work presented in this thesis.

3.1.3 Our choice of environmental indicator

In this thesis, we use two methods to measure galaxy environments. For the work at intermediate redshifts ($0.5 < z < 1.0$) we choose to use a binary method which classifies galaxies into cluster or group members, and a field or control sample to compare with. We adopt this approach because it allows us to do a more in-depth analysis, which includes cluster radial profiles in order to study where environmental quenching takes place and its timescale. This method is crucial for this thesis, as it defines the cluster sample used in Chapters 4 and 5. We therefore devote the rest of this chapter to describing this technique, explaining how it works, how it was optimised, and how it was tested.

The second environmental indicator we use is based on fixed apertures and it is implemented only in Chapter 6. The reason for using a different method is that, in this chapter, we wish to perform a self-consistent analysis of the evolution of galaxy environments in the redshift range $0.5 < z < 3.0$. We found that our first method breaks down above $z = 2$, where large structures are virtually nonexistent and the galaxy field is remarkably homogenous, compared to lower redshifts. Hence, we consider that, in this scenario, a continuous measure of galaxy environment is more suitable. The details of this second method are presented in Section 6.3.

3.2 Our cluster detection method at $z \leq 1$

We use a Friends-of-Friends (FoF) algorithm (Huchra & Geller 1982; Geller & Huchra 1983; Merchán & Zandivarez 2005) to locate cluster and group candidates in the UDS. For brevity, we refer to candidate groups and clusters in our sample as "clusters" hereafter. The main reason for choosing a discrete classification method over a continuous one is the ability of the former to identify structures of galaxies. This allows us to find the centre of each structure, stack them and study the properties of galaxies as a function of their location within the parent structure.

The FoF method is characterised by three parameters: two linking distances, projected ($d_{\rm link}$) and along the line of sight ($z_{\rm link}$), and a detection threshold ($N_{\rm min}$), which is the minimum number of member galaxies per structure. The algorithm starts by selecting one galaxy at $[\mathbf{r_0}, z_0]$ from the catalogue which has not been assigned to any structure. All other galaxies fulfilling $|\mathbf{r_0} - \mathbf{r_i}| \leq d_{\rm link}$ and $|z_0 - z_i| \leq z_{\rm link}$ are then designated as "friends". The terms $\mathbf{r}$ and z correspond to the position on the sky and redshift, respectively. The method is iterative and continues searching for friends of the friends until no remaining galaxy fulfils the conditions. The structure is classified as a cluster candidate if the number of linked galaxies is greater than $N_{\rm min}$.

Our cluster finding algorithm was optimised using the UDS DR8 (described in Chapter 2). In addition to this, the spectroscopic redshifts from UDSz (see

Section 2.1.4) were used to confirm our cluster candidate sample.

3.2.1 Optimising the FoF algorithm

The completeness and contamination rates of the cluster sample strongly depend on the parameters $d_{\rm link}$, $z_{\rm link}$, and $N_{\rm min}$. We optimised these parameters to maximise the completeness of the cluster sample whilst also ensuring the cluster sample has no more than 5% contamination.

To estimate the contamination rate we ran the FoF algorithm on a mock galaxy catalogue using a range of FoF parameters. We created mock catalogues that had the same number, mean density, and redshift distribution of galaxies as in the UDS, but the RA and Dec were randomised so that the mock catalogue did not contain any groups or clusters. The contamination rate is defined as:

$$q_{\rm cont} = \frac{N_{\rm mock}}{N_{\rm UDS}} \tag{3.2}$$

where $N_{\rm mock}$ is the number of clusters detected in the mock catalogue, and $N_{\rm UDS}$ is the number of clusters detected in the UDS using the same FoF configuration.

To determine the completeness rate, we injected mock clusters into the UDS catalogue and then attempted to recover them with the FoF algorithm. The parameters of these simulated clusters are chosen to be similar to the expected values for clusters at $z \sim 1$. Hence, mock clusters are constructed as $N_{\rm sim} = 20$ galaxies randomly distributed within an aperture of radius $R_{\rm sim} = 0.8$ Mpc. Each galaxy is assumed to have a stellar mass of $M_* = 10^{10}{\rm M}_\odot$. These simplistic mock clusters result in a conservative estimate of the completeness as real clusters are typically more centrally concentrated, and therefore are easier to detect with a FoF algorithm. All mock clusters are placed at $z_{\rm sim} = 0.75$, and redshift errors for each galaxy are simulated by randomly sampling a Gaussian distribution of dispersion equal to the photometric redshift uncertainty, $\sigma_{\rm z} = (1 + z)0.023$.

We injected 100 mock clusters in low-density regions of the UDS to prevent the mock clusters from overlapping with each other or with existing structures in the UDS. The FoF algorithm is then used to recover the mock clusters. The threshold for recovering a mock cluster is when at least 80% of the injected galaxies are detected and the offset of the centre of mass is less than 30% of $R_{\rm sim}$. The completeness rate ($q_{\rm comp}$) is defined as the ratio between the number of successfully recovered clusters and the number of mock clusters injected into the simulation. A hundred of these simulations are run to obtain the average completeness rate of recovering 10,000 mock galaxy clusters.

We optimise the FoF algorithm by tuning the parameters to maximising the completeness-to-contamination ratio ($r_{\rm comp/cont}$) while keeping the value of $q_{\rm cont}$ low.

$$r_{\rm comp/cont} = \frac{q_{\rm comp}}{q_{\rm cont}} \tag{3.3}$$

The best performing values are: a linking projected distance of $d_{\rm link} = 300$ kpc, and a linking distance along the line of sight of $z_{\rm link} = 40$ Mpc. At a minimum threshold of $N_{\rm min} = 10$ galaxies these parameters yield completeness and contamination rates of 31% and 5%, respectively. Note that we prefer a sample with low contamination at the expense of completeness, which is important for finding the elusive trends with environment. Allowing for higher contamination levels would decrease the signal-to-noise ratio (S/N) of the cluster sample. We also note that the completeness

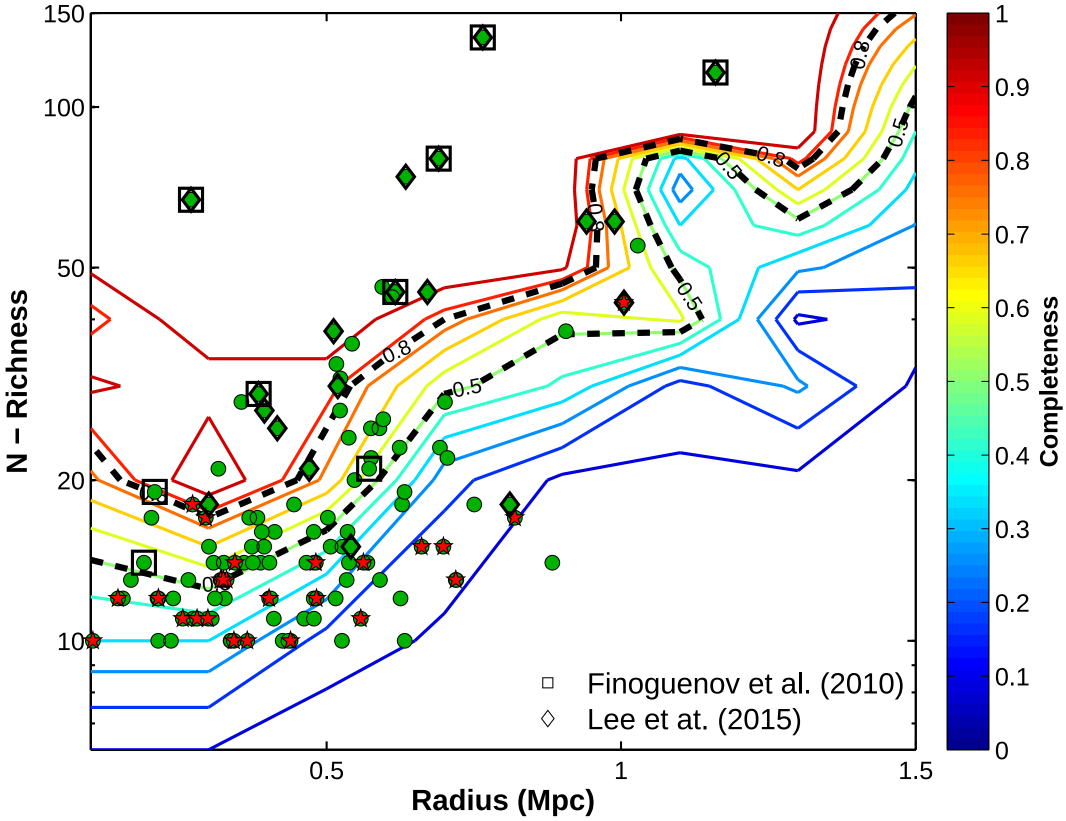

Figure 3.1. Completeness contours as a function of size and richness of clusters, based on simulated galaxy clusters. Contours of 50% and 80% completeness are highlighted with the thick dashed lines. The dots and stars represent cluster candidates from the UDS. Green dots represent good detections and red stars represent clusters excluded due to a large offset in the centre of mass or low S/N after background subtraction. In addition, cluster candidates coincident with published detections from Finoguenov et al. (2010) (boxes) and Lee et al. (2015) (diamonds) are included.

rate we estimate here is for optimisation purposes and corresponds to a lower limit. So far we have included one type of mock clusters, with a fixed set of properties ($N_{\rm sim}$, $R_{\rm sim}$ and $z_{\rm sim}$,). In Figure 3.1 we show that completeness varies with the cluster properties and most realistic clusters have much higher completeness rates ($\geq$ 80% for structures with $\log M_* > 11.9$). Furthermore, in Section 3.2.6 we also see that in the regime where completeness is lower, the sample is dominated by field contaminants. This ensures that low detection completeness does not result in a highly contaminated field sample.

3.2.2 Limitations of the FoF algorithm

To test the limitations of our FoF cluster finding algorithm we estimated the recovery rate of mock clusters which have a variety of richness ($N_{\rm sim}$), size ($R_{\rm sim}$) and redshift ($z_{\rm sim}$). Figure 3.1 shows that low-richness clusters are only detected if they are also compact. The completeness of our selection method decreases for clusters with small radii, as small deviations in the centre of mass position become significant compared to the size of the cluster. This means that the measured centre of mass for many of the mock clusters deviates from the true centre of mass by more than 30% of $R_{\rm sim}$.

However, this effect becomes important at implausibly small radii (< 100 kpc), so it does not affect our results.

Figure 3.1 shows that our method has low completeness for those clusters with fewer than 20 FoF member galaxies. However, this completeness is a lower limit because the mock clusters are less likely to be identified by the FoF algorithm due to the random, rather than centrally concentrated, spatial distribution of their member galaxies.

3.2.3 Cluster centre and effective radius

We define the projected centre of a candidate cluster as the centre of mass of its FoF members, and its redshift is defined as the median of the photometric redshifts of its FoF members. The effective radius of a cluster, $R_{0.85}$, corresponds to the projected radius that encloses 85% of the stellar mass of the system.

The centre of a cluster can also be defined as the mean or median of the RA and Dec of all FoF members. The cluster centre should not depend strongly on the definition used, unless the cluster has no well-defined centre. Therefore, we remove 10 clusters from our sample whose measured centroid deviates by more than 30% of $R_{0.85}$ depending on which definition is used (see Fig 3.2).

3.2.4 Cluster galaxy membership

The FoF algorithm is optimised to identify clusters in the UDS, but the galaxy membership of these clusters will be incomplete due to photometric redshift errors. To correct for missing galaxies, we define candidate cluster members as all galaxies within a cylinder around the centre of mass of each cluster. Each cylinder has a radius of $R_{\rm cyl} = 1$ Mpc, which is the typical size of a galaxy cluster, and a depth of $\delta z_{\rm cyl} = 2.5\sigma_{\rm z}$, which corresponds to ~ 250 Mpc in our redshift range.

The large photometric redshift uncertainties means we must use long cylinders to avoid missing cluster galaxies, but this implies that the cylinders may include a significant fraction of field galaxies, which are considered contaminants. These contaminants can be removed by statistically subtracting the field galaxies expected in each cylinder.

3.2.5 Construction of a field galaxy sample

We construct a sample of field galaxies to remove the field contribution within the cylindrical volume containing the cluster members, and to use as a second environment to compare with our cluster sample.

The field sample is constructed from the UDS. For each cluster cylinder, a field sample is defined as all galaxies in the UDS (which are not candidate cluster members) that lie within the same redshift interval as the cylinder. Doing this ensures that the field sample follows exactly the same redshift distribution as the clusters. The number of galaxies in the field is then scaled by the ratio of unmasked pixels in the cluster region to the field region, so that the field corresponds to the same volume as the cluster, i.e. a cylinder with radius 1 Mpc and depth 250 Mpc. The rescaled field number count (N^*_{Field}) can be expressed as the original number scaled by a normalisation factor, f:

$$N^*_{Field} = f N_{\rm Field} = \frac{n_{\rm cyl}}{n_{\rm Field}} N_{\rm Field} \tag{3.4}$$

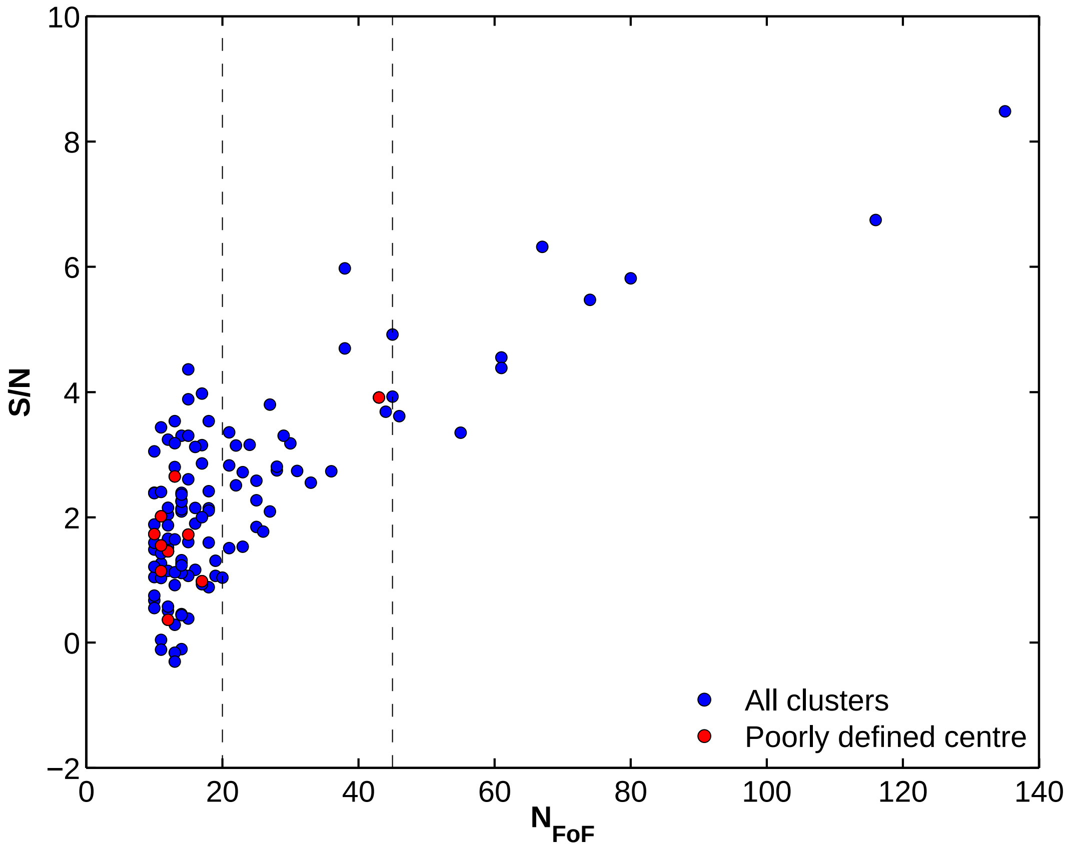

Figure 3.2. Signal-to-noise ratio of the cluster detections as a function of richness of our cluster sample, using the method described on Section 3.2.6. Dashed lines divide the richness into the three bins we utilise in the following sections. Clusters with poorly defined centres are shown as red dots, which seem to be concentrated in the lowest richness bin ($N < 20$ galaxies), making this the most contaminated and unreliable regime.

where $n_{\rm cyl}$ is the number of unmasked pixels inside the aperture corresponding to the cylinder and $n_{\rm Field}$ is the total number of unmasked pixels across the field sample. Finally, all the separate field regions corresponding to each detected cluster are combined together to produce the total field galaxy sample. We define a field sample for each cluster, but several clusters have similar redshifts so the total combined field sample contains some duplication of UDS galaxies. This duplication amounts to less than 10% of the total field sample.

3.2.6 Signal-to-noise ratio of the cluster candidate detections

To determine a quality control for our cluster candidate detections, we define the signal-to-noise ratio of each cluster detection as

$$S/N = \frac{N_{\rm cluster} - fN_{\rm field}}{\sqrt{\sigma^2_{\rm cluster} + \sigma^2_{\rm field}}} = \frac{N_{\rm cluster} - fN_{\rm field}}{\sqrt{N_{\rm cluster} + f^2 N_{\rm field}}}, \tag{3.5}$$

where $N_{\rm cluster}$ is the number of galaxies in the cylindrical volume around the cluster, $N_{\rm field}$ is the number of galaxies in the field corresponding to the same redshift interval, and f is the scale factor that resizes the field to the cylindrical volume of the cluster.

Figure 3.2 displays the richness (defined as the number of FoF members) and the S/N of our cluster candidate sample. Richer clusters have a higher S/N. Only 3% of clusters with more than 20 members have poorly defined centres, whilst 17% of clusters with less than 20 member galaxies have poorly defined centres, and 25% have a S/N lower than unity. Based on both the low S/N and the low completeness rate found in Section 3.2.2, we decide to exclude those cluster candidates with fewer than 20 member galaxies. This ensures a high quality cluster sample, although it significantly reduces the sample size. This in not an inconvenience for us, given that we require a clean sample rather than a complete one.

3.3 Clusters in the UDS

The FoF algorithm identifies 37 galaxy cluster candidates at $0.5 < z < 1.0$ in the UDS field. Eleven cluster candidates contain more than 45 FoF members, whilst 26 have between 20 and 45 members. This results in a sample of 2210 cluster galaxies[1] (of which 98 are classified as PSBs) and 13,837 field galaxies (220 of which are PSBs). We also identify 87 cluster candidates with less than 20 and more than 10 FoF members, but we do not analyse these further as this sample has a high level of contamination (shown in Figure 3.2).

The catalogue of our cluster candidates is provided in Table 3.1 and their redshift distribution is shown in Figure 3.3. A spike in the redshift distribution of clusters is visible at $z \sim 0.65$ due to the presence of a well-known galaxy overdensity, including a massive cluster in the CANDELS-UDS region (Geach et al. 2007). These structures are not fragments of the same massive cluster as they appear evenly spread across the UDS field. Instead, most of these structures are likely to be smaller clusters surrounding the massive cluster, since clusters of galaxies are highly clustered (Galametz et al. 2018).

3.3.1 Spectroscopic confirmation of cluster candidates

To spectroscopically confirm our cluster sample, we utilise more than 6800 spectroscopic redshifts from the UDS field, including 1511 secure redshifts from the UDSz (ESO Large Programme, Almaini et al., in prep) and over 3000 archival redshifts from Subaru FOCAS and AAT 2dF (Akiyama et al. 2010; in prep), VLT VIMOS (Simpson et al. 2010; in prep), AAOMEGA (Smail et al. 2008) and VIPERS (Scodeggio et al. 2016). We classify a cluster as spectroscopically confirmed if it contains at least five spectroscopic galaxies within a cylinder of ± 1000 kms^{-1} length and 1 Mpc radius (Eisenhardt et al. 2008). In addition, the median of the spectroscopic cluster galaxies must not be offset by more than 1σ from the photometric redshift of the candidate cluster. Eleven of our cluster candidates fulfil these conditions (see Table 3.1), of which three have not been previously presented in the literature.

3.3.2 Comparison of cluster candidates with previous studies of clusters in the UDS

Clusters in the UDS have been located by Finoguenov et al. (2010) through the detection of extended *XMM–Newton* X-ray emission, by van Breukelen et al. (2006)

[1] Cluster galaxies are defined as all the galaxies within the cylinder encompassing the cluster.

Table 3.1. Catalogue of galaxy cluster candidates detected in the UDS using the FoF algorithm. Identification number is provided in column 1, RA and Dec $(2-3)$, photometric redshift (4). Column 5 corresponds to the median spectroscopic redshift of the spectroscopically confirmed clusters (see Section 3.3.1) and the number of spectroscopic redshifts associated with the structure (6). Three measurements of the richness of the clusters: number of FoF members (7), field subtracted number of galaxies within 1 Mpc from the cluster centre (8) and field subtracted stellar mass within 1 Mpc from the centre (9). Column 10 provides references if the structure has been previously detected. The bottom two rows correspond to clusters that are spectroscopically confirmed despite having fewer than 20 FoF members.

ID	RA (deg)	Dec (deg)	phot-z	median spec-z	N($z_{\rm spec}$)	$\rm N_{FoF}$	$\rm N_{Sub}$ (1 Mpc)	$\rm M_{Sub}$ $\log(M_*)$	Reference
(1)	(2)	(3)	(4)	(5)	(6)	(7)	(8)	(9)	(10)
UDSC01FOF	34.70321	−5.14147	0.546			21	23	11.9312	b
UDSC02FOF	34.28647	−5.07732	0.609			22	22	11.2892	
UDSC03FOF	34.24918	−5.18202	0.618			21	13	11.8515	a
UDSC04FOF	34.64570	−4.96700	0.620	0.589	14	38	46	12.0126	a, b
UDSC05FOF	34.59033	−5.29313	0.627			28	25	11.9037	
UDSC06FOF	34.35261	−5.41159	0.628			45	52	12.1130	b, c
UDSC07FOF	34.42521	−5.46676	0.631			25	24	11.8822	
UDSC08FOF	34.18869	−5.14456	0.631			45	39	11.8729	b
UDSC09FOF	34.29001	−5.13710	0.632			27	18	11.8189	
UDSC10FOF	34.53183	−5.36065	0.635			27	38	11.8080	a, b
UDSC11FOF	34.67991	−5.38076	0.637			28	26	11.3117	
UDSC12FOF	34.28599	−5.42808	0.638			55	32	11.8175	
UDSC13FOF	34.58946	−5.38840	0.638			38	67	12.3032	
UDSC14FOF	34.39740	−5.22350	0.638	0.647	20	135	111	12.4485	a, b, c, d
UDSC15FOF	34.54191	−5.25419	0.641	0.647	10	74	57	12.2359	b
UDSC16FOF	34.60487	−5.41888	0.646	0.647	13	67	73	12.3414	b, c, d
UDSC17FOF	34.64400	−5.01744	0.648			44	36	11.8114	
UDSC18FOF	34.62682	−5.34075	0.651			31	25	11.6202	
UDSC19FOF	34.34840	−5.18454	0.651	0.649	10	24	30	11.8912	
UDSC20FOF	34.53353	−5.51288	0.671			43	36	11.8701	b
UDSC21FOF	34.49045	−5.45092	0.674	0.695	7	116	79	12.3302	b, c
UDSC22FOF	34.37161	−4.69193	0.681			25	15	11.4853	b
UDSC23FOF	34.21696	−5.20876	0.814			23	21	11.8909	a
UDSC24FOF	34.52203	−4.73357	0.850			30	27	11.9332	a, b
UDSC25FOF	34.82970	−5.08690	0.872	0.872	9	29	30	12.1240	b, c
UDSC26FOF	34.63429	−5.01229	0.874	0.874	31	80	67	12.3855	a, b, c
UDSC27FOF	34.36706	−4.70291	0.876			26	15	11.4445	
UDSC28FOF	34.71698	−5.35764	0.899			46	37	12.1644	
UDSC29FOF	34.27406	−5.16789	0.910			20	9	11.6155	
UDSC30FOF	34.76268	−4.70390	0.910			36	24	12.0208	a
UDSC31FOF	34.52417	−5.37735	0.918			25	22	11.7250	
UDSC32FOF	34.87913	−5.22070	0.926			23	12	11.9276	
UDSC33FOF	34.80408	−4.91053	0.926			21	33	11.9349	c
UDSC34FOF	34.34259	−5.20107	0.937	0.918	6	61	49	12.0711	a, b
UDSC35FOF	34.28586	−4.96203	0.953			33	27	11.8483	
UDSC36FOF	34.04102	−4.86472	0.953			61	50	12.1284	b
UDSC37FOF	34.28933	−4.76095	0.957			22	33	12.0459	a
UDSC38FOF	34.50443	−4.79895	0.568	0.583	14	13	22	11.9007	
UDSC39FOF	34.39913	−5.07272	0.800	0.801	10	13	25	11.9074	

[a] Detected by van Breukelen et al. (2006), [b] detected by Lee et al. (2015), [c] detected by Finoguenov et al. (2010), [d] detected by Geach et al. (2007)

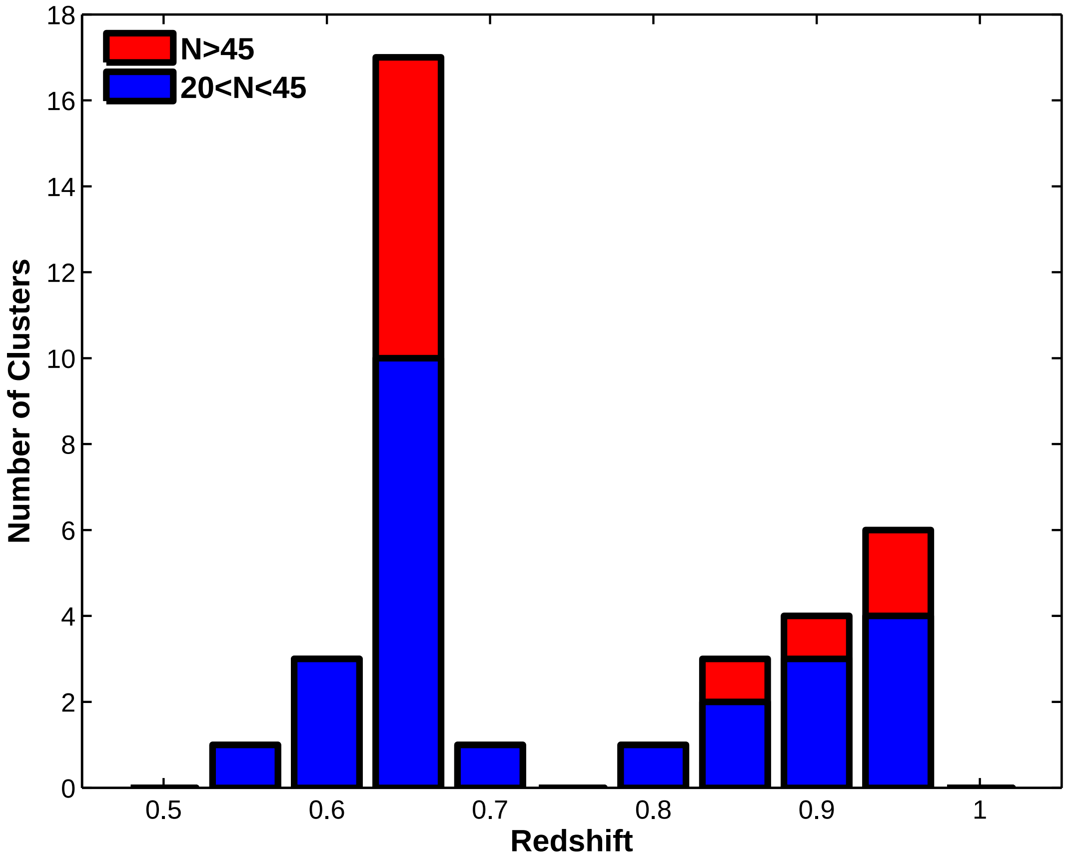

Figure 3.3. Distribution of detected clusters as a function of redshift. In the histogram red colour indicates clusters with more than 45 members and blue indicates clusters with more than 20 but less than 45 galaxy members.

and Lee et al. (2015), who searched for galaxy overdensities in the optical and near infrared photometric surveys, and by Geach et al. (2007), who used low-power radio galaxies as beacons for overdensities. We compare cluster samples derived from these methods with our FoF cluster sample to check the robustness of our detection method. Throughout this comparison, we use our whole sample of cluster candidates with a richnesses greater than 10 FoF galaxies. Although many of the cluster candidates with less than 20 FoF members are likely to be contaminants, some of them are expected to be real clusters, as shown by Figure 3.1.

The two spectroscopically confirmed clusters at $z = 0.65$ from Geach et al. (2007) are two of the most massive structures we identify with our FoF algorithm. We locate 83.3% (10/12) of the cluster candidates detected by van Breukelen et al. (2006), who used an algorithm based on FoF and Voronoi tessellation[2]. However, there seems to be a systematic bias in their cluster redshifts with respect to ours as theirs tend to be systematically lower at $z > 0.7$. This offset is probably due to the relatively unreliable photometric redshifts from the UDS DR1 catalogue used

[2]We define a cluster match if the RA and Dec of the cluster centre matches to within 2 arcmin ($\sim$ 1 Mpc) and $\Delta z \lesssim \sigma_z$, where σ_z represents the total photometric redshift uncertainty i.e. the combination of the literature and our photometric redshift uncertainties. Furthermore, we ignore known or candidate clusters from the literature that fall within masked regions of our catalogue or lie outside our $0.5 < z < 1.0$ redshift interval.

by van Breukelen et al. (2006), which was much shallower than the DR8 catalogue. We recover 85.2% (17/20) of the cluster candidates listed in Lee et al. (2015), where they locate clusters as galaxy overdensities in spatial and photometric redshift space. We also locate 78.5% (11/14) of the X-ray selected cluster candidates in Finoguenov et al. (2010). The 3 structures that we miss are close to our lower redshift limit at $z = 0.514$, 0.517 and 0.548.

Two X-ray selected cluster candidates at $z = 0.548$ and $z = 0.514$ (named SXDF66XGG and SXDF42XGG, respectively in Finoguenov et al. 2010) may be misclassified groups of X-ray AGN that are close in projection on the sky. No galaxy excess is detected near either of these cluster candidates. However, three *Chandra* (Kocevski et al. 2018) X-ray point sources are located at angular separations of $6.96''$, $8.14''$ and $15.20''$ from the centre of the SXDF66XGG cluster, each of them with a galaxy counterpart within 1 arcsec. Similarly, two X-ray point sources from the Subaru *XMM–Newton* Deep Survey (Akiyama et al. 2015) are found within $7.94''$ and $10.70''$ from the centre of SXDF42XGG. These two sources have galaxy counterparts offset $1.51''$ and $3.81''$, respectively, from the X-ray source, which is within the *XMM* point-source error circle.

The cluster candidate SXDF24XGG, at $z = 0.517$, shows a slight excess of galaxies in our catalogue. We detect the candidate as a group of 5 FoF galaxies when we optimise the algorithm to detect clusters at $z \sim 0.5$. When the algorithm is optimised to locate clusters across the redshift range $0.5 < z < 1.0$ it begins to break down at both redshift extremes, but especially at low redshift. Hence, it is likely that this small cluster is missed by our original detection algorithm.

We conclude that we do not detect all the X-ray cluster candidates from Finoguenov et al. (2010) because the presence of one or more X-ray point-sources (AGN) means that some cluster candidates are falsely identified as extended sources due to the low resolution of the *XMM–Newton* data. Furthermore, the X-ray cluster detection method is highly efficient at low redshift where our ability to detect clusters through the FoF algorithm decreases. This is supported by the test simulations shown in Figure 3.1 where some X-ray cluster candidates lie in the low completeness regime of our method.

3.4 Summary and conclusions

In this chapter, we reviewed the dominant methods used to define galaxy environment to-date. We then present a method (based on a FoF algorithm) that we use to define the cluster and field galaxy samples we use in Chapters 4 and 5 of this thesis. We also presented the optimisation of the FoF parameters to perform on the photometric data from the UDS. The optimal linking parameters are $d_{\rm link} = 300$ kpc and $z_{\rm link} = 40$ Mpc, with a detection threshold of 20 galaxies per structure. We estimated the completeness and contamination rates of this configuration is 31% and 5%, respectively. These parameters yield a sample of 37 candidate galaxy clusters in the redshift range $0.5 < z < 1.0$. We performed a number of tests in order to judge the reliability of the method. These include studying the fraction of simulated clusters the algorithm was able to recover and an estimation of the S/N values for each structure. We also used the available spectra to confirm eleven of our cluster candidates. Finally we compare our cluster sample with previous cluster studies in the same field. We found our sample is broadly consistent with these studies which use disparate detection methods.

The analysis we carry out in Chapter 6, of environmental effects at much higher redshifts ($z \lesssim 3$), requires the use of a different environmental measurement in order to perform a systematic and consistent study from low to high redshift. We choose a fixed aperture method for this purpose, which we describe in Section 6.3.

Chapter 4

The enhancement of rapidly quenched galaxies in distant clusters at $0.5 < z < 1.0$

In this chapter, we investigate the relationship between environment and galaxy evolution in the redshift range $0.5 < z < 1.0$. Galaxy overdensities are selected using a Friends-of-Friends algorithm, applied to deep photometric data in the UDS field (see Chapter 3). A study of the stellar mass functions reveals clear differences between galaxies in cluster and field environments, with a strong excess of low-mass, rapidly quenched galaxies in cluster environments compared to the field. Cluster environments also show a corresponding deficit of young, low-mass star-forming galaxies, which show a sharp radial decline towards cluster centres. By comparing mass functions and radial distributions, we conclude that young star-forming galaxies are rapidly quenched as they enter overdense environments, becoming post-starburst galaxies before joining the red sequence. Our results also point to the existence of two environmental quenching pathways operating in galaxy clusters, operating on different timescales. Fast quenching acts on galaxies with high specific star-formation rates, operating on timescales shorter than the cluster dynamical time (< 1 Gyr). In contrast, slow quenching affects galaxies with moderate specific star-formation rates, regardless of their stellar mass, and acts on longer timescales ($\gtrsim 1$ Gyr). Of the cluster galaxies in the stellar mass range $9.0 < \log(M_*/M_\odot) < 10.5$ that were quenched during this epoch, we find that 73% were transformed through fast quenching, while the remaining 27% followed the slow quenching route.

The work presented in this chapter is part of the paper Socolovsky et al. (2018). Although the majority of the analysis is done by me, I did not take part in the production of the catalogues. These include photometric redshifts and stellar masses from Simpson et al. (2013), and the application of the PCA classification from Wild et al. (2016). Furthermore, the stellar population synthesis models presented in Section 4.4.4 are also taken from Wild et al. (2016).

4.1 Introduction

In Chapter 1 we discussed how galaxy properties, such as morphology and star formation activity, correlate with both environment (Dressler 1980; Kauffmann et al. 2004; Balogh et al. 2004; von der Linden et al. 2010; Haines et al. 2015) and the stellar mass of the galaxy (van der Wel et al. 2008; Bamford et al. 2009). Massive galaxies and those in dense environments are predominantly spheroidal and quiescent, whereas lower mass and field galaxies are mainly disc-dominated and star-forming. This suggests the existence of two distinct quenching modes, "environmental quenching" and "mass quenching" (see Figure 1.9).

Mass is generally believed to be a major driver of galaxy evolution across redshift. In contrast, there is less agreement regarding the importance of galaxy environment. It appears evident that the effect of environmental density increases towards low redshift (Grützbauch et al. 2011; Scoville et al. 2013). However, some studies find that most galaxy properties correlate with halo mass rather than with environment. Several studies have investigated the timescale of environmental quenching. Semi-analytic models of galaxy formation require gas to be removed on long timescales ($\sim$ 3–7 Gyrs) to explain the fraction of passive satellites in clusters (Font et al. 2008; Kang & van den Bosch 2008; Weinmann et al. 2010; McGee et al. 2011; De Lucia et al. 2012; Wheeler et al. 2014). However, the rarity of transitional galaxies can only be explained if the quenching of star formation is rapid (Muzzin et al. 2012, 2014; Wetzel et al. 2012; Mok et al. 2013). Both observational constraints can be satisfied by a delayed-then-rapid quenching model (Wetzel et al. 2013). In this model galaxies experience a delay between the moment they become satellites and when their SFR starts to decline. This time delay can span over 2–4 Gyrs, but once the SFR begins to decline quenching occurs quickly ($<$ 0.8 Gyrs).

Some popular mechanisms used to explain environmental quenching invoke interactions between the intracluster or intragroup medium and galaxies, such as ram pressure stripping (Gunn & Gott 1972), which can quench a galaxy on timescales $<$ 1 Gyr, or strangulation (Larson et al. 1980), which acts on longer timescales $\sim$ 4 Gyrs (Bekki et al. 2002). Another kind of process that is frequent in dense environments is galaxy-galaxy interactions, such as harassment, mergers and tidal interactions. Harassment consists of small and repeated perturbations that can quench a galaxy on long timescales, while mergers produce a much stronger disruption which may lead to rapid quenching. Therefore, by measuring the timescale and efficiency of environmental quenching, we can gain insight into where and when these processes act and which is the most important.

As mentioned in Chapter 1, it is useful to study galaxies in transition in order to understand the mechanisms responsible for quenching star formation. We use the rare population of PSB galaxies, that have undergone rapid quenching within the last Gyr, in order to study the effects and timescale of environmental quenching.

In this chapter we investigate star-forming, passive and PSB galaxies in clusters and groups at $0.5 < z < 1$ to understand the mechanisms responsible for environmental quenching during this period. In Section 4.2 we describe our data and galaxy classification method. We present our results in Section 4.3 and discuss their significance in Section 4.4. Finally, our conclusions are listed in Section 4.5.

4.2 Data sets and galaxy classification

The work presented in this chapter is entirely based on the UDS DR8, described in detail in Section 2.1. The galaxy catalogue we use in this chapter is magnitude-limited to $K < 24.3$ to ensure the 95% detection completeness (Hartley et al. 2013). It consists of 23 398 galaxies in the redshift interval $0.5 < z < 1.0$. Photometric redshifts and stellar masses were derived by Simpson et al. (2013) via SED fitting to the photometry in 11 bands: U, B, V, R, i', z', J, H, K, 3.6μm and 4.5μm. Testing the photometric redshifts against the available spectroscopic sample (over 5000 spectra, including $\sim$ 1500 from the UDSz programme in addition to archival data), revealed a median absolute deviation of $\sigma_{\rm NMAD} \sim 0.023$ below redshift $z = 1$.

The galaxy classification, as described in Section 2.2, is based on the PCA method developed by Wild et al. (2016). The supercolour method has been proven to successfully classify galaxies using only photometry. The spectroscopic confirmation of the method can be found in Wild et al. (2014) and Maltby et al. (2016). It was found that 80% of PSB candidates show the strong Balmer absorption lines characteristic of post-starburst galaxies $W_{\rm H_\delta} > 5$ Å . Using stricter criteria to exclude galaxies with significant [OII] emission, the confirmation rate drops to 60% (Maltby et al. 2016).

Throughout this chapter, we use galaxies classified by the supercolour PCA method (see Figure 4.1). These include star-forming (SF), passive (PAS), post-starburst (PSB), metal-poor and dusty galaxies (the last two are excluded from our sample). Wild et al. (2014) subdivide the SF population into 3 groups of decreasing SSFR: SF1, SF2, and SF3. For the purpose of our work we also split the PAS population into three populations of increasing mean stellar age, from PAS1 to PAS3. This dividing line was determined by splitting PAS galaxies along the vector $(\mathrm{SC1}, \mathrm{SC2}) = (-5, -2)$. The borders ($\mathrm{SC2} = -\frac{5}{2}\mathrm{SC1} - 20$ and $\mathrm{SC2} = -\frac{5}{2}\mathrm{SC1} - 31$) are chosen so that they evenly split the PAS population into 3 subgroups. The locations of each of the 7 populations on the SC diagram are shown in the bottom panel of Figure 4.1.

Some of the physical properties of galaxies quoted in this section, such as SSFRs and r-band light-weighted mean stellar ages, are also derived from the supercolour formalism (see Chapter 2). These quantities are directly obtained from the model SEDs used to calibrate the PCA method. The mean stellar age corresponds to the mean R-band weighted stellar age, which roughly corresponds to the time since the last burst of star formation took place. For non-star-forming populations (i.e. PAS and PSB), this is the approximate time since the bulk of the stellar mass was assembled.

In total, our galaxy catalogue consists of 11 625 SF1, 3 486 SF2, 2 055 SF3, 575 PAS1, 793 PAS2, 838 PAS3 and 418 PSBs to a magnitude limit of $K < 24$ and in the range $0.5 < z < 1.0$. The 90% mass completeness limit for each type of galaxy using the method of Pozzetti et al. (2010) are as follows. The mass limits at $z = 1.0$ are $10^{9.0}\mathrm{M}_\odot$ for SF, $10^{9.5}\mathrm{M}_\odot$ for PAS and $10^{9.3}\mathrm{M}_\odot$ for PSB galaxy populations. For the subpopulations we find the following values: SF1 $10^{8.9}\mathrm{M}_\odot$, SF2 $10^{9.2}\mathrm{M}_\odot$, SF3 $10^{9.4}\mathrm{M}_\odot$, PAS1 $10^{9.5}\mathrm{M}_\odot$, PAS2 $10^{9.57}\mathrm{M}_\odot$ and PAS3 $10^{9.61}\mathrm{M}_\odot$.

4.3 Results

In this section we compare the properties of galaxies identified in our 37 candidate galaxy clusters (defined in Chapter 3) with those identified in the field, focussing on the redshift range $0.5 < z < 1.0$. The "cluster" sample consists of galaxies identified in overdense regions containing at least 20 members, linked by the Friends-of-Friends algorithm, as described in Section 3.2.

In Section 4.3.1 we compare the PCA supercolours for the cluster and field samples, while in Section 4.3.2 we compare the stellar mass functions. In Section 4.3.3 we investigate the radial distribution of galaxies for the cluster populations.

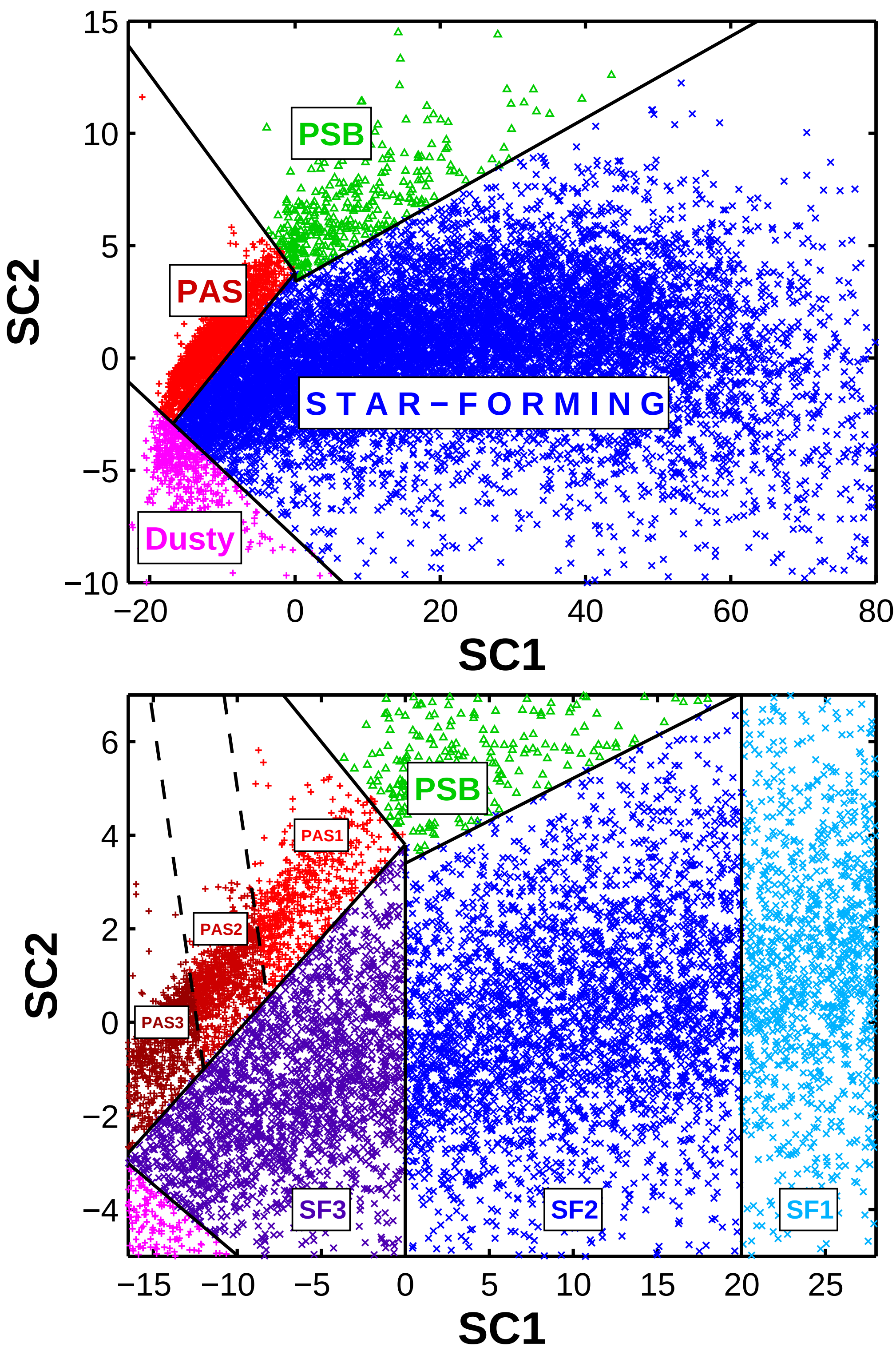

Figure 4.1. Top panel: the SC1–SC2 diagram for the galaxies in our sample, based on the PCA classification described in Wild et al. (2014). Galaxies belonging to different populations are represented in different colours. Solid black lines demarcate the borders between the main SC populations. Bottom panel: zoom in of the same diagram showing the sub-populations described in this section. Dashed black lines delimit the divisions of the passive galaxy region by mean stellar age.

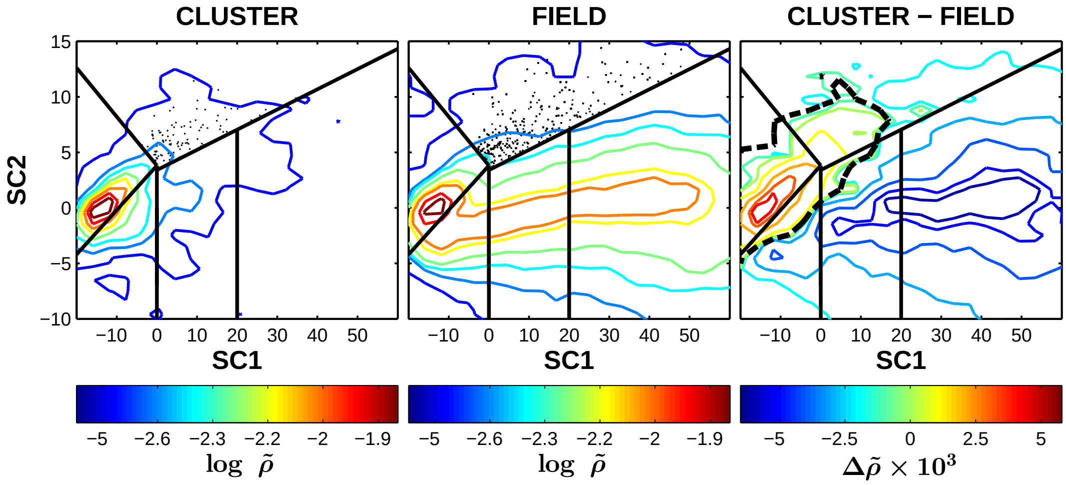

Figure 4.2. The distribution of UDS galaxies at $0.5 < z < 1.0$ across the SC-space. Straight solid black lines represent the boundaries between the different galaxy populations and black dots the PSBs in the sample. Colour contours show the number of galaxies per bin normalised by the total number of galaxies in the diagram, where the bin size is $\Delta\mathrm{SC1} \times \Delta\mathrm{SC2} = 4 \times 1$. The panel on the left shows the distribution of cluster galaxies (note it has been field subtracted). The central panel shows the distribution of field galaxies. The right-hand panel shows the difference between cluster and field densities, with the dashed black contour representing the regime where field and cluster have the same density.

4.3.1 Cluster and field galaxy populations

In Figure 4.2 we present the number density of galaxies across the SC1–SC2 diagram for our candidate galaxy clusters and the field. For the cluster sample, the densities across the SC diagram are obtained after subtracting the corresponding values for the field (correcting for the volumes sampled), to correct for the contamination from field galaxies in the cluster volumes. We find significant differences between the cluster and field populations, which are emphasised in the final panel, which displays the difference between the cluster and field regions.

We observe that galaxies in clusters are, in general, more evolved than those in the field. The differences are reflected in the overall shift of cluster galaxies towards the left side of the SC-diagram, producing an enhancement of the quiescent galaxies (PAS) and star-forming galaxies in the SF3 class, characterised by their high mean stellar ages and low SSFRs. Following the same trend, there is a lack of young star-forming objects in clusters (at high values of SC1). The SF1 class, with the highest SSFR, is common in the field but rare in clusters.

There are PSBs in both environments, but their distributions over the SC-space is significantly different. While PSBs in the field are found to be widespread over the upper region of the diagram, their counterparts in dense environments only populate the area closest to the border with the PAS population (SC2 $<$ 10). A two-sample Kolmogorov-Smirnov (KS) test applied only to SC2, rejects the null hypothesis that the field and cluster PSBs are drawn from the same underlying distribution (giving a probability of 1.45×10^{-6}). This difference may suggest that PSBs are formed via different mechanisms, depending on their environment. We explore this result and its possible implications in Section 4.4.4.

4.3.2 Mass Functions of cluster galaxies vs. the field

Stellar mass functions can provide further information on the evolution of galaxies and, in particular, about the range of masses affected by environmental quenching. In this section we present the stellar mass functions of SF, PAS and PSB galaxies split by environment. Additionally, we split the SF category by decreasing SSFR (SF1, SF2 and SF3) and the PAS sample by increasing mean stellar age (PAS1, PAS2, PAS3), using the classification boundaries defined in Section 4.2.

The stellar mass functions shown in Figure 4.3 are computed using the cluster and field samples. Since the cluster total densities are arbitrary, given that the volume of the cylinder is chosen artificially, the cluster mass functions are normalised so that the total density (of all galaxies) matches the total density in the field. This allows us to compare the shapes of the mass functions across environments and populations, but implies that a comparison of normalisations (i.e. total densities) is only meaningful within the same environment. Although the normalisation is arbitrary, all densities are offset by the same amount from the true cluster density; we parametrise this offset by introducing the quantity ξ whose exact value is unknown to us.

$$\xi = \frac{total\ density\ in\ clusters}{total\ density\ of\ the\ field} \tag{4.1}$$

Cluster galaxy mass functions are computed using the cluster sample described in Section 3.3, consisting of 37 candidate clusters at $0.5 < z < 1.0$ with more than 20 members linked by the FoF algorithm. The field mass function is subtracted in order to remove background contamination. We fit simple Schechter functions to all our mass functions except to the cluster PSBs, to which we fit a double Schechter mass function, with two power laws and one exponential (Pozzetti et al. 2010). This is because we believe the cluster PSB class comprises two different populations; one which is identical to that observed in the field and one that is produced by environmental quenching (see also Wild et al. 2016). The list of fitted Schechter parameters is given in Table 4.1. Fits were performed using a Maximum Likelihood method using unbinned data (Marshall et al. 1983).

The stellar mass functions of the three main populations show significant differences as a function of environment, with PSBs showing the largest difference between clusters and the field. The probability (p-value) of both populations being drawn from the same distribution according to a KS test is $p_{\rm KS} = 4.2 \times 10^{-6}$. The stellar mass function of this population suggests that they are very strongly clustered, as the number density is more than 3 ξ times larger in clusters than in the field. The shape of the mass function is also very different; PSBs in clusters are predominantly low-mass galaxies ($M_* < 10^{10.5}$ M$_\odot$) while in the field the range of masses is broader.

The PAS population also shows a strong environmental dependence. Passive galaxies are more abundant in clusters, as expected, with 2.5 ξ times the density of the field. More interesting is the different shape of the passive galaxy mass function in clusters with respect to the field, with evidence for an excess of low-mass galaxies; we reject the null hypothesis that the populations are drawn from the same underlying distribution at significance $p_{\rm KS} = 10^{-3}$. Furthermore, we see that this excess is mainly produced by the "younger" passive galaxies (i.e. the most recently quenched), with PAS1 presenting $p_{\rm KS} = 10^{-4}$ between field and cluster.

The SF population also presents a stellar mass distribution that depends on environment ($p_{\rm KS} = 3.6 \times 10^{-9}$), with a deficit of low-mass galaxies in cluster environments. Unlike the PAS and PSB populations, the overall density in the field

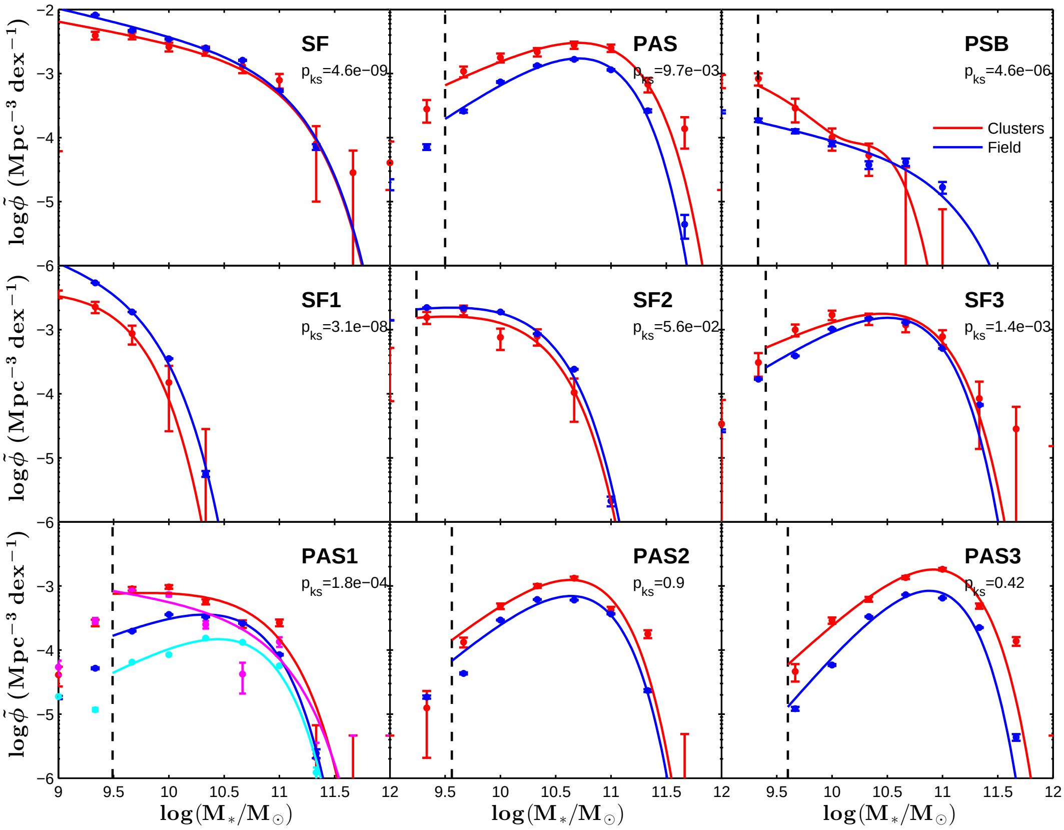

Figure 4.3. Stellar mass functions of galaxies in clusters (red) and the field (blue) at $0.5 < z < 1.0$. The cluster mass functions are normalised so that the total (integrated) density of galaxies matches the field. The first row corresponds to the three main galaxy populations: SF, PAS and PSB, from left to right. The second and third rows represent the mass functions of the three sub-populations of the SF and PAS categories, respectively, ordered from young to old (from left to right). In the panel corresponding to the PAS1 population, the stellar mass functions of galaxies quenched during the redshift interval $0.5 < z < 1.0$ are represented with magenta and cyan lines for cluster and field, respectively. The vertical dashed black line indicates the 90% mass completeness limit. Additionally, each panel shows the probability that the field and cluster samples are drawn from the same underlying population, according to a KS test, as applied to the sample before statistical background subtraction.

is $\sim 1.2\ \xi$ times higher than in clusters, which indicates that SF galaxies have no preference for dense environments. Some studies have found the opposite trend, suggesting a high fraction of star-forming galaxies in dense environments at $z \sim 1$ (Elbaz et al. 2007; Cooper et al. 2008). However, these were conducted using an optical galaxy selection, which has been shown to be strongly biased towards blue star-forming galaxies at high redshift. With the rise of near-infrared surveys, it was found that the star formation–density relation was in place already at $z \sim 1$–1.5 (Williams et al. 2009; Chuter et al. 2011).

Studying the three SF sub-populations we find a strong dependence of quenching with both SSFR and stellar mass. The population with the highest SSFR (SF1) is found to be strongly suppressed in clusters. This suppression is also mass-dependent and is more efficient at low stellar masses; a KS test rejects the null hypothesis that mass distributions in clusters and the field are drawn from the same underlying population ($p_{\rm KS} = 3.1 \times 10^{-8}$). For the intermediate class (SF2) we find a slight suppression in the relative number density in cluster environments, but no evidence for a change in the shape of the mass function. In contrast to SF1 galaxies, the relative abundance of the SF3 population appears to be enhanced in cluster environments, with evidence for an excess of low-mass galaxies in particular; a KS test rejects the null hypothesis that the mass functions are drawn from the same underlying population with $p_{\rm KS} = 1.4 \times 10^{-3}$.

For the purpose of estimating timescales (see Section 4.4.1) we also evaluate the mass functions of those PAS1 galaxies which were quenched during the epoch $0.5 < z < 1.0$ (based on mean stellar age from SC fits). This sub-population is shown in magenta (clusters) and cyan (field) in the lower-left panel of Figure 4.3. We find that cluster galaxies satisfying this condition are systematically less massive than when the whole sample was employed. This means that the most recently quenched objects are mostly low-mass galaxies, and the most massive PAS galaxies were likely to have been in place already by $z = 1$. Furthermore, isolating those galaxies that quenched during this epoch sharpens the apparent difference between cluster and field PAS1 galaxies, based on a KS test ($p_{\rm KS} = 1.4 \times 10^{-13}$).

In summary, we find an excess of low-mass galaxies among the PAS, PSB and SF3 populations in clusters. In contrast, we find that galaxies with high SSFR (SF1 and SF2) are suppressed in such environments. Additionally, the quenching of high SSFR galaxies in clusters seems to be mass-dependent, affecting low-mass galaxies more efficiently than massive systems.

4.3.3 Radial distribution of galaxies in clusters

The radial distribution of different galaxy populations in clusters can, in principle, provide information on where quenching is taking place and the likely timescales. We define the centre of a cluster as its centre of mass and measure projected distances to all galaxy members within 1 Mpc. Additionally, clusters are split in two richness bins ($20 < N_{\rm FoF} < 45$ and $N_{\rm FoF} > 45$ members) to reduce the influence due to variation in size, and stacked together to produce radial profiles.

The radial trends of all PAS galaxies, PSBs and SF1s are shown in Figure 4.4. We plot only SF1 galaxies instead of the total SF population because, as the mass functions demonstrated, this population has the strongest environmental dependence.

The radial plots show the expected trends for the star-forming and quiescent galaxies. As in previous studies, red passive galaxies tend to reside in the inner, denser regions of the clusters while blue star-forming galaxies prefer the outskirts and

Table 4.1. Schechter parameters of all 9 galaxy population mass functions. We use single Schechter functions except for the cluster PSBs. M^* units are given in solar masses and ϕ^* in $\mathrm{Mpc}^{-3}\mathrm{dex}^{-1}$. The variable ξ represents the relative change in normalisation of a cluster with respect to the field. The last two entries (*) correspond to the mass functions of galaxies quenched at $0.5 < z < 1.0$, while the rest correspond to the entire sample.

		Cluster	Field
SFT	α	-1.310 ± 0.010	-1.402 ± 0.006
	$\log M^*$	10.914 ± 0.025	10.930 ± 0.010
	$\log \phi^*$	$(-3.140 \pm 0.003)\xi$	-3.118 ± 0.002
PAS	α	-0.170 ± 0.022	0.183 ± 0.013
	$\log M^*$	10.787 ± 0.015	10.633 ± 0.006
	$\log \phi^*$	$(-2.455 \pm 0.056)\xi$	-2.699 ± 0.032
PSB	α_1	-1.493 ± 0.113	-1.378 ± 0.027
	$\log M^*$	9.789 ± 0.071	10.903 ± 0.039
	$\log \phi_1^*$	$(-3.624 \pm 0.033)\xi$	-4.879 ± 0.009
	α_2	2.448 ± 0.297	
	$\log \phi_2^*$	$(-4.902 \pm 0.053)\xi$	
SF1	α	-0.804 ± 0.047	-1.448 ± 0.020
	$\log M^*$	9.334 ± 0.020	9.539 ± 0.010
	$\log \phi^*$	$(-2.653 \pm 0.002)\xi$	-2.444 ± 0.006
SF2	α	-0.739 ± 0.029	-0.726 ± 0.015
	$\log M^*$	10.108 ± 0.022	10.125 ± 0.009
	$\log \phi^*$	$(-2.892 \pm 0.017)\xi$	-2.745 ± 0.009
SF3	α	-0.192 ± 0.028	0.103 ± 0.016
	$\log M^*$	10.546 ± 0.017	10.462 ± 0.007
	$\log \phi^*$	$(-2.688 \pm 0.063)\xi$	-2.745 ± 0.067
PAS1	α	-0.859 ± 0.025	-0.286 ± 0.026
	$\log M^*$	10.659 ± 0.024	10.473 ± 0.014
	$\log \phi^*$	$(-3.291 \pm 0.013)\xi$	-3.394 ± 0.039
PAS2	α	0.393 ± 0.036	0.488 ± 0.025
	$\log M^*$	10.488 ± 0.018	10.466 ± 0.008
	$\log \phi^*$	$(-2.864 \pm 0.040)\xi$	-3.130 ± 0.022
PAS3	α	0.640 ± 0.038	1.082 ± 0.027
	$\log M^*$	10.704 ± 0.016	10.564 ± 0.007
	$\log \phi^*$	$(-2.746 \pm 0.026)\xi$	-3.197 ± 0.011
PSB*	α_1	-1.616 ± 0.282	-2.010 ± 0.035
	$\log M^*$	9.547 ± 0.113	10.984 ± 0.081
	$\log \phi_1^*$	$(-3.544 \pm 0.076)\xi$	-6.145 ± 0.008
	α_2	1.549 ± 0.437	
	$\log \phi_2^*$	$(-4.902 \pm 0.123)\xi$	
PAS1*	α	-1.253 ± 0.022	-0.071 ± 0.039
	$\log M^*$	10.792 ± 0.027	10.477 ± 0.017
	$\log \phi^*$	$(-3.765 \pm 0.008)\xi$	-3.760 ± 0.239

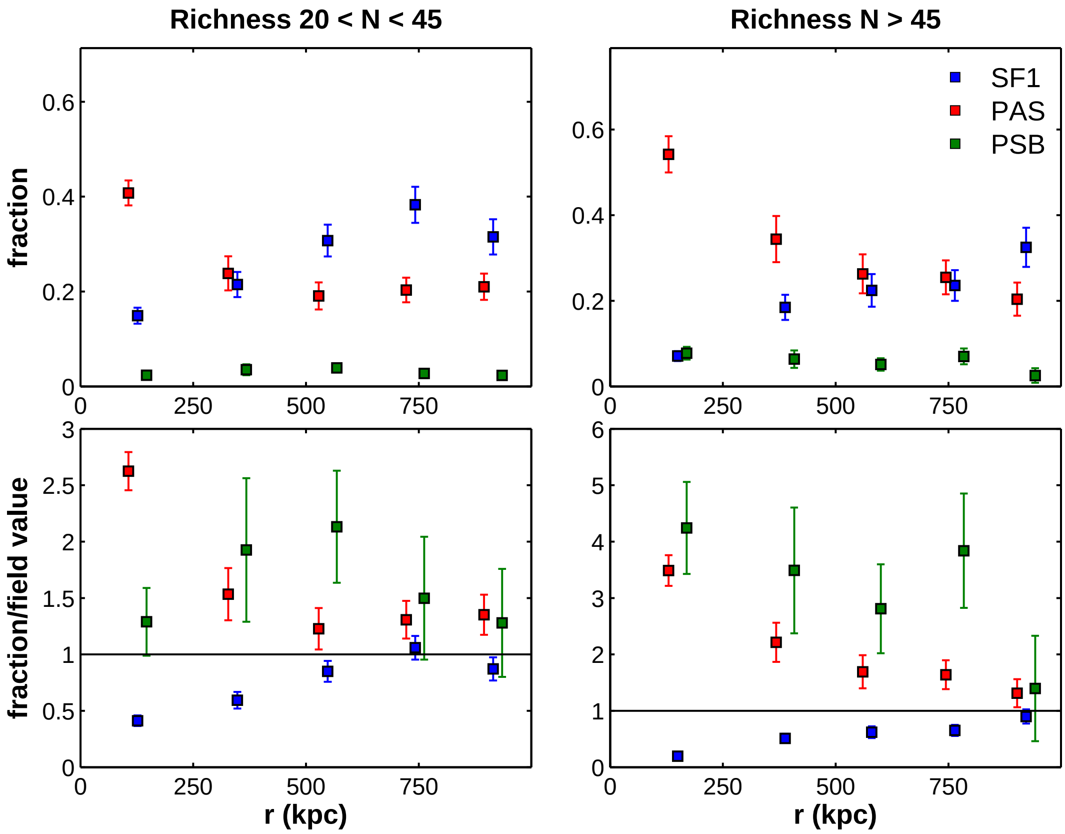

Figure 4.4. Radial plots of SF1, PAS and PSB galaxies in two cluster richness bins: clusters with between 20 and 45 and with more than 45 FoF selected members. In the top row the fraction of each population is represented as a function of cluster-centric distance. In the bottom row the fraction is normalised by the corresponding value in the field.

dominate at large cluster-centric distances (Oemler 1974; Muzzin et al. 2014). This difference is reflected in a KS test, which gives rise to $p_{\mathrm{KS}} = 10^{-12}$ and 1.0×10^{-11} for the low and high richness bins, respectively. Additionally, we find that the crossover point between the SF1 and PAS populations scales with richness, as expected if galaxy clusters are roughly self-similar.

PSBs are found to favour the dense cluster environment, and within 500 kpc the fraction of these galaxies is several times higher than the field. Although PSBs do not follow a clear radial trend, a KS test applied on the radial distributions reveals that formally their cluster-centric distances cannot be distinguished from those of the passive population (Table 4.2). There is some evidence, however, that PSBs are not as concentrated in the core region as PAS galaxies. This is broadly consistent with Muzzin et al. (2014), who found that PSBs reside in the inner volumes of clusters but avoid the very central region. We note, however, that they also showed that this trend weakens and the PSBs mimic the distribution of quiescent galaxies when line-of-sight velocity is omitted.

The radial distributions of SF1, SF2 and SF3 galaxies, shown in Figure 4.5, show a strong dependence of SSFR with cluster-centric radius. The population with the highest SSFR, SF1, presents a strong radial gradient, avoiding the inner regions of clusters. SF2s exhibit a rather flat radial profile which drops in the innermost bins.

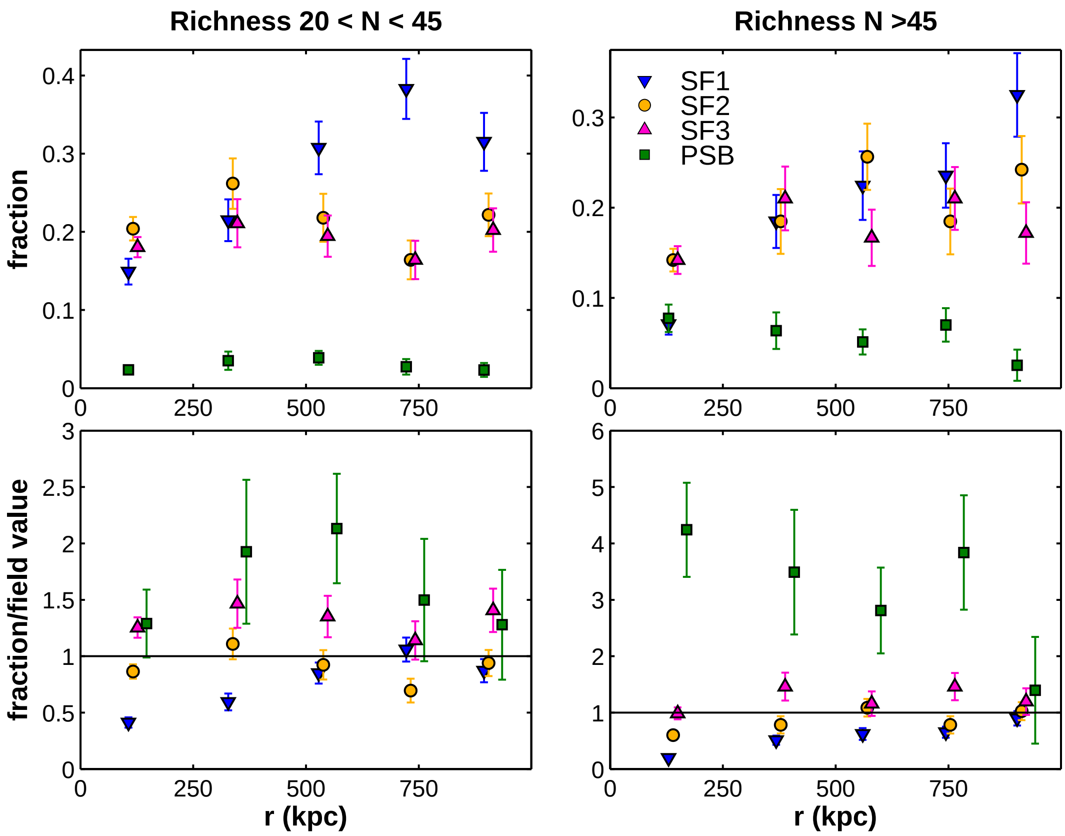

Figure 4.5. Radial plots of SF1, SF2 and SF3 galaxies in two cluster richness bins: clusters with more than 20 and fewer than 45 and clusters with more than 45 FoF selected members. In the first row the fraction of each population is represented while in the second one the fraction is normalised by the value in the field.

Table 4.2. The p-value of a KS-test when applied to radial distributions of different populations.

	$20 < N < 45$		$N > 45$	
	SF1	PSB	SF1	PSB
PAS	4.1×10^{-11}	0.23	8.0×10^{-11}	0.69
PSB	0.036	-	1.9×10^{-3}	-

Finally, SF3s are the only SF population whose fraction is higher in clusters than in the field, although the profile is flat, similar to the SF2s.

In conclusion, the radial profiles show a pattern suggesting the more passive populations (PAS, PSB and SF3) are more common in dense environments than in the field and prefer to inhabit small and intermediate cluster-centric radii. In contrast, high-SSFR (SF1 and SF2) galaxies avoid the central regions of clusters.

4.4 Discussion

In this work we present the following observational evidence, indicating that dense environments have a substantial impact on galaxy evolution in the redshift range $0.5 < z < 1.0$:

1. There is a high abundance of low-mass passive galaxies and PSBs in clusters (Figure 4.3), and a corresponding suppression of galaxies with high SSFR (particularly the SF1 class) compared to the field (Figure 4.3 & 4.4). This general trend can also be seen in the distribution of galaxies in supercolour space (SC1 vs SC2; see Figure 4.2), which shows that the cluster galaxy sample is skewed towards populations with lower SSFR.

2. There are strong radial gradients of passive and star forming fractions with cluster-centric distance. Passive galaxies dominate the central region of clusters where the galaxy density is higher, while star-forming galaxies prefer the outskirts (Figure 4.4 and 4.5). In particular, galaxies with high SSFR (SF1) show the steepest radial gradients.

In the analysis below we use the stellar mass functions to estimate the evolutionary connection between the various galaxy populations, and in particular the contribution due to quenching in dense environments. We then identify the most likely quenching pathways, which we describe with a simple evolutionary model.

4.4.1 Contributions and timescales

In this section we estimate the contribution of each population to the descendant class due to environmental processes. To achieve this we match the shapes of the stellar mass functions. This can be done because the SC classified galaxies correspond to 92.7% of the total sample (the rest correspond to rarer dusty, metal-poor or non-classified galaxies), so we assume that they evolve from one population to another without missing a significant fraction.

In the absence of enhanced quenching processes, we may consider a "slow fading" route, driven by the gradual decay of SSFR as galaxies build up stellar mass, which qualitatively agrees with the observed shift towards higher mass as galaxies age (see Figure 4.3). In contrast, environmental processes are thought to act rapidly (Muzzin et al. 2012; Wetzel et al. 2012, 2013; Mok et al. 2013), so that galaxies do not build up a significant amount of stellar mass in the process of being quenched. In this scenario, galaxies migrate to a different population while the shape of the original mass function remains unchanged. Therefore, there are two processes that contribute to the build up of the cluster galaxy mass function according to this simple evolutionary scheme; accretion of field galaxies of the same type, and injection of galaxies from other populations due to the action of the environment. Consequently, some cluster mass functions are composites of other populations, while this is not the case in the field, as transitions are assumed to occur more gradually with enough time for the stellar mass to change significantly. The last assumption is not true for field PSB galaxies, given that the transition into PSB is always quick. However, the significant difference in the shapes of the cluster and field PSB mass functions prevents the appearance of degeneracies between the two environments.

We estimate the composition of the cluster populations by fitting each stellar mass function with a simple model (see Equation 4.2), consisting of a linear combination of other populations [1],

$$\tilde{\phi}^{i}_{\mathrm{Cluster}} = \alpha\phi^{i}_{\mathrm{Field}} + \sum_{j} \beta_j \phi^{j}_{\mathrm{Field,Cluster}} \tag{4.2}$$

where ϕ are the various galaxy mass functions. The subindex i corresponds to the population we are trying to model and the subindex j to all the possible contributors. The terms α and β represent the relative contributions of the progenitor classes to the target population. The fitting is conducted using a Monte-Carlo method, minimising χ^2 while the data points are allowed to vary within errorbars.

The key assumptions made when using equation 4.2 is that quenched galaxies do not experience rejuvenation, i.e. there is no flow of galaxies from PAS and PSB populations towards the SF class, or from PAS galaxies into PSBs; and that environmental quenching is mass-independent, i.e. it does not change the shape of the stellar mass function. Additionally, PSBs and SF3s are the only populations that share a boundary with the passive sequence (in the SC-diagram, see Figure 4.1). Hence, in order to become passive a galaxy must evolve across this boundary. Therefore we only consider these two populations as contributors to the PAS populations. We assume the field SF mass function is the population being quenched, i.e. we assume these galaxies are quenched when they enter a cluster environment.

No assumption is made regarding the progenitors of cluster PSBs, hence all SF and field PSBs are considered potential candidates and introduced in Equation 4.2. We find that the shape of the cluster PSB mass function is recovered if $96.1 \pm 7.1\%$ of its galaxies are accreted from the SF1 class and $3.8 \pm 0.7\%$ are accreted from the field PSB population. This is because field SF1 galaxies are the only population with a similar shape to cluster PSBs, i.e. steep at the low-mass end. The contributions from SF2s and SF3s are less than 1% (see Table 4.3).

We also include all the SF populations in order to reproduce the cluster SF3 mass function. We find that the excess of low-mass SF3s in clusters is reproduced by adding a contribution solely from the SF2 population, with $12.6 \pm 3.7\%$ of cluster SF3s evolving from field SF2s, while accretion from field SF3s accounts for the remaining $87.1 \pm 3.8\%$. The field SF1 mass function does not provide a good fit to the cluster SF3 mass function, implying that essentially all environmentally quenched SF1s evolve through the PSB route.

4.4.2 The visibility time of the PSB phase

In order to estimate the visibility time of the PSB phase, we first apply the analysis to the subset of the younger PAS1 galaxies that were quenched over the redshift range $0.5 < z < 1.0$ (magenta and cyan lines in Figure 4.3). These galaxies are

[1] As an important caveat, we note that this model does not allow for effects of merging, which would imply evolution from one population to another with a significant change in stellar mass.

Table 4.3. The estimated contribution to the cluster galaxy populations (1st column) from the progenitor classes, based on fitting the galaxy mass functions (see Equation 4.2). Contributions are expressed as fractions of the progenitor and the target populations. Those entries marked with (f) correspond to the field, otherwise they represent cluster populations. The third column corresponds to the contribution relative to the progenitor populations, while the fourth column represents the fraction of the final population that comes from each progenitor class.

	Φ	Contribution	%
PSB*	SF1(f)	$\beta = 0.11 \pm 0.01$	$96.1 \pm 7.1\%$
	SF2(f)	$\beta \sim 10^{-4}$	$< 1\%$
	SF3(f)	$\beta \sim 10^{-5}$	$< 0.1\%$
	PSB*(f)	$\alpha = 0.23 \pm 0.04$	$3.8 \pm 0.7\%$
SF3	SF1(f)	$\beta = 0.013 \pm 0.005$	$< 1\%$
	SF2(f)	$\beta = 0.12 \pm 0.04$	$12.6 \pm 3.7\%$
	SF3(f)	$\alpha = 1.4 \pm 0.2$	$87.1 \pm 3.8\%$
PAS1*	SF3	$\beta = 0.22 \pm 0.02$	$26.6 \pm 3.1\%$
	PSB	$\beta = 3.41 \pm 0.45$	$73.3 \pm 3.0\%$
	PAS1*(f)	$\alpha = 0.02 \pm 0.01$	$< 1\%$

* Galaxies quenched at $0.5 < z < 1.0$ selected using mean stellar age information.

selected at a given redshift based on their mean stellar age, as obtained from the SC fitting procedure (see Section 2.2). As mentioned previously, we only consider cluster PSBs, cluster SF3s and field PAS1 as potential progenitors for the PAS galaxies. The similarity in shape of the cluster SF3 and field PAS1 mass functions does lead to some degeneracy affecting the contributions of these populations. This, however, does not affect the contribution from PSBs. We find that $73.3 \pm 3.0\%$ of the cluster PAS1 population that were quenched in the redshift range $0.5 < z < 1.0$ come from cluster PSBs (with the remaining $26.6 \pm 3.1\%$ from cluster SF3s and/or field PAS1s).

We use these contributions to estimate the visibility timescale ($\tau_{\rm vis}$) for the PSB phase. The redshift range $0.5 < z < 1.0$ corresponds to a time interval $\Delta t = 2.7 \pm 0.3$ Gyr. The visibility timescale is calculated dividing Δt by the expected number of times the observed PSB population has evolved into PAS1 galaxies during this time interval (i.e. β_{PSB}).

$$\tau_{{\rm vis},j} = \frac{\Delta t}{\beta_j} \tag{4.3}$$

Expressed in terms of the parent population, the PSB contribution to PAS1s corresponds to 3.41 ± 0.45 times the observed number of PSBs in clusters. This means that more than three times the current number of these galaxies must have faded into the red sequence over a time period of ~ 2.7 Gyrs. Therefore, the visibility time for PSBs is 0.8 ± 0.1 Gyrs.

In Section 4.4.4 we explore the visibility time for the PSB phase from a theoretical perspective, using stellar population synthesis models (Wild et al. 2016). These simulations estimate visibility times between 0.4–1 Gyrs, consistent with the estimates obtained using stellar mass functions.

4.4.3 Evolutionary pathways

We now develop a simple evolutionary model to link the various populations considered in this paper.

We assume that the evolution of low-mass galaxies ($M_* < 10^{10.5}$ M$_\odot$) in the field at $z < 1$ is mainly dominated by slow, undisturbed evolution. An isolated star-forming galaxy builds up stellar mass so that the SSFR drops and the galaxy slowly fades and moves through the star-forming classes (SF1, SF2, SF3) to eventually become passive (PAS). This slow fading is shown by the green arrows in Figure 4.6. In order to produce the bulk of the PSB population additional (rapid) quenching mechanisms are needed.

We suggest that the cluster environment causes the deviations from the slow fading path. Based on the contributions calculated in Section 4.4.1, we conclude that this can happen in two ways. Rapid quenching affects galaxies with very high SSFR (SF1), which are quenched rapidly during infall, giving rise to PSBs. This explains the sharp upturn of the PSB stellar mass function at the low-mass end, which matches the field SF1 mass function. Secondly, galaxies with intermediate SSFRs (SF2) may also be quenched, causing them to prematurely evolve into SF3 galaxies. These environmentally-driven paths are represented with red arrows in Figure 4.6. After quenching has taken place all galaxies converge to the quiescent population, regardless of the quenching pathway they followed. First they evolve to the youngest passive population (PAS1), then progressively evolve into PAS2 and PAS3 as they age and/or dry-merge. We note, as a caveat, that if in contrast with our assumptions, environmental quenching were dependent on stellar mass, the conclusions may be different.

We now analyse the insight provided by the radial distributions, which in principle can probe the location of the environmental quenching and constrain the likely timescales. The SF1 population is found to be strongly depleted in the cluster core; a KS test confirms its distribution is inconsistent with a flat distribution ($p_{\mathrm{KS}} \sim 10^{-5}$). This implies that the timescale for this quenching process is short, and less than the typical dynamical timescale of clusters ($< 10^9$ years), as otherwise the radial trend would dilute. In contrast, neither the SF2 or SF3 populations show strong radial trends ($p_{\mathrm{KS}} \sim 0.24$). Therefore the second evolutionary path must be a more gradual process and take longer than the dynamical timescale, i.e. $\gtrsim 10^9$ years.

Finally, we note that PSBs show no strong radial gradients, which implies that either environmental quenching occurs everywhere within the inner Mpc of the cluster, or the visibility time of the PSB phase is comparable to the dynamical timescale, $\sim$ 1 Gyr. As noted above, however, the quenching timescale to convert SF1 galaxies into PSBs must be considerably shorter.

In summary, our results suggest that more than one quenching mechanism acts in clusters, which seem to act on different timescales. One of them preferentially influences low-mass galaxies with high SSFR, while a second quenches galaxies with intermediate SSFRs.

4.4.4 PSBs in clusters and the field

The properties of PSB galaxies within clusters differ from PSBs in the field: their distribution in SC1–SC2 space is different as well as their mass functions. This suggests PSB galaxies may be produced through different processes depending on their environment.

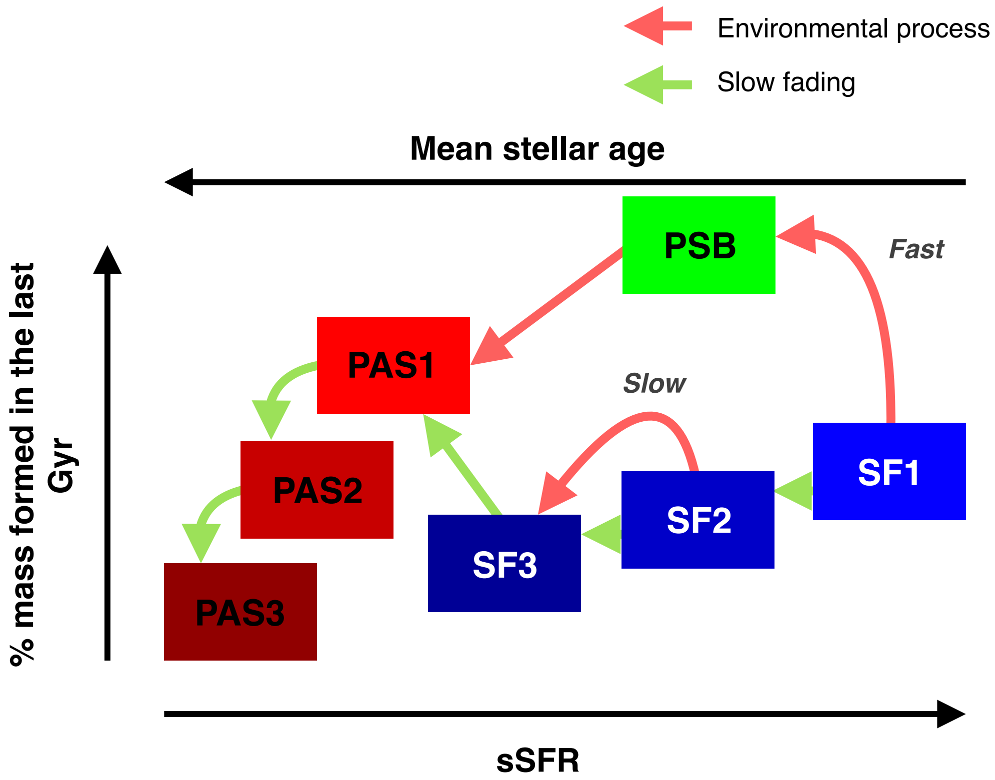

Figure 4.6. Scheme of our proposed evolutionary pathways. Green arrows illustrate the evolution of galaxies with constant SFR while the red arrows represent evolution driven by environment i.e. SFR being truncated by some environmental mechanism.

To analyse the possible origins of PSB galaxies we use the stellar population synthesis models presented in Wild et al. (2016). These models consist of three different star formation histories (SFH; see Figure 4.7): (1) with constant SFR, corresponds to unaltered evolution and a gradual drop in SSFR (solid line); (2) exponentially declining SFH with a decay time of 100 Myrs, representing galaxies that have undergone a strong burst of star formation that is rapidly truncated due to depletion of the gas reservoir (dotted line); and (3) exponential truncation of star formation with decay time of 400 Myrs after an extended period of continuous star formation of 1, 3 and 6 Gyrs since formation (dashed lines). In our case, this rapid truncation is assumed to be the effect of environmental quenching.

We see that the last two SFHs can lead to a PSB phase. In either case the maximum value of SC2 reached depends on the rapidity of the quenching event and the fraction of the stellar mass built up during the last Gyr. Hence PSBs formed immediately after a starburst event systematically reach higher values of SC2 than PSBs which were quenched after a more extended episode of star formation.

The distribution of PSBs in the SC diagram (Figure 4.2, described in Section 4.3.1) suggests that PSBs are triggered by different mechanisms in different environments. In particular, PSBs in clusters are unlikely to be produced after a significant starburst, in which the galaxy formed a considerable fraction of its stellar mass. Instead, they are more likely to have originated via rapid quenching after an

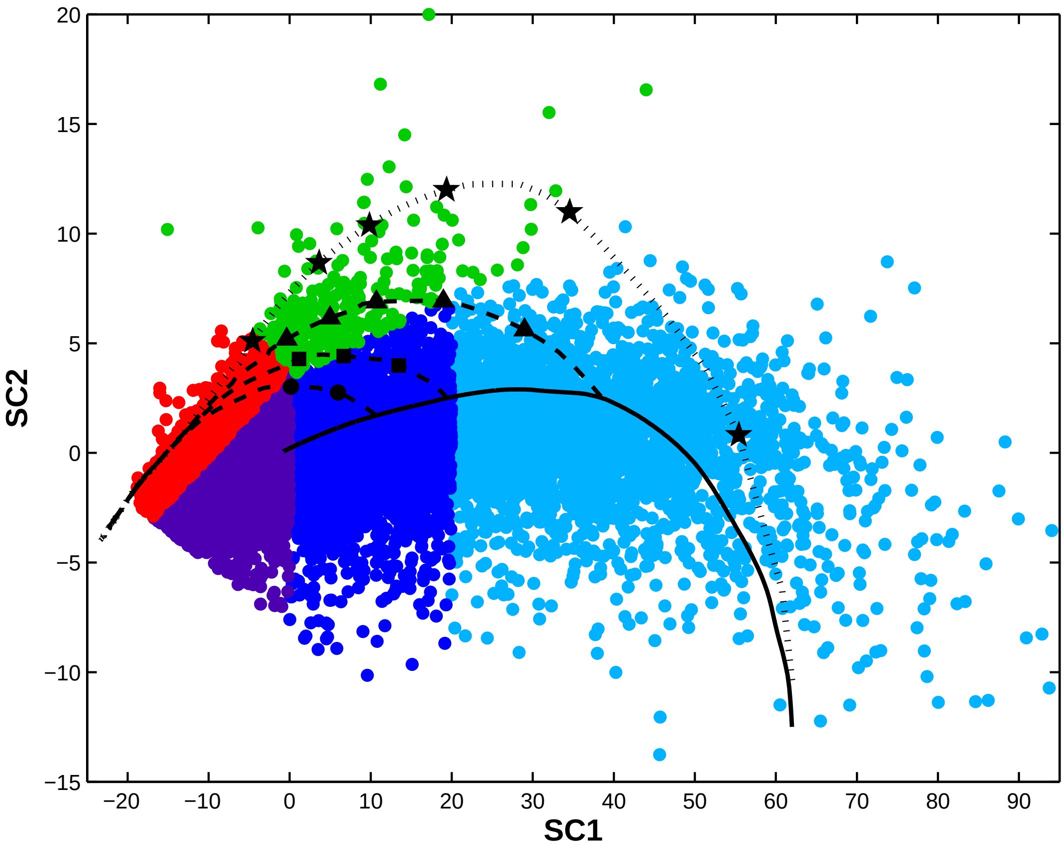

Figure 4.7. Evolutionary tracks in supercolour space, based on the Bruzual & Charlot (2003) models used in Wild et al. (2016). Filled circles represent the galaxies in our sample and their colours correspond to the population they belong to (Figure 4.1). The solid line traces the evolution with constant SFR. The dotted line represents an exponentially decaying SFR with a timescale of 0.1 Gyr. Dashed lines correspond to continuous SFR and exponential truncation (with a timescale of 400 Myr) of the star formation at different times: 1, 3 and 6 Gyr after formation (triangles, squares and circles, respectively). Black symbols mark intervals of 0.2 Gyr starting when the SFR first drops.

extended period of star formation or after a more marginal burst of star formation. We find that PSBs in clusters are concentrated at SC2 < 10 while in the field they reach much higher values (SC2 ~ 15; see Figure 4.2). In addition, this quenching must be fast ($\tau_Q \sim 400$ Myrs, from simulations) to cause a galaxy to leap off the slow evolution path into the PSB regime. With much longer SFR decay times the evolution would be indistinguishable from the undisturbed case. This matches the quenching timescale < 1 Gyr suggested by the radial gradient of SF1 galaxies in clusters.

Additionally, the models show that the visibility time of the PSB phase is longer if a higher value of SC2 is reached. Hence, those preceded by a starburst tend to have longer visibility times than those produced by rapid truncation after more extended star formation. Similarly, if the episode of star formation carries on for too long before being truncated, the galaxy will not reach the PSB regime at all. These two factors constrain the value of the PSB visibility timescale to the range $0.4 < \tau_{\text{vis}} < 1$ Gyr.

In conclusion, PSBs in galaxy clusters are more likely to be produced via rapid truncation after an extended period of star formation or after a minor starburst rather than being the result of a major starburst. Simulations confirm, regardless of the underlying process, that the quenching must act quickly to produce the PSB imprint, otherwise galaxies would stay too close to the undisturbed evolutionary pathway.

4.4.5 Mechanisms that can cause fast- and slow-quenching

Our results suggest that cluster galaxies at $0.5 < z < 1$ quench via at least two different pathways. A single mechanism may be responsible, which affects galaxies differently depending on their properties, or several quenching mechanisms may act simultaneously to produce the different evolutionary sequences.

One pathway, which we refer to as 'fast-quenching', acts on short timescales, quenching galaxies faster than a cluster dynamical time. It predominantly affects galaxies with high SSFRs and is more efficient at quenching low-mass galaxies. It becomes significant at cluster-centric radii $R \lesssim 750$ kpc. The other pathway, which we label 'slow-quenching', acts on longer timescales, comparable to, or greater than, the cluster dynamical timescale ($\tau_{\rm slow} \gtrsim 1$ Gyr). Slow quenching predominantly affects galaxies which exhibit moderate SSFRs, and shows no trend with stellar mass nor cluster-centric radius.

We consider it unlikely that the enhanced quenching in clusters is produced by internal galaxy processes, such as AGN or stellar feedback. Powerful AGN feedback is generally believed to occur in massive galaxies, so it is unlikely to cause the fast-quenching described above, which is more efficient at quenching low mass galaxies. Furthermore, star-formation-driven winds are also unlikely to be the primary cause, as Figure 4.7 shows no evidence for strong starbursts in cluster galaxies.

The main contenders for the mechanisms responsible for fast- and slow-quenching are interactions between the ICM and galaxies (such as ram pressure stripping and strangulation), and galaxy-galaxy interactions (such as harassment, mergers and tidal interactions).

Ram pressure stripping of the cold gas reservoir within a galaxy can quench star formation in a few hundred Myrs (Steinhauser et al. 2016). This mechanism acts preferentially in the central region of galaxy clusters or groups (Rasmussen et al. 2006; Kawata & Mulchaey 2008), where the ICM is densest and galaxies have high velocities. Furthermore, ram pressure stripping removes the cold gas reservoirs of low-mass galaxies more efficiently than high-mass galaxies as their lower gravitational potential is unable to keep the gas bound against the ram pressure. These characteristics can produce the observed properties of the fast-quenching mode described above, so ram pressure stripping is one of the contenders for causing the fast-quenching in clusters.

Galaxy mergers may also quench galaxies quickly. A merger can funnel gas into the centre of a galaxy, triggering a nuclear burst of star formation that may deplete the gas reservoir in a fraction of a Gyr. Although the merger cross section is small in the centre of clusters (Ostriker 1980; Makino & Hut 1997), these encounters frequently occur in cluster outskirts, as well as in groups. Our cluster sample is likely to have a broad range of velocity dispersions. By comparing our sample with the X-ray sample from Finoguenov et al. (2010) we estimate the majority of our structures have velocity dispersions of $\sigma_{\rm v} = 300 - 500$ km s^{-1}, so mergers may be frequent. However, the only type of merger able to produce the PSB stellar mass distribution is a major merger between two low-mass galaxies (i.e. two SF1s) and the resulting starburst would cause a high value of SC2, that is inconsistent with the typical values of SC2 found in cluster PSBs. Therefore, some external mechanism (e.g. gas stripping by ICM) may be required to decrease the gas fraction present in these galaxies in order to prevent a major starburst from occurring.

Galaxy encounters which cause tidal interactions, such as galaxy harassment, are much more frequent in groups and clusters than mergers, and these processes can strip gas from galaxies and reduce their SFR. Due to the high relative velocities of galaxies in clusters, these interactions are too quick and inefficient to be the direct cause of fast-quenching evolution (Boselli & Gavazzi 2006; Byrd & Valtonen 1990), but they may be responsible for slow-mode quenching.

At this point we are unable to pinpoint the mechanism that produces the fast-quenching within $0.5 < z < 1$ clusters. However, future studies of the morphology of cluster PSBs may shed some light on which mechanism is responsible (we explore this further in Chapter 5). Mergers would produce PSBs with disturbed/spheroidal morphologies, as the interaction disrupts the structures of the galaxies, whilst ram pressure stripping/strangulation would result in PSBs with more disc-like morphologies, as the galaxy would quench before the disc fades.

Many of the features exhibited by the slow-quenching mechanism can be explained by galaxy strangulation, where the hot gas envelope of the galaxy is removed by the ICM. For example, strangulation halts star formation gradually over ~ 4 Gyrs (Bekki et al. 2002). The hot gas reservoir of a galaxy is easily removed through interactions with the ICM, therefore strangulation affects both high and low-mass galaxies equally.

However, there are other potential processes responsible for slow-quenching. Galaxy harassment, as mentioned before, could significantly affect the star formation of a galaxy after a number of encounters, which requires a few Gyrs. Similarly, mergers involving galaxies with low gas content and intermediate SSFRs (SF2) may quench galaxies without following the PSB route.

4.5 Conclusions

In this chapter we have analysed the environmental dependence of different galaxy populations. The galaxy populations are selected using the PCA classification scheme described in Chapter 2 which separates the galaxy sample into star-forming, passive, and recently-quenched (PSB) galaxies, using photometric data. The environmental measurement, i.e. cluster or field membership, is described in Chapter 3. Then we compare the cluster and field stellar mass functions, and the radial distributions for cluster populations. Our key findings can be summarised as follows:

1. We find evidence for an overabundance of low-mass passive galaxies and PSBs in galaxy clusters compared to less dense environments. The PSB population shows a very steep stellar mass function in clusters, dominated by galaxies at low mass ($M_* < 10^{10}$ M$_\odot$).

2. Galaxy clusters show a relative underabundance of galaxies with high specific star-formation rates (SF1 galaxies). The SF1 mass function is steep, suggesting that rapid quenching of this population in dense environments provides a natural explanation for the corresponding excess of PSBs.

3. The radial distribution of galaxy types reveals a decline in the fraction of star-forming galaxies towards cluster cores, with a corresponding steep rise in the passive galaxy population. The SF1 population shows a very steep decline towards cluster cores, suggesting very rapid quenching of these galaxies on entering dense environments, on a timescale less than the cluster dynamical timescale (< 1 Gyr).

4. We measure a typical visibility time for the PSB phase of galaxies within clusters of 800 ± 100 Myrs, based on a comparison of stellar mass functions.

5. We find that PSBs in galaxy clusters are most likely to be produced by a rapid truncation following an extended period of star formation or after a minor starburst, rather than gas depletion after a major starburst. This may imply that environmental mechanisms typically quench galaxies without triggering any significant burst of star formation.

To explain the relative abundances and radial distributions, we suggest there are two main quenching pathways occurring in clusters: rapid quenching and slow quenching. The first path affects galaxies with high SSFR (SF1), predominantly at low mass, which quench rapidly to become PSBs and thereafter build up the low-mass end of the passive red sequence. The second pathway affects star-forming galaxies with moderate SSFR (SF2), accelerating their decay in SSFR over an extended period of time, comparable to the dynamical timescale of a galaxy cluster. This scenario is valid within our assumptions (in Section 4.4.1), if other factors are considered (e.g. the mass dependence of environmental quenching), the conclusions may change.

The processes behind fast environmental quenching need to act on timescales shorter than 1 Gyr, quench preferentially high SSFR/low-mass galaxies, and produce a strong radial dependence without inducing a strong starburst. Ram-pressure stripping provides a likely explanation, although we cannot rule out a contribution from other processes (such as merging). Similarly, the processes behind slow quenching act on timescales comparable to the cluster dynamical time or longer, affecting galaxies with intermediate SSFR regardless of their stellar mass. Such trends can be explained through strangulation, gradual galaxy harassment, or gas-poor mergers. We explore these mechanisms in Chapter 5, with the incorporation of galaxy structure information.

In summary, we conclude that environmental processes appear to have a significant impact on the properties of low-mass galaxies in the redshift range $0.5 < z < 1.0$.

Chapter 5

Mass–size relation and environment

In this chapter, we analyse the structure of galaxies with high SSFR in cluster and field environments in the redshift range $0.5 < z < 1.0$. In Chapter 4 we have shown that these galaxies are strongly depleted in dense environments due to rapid environmental quenching, giving rise to PSB galaxies. We use effective radii and Sérsic indices as tracers of galaxy structure, determined using imaging from the UDS. We find that the high-SSFR galaxies that survive into the cluster environment have, on average, larger effective radii than those in the field. We suggest that this trend is likely to be driven by the most compact star-forming galaxies being preferentially quenched in dense environments. We also show that the PSBs in clusters have stellar masses and effective radii that are similar to the missing compact star-forming population, suggesting that these PSB galaxies are the result of size-dependent quenching. We propose that both strong stellar feedback and the stripping of the extended halo act together to preferentially and rapidly quench the compact and low-mass star-forming systems in clusters to produce PSBs. We also present the stacked spectra of 124 high-SSFR galaxies showing that more compact galaxies are more likely to host outflows, which supports our hypothesis.

The work presented in this chapter is part of Socolovsky et al. 2019. Although the majority of the analysis is done by me, I did not take part in the production of the catalogues. These include photometric redshifts and stellar masses from Simpson et al. (2013), structural parameters R_e and n from Almaini et al. (2017) and the application of the PCA classification from Wild et al. (2016). Furthermore, the spectral analysis on galactic outflows, presented in Section 5.4.2, is provided by David Maltby, second author of Socolovsky et al. (2018b; submitted).

5.1 Introduction

In the local Universe the most massive galaxies are passive and elliptical, while low-mass galaxies tend to be star-forming and have disc-dominated morphologies. Several studies at high redshift show that massive passive galaxies are already in place at $z = 2$ (van der Wel et al. 2008; Baldry et al. 2012). In contrast, the observed number of quenched low-mass galaxies increases towards the present day (Drory et al. 2009; Baldry et al. 2012; Moutard et al. 2016, 2018). This downsizing in the passive population is generally associated with environmental quenching, and has been measured up to $z \sim 1$ (Muzzin et al. 2013; Tomczak et al. 2014; Socolovsky et al. 2018).

There are various proposed mechanisms to explain environmental quenching (see

Chapter 1), but consensus has not yet been reached on which the dominant processes are. Interactions with the intra-cluster medium, such as strangulation (Larson et al. 1980) or ram-pressure stripping (Gunn & Gott 1972), are some of the preferred mechanisms to explain how star-forming galaxies quench in cluster-like environments. Alternative mechanisms invoke galaxy-galaxy interactions, such as mergers, harassment or tidal stripping (Moore et al. 1996; Toomre & Toomre 1972; Faber 1973), which are also frequent in high and intermediate-density environments. As we saw in Chapter 4, it is difficult to distinguish between these mechanisms based on properties such as stellar mass or quenching timescales. Hence, in this chapter we incorporate galaxy structural information to help with this issue.

Galaxy structure provides a window into the evolutionary history of galaxies. Therefore, the study of galaxy structure can be very insightful in order to disentangle the driving quenching mechanisms. Gravitational interactions (including major mergers) may induce the migration of gas and stars towards the galaxy centre, producing more compact and concentrated light profiles. This contrasts with the faded stellar discs generated when the gas is ram-pressure stripped via interaction with the ICM. The environmental dependence of the galaxy stellar-mass–size relation for early-type galaxies has been extensively studied in the past. Cooper et al. (2012) and Lani et al. (2013) used local density as a tracer of environment at $z > 1$, and found that red sequence galaxies at fixed stellar mass present larger radii in high density environments. A different type of study, i.e. comparing cluster and field galaxies at $z = 1.6$, also showed that early-type galaxies are larger in the cluster environment (Papovich et al. 2012). In contrast, at lower redshift Kelkar et al. (2015) found no significant difference between cluster and field galaxies at $z \sim 0.6$. They concluded that the size evolution in the field might have caught up with the cluster, erasing the observed differences at higher redshifts.

Previous studies seem to agree that the growth in size of passive galaxies in dense environments is driven by dry merging and tidal interactions (e.g. Cooper et al. 2012; Lani et al. 2013; Kuchner et al. 2017). Another explanation is based on the possibility of a progenitor bias, i.e. that the change in the size-mass relation may be caused by larger galaxies that form later in the Universe (e.g. Poggianti et al. 2013; Carollo et al. 2013). However, not much work has been done on how the mass-size relation of star-forming galaxies is affected by environment at high redshift. In the low-redshift Universe, some authors have found that late-type galaxies are larger in the field than in galaxy clusters (Bamford et al. 2007; Maltby et al. 2010; Cebrián & Trujillo 2014). In this chapter we extend the study of the mass-size relation of star-forming galaxies in different environments to $z = 1$.

As seen in Chapter 4, the most depleted population in clusters at $0.5 < z < 1.0$ corresponds to low-mass galaxies with high SSFRs. The study of the stellar mass function revealed that these high-SSFR galaxies experience environmental quenching in galaxy clusters, to give rise to the cluster low-mass PSB population. The analysis presented in Chapter 4 also allowed us to constrain the timescales of environmental quenching. The strong deficit of galaxies with high SSFRs in the centre of clusters showed that these must be rapidly quenched, on timescales shorter than the cluster dynamical time (i.e. < 1 Gyr). However, despite the significant amount of information gained, we were not able to narrow down the range of candidate mechanisms for environmental quenching. In this chapter we use galaxy structure in an attempt to narrow down the range of possible quenching processes. As we concluded in the previous chapter, galaxy structure potentially provides the information needed to distinguish between ram-pressure or merger-driven quenching. Therefore, here we investigate the quenching mechanisms by studying the stellar mass–size relation of PSBs and their progenitors, SF1 galaxies.

The structure of this chapter is as follows. In Section 5.2 we present our data, the classification method and a description of how structural parameters are measured from ground-based imaging. We also present a brief description of the cluster-finding algorithm, developed in Chapter 2. We present our results in Section 5.3 and discuss their possible implications in Section 5.4. Finally, our conclusions are listed in Section 5.5.

5.2 Data sets and galaxy classification

The work presented in this chapter is a continuation to the work presented in Chapter 4, therefore, we use the same galaxy catalogues based on the UDS DR8. However, in this chapter we include the analysis of galaxy structure, which is derived using the deeper K-band imaging from the UDS DR11. All the details about the UKIDSS UDS and the description of the data releases that are relevant to this thesis can be found in Chapter 2.

5.2.1 Galaxy catalogue and classification

The galaxy catalogue we use is based on the UDS DR8. The detection limit in the K-band is $K = 24.6$, nevertheless, our catalogue is limited to $K < 24.3$ to ensure a 95% completeness (Hartley et al. 2013). The missing 5% corresponds mainly to low surface brightness galaxies. Additionally, stars are removed according to the method described in Simpson et al. (2013). This leads to a catalogue with 23,398 galaxies in the redshift range $0.5 < z < 1.0$

Photometric redshifts and stellar masses are computed by Simpson et al. (2013) via SED fitting, see also Chapter 2.1.5 for the key features of the method. When tested against the available $\sim$ 5000 spectroscopic redshifts, the median absolute deviation of the photometric redshift was estimated in $\sigma_{\rm NMAD} \sim 0.023$ up to $z = 1$, with 5% outliers, defined as sources with $\Delta z/(1 + z) > 5\sigma_{\rm NMAD}$, once AGN are removed.

Galaxies are photometrically classified according to the PCA method (Wild et al. 2014) described in Section 2.2. SSFRs are directly obtained from the sample of models used to construct the eigenspectra.

5.2.2 Cluster and field samples

The cluster and field samples are drawn from Chapter 3. The sample, consisting of 37 galaxy overdensities at $0.5 < z < 1.0$, is likely to be dominated by group-like structures ($\sigma_v = 300$–$500\,{\rm km\,s^{-1}}$) combined with more massive galaxy clusters. For the purposes of this study, henceforth we refer to these overdensities collectively as "clusters". A threshold of at least 20 detected members is applied to ensure a high signal-to-noise (S/N; see Chapter 3). Every galaxy located within 1 Mpc from the projected centre of mass and $2.5\sigma_z$ ($\sigma_z = 0.023(1 + z)$) from the median redshift of the measured structure was included in the cluster sample to ensure membership completeness. These criteria are applied to both galaxies with and without spectroscopic redshifts for consistency. The field sample is constructed using all the galaxies in the UDS field that were not associated with an overdensity, while forced to follow the redshift distribution of the cluster sample. In total the samples consist of 2,210 cluster galaxies and 13,837 field galaxies between $0.5 < z < 1.0$.

5.2.3 Galaxy size and Sérsic index from UDS DR11

Structural parameters (i.e. effective radius, R_e and Sérsic index, n) were determined using the K-band image from the UDS DR11 ($J = 25.6$, $H = 25.1$, $K = 25.3$; 5σ, AB). The software employed was GALAPAGOS (Barden et al. 2012), which makes use of GALFIT (Peng et al. 2002) in order to fit a Sérsic light profile (Sérsic 1968) to each galaxy in the UDS. We refer the reader to Almaini et al. (2017) for further details.

A correct treatment of the point-spread function (PSF) is critical for our analysis, given that many of the galaxies we are interested in present half-light radii smaller than 0.5 arcsec. Therefore, variations of the PSF across the UDS field were studied (Lani et al. 2013). The solution adopted was to divide the USD field into 16 sub-regions and using the stacked light profiles of stars in each region to obtain a measurement of the local PSF. The PSF was found to have FWHM varying between 0.75 - 0.81 arcsec across the field.

We rejected poor fits ($\chi^2_\nu > 100$) which corresponds to 1.7% of our sample. Similarly, we rejected $\sim$ 7% of galaxies where GALFIT did not converge to one solution. Most of these rejections correspond to objects with low surface brightness and near masked regions. The rejection rate was similar for star-forming, passive and PSB galaxies; and for cluster and field galaxies.

In Figure 5.1 we compare our K-band sizes with those obtained using the H-band from the overlapping *Hubble Space Telescope* (*HST*) CANDELS survey (van der Wel et al. 2012), which covers $\sim$ 7% of the UDS field. Space- and ground-based effective radii are found to be in good agreement. We find that ground-based sizes are systematically 10% smaller than the space-based ones, which is consistent with the expected variation across wavelengths (Kelvin et al. 2012). We impose a K-band cut of $K = 23.5$ (vertical line in Figure 5.1) to reject faint galaxies with unreliable R_e values. This flux limit corresponds to a 25% scatter in $\delta R_\mathrm{e}/R_\mathrm{e}$, estimated using the normalized median absolute deviation and rejects 11.5% of the total sample.

After applying these quality cuts and matching with the supercolour catalogue we are left with a sample of 5421 (1453) SF, 1146 (307) PAS and 95 (26) PSB field (cluster) galaxies.

5.3 Results

5.3.1 The stellar mass–size/Sérsic index relations

In order to put our study in context, we start by looking at the stellar mass–size relations of the main galaxy populations: star-forming, passive and PSB (blue, red and green, respectively, in Figure 5.2). The thicker points correspond to the median R_e in stellar mass bins and the red and blue lines correspond to fits to the data-points of the same colour, fitted using minimum χ^2. The passive stellar mass–size relation flattens towards low masses (van der Wel et al. 2014), which can be appreciated in our data as well (in Figure 5.2). This flattening is produced by the segregation of the passive galaxy population into spheroids and discs, which have different slopes (Schawinski et al. 2014). There is a higher fraction of disc-dominated quiescent galaxies at low stellar masses, consequently, the slope is shallower. Consequently we

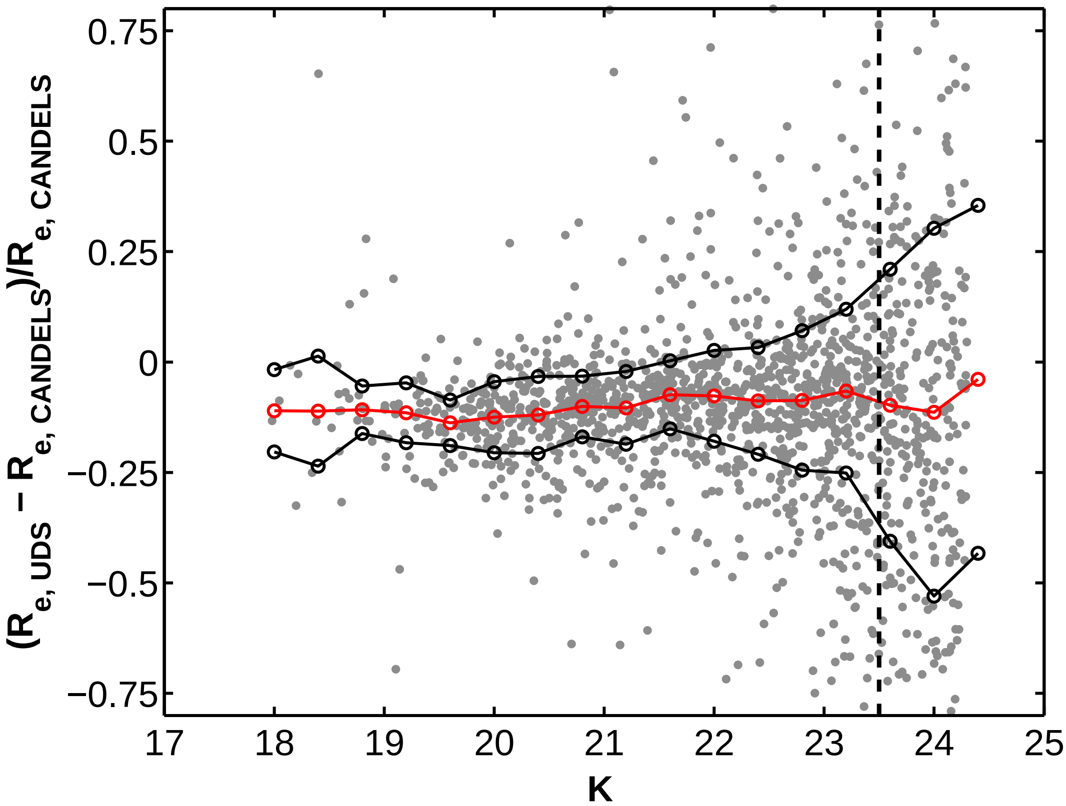

Figure 5.1. Relative difference between the effective-radii measured from ground-based UDS DR11 K-band imaging and *HST* CANDELS H-band imaging as a function of K-magnitude ($0.5 < z < 1.0$). The median values and median absolute deviations are displayed as red and black circles, respectively. Ground-based sizes are systematically 10% smaller than the ones measures from space. This is due to both the lower background noise in space-based images and the expected variation between filters (Kelvin et al. 2012). We choose a magnitude limit of $K = 23.5$ (vertical line), which corresponds to a 25% scatter, to only select reliable effective radii.

fit a model consisting of a linear fit with two slopes. The stellar mass at which the slope changes (M_0) is left as a free parameter. The mass–size relation is forced to be continuous, so the free parameters of the fit are the two slopes (m_1 and m_2), M_0 and the effective radius at $M_* = M_0$ ($R_{\mathrm{e},0}$),

$$\log R_{\mathrm{e}}(M_*) = \begin{cases} m_1 \log(M_*/M_0) + \log R_{\mathrm{e},0} & \text{if} \quad M_* < M_0 \\ m_2 \log(M_*/M_0) + \log R_{\mathrm{e},0} & \text{if} \quad M_* > M_0 \end{cases}, \tag{5.1}$$

where the stellar masses are expressed in logarithm. We find that the mass at which the passive slope changes is $M_0 = 10^{10.52} M_\odot$. In order to simplify the comparison with the star-forming population we evaluate the intercept value always at this stellar mass. The best-fitting parameters are presented in Table 5.1.

We observe that passive galaxies have smaller effective radii than star-forming galaxies of the same stellar mass (e.g. van der Wel et al. 2014). However, at high stellar masses $\gtrsim 10^{11} M_\odot$ the size of star-forming galaxies is comparable to that of the passive population. This is in good agreement with the observations from previous studies (Shen et al. 2003; van der Wel et al. 2014). Additionally, the shallow slope of the star-forming population is expected for disc galaxies that grow through star formation (in-situ or triggered by wet mergers). These gas-rich systems increase in stellar mass while the size growth is dampened by dissipative gas processes. In contrast, massive quiescent galaxies present a steep mass–size relation, driven by dissipationless dry mergers. However, passive galaxies with masses below $10^{10.52} M_{\odot}$ have a slope which is consistent with the star-forming population. This is likely to be produced by a dominant population of passive discs (S0s) at low stellar masses.

Table 5.1. Table of best fitting parameters to the mass–size relations of the SF and PAS populations

SF	**PAS**
$m = 0.11$	$m_1 = 0.10$
$R_{\mathrm{e},0} = 1.77$	$m_2 = 0.62$
	$R_{\mathrm{e},0} = 0.16$
	$M_0 = 10.52$

We also show the dependence of effective radius on stellar mass for PSB galaxies (green dots on Figure 5.2). This interesting population presents a remarkably flat mass–size relation, which is broadly consistent with the flat low-mass end of the quiescent mass–size relation. Furthermore, most PSBs lie half way between the star-forming and passive relations. These two facts suggest that PSBs are recently quenched galaxies that are making their way towards the passive sequence. Therefore, at this redshift, PSB galaxies may be a key step in the growth of the low-mass end of the red sequence at $0.5 < z < 1.0$, suggesting that they might be driving the flattening of the quiescent mass–size relation, hence, PSBs may be evolving into S0 galaxies. Note that, although in general the overall trends (i.e. without splitting by environment) are dominated by the more numerous field population, this is not true for low-mass PSBs and low-mass passive galaxies. These two populations are almost exclusive from high-density environments, which means that their overall trends may be dominated by the cluster trends.

In Figure 5.3, we show the dependence of Sérsic index (n) with stellar mass, or the mass–n relation. The thick points joined by lines represent the median values of n in bins of stellar mass. Blue corresponds to star-forming, red to passive and green to PSB galaxies. We find the expected trends as a function of galaxy type. Passive galaxies show preference for high stellar masses and high Sérsic indices ($n \sim 4$). Star-forming galaxies tend to occupy a larger region of the mass–n plane with typical Sérsic index values $n \sim 1$ and low stellar masses. Across all populations, median Sérsic index correlates with stellar mass. The passive and PSB population seem to share the same mass–n relation. However, PSBs tend to have lower stellar masses, and therefore, lower n values than quiescent galaxies.

These results suggest that PSBs represent a transient phase between star-forming and passive galaxies. Galaxies in this phase may be fading discs, which would explain why the Sérsic index increases gradually. However, since these galaxies are discs after all, the slope of their mass–size relation does not change significantly with respect to the star forming population they come from. However, Almaini et al. (2017) and Maltby et al. (2018) find that more massive PSB galaxies at high redshift ($\log M_*/\mathrm{M}_{\odot} > 10.5$ and $1.0 < z < 2.0$) tend to be ultra compact, which does not seem to be the case for lower-mass PSB galaxies at $0.5 < z < 1.0$. This may suggest a more gas-rich dissipative origin for high-mass PSB galaxies at those

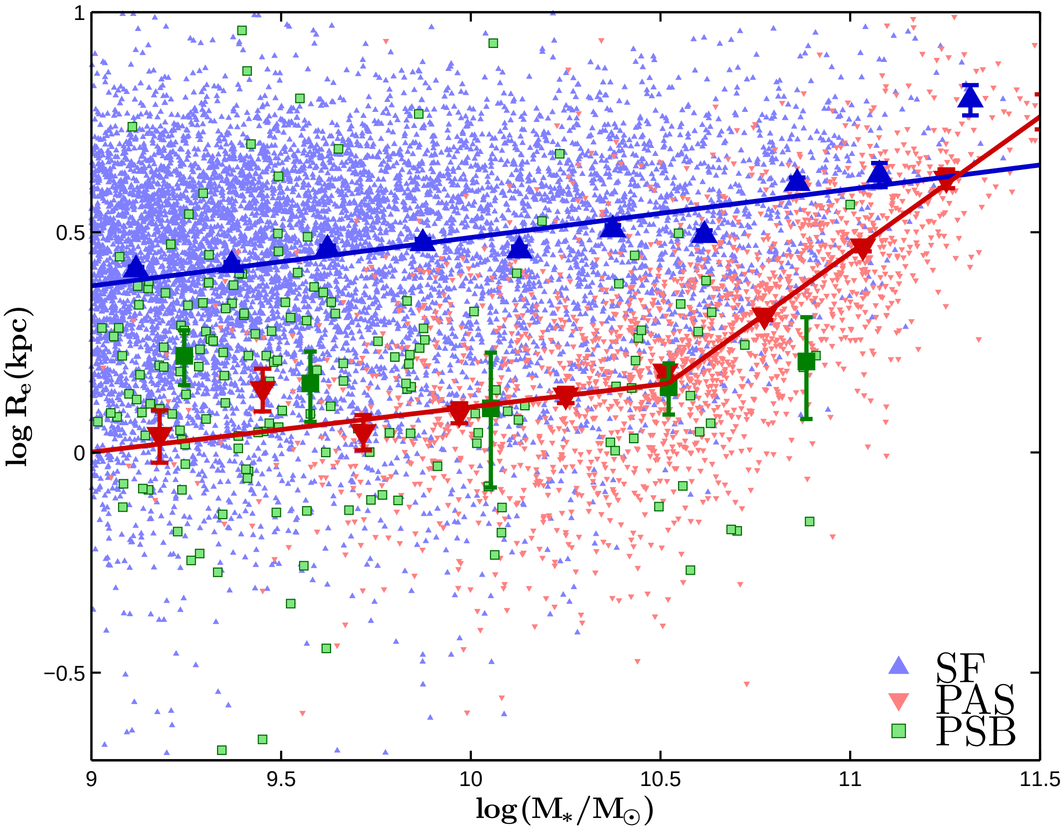

Figure 5.2. Effective radius (R_e) as a function of stellar mass for all the galaxies at $0.5 < z < 1.0$ in the UDS. The sample is divided into the main galaxy populations: star-forming (blue dots), passive (red dots) and PSBs (green circles). We also fit a linear model to the stellar mass–size relations of the passive and star-forming populations, red and blue solid lines, respectively. We observe that PSBs are located in between the quiescent and star-forming mass-size relation and their sizes do not seem to correlate with stellar mass.

earlier epochs, and lends weight to the idea that low-mass PSBs at $z < 1.0$ may have a different origin to the high-mass systems at higher redshifts.

5.3.2 The impact of environment on galaxy size as a function of specific star formation rate

In Section 5.3.1, we studied the global relationships between R_e and n with stellar mass, i.e. without splitting the sample by environment. This served as an introductory step to familiarise ourselves with the global trends, before we present the specific trends with environment, which we analyse in this and the next sections.

In Figure 5.4 we show the dependence of the median R_e on SSFR for the star-forming galaxies in our sample. We find that R_e increases approximately linearly with $\log SSFR$. When we split galaxies by environment, we observe that cluster galaxies with high SSFRs have larger median R_e than their field counterparts. The vertical dashed lines in Figure 5.4 correspond to the approximate boundaries between the three star-forming subpopulations, described in Section 2.2, which correlate well with SSFR. Thus, most of the galaxies with SSFR $> 10^{-9.0}$ yr^{-1} belong to the population of young star-forming galaxies, i.e. SF1.

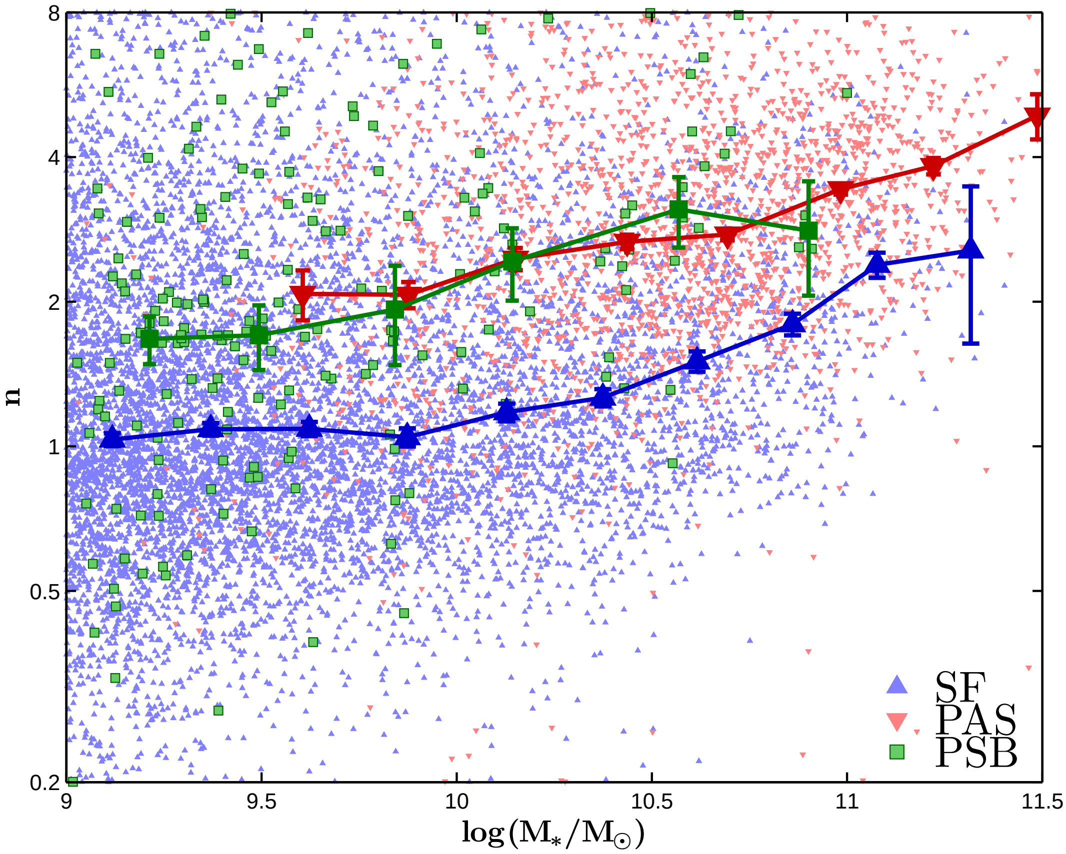

Figure 5.3. Sérsic index as a function of stellar mass for galaxies at $0.5 < z < 1.0$ in the UDS. Star-forming galaxies are represented in blue, passive galaxies in red and PSBs as green circles.

In Figure 5.5 we show the stellar-mass–size relation for SF1 galaxies as a function of environment. The values correspond to the median galaxy size in each mass bin, and the errorbars represent the error on the median, estimated using a bootstrapping technique. The lower mass limit corresponds to the mass completeness limit ($10^{9.0}\mathrm{M}_\odot$). The stellar-mass–size relation does not extend beyond $10^{10.5}\mathrm{M}_\odot$ because there are no SF1 galaxies with higher masses in our survey. As expected, in both environments galaxies increase in size for increasing stellar mass (Shen et al. 2003; van der Wel et al. 2014). However, it is evident that the remaining SF1 galaxies in clusters (that are not yet significantly affected by environmental quenching) are on average larger than in the field at all stellar masses. We fit a linear model with fixed slope ($\log R_\mathrm{e}/\log M_* = 0.154$) to the data from both environments and compare the intercepts to quantify the level of agreement. The intercept value in the cluster environment is $\log R_\mathrm{e}(M_* = 10^{9.5}M_\odot) = 0.542 \pm 0.013$, in contrast with a field value of $\log R_\mathrm{e}(M_* = 10^{9.5}M_\odot) = 0.498 \pm 0.002$. This represents a 3.4σ discrepancy between the cluster and field environments. We note, however, that our cluster sample contains contaminants from the field, which dilutes the differences between environments. Hence, the difference measured here is likely to be a lower limit and the real level of significance may be much higher.

In Chapter 4 we found that the relative fraction of SF1 galaxies is suppressed in cluster environments (see Figure 4.3). Here, in Figures 5.4 and 5.5 we have shown

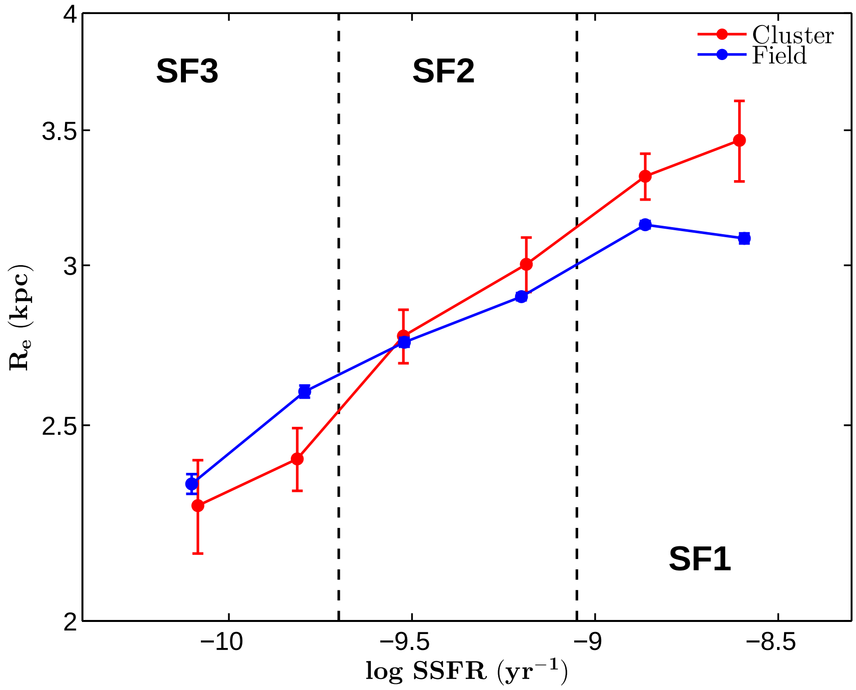

Figure 5.4. Median effective radius of star-forming galaxies as a function of SSFR at $0.5 < z < 1.0$. The red and blue lines correspond to cluster and field environments, respectively. The data points are centred on the median SSFR in each bin and the 1σ confidence error bars are estimated using bootstrapping. The vertical dashed lines delimit the regions typically occupied by the different star forming populations: SF1, SF2 and SF3, in order of decreasing mean SSFR. The SF1 galaxies (with the highest SSFR) are found to be, on average, larger in the cluster environment than in the field.

that the SF1 galaxies that survive in the cluster are on average larger than the general SF1 population in the field. This is unlikely to be driven by an increase in the SSFR of cluster galaxies as a result of an interaction with the cluster environment. This is because SF1 galaxies are the largest population in R_e, on average (see Figure 5.4), so increasing the SSFR of SF2 or SF3 galaxies to become SF1 galaxies would decrease the median R_e rather than increase it. From this, we conclude that dense environments affect the mass–size relation of young, highly star-forming galaxies.

5.3.3 A lack of compact star-forming galaxies in galaxy clusters

In this section we examine the distributions of galaxy size and Sérsic index as a function of environment for our SF1 galaxies. We look first at the distribution of galaxies across the mass–size and mass–Sérsic index planes (left and central panels of Figures 5.6 and 5.7). The first two panels on the left in Figure 5.6 show the distribution of SF1 galaxies on the stellar-mass–size plane, the left panel corresponds to clusters and the central one to the field. The straight line in both panels corresponds to a linear fit to the mass–size relation in the field, which we use as a reference,

$$\log R_e = 0.202 \log M_* - 1.426. \quad (5.2)$$

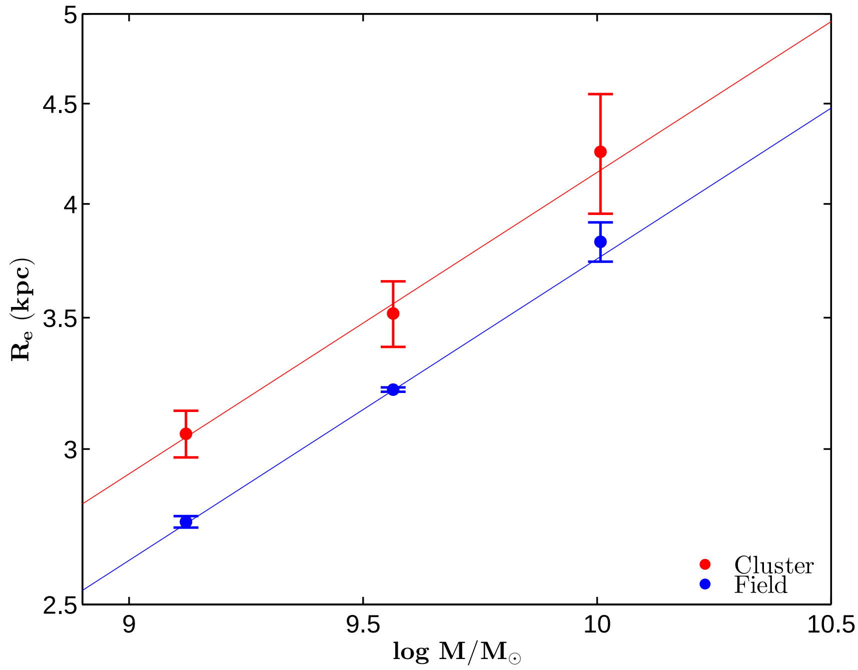

Figure 5.5. Stellar-mass–size relations of cluster (red) and field (blue) high-SSFR galaxies (SF1 galaxies) at $0.5 < z < 1.0$. The errorbars correspond to the 1σ confidence intervals estimated using bootstrapping. We fit a linear model to each mass–size relation (solid lines) in order to compare them. We find that cluster SF1 galaxies are systematically 9% larger than their field counterparts at all masses.

We observe that the cluster and field distributions are notably different. The cluster distribution peaks above the field mass–size relation, indicating larger sizes at the same stellar mass. In Figure 5.7 we look at the distribution of SF1 galaxies across the mass–Sérsic index plane. The dashed line corresponds to a linear fit to the field mass–n relation, which is consistent with $n = 1$. We find that the cluster distribution (left) peaks at lower values of n than in the field (centre).

In the right-hand panels of Figures 5.6 and 5.7 we compare the cluster and field distributions of normalized R_e and n. For Figure 5.6 removing the mass dependence of the field sample (eq. 5.2). To remove the contaminants from the cluster sample we statistically subtract the contribution due to field galaxies that are erroneously included in the cluster sample.

The distributions of $R_{e,norm}$ and n are normalized to unity to allow direct comparison of their shape. We see that the distributions of $R_{e,norm}$ in high and low-density environments are significantly different ($p_{KS} = 1.2 \times 10^{-5}$). As suggested from the previous results, the cluster SF1 population is skewed towards higher $R_{e,norm}$ values, as compared to the field. This galaxy population is known to be strongly depleted in dense environments (Socolovsky et al. 2018). This trend is likely to be produced by the preferential quenching of the compact SF1 galaxies. We tested this trend by analysing the stacked light profiles of cluster and field SF1 galaxies, finding the same trend, i.e. cluster SF1 galaxies present more extended profiles on average. This implies that the results are not due to issues with Sérsic fitting. We also find a moderate but significant difference in the distribution of n between cluster and field SF1 galaxies ($p_{KS} = 7.2 \times 10^{-3}$). Cluster SF1 galaxies seem to have a narrower

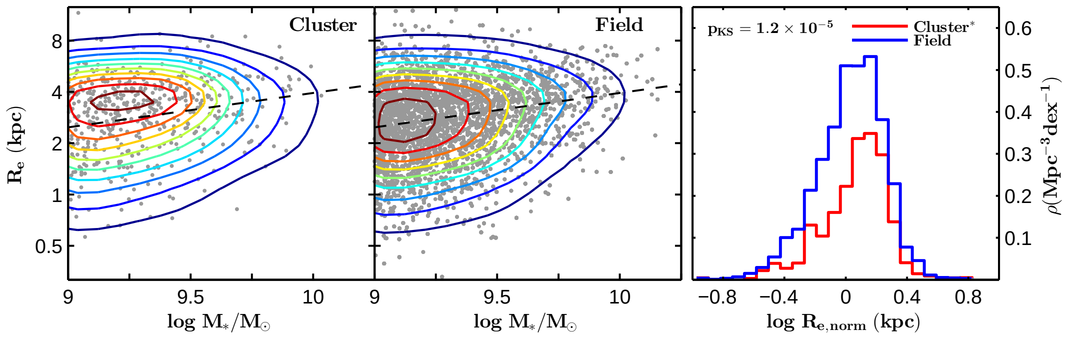

Figure 5.6. The stellar-mass–size relation for SF1 galaxies in the UDS at $0.5 < z < 1.0$. The grey dots represent the position of individual galaxies across the mass–size plane. The contours show the number of galaxies per unit area on the diagram and normalized by the comoving volume of the field. The left and central panels correspond to cluster and field galaxies, respectively. The black dashed line in the first two panels corresponds to the best-fitting linear model to the field population. The right-hand panel represents the distribution of the variable $R_{\mathrm{e,norm}}$ or the ratio between the effective radius of a galaxy and the value predicted by the best-fit model to the field data. The red line corresponds to the cluster and the blue to the field populations (note the asterisk next to the cluster label indicating it is the background-subtracted cluster sample). The field and cluster distributions are significantly different, according to a KS test (p_{KS} is quoted on the top left corner), with the cluster SF1 galaxies being, on average, larger than in the field.

distribution around $n = 1$, while they have slightly higher n in the field. Thus, SF1 galaxies with slightly higher n might also be preferentially quenched in clusters.

In summary, we find that the remaining SF1 galaxies in dense environments are on average larger, potentially because the compact SF1 galaxies are preferentially missing in dense environments. These compact SF1 galaxies also have higher Sérsic indices.

5.3.4 The cluster post-starburst mass–size relation

In Chapter 4, we showed that PSB galaxies are the descendants of SF1 galaxies in clusters at $0.5 < z < 1.0$. We found that the stellar mass function of cluster PSBs present a very distinctive steep low-mass slope. Such a steep slope is only matched by the SF1 mass function. This implies that the only possible progenitors to PSBs are SF1 galaxies. To build on this result, we analyse the mass–size relation of PSBs to gain insight into the potential transformations that SF1 galaxies undergo as they quench in clusters.

Figures 5.8 and 5.9 show the difference between the cluster and the field SF1 galaxy distributions across the mass–size and mass–Sérsic index planes as colour contours. Both cluster and field distributions are normalized to unity to highlight their differences. Superimposed on the contours, the best-fitting line to the field SF1 mass–size and mass–n relations are presented (eq. 5.2), to aid the comparison with Figures 5.6 and 5.7.

Although PSBs in clusters are generally more compact than the average size of the SF1 galaxies, we find that the distribution of the cluster PSBs in the mass–size (Figure 5.8) and mass–n (Figure 5.9) planes coincides with the region where cluster SF1 galaxies are missing with respect to the field, i.e. 48/54 of the PSBs are found below the SF1 mass–size relation of the field. Additionally, cluster PSBs

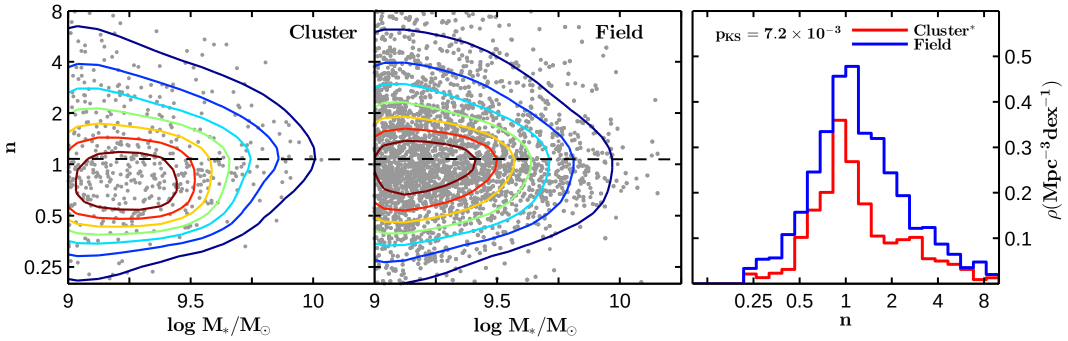

Figure 5.7. The stellar-mass–Sérsic index relation for SF1 galaxies in the UDS at $0.5 < z < 1.0$. The grey dots represent the position of individual galaxies across the mass–Sérsic index plane. The contours show the number of galaxies per unit area on the diagram and normalized by the comoving volume of the field. The black dashed line in the first two panels corresponds to the best-fitting linear model to the field population. The left and central panels correspond to cluster and field galaxies, respectively. The right-hand panel shows the distributions of n in clusters (red) and in the field (blue; the asterisk next to the cluster label indicates that it is the background-subtracted sample). We observe that cluster galaxies tend to have lower n values with respect to the field.

typically have $n \sim 1.5$, which indicates that they partially maintain a disc-like nature. A KS test fails to reject the null hypothesis that compact field SF1 galaxies, i.e. those located below the field mass–size relation, ($n \sim 1.3$) and cluster PSBs follow the same n distribution ($p_{\mathrm{KS}} = 0.45$). This suggests that the compact SF1 galaxies undergo a gentle evolution to become PSBs in dense environments, without significant structural transformation.

5.4 Discussion

5.4.1 The effect of the group environment on the star-forming population

In Section 5.3.3, we showed that the remaining high-SSFR galaxies (SF1 galaxies) in clusters are on average larger than the SF1 galaxies located in the field. We also show that this trend is most likely driven by a lack of SF1 galaxies with small R_e at a given stellar mass, see Figures 5.6 and 5.7. There are two plausible explanations for this observation: 1) environment affects SF1 galaxies in such way that their R_e increases; or 2) compact galaxies are being preferentially quenched in the cluster environment. We expand on these scenarios below.

Previous observational work has found that elliptical systems tend to be larger in high density environments than in the field at $z \gtrsim 1$ (Cooper et al. 2012; Lani et al. 2013). From a theoretical point of view, this has been explained through either the repeated interaction between galaxies (harassment) or dry mergers that take place in crowded environments (van Dokkum 2005; Shankar et al. 2013; Oogi & Habe 2013). However, major mergers and harassment are thought to disrupt galactic discs and lead to an enhancement of the bulge component (Toomre & Toomre 1972; Farouki & Shapiro 1981; Moore et al. 1996; González-García & Balcells 2005; Aceves et al. 2006). Consequently, major merging and harassment do not provide a viable explanation for the large sizes of the cluster SF1 population, which consists mainly of

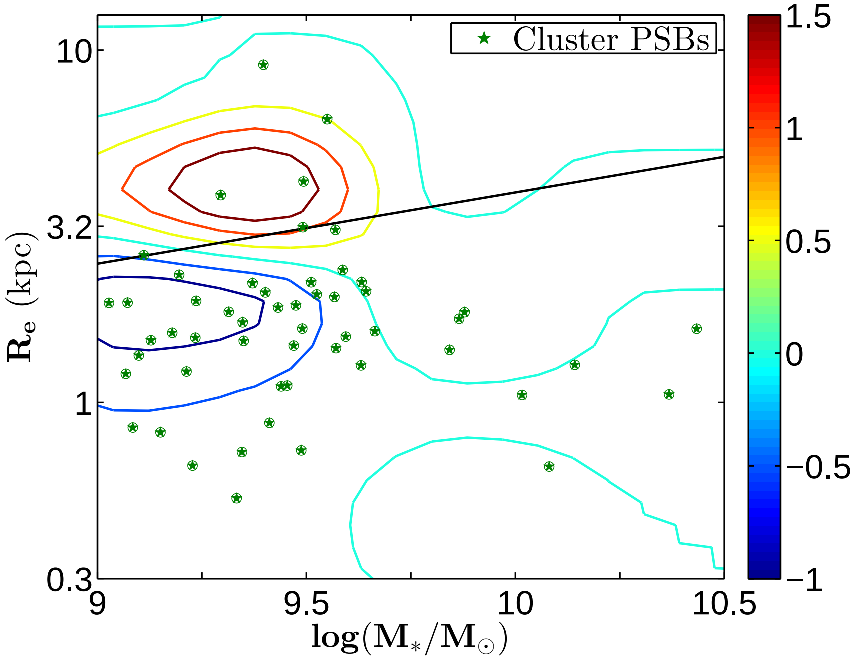

Figure 5.8. Comparison of mass–size relations of SF1 galaxies and PSBs in the redshift range $0.5 < z < 1.0$. The contours represent the differential distribution of SF1 galaxies (i.e. the cluster minus the field distributions). The green stars show the location of cluster PSB galaxies. The solid line represents the mass–size relation of field SF1 galaxies for comparison. Cluster PSBs are located in the regions of the mass–size relation where SF1 galaxies are depleted in clusters with respect to the field, i.e. below the solid black line.

star-forming discs with typical Sérsic indices $n \sim 1$ (see Figure 5.7). Conversely, minor galaxy mergers are thought to enable the growth of the disc component (Younger et al. 2007; Naab et al. 2009; Sil'Chenko et al. 2011). However, we expect SF1 galaxies to evolve into PSBs through environmental quenching (Socolovsky et al. 2018), and PSBs are compact. Therefore, we cannot discard the possibility of two independent processes acting simultaneously on the SF1 population: minor mergers may be responsible for the increase in size of cluster SF1 galaxies and major gas-rich mergers (e.g. between two SF1 galaxies) might be quenching them into compact PSBs (Wild et al. 2016). Note that these two processes are disconnected from each other, i.e. galaxies may undergo one of them rather than one after the other.

The main weakness of the major merger hypothesis is the observed range of Sérsic indices for both SF1 and PSB galaxies in clusters. The median Sérsic index of cluster PSBs is $n \sim 1.5$, which is low for a post-major merger scenario (González-García & Balcells 2005). Although some simulations have shown that a disc can form after a major wet merger (Athanassoula et al. 2016), the time required for this to occur is significantly longer than the expected duration of the PSB phase ($\lesssim 1$ Gyr; Wild et al. 2016; Socolovsky et al. 2018). At $z < 0.1$, PSBs have high Sérsic index values and are thought to be major merger remnants that tend to reside in low-density environments (Zabludoff et al. 1996; Blake et al. 2004; Pawlik et al. 2018). In contrast we suggest our PSBs originate via some kind of gentle gas removal in galaxy clusters. Hence, these results are not contradictory. On the other hand, minor mergers with dwarf galaxies that we cannot observe provide a feasible explanation. However, this may be difficult to reconcile with the observed Sérsic

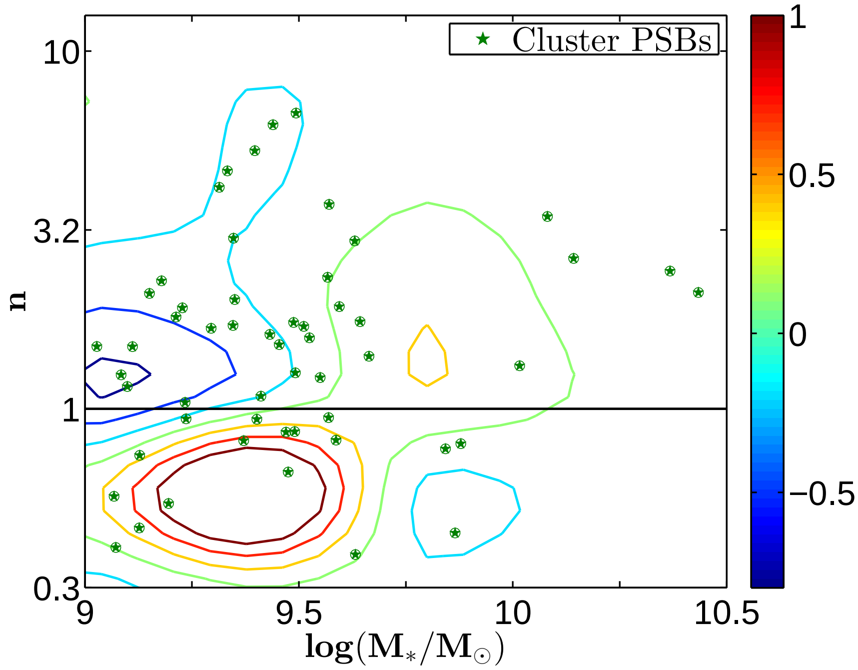

Figure 5.9. Comparison of mass–Sérsic index relations of SF1 galaxies and PSBs in the redshift range $0.5 < z < 1.0$. The contours represent the differential distribution of SF1 galaxies (i.e. the cluster minus the field distributions). The green stars show the location of cluster PSB galaxies. The solid line represents the mass–Sérsic index relation of field SF1 galaxies for comparison. As in the case of the stellar mass–size relation, cluster PSBs are located in the regions where SF1 galaxies are depleted in clusters with respect to the field, in this case above the black line.

index of SF1 galaxies ($n \sim 1$).

Instead, we favour the hypothesis in which compact SF1 galaxies are preferentially quenched in dense environments. This naturally leads to the remaining SF1 population appearing on average larger in the cluster while the quenched galaxies (PSBs) are smaller than the typical SF1 in the field. This preferential quenching of compact objects is hard to reconcile with the environmental mechanisms mentioned in Chapter 1. For example, ram-pressure stripping and tidal interactions are expected to act more efficiently in more extended galaxies, with shallower gravitational potentials so that the gas is more easily disturbed (Bothun et al. 1993; Abadi et al. 1999; Moore et al. 1999). Scenarios involving quenching induced by galaxy mergers were also considered, but these are not expected to depend on galaxy size.

Given that purely environmental processes fail to describe our results, we suggest that the rapid environmental quenching of compact SF1 galaxies is a combination of both, internal and external mechanisms. Our hypothesis, summarized in Figure 5.10, is based on a "bathtub"-type model (Bouché et al. 2010), in which the star formation in a galaxy is regulated by the balance between gas inflows and outflows. Broadly speaking, gas in galaxies is present in two phases: a cold reservoir, and hot reservoir. The cold gas reservoir (or interstellar medium, ISM) corresponds to the dense gas typically found within the disc, and represents the instantaneous fuel for star formation. The hot gas reservoir refers to the extended halo of diffuse gas in which the galaxy is embedded (circumgalactic medium, CGM). The gas in the CGM is too hot to collapse into stars but has the potential to cool down with time and

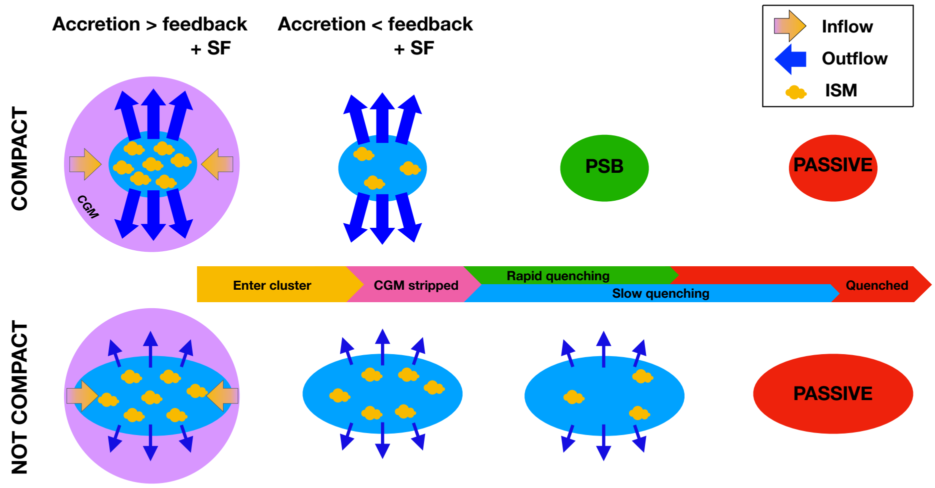

Figure 5.10. Diagram illustrating the different environmental quenching pathways followed by high-SSFR galaxies depending on whether they are compact (top row) or not (bottom row). The ellipses represent the location of the stars, the yellow clouds represent the ISM and the purple circles are the CGMs. The blue arrows pointing outwards from the galactic disc represent the outflows, stronger on the top sequence. The yellow arrows pointing inward represent the inflow of gas, which stops immediately as the galaxy comes in contact with the ICM. In the compact SF1 case the strong outflows expel most of the ISM in a short timescale, which rapidly quenches the galaxy leading to the PSB phase. Non-compact SF1 galaxies host weaker outflows, therefore they are able to sustain their star formation over a longer period of time. However, the ending state for both pathways is a red, quiescent galaxy.

feed the ISM through cold streams, for this reason the CGM is also referred to as the long-term gas reservoir.

The inflows (represented with yellow arrows in Figure 5.10) consist of gas from the cosmic web being accreted by the galaxy. On its infall, this gas forms the CGM. As it cools down, it migrates inward. In contrast, outflows (blue arrows in Figure 5.10) send gas from the ISM back into the CGM. These outflows could be driven by stellar, supernovae or AGN feedback. Nevertheless, the expelled gas can be recycled after some cooling time, when it is reaccreted into the ISM. However, if the galaxy becomes a satellite in a group/cluster, the CGM is largely stripped away via interaction with the intra-cluster medium (Larson et al. 1980). The ICM also halts the accretion of gas from the cosmic web, so that cluster galaxies are left only with their short-term reservoir to fuel star formation. Although all galaxies have their hot gas reservoir stripped away almost instantaneously, this has no immediate effect on the ongoing star formation. Therefore, those galaxies with the highest SSFRs and/or strongest galactic outflows will deplete their cold gas reservoir faster and, consequently, quench. This scenario is similar to the 'overconsumption' process described in McGee et al. (2014), which is proposed to rapidly quench satellite galaxies at $z \sim 1.5$.

Some studies have found that compact galaxies are more efficient at transforming gas into stars (Young 1999). Similarly, at fixed SFR, compact in size means higher star-formation surface density, which is associated with stronger outflows (Heckman et al. 1990). In this study, we do not find higher SFRs in compact SF1 galaxies but they may host stronger stellar-wind-driven outflows. From a theoretical viewpoint, the strength of these super-winds scales with star-formation rate density ($\Sigma_{\rm SFR}$). Compact SF1 galaxies have higher $\Sigma_{\rm SFR}$ due to their compact nature. Whilst having the same SFR as the rest of SF1 galaxies, therefore, they are expected to produce stronger outflows (top row of Figure 5.10). On the other hand the rest of the SF1 population (i.e. not compact; second row of Figure 5.10), may have more modest outflows which would allow them to stay star-forming for a longer timescale before they also run out of fuel ("delayed-then-rapid" environmental quenching scenario, Wetzel et al. 2013). This theory provides a successful explanation for why compact SF1 galaxies quench faster than their more extended counterparts. They are more efficient at evacuating their cold gas reservoir after the cluster environment prevents the replenishment of gas by blocking the inflows.

In summary, stellar and supernova winds in combination with the interaction with the ICM may cause the rapid quenching predicted in Chapter 4 for SF1 galaxies in overdense environments. This hypothesis anticipates that environmental quenching does not trigger significant structural evolution. PSBs appear, on average, more compact than the general SF1 population because they are primarily the descendants of the compact SF1 galaxies.

This theory predicts stronger outflows in compact SF1 galaxies than in large ones. This can be tested by looking at outflow signatures in spectra of galaxies above and below the mass–size relation of the field SF1 sample.

5.4.2 Spectral analysis: evidence for strong outflows in compact star-forming galaxies

In this study, we find evidence that compact galaxies with high SSFR (SF1s), are more susceptible to being quenched in the cluster environment. We hypothesise that this result could be explained by a combination of both environmental and secular processes in the following scenario: i) upon cluster infall, interaction with the ICM removes the galaxy's extended hot gas reservoir, shutting down cosmic accretion; and ii) the strong stellar feedback in these compact galaxies causes significant outflows which rapidly expel any remaining cold gas from the central regions. This scenario would naturally lead to the rapid quenching of compact SF1 galaxies in clusters and their subsequent evolution into cluster PSBs.

To test this hypothesis we use the available deep optical spectra in the UDS field to determine whether the strong gaseous outflows required are present in our compact SF1 population. These spectra are provided by UDSz, the spectroscopic component of the UDS (ESO Large Programme 180.A-0776, PI: Almaini), which used both the VIMOS and FORS2 instruments on the ESO VLT to obtain optical spectra for > 3500 galaxies in the UDS field (see Bradshaw et al. 2013; McLure et al. 2013). For our field/cluster SF1 galaxies, we find that 124 low-resolution VIMOS spectra ($R \sim 200$) are available and that these spectra are evenly distributed throughout the SF1 mass–size relation (see Figure 5.11). In the following, we define all galaxies with optical spectra that lie above the fit to the mass–size relation to be 'extended', and those that lie below to be 'compact'.

In order to determine the presence of gaseous outflows, we use the Mg II absorption doublet ($\lambda\lambda\, 2796,\, 2803$ Å), which is a sensitive tracer of low-ionisation interstellar gas. The detection of a blue-shifted component to this absorption line is generally indicative of galactic-scale outflows along the line-of-sight to the observer. Unfortunately, the signal-to-noise (S/N) in the VIMOS spectra is not sufficient to

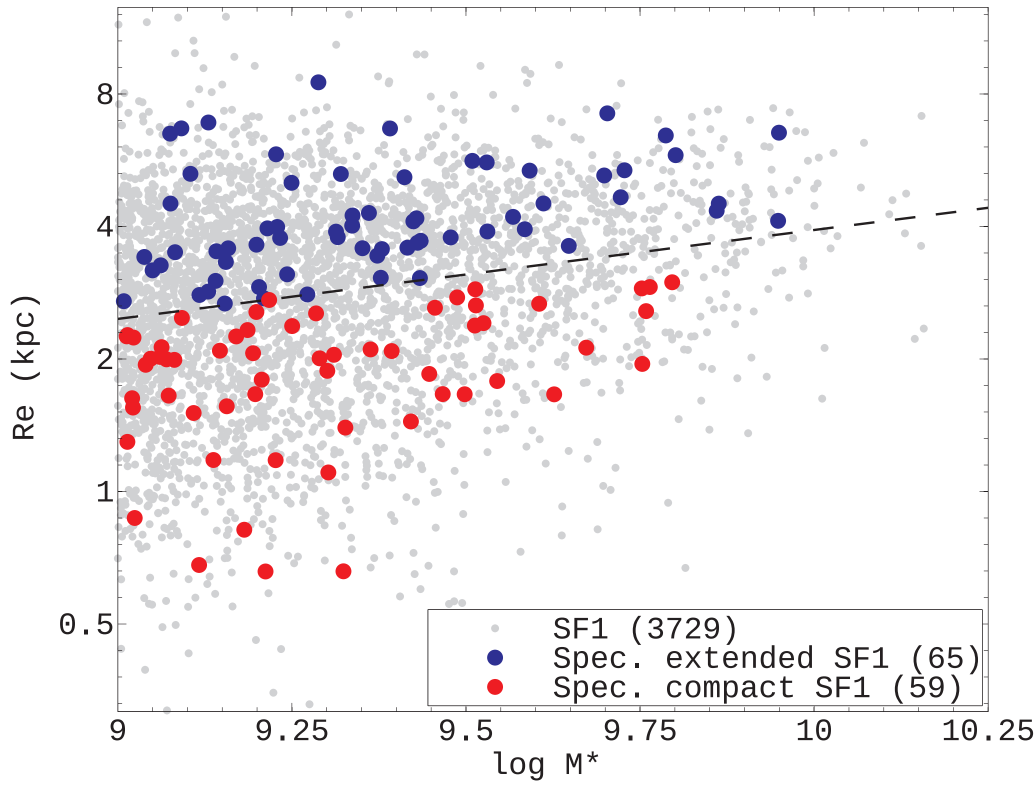

Figure 5.11. The stellar-mass–size relation for SF1 galaxies in the UDS field ($0.5 < z < 1$), showing the sample with available optical spectra from UDSz. The linear fit to the field mass–size relation is also shown for reference [black-dashed line; see equation (5.2)]. We define all galaxies with optical spectra that lie above the fit to the mass–size relation as 'extended' (blue points), and those that lie below as 'compact' (red points). Relevant sample sizes are shown in the legend.

reliably determine the structure of the Mg II profile on an individual galaxy basis. We therefore increase the effective S/N via a stacking analysis, combining the individual rest-frame spectra following an optimised flux normalisation. For this we generate two median-stacked spectra: i) a red-optimised stack ($\lambda > 3500$ Å), using a flux normalisation over the Balmer break region; and ii) a blue-optimised stack ($\lambda < 3700$ Å), using a flux normalisation over the Mg II continuum. For the blue-optimised stack, we also apply an upper 2σ clip to individual spectra that deviate from the median flux within the Mg II region ($2775 < \lambda < 2825$ Å). This clipping removes a handful of spectra (< 10 per cent) that exhibit Mg II emission, which would otherwise bias our stacking analysis. The final median-stacked spectrum is a splice of the red- and blue-optimised stacks. The median-stacked spectra for both our 'extended' and 'compact' SF1 galaxies are shown in Figure 5.12.

For both our median stacks, we also perform a full spectral fit (stellar component plus gas emission lines) using the penalised pixel-fitting method (PPXF; Cappellari & Emsellem 2004; Cappellari 2017) and the MILES spectral templates (Vazdekis et al. 2010). These fits are presented in Figure 5.12 and clearly demonstrate that in our median stacks, several spectral features (e.g. Balmer lines, [O II], [O III]) are all well-centred with respect to their rest-frame wavelengths. Consequently, we conclude that any observed offset $\Delta\lambda$ in the Mg II doublet from the rest-frame wavelength is

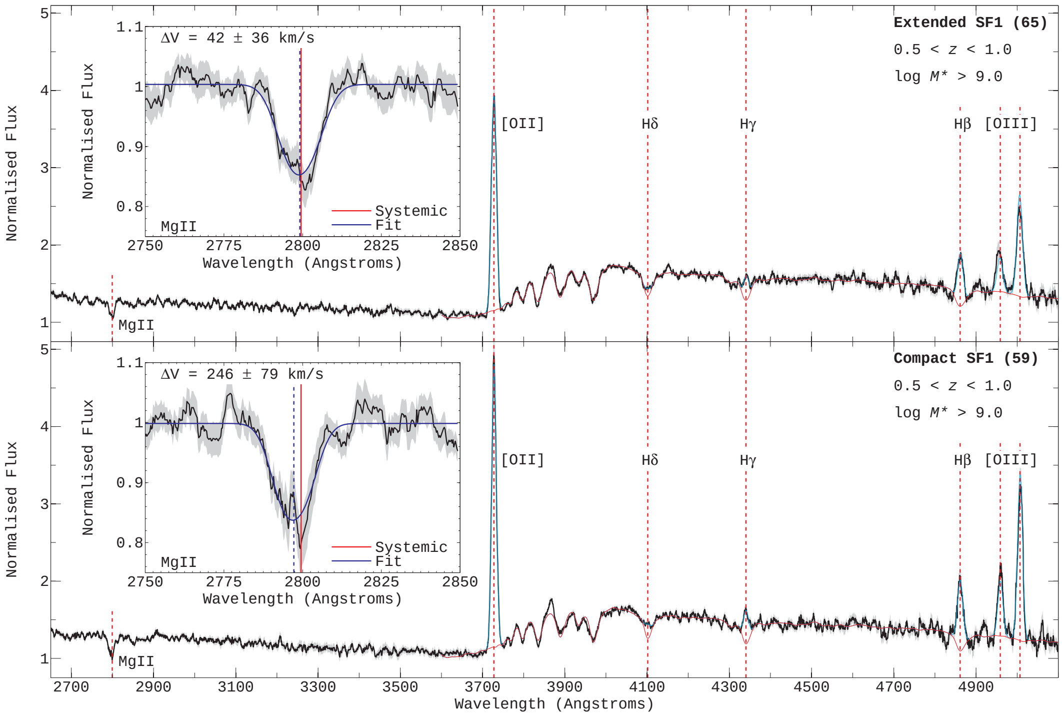

Figure 5.12. Stacked optical spectra for ‘extended’ and ‘compact’ SF1 galaxies in the UDS field at $0.5 < z < 1$. Top panel: a stacked optical spectrum for extended SF1 galaxies (i.e. those that lie above the fit to the mass–size relation in Figure 5.11). For reference, we also show the full spectral fit obtained from PPXF for both the stellar component (red line) and the gas emission lines (cyan lines). Bottom panel: an analogous stacked spectrum and PPXF fit for compact SF1 galaxies (i.e. those that lie below the fit to the mass–size relation in Figure 5.11). Relevant sample sizes are shown in the legend. In each case, the sub-panel shows the best fit to the Mg II absorption profile, using a model comprising a single ‘Gaussian convolved’ doublet with a free centroid. These fits yield the typical velocity offset Δv of the Mg II doublet from the systemic redshift. For extended SF1 galaxies, we find this velocity offset to be minimal ($\Delta v = 42 \pm 36\,\mathrm{km\,s^{-1}}$). In contrast, for compact SF1 galaxies, we require a more significant blue-shift in the doublet to explain the structure of the Mg II profile, and therefore a stronger velocity offset ($\Delta v = 246 \pm 79\,\mathrm{km\,s^{-1}}$). These results imply the presence of stronger galactic-scale outflows in more compact SF1 galaxies.

likely due to a genuine velocity offset δv from the systemic redshift, and not related to any uncertainties in our stacking procedure or individual spectroscopic redshifts.

In our low-resolution spectra, the Mg II doublet is unresolved and consequently the Mg II absorption cannot be simply modelled by two Gaussian components. We model the Mg II profile as a single component, but with a free centroid. This simple model gives a typical offset of the Mg II line from the systemic, which can be used to give a characteristic velocity offset (which can be used to infer the typical outflow velocity). In this model, we also use a doublet for Mg II, using a fixed line ratio (i.e. 1.1:1; as observed for high-z star-forming galaxies) and a narrow width for each line. This doublet is then convolved with a broader Gaussian in the fitting process of either fixed or free width to account for the instrumental resolution. For our 'extended' and 'compact' SF1 galaxies, the relevant fits to the Mg II profile are presented in Figure 5.12. In each case, we determine the velocity offset Δv of the Mg II absorption profile from the systemic redshift. The 1σ uncertainties in these measurements are determined using the variance between analogous fits performed on 1000 simulated spectra generated via a bootstrap analysis.

In the case of extended SF1 galaxies, we find the velocity offset of the Mg II profile from the systemic redshift is minimal ($\Delta v = 42 \pm 36\,\mathrm{km\,s^{-1}}$). This indicates that no significant outflowing (i.e. blue-shifted) component is required. However, for compact SF1 galaxies, we find a significant excess of blue-shifted absorption indicative of high-velocity gaseous outflows. In this case, our best-fit model yields a significant velocity offset in the Mg II absorption profile ($\Delta v = 246 \pm 79\,\mathrm{km\,s^{-1}}$). This indicates that the strong stellar feedback inherent to these compact star-forming galaxies is likely causing strong galactic-scale outflows or winds in their interstellar medium.

Taken together, these results indicate that strong galactic-scale outflows are commonplace in compact SF1 galaxies, but not a significant factor in the more extended SF1 galaxies. This supports our hypothesis that when SF1 galaxies infall to the cluster environment and have their extended gas reservoirs removed by ICM interactions, the subsequent evolution is strongly dependent on the compactness of the galaxy. For extended galaxies, the lack of strong outflows leads to the galaxy retaining its cold gas disc and therefore the continuation of star formation. In contrast, for compact galaxies the stronger outflows present will quickly lead to the removal of the remaining cold gas disc, which would result in the rapid quenching of star formation and the subsequent evolution of these galaxies into cluster PSBs.

5.5 Conclusions

We present the first evidence that the structure of galaxies with high SSFRs (SF1s) differs with environment at $0.5 < z < 1.0$. Using K-band structural parameters available for the UDS, we find that high-SSFR galaxies in clusters are typically larger than analogous galaxies in the field. In Chapter 4, we found that these galaxies are strongly depleted in dense environments and undergo rapid quenching to become cluster PSBs. We therefore suggest that the observed difference in size is caused by the preferential quenching of compact galaxies in dense environments. We summarise our main findings as follows:

1. We find that PSB galaxies have intermediate properties between the quiescent and the total star-forming populations. Although smaller than star-forming

galaxies of similar mass, their mass–size slope is more consistent than with the passive population. Nonetheless, passive and PSB galaxies share the same mass–n relation. This may indicate that PSB galaxies are fading discs (S0s) which are contributing to the flattening of the passive mass-size relation at low stellar masses.

2. Using the mass–size relation, we find that galaxies with high SSFR in the cluster environment are on average larger than their counterparts in the field.

3. Examining the distribution of effective radii, R_{e}, we find that the difference in size is likely to be driven by a lack of compact SF1 galaxies in clusters. This suggests a preferential environmental quenching of the most compact galaxies. From a similar analysis of the distribution in Sérsic indices, we infer that the missing compact SF1 galaxies had higher Sérsic index, n, than the typical SF1 galaxy in the field.

4. We find that the structural parameters of the missing compact SF1 galaxies are compatible with those of the cluster PSB population. Building on the work of Chapter 4, this suggests that compact SF1s are the main progenitors of cluster PSBs, rather than the SF1 population as a whole. These galaxies are rapidly quenched and evolve into the PSB population with no significant structural evolution.

Taken together, these results indicate that at $0.5 < z < 1.0$ rapid quenching within clusters is size-dependent, which may explain why cluster PSBs are significantly smaller than the typical SF1 galaxy or indeed the general star-forming population (Maltby et al. 2018).

Regarding the quenching mechanisms, we suggest that the most likely scenario combines secular and environmental processes. The interaction with the ICM blocks the inflow of gas into the galaxy, which results in the exhaustion of the gas reservoir through star formation and outflows. Therefore, compact SF1 galaxies, which have higher surface star formation densities (similar SFR in a smaller radius), rapidly run out of fuel due to their stronger outflows. This hypothesis is supported by the spectroscopic data available for 124 of the SF1 galaxies. The spectra show evidence that the Mg II absorption feature contains a significant blueshifted component, indicative of outflows, in those galaxies that lie below the field SF1 mass–size relation in comparison to those above it. This provides evidence supporting our model, suggesting that compact SF1 galaxies tend to host stronger galactic outflows.

In conclusion, we find evidence for size-dependent environmental quenching in clusters at $0.5 < z < 1.0$. Our results show that compact star-forming galaxies, at fixed stellar mass, are preferentially and rapidly quenched in clusters to become PSBs.

Chapter 6

Galaxy environment since z=3: the evolution of environmental quenching

In this chapter, we use the deeper data from the 11th data release of the UDS to extend the analysis of the stellar mass functions presented in Chapter 4 to lower stellar masses and higher redshifts. In the $0.5 < z < 1.0$ redshift regime, the deeper DR11 data allows us to reach stellar masses of $M_* < 10^{9.0}\mathrm{M}_\odot$, even for the passive population. Additionally, we are able to probe environmental quenching all the way out to $z = 3.0$, when the Universe was only 2.2 Gyrs old. This will allow us to witness the evolution of environmental effects with cosmic time, and potentially pinpoint the epoch at which environmental quenching becomes established and begins to play a significant role in galaxy evolution.

In this Chapter we study the redshift evolution of the stellar mass function, first independently of environment in order to confirm and extend to higher redshift the findings from Wild et al. (2016) at $z < 2.0$, which used the data from the DR8. We then introduce our measure of environment, determined using a fixed aperture method. We combine this information to study the dependence of galaxy star-formation properties on stellar mass, galaxy type and environment across a very wide redshift range ($0.5 < z < 3.0$).

The work presented in this chapter corresponds to a preliminary analysis, as yet unpublished. The majority of the work is done by me, however, I did not take part in the production of the catalogues. These include photometric redshifts and stellar masses from Simpson et al. (2013), and the application of the PCA classification from Wild et al. (2016).

6.1 Introduction

Overdensities in the local Universe (galaxy clusters and groups) are clearly dominated by early-type, red and passive galaxies (Dressler 1980; Balogh et al. 2004; Kauffmann et al. 2004; von der Linden et al. 2010). However, this has not always been the case. Back at the "Cosmic Noon" epoch, at $z \sim 2$, cluster-size overdensities were dominated by massive star-forming galaxies (Overzier et al. 2008; Galametz et al. 2010; Hatch et al. 2011; Shimakawa et al. 2014). This suggests a strong evolution in the environmental dependency of galaxy properties from $z \sim 3$ to the present day. Despite the existing amount of work in this field, we still do not know the epoch when the effect of dense environments started to shape galaxy properties, setting off the process we know as environmental quenching.

At present, there is general consensus that the correlation between passive fraction, SFR, SSFR and colour with environment for galaxies with $M_* > 10^{9.3}\mathrm{M}_\odot$ seen in the local Universe, were well in place by $z = 1$ (Chuter et al. 2011; Muzzin et al. 2012; Foltz et al. 2015; Balogh et al. 2016). There is also general consensus that the cluster red sequence is well in place by $z = 1$ (Muzzin et al. 2012; Foltz et al. 2015; Balogh et al. 2016). However, at $z > 1.0$ the situation is very different. Some studies find enhanced quenched fractions in high-density environments at $z \sim 1.5$ (Kodama et al. 2007; Bauer et al. 2011; Quadri et al. 2012; Strazzullo et al. 2013; Balogh et al. 2016; Cooke et al. 2016), whilst others find significant ongoing star formation in massive structures (Brodwin et al. 2013; Fassbender et al. 2014; Bayliss et al. 2014; Webb et al. 2015; Bonaventura et al. 2017). Other studies, which look at environmental quenching in groups, have found that the passive fraction increases significantly from $z = 1.5$ to $z = 1$ (Gerke et al. 2007; Cooper et al. 2007; Kawinwanichakij et al. 2016; Darvish et al. 2016). One possible reason for these discrepancies is the fact that many studies focus on a very specific epoch or limited cluster sample, so that cosmic variations can be important. There are only a handful of studies that treat environment in a consistent way across redshift. For example Chuter et al. (2011) studied the dependence of galaxy colour with environment until $z \sim 2$. Other studies also looked at how the star formation properties change with redshift up to $z \sim 3$ (e.g. Kawinwanichakij et al. 2016; Darvish et al. 2016).

In addition to this, the way environmental processes affect galaxies and the evolution with redshift is also unclear. In the low-redshift Universe, there are many studies showing that the effects of mass and environment, i.e. mass and environmental quenching, are independent from each other (Baldry et al. 2006; van den Bosch et al. 2008; Peng et al. 2010; Kovač et al. 2014). However, there is also evidence for a strong connection between secular and environmental processes (see Bolzonella et al. 2010; De Lucia et al. 2012; Mortlock et al. 2015; Darvish et al. 2015, 2016).

Our approach consists of measuring galaxy environment in a consistent way in the redshift range $0.5 < z < 3.0$. The environmental indicator we use is a fixed aperture method, which provides a simple way of tracing galaxy number density in a fixed scale, given by the diameter of the aperture, and dealing with the irregular edges and masked regions present in the UDS field. Given the size of the survey (~ 1 deg^2) we expect to probe environments in a broad dynamical range, but we also expect a small bias due to cosmic variance. We then study galaxy properties such as the stellar mass function, passive fraction, SFR and SSFR, and how these evolve with both redshift and environment.

The structure of this chapter is as follows. In Section 6.2 we provide a brief description of the data specific to the work presented in this chapter. In Section 6.3 we describe the main features of the environmental density measure used. We present our results in Section 6.4 and discuss them in Section 6.5. We then present a summary and conclusions in Section 6.6.

6.2 Data and galaxy classification

The work presented in this chapter is based on the latest UDS data release (DR11; Almaini et al. in preparation), already introduced in Section 2.1.

Here we only provide a brief summary of the most relevant details for the work presented in this chapter. The galaxy catalogue we use is magnitude-limited to

$K < 25.0$ with a 95% detection completeness (Hartley et al. in preparation), and the catalogue incorporates 91 321 galaxies in the redshift range of interest ($0.5 < z < 3.0$). The determination of photometric redshifts and stellar masses was outlined in Chapter 2, therefore, we will just quote the dispersion of the photometric redshifts tested against ~ 7000 spectroscopic redshifts (including data from UDSz, VANDELS, VIPERS and 3DHST), which is $\sigma_{\mathrm{NMAD}} = 0.0183(1 + z)$ once known AGN are excluded.

The supercolour classification, described in Section 2.1, has also been run on UDS DR11 (Wilkinson et al. in preparation). This galaxy classification is run on a catalogue magnitude-limited to $K < 24.5$. This yields a final sample of 46 627 SF1, 8 159 SF2, 8 663 SF3, 4 636 passive and 1 884 PSB galaxies, once the corresponding stellar mass completeness limits have been applied (see Chapter 2 for the stellar mass completeness limits). This sample spans the redshift range $0.5 < z < 3.0$. Other galaxy properties presented in this chapter, such as SFRs and SSFRs, were derived using the supercolour formalism, as described in Chapter 2.

6.3 Measuring galaxy environment consistently at $0.5 < z < 3.0$

The main goal of this chapter is to study the evolution of environmental effects over a wide span of cosmic time. In particular, we target the redshift range $0.5 < z < 3.0$, equivalent to an interval of ~ 6.5 Gyrs, commencing when the Universe was only 2.2 Gyrs old. This redshift range is of particular interest because it includes the peak of SFR density of the Universe ($z \sim 2$; Benson et al. 2003). This epoch is when a significant fraction of the galaxies present in the local Universe formed and the most massive galaxies ($> 10^{11}\mathrm{M}_{\odot}$) were assembled (Wild et al. 2016).

In order to achieve our aims, we need to define an environmental measure that is versatile enough to perform successfully across this broad range of redshifts, and do it in the most consistent way possible, so that we can compare results at different epochs. However, measuring environments in a consistent way throughout a broad redshift range is a very difficult task. The first problem we encounter is the dependence of the sample completeness with redshift, as we go further away we start missing the faintest objects, until we are left with only the most massive ones. The correct way to deal with this is to apply the same stellar mass cut for the entire sample (usually the value corresponding to the highest redshift). The problem with this approach is that, when using very broad redshift ranges, one throws away a significant amount of information corresponding to galaxies below the global mass limit at low redshift. Another solution is to use relative densities, i.e. normalise the density for a galaxy by the average density across the field at the same redshift. This method gives an estimate of how overdense the environment of the target galaxy is with respect to the typical density at the same epoch applying the same cuts. However, this is an approximated correction, therefore, one has to be careful when comparing across different epochs. Finally, as the global distribution of galaxies evolves with redshifts, the overdensity value may have different physical meanings at different epochs. For example, the distribution of galaxies in the high-redshift Universe is much more homogenous than locally, consequently, a small group at this epoch might produce the same overdensity level as a mature cluster at $z = 0$. Therefore, it is practically impossible to measure environment fully consistently across wide redshift ranges.

Taking the previous discussion into consideration, we select a Monte-Carlo fixed-aperture method to perform our environmental measure. The method consists of using a regular fixed-aperture density indicator, as described in Section 3.1.1. We place cylindrical volumes around each galaxy and count the number of neighbours within, then we divide this number by the expected number of galaxies in the volume assuming the average density of galaxies in the same redshift interval across the entire field of view. We then run this method 5000 times on catalogues with simulated photometric redshifts. These mock redshifts are randomly generated sampling a Gaussian distribution centred on the measured redshift and with a width corresponding to the expected photometric redshift dispersion [$\sigma_{\rm NMAD} = 0.0183(1 + z_{\rm phot})$]. This approach provides a more robust measure of environment, which is determined from the median of all 5000 realisations. Furthermore, errors are estimated using the median absolute deviation (MAD) from the median, using the standard procedure, $\Delta z = 1.48$ MAD($\rho_{\rm MC}$).

For each realisation, the fixed aperture method uses circular apertures, therefore, the volume used to measure the density is a cylinder. The depth of these cylinders (d_z) is $d_z = 0.0183(1 + z_{\rm phot})$ i.e. chosen according to the magnitude of the photometric redshift uncertainties. For illustration purposes, we give some depth values expressed in light-travel time units: $d_z \sim 0.5$ Gyrs at $z = 1$, $d_z \sim 0.4$ Gyrs at $z = 2$ and $d_z \sim 0.3$ Gyrs at $z = 3$. With respect to the size of the aperture, the diameter ($d_{\rm Ap}$) was chosen based on the known preference of passive galaxies to reside in dense environments up to at least $z = 2$. Therefore, we choose the $d_{\rm Ap}$ that maximises the difference between the density distributions of passive and star-forming galaxies at each epoch. This optimisation is carried out independently in two redshift slices, with the following optimal values: $d_{\rm Ap} = 600$ kpc at $0.5 < z < 1.0$ and $d_{\rm Ap} = 400$ kpc at $1.0 < z < 2.0$. At higher redshifts ($z > 2.0$) the existence of such trends with environment are uncertain, therefore, we simply use the same diameter as in the preceding redshift slice (i.e. $1.0 < z < 2.0$). In optimising the aperture size, the method used to quantify the statistical difference between the density distributions of passive and star-forming galaxies was a 2-sided Kolmogorov-Smirnov (KS) test. Here we quote the resulting p-values, which represent the probability that the two probed samples are drawn from the same parent probability distribution for the adopted apertures: $p_{\rm KS} \sim 10^{-98}$ at $0.5 < z < 1.0$, $p_{\rm KS} \sim 10^{-52}$ at $1,0 < z < 2.0$ and $p_{\rm KS} \sim 10^{-5}$ at $2.0 < z < 3.0$. We note that although the significance drops with increasing redshift, the density distribution of passive and star-forming galaxies remains remarkably dissimilar even in the highest redshift bin.

Finally, we acknowledge that the apertures used in our method are relatively small, hence our method is more likely to be tracing the immediate surroundings of the galaxies in our sample, i.e. the local dark matter halo. However we make sure that, especially at high redshift, the galaxy number count in the aperture is not dominated by very low numbers, in fact at $z > 2.0$, galaxies with $\log(1 + \delta) > 0$ typically have 3 companions or more per aperture. Furthermore, using small apertures makes sense for the kind of study we are conducting. By using small apertures we are able to better characterise the densest environment, which is our main interest. Whilst our density resolution drops in the low density regime, this aspect is not a problem for us since everything that is not in overdense environments is regarded as the field. As a final caveat, we remind the reader that we cannot directly compare our measurements of environment at different redshifts, we can only use our densities to compare different classes of galaxy within a given redshift bin.

6.4 Results

6.4.1 The evolution of the galaxy stellar mass function since $z = 3$

In this section, we focus on the redshift evolution of the galaxy stellar mass function of the star-forming, passive and post-starburst populations. These trends are observed in Wild et al. (2016) at $z < 2.0$ using UDS DR8 data. Our goal is to confirm their results and extend the analysis to $z = 3.0$. We also wish to study the dependence of these trends with environment, which is carried out in the following sections.

Figure 6.1 shows the evolution of the stellar mass function with redshift for the three main galaxy populations: star-forming (left-hand panel), passive (central panel) and PSB (right-hand panel). The plotted curves correspond to best-fitting Schechter functions to each population's stellar mass distribution down to their mass completeness limit for the given redshift. In the case of PSB galaxies a double Schechter function was used at $0.5 < z < 1.0$ (see Chapter 4). The fitting is done in the same way as in Chapter 4, which consists of a Bayesian maximum likelihood method used to fit a probability distribution to a set of unbinned data. We use a Monte-Carlo Markov Chain (MCMC) method to sample the parameter space and obtain the errors associated with the best-fitting parameters. The normalisation is fixed afterward to match the total density of each population, i.e. the number of galaxies per unit comoving volume. The comoving volume corresponds to the volume of the redshift slices overlapping with the area of the survey. The six redshift slices we split our sample into are the following (with the equivalent time intervals in Gyrs): $(0.5, 0.7) = 1.3$ Gyrs, $(0.7, 1.0) = 1.4$ Gyrs, $(1.0, 1.5) = 1.5$ Gyrs, $(1.5, 2.0) = 1.0$ Gyrs, $(2.0, 2.5) = 0.7$ Gyrs and $(2.5, 3.0) = 0.5$ Gyrs.

With respect to the star-forming population, we find little evolution with redshift. This is because, although star-forming galaxies are undergoing quenching, new galaxies are continuously growing through star formation, keeping the density approximately constant. The shape of the mass function remains unchanged across redshift, whilst the normalisation decreases slightly since $z \sim 2.0$.

In contrast, the passive mass function undergoes a strong redshift evolution. We observe the expected build up of the red sequence as a steady increase in the normalisation of the mass function with cosmic time, resulting in a final ($z = 0.5$) density approximately 27 times higher than that at $z \sim 3.0$ over the stellar mass range $M_* > 10^{10.0}\mathrm{M}_\odot$. Furthermore, we find that the density of massive quiescent galaxies evolves first, rapidly increasing from redshift $z = 3$ to $z \sim 1$. In contrast, at $z < 1$ it is the density of low-mass passive galaxies which increases towards lower redshifts, causing the α value to decrease significantly (see Table 6.1). This could be partially driven by the bias produced by the increasing mass completeness limit with redshift (see Chapter 2). However, the steep decrease in the density of passive galaxies towards the low-mass end at $1.0 < z < 2.0$, which is above the mass completeness cut, suggests that this is a real trend.

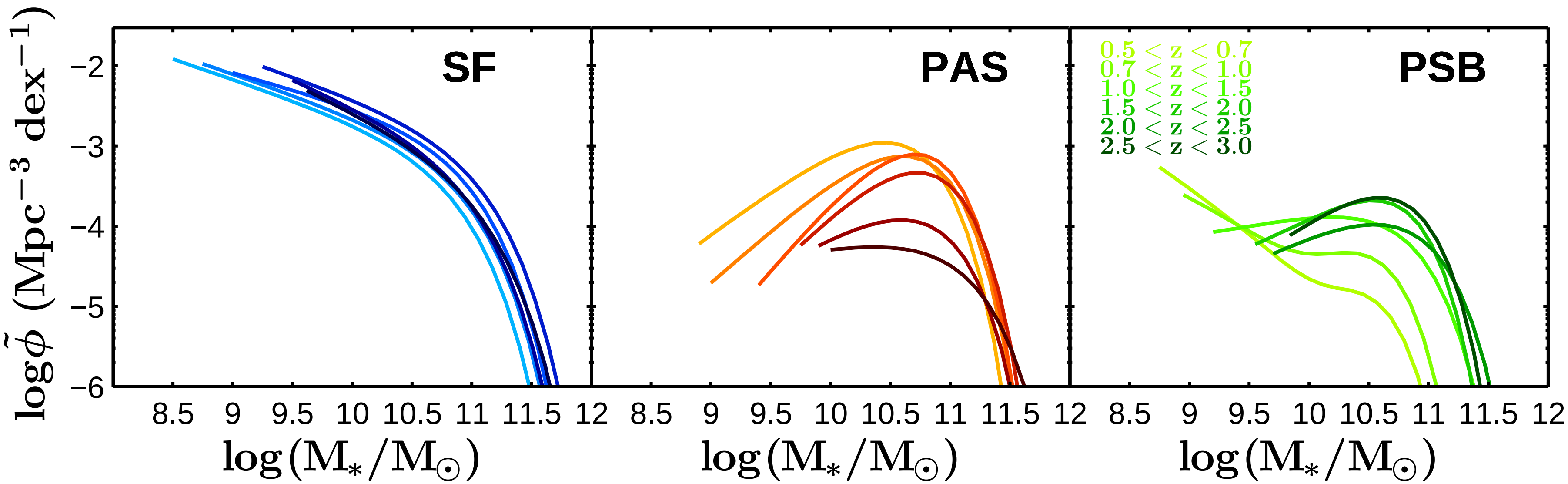

Figure 6.1. Redshift evolution of the galaxy stellar mass function of star-forming (blue), passive (red) and PSB (green) galaxies, from $z = 3$ (darkest colour) until $z = 0.5$ (lightest colour). The lines correspond to best-fitting simple Schechter functions for the star-forming and passive population, while the PSB population requires a double Schechter model at $z < 1$. The figure shows how the stellar mass function of star-forming galaxies barely changes with redshift, as star-forming galaxies that quench are continuously replenished by newly formed ones. In contrast, the passive population exhibits a normalisation which only increases with redshift as galaxies that become passive, remain passive in most cases. The PSB population shows the most dramatic change with cosmic time. PSBs in the high-z Universe are massive and frequent, however, as redshift decreases the number of massive PSBs dramatically drops while an upturn of the mass function at low stellar masses becomes evident at $z \sim 1.5$. This trend continues, leading to a PSB population completely dominated by low-mass galaxies by $z = 0.5$.

Finally, the stellar mass function of PSB galaxies experiences the strongest transformation across redshift. We observe that at high redshift PSB galaxies tend to be massive, with typical stellar masses of $M_* \sim 10^{10.75}\mathrm{M}_\odot$ (also seen by Wild et al. 2016; Almaini et al. 2017). However, towards lower redshifts, the number density of high-mass PSB galaxies decreases rapidly (their density drops by a factor of 7 across $0.5 < z < 2.0$), so that they become a very rare population by $z = 1$ and below.

Simultaneously, the density of low-mass PSB galaxies increases dramatically since $z \sim 2.0$ (Wild et al. 2016; Maltby et al. 2016, 2018). Consequently, at $z < 1.0$ the PSB population is dominated by low-mass galaxies.

In Figure 6.2 we present these results in a slightly different way and compare the different mass functions corresponding to different galaxy populations at fixed redshift. This figure shows that the shape of the passive and PSB mass functions are practically indistinguishable at $z > 2.0$. However, at lower redshifts the PSB population develops an upturn towards low stellar masses. As a consequence of this upturn, the PSB mass function seems to trace the star-forming mass function at $z \leq 1$ (Wild et al. 2016). Additionally, the increase in numbers of low-mass PSB galaxies is followed by an subsequent increase in the density of low-mass passive galaxies, with a delay of $\Delta z \sim 0.5$. This is suggestive of PSB galaxies being a key stage in the growth of the red sequence (Wild et al. 2016), accounting for a significant fraction of the galaxies that join the red sequence at all redshifts.

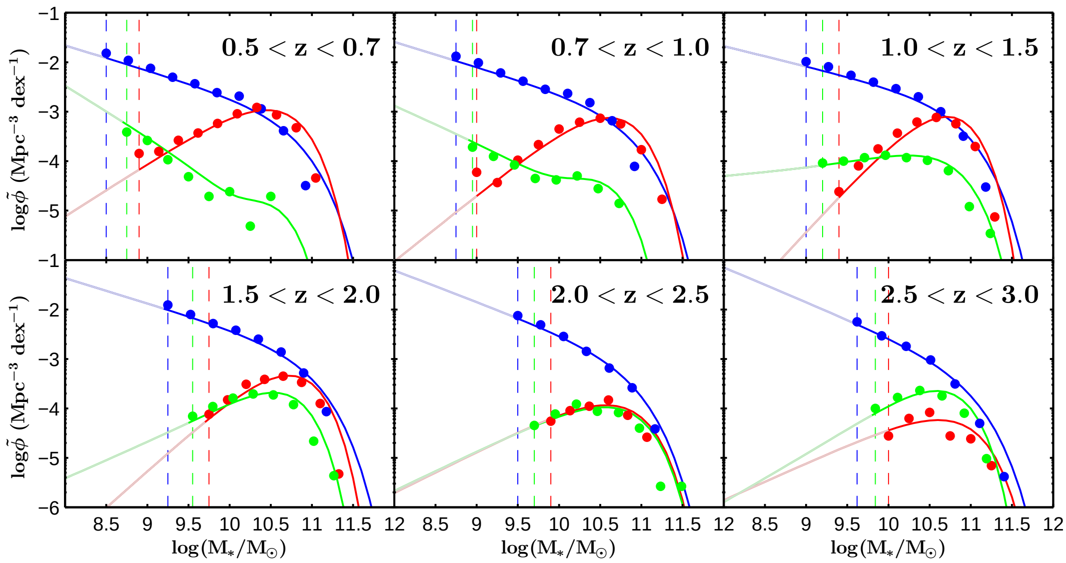

Figure 6.2. Comparison of the galaxy stellar mass function of star-forming (blue), passive (red) and PSB (green) galaxies across cosmic time, from $z = 3$ until $z = 0.5$. The data-points correspond to the binned masses. Each vertical dashed line corresponds to the 90% stellar mass completeness limit of the mass function of the same colour. The figure shows that the PSB mass function develops a strong upturn at low stellar masses since $z < 1$, so that the slope of the low-mass end behaves like the star-forming mass function. $1.0 < z < 1.5$ represents a transition epoch in which the distribution in mass of PSBs is half way between passive and star-forming galaxies. This is in contrast with the trend at $z > 1.5$, where the PSB mass function is closer to that of the quiescent population, in both normalisation and shape.

		$0.5 < z < 0.7$	**$0.7 < z < 1.0$**	**$1.0 < z < 1.5$**	**$1.5 < z < 2.0$**	**$2.0 < z < 2.5$**	**$2.5 < z < 3.0$**
	α	-1.509 ± 0.013	-1.510 ± 0.011	-1.405 ± 0.012	-1.513 ± 0.016	-1.635 ± 0.032	-1.709 ± 0.038
SFT	$\log M^*$	10.727 ± 0.035	10.793 ± 0.028	10.806 ± 0.021	10.924 ± 0.028	10.827 ± 0.044	10.952 ± 0.056
	$\log \phi^*$	-0.675 ± 0.004	-0.848 ± 0.004	-1.192 ± 0.004	-1.142 ± 0.005	-1.543 ± 0.009	-1.670 ± 0.010
	α	0.090 ± 0.057	0.336 ± 0.070	0.813 ± 0.058	0.619 ± 0.115	0.003 ± 0.126	-0.497 ± 0.096
PAS	$\log M^*$	10.415 ± 0.025	10.479 ± 0.024	10.452 ± 0.016	10.521 ± 0.030	10.579 ± 0.051	10.809 ± 0.068
	$\log \phi^*$	-2.891 ± 0.217	-3.076 ± 0.060	-3.154 ± 0.022	-3.325 ± 0.051	-3.832 ± 0.190	-4.315 ± 0.085
	α_1	-2.086 ± 0.028	-1.824 ± 0.053	-0.615 ± 0.030	0.092 ± 0.037	-0.228 ± 0.051	0.183 ± 0.042
	$\log M^*$	10.220 ± 0.063	10.248 ± 0.045	10.592 ± 0.019	10.458 ± 0.019	10.662 ± 0.025	10.500 ± 0.019
PSB	$\log \phi_1^*$	-4.823 ± 0.010	-4.791 ± 0.008	-3.917 ± 0.021	-3.611 ± 0.176	-3.920 ± 0.097	-3.587 ± 0.099
	α_2	0.406 ± 0.236	-0.306 ± 0.152	-	-	-	-
	$\log \phi_2^*$	-5.071 ± 0.292	-4.450 ± 0.040	-	-	-	-

Table 6.1. Best-fitting Schechter parameters to the mass function of star-forming, quiescent and PSB galaxies in different redshift slices. We use a double Schechter function for the PSB population at $z \leq 1$. M^* is expressed in $M_\odot$ and ϕ^* in $\mathrm{Mpc}^{-3}\mathrm{dex}^{-1}$.

These results are in good agreement with those from Wild et al. (2016), where they describe the same trends for the star-forming, passive and PSB mass functions at $z < 2.0$ using the UDS DR8 data. Nonetheless, with DR11 we manage to go roughly 0.3 dex lower in stellar mass for every galaxy population and redshift bin in their study. Furthermore, we extend the analysis to the redshift range $2.0 < z < 3.0$, confirming that the trends observed at $z \sim 2.0$ do not change significantly.

6.4.2 Galaxy star formation properties as a function of stellar mass and environment

In Section 6.4.1 we studied the redshift evolution of various galaxy populations. Now we extend this analysis using the environmental measure described in Section 6.3 to study how local density affects galaxy evolution across a wide redshift range and trace the epoch at which it becomes important. Note that, as mentioned in Section 6.3, it is very difficult to measure environment in a consistent way over a wide redshift range. Therefore, we refrain from directly comparing results based on our density measurements between different epochs. However, we can robustly compare the densities of galaxies at similar redshifts, which we exploit in this section. When it comes to the redshift evolution of the environmental trends, we describe the global evolution of the correlations, rather than relying on density values, which are subjected to arbitrary biases. Nevertheless, we refer to density values for descriptive purposes, i.e. as a tool to guide the reader through the results more effectively.

To begin with, we use our environmental measures to reproduce the plot shown in Figure 1.9 of the Introduction of this thesis (from Peng et al. 2010). This shows how the fraction of passive galaxies (first column of Figure 6.3) and the average SSFR (second column) depend on both stellar mass and local density. Note that the passive fraction is calculated by dividing the number of passive and PSB galaxies by the total number of galaxies per bin ($\Delta M \times \Delta\rho$). We do this in three redshift intervals in order to account for the redshift evolution of the galaxy population: $0.5 < z < 1.0$, first row; $1.0 < z < 2.0$, second row; and $2.0 < z < 3.0$, third row. The passive fraction and average SSFR are calculated in 2D bins which increase in size with redshift. This is necessary because the observed trends weaken and the signal-to-noise drops towards high redshift, forcing us to use a coarser binning. The bin sizes are $(\Delta\rho, \Delta M_*) = (0.38, 0.25)$, $(0.5, 0.4)$ and $(0.7, 0.67)$ for the first, second and third redshift intervals respectively. The plots presented in Figure 6.3 are used for a qualitative analysis of the trend with stellar mass and environment, a more detailed study is carried out later on in this section.

In the lowest redshift interval ($z < 1$), we observe that the passive fraction is separately dependent on both stellar mass and environmental density. We find that almost every galaxy with $M_* > 10^{11}\mathrm{M}_\odot$ or $\log(1+\delta) > 0.8$ is quenched. This result is consistent with the results from Peng et al. (2010), the original description of these trends at $z < 1$. For SSFR we find that, as expected, this follows the opposite trends and anticorrelates with these two parameters. However, we note that the curves of constant passive fraction and average SSFR have roughly the same shape.

At $1.0 < z < 2.0$, we observe that the trends with mass and environment observed at lower redshift weaken. The dependence of both the passive fraction and mean SSFR on density is notably reduced, while the correlation with stellar mass is slightly reduced but remains strong. This is reflected in the shape of the respective contours (which are almost vertical). However, the red fraction still increases (and SSFR decreases) slightly towards high overdensity values. Finally, when we look at the highest redshift interval ($z > 2$), we observe that the passive fraction is $f_{\rm Q} < 0.3$ almost everywhere but in the regime of the highest density [$\log(1+\rho) \sim 1.0$] and highest stellar mass ($\sim 10^{11.5}{\rm M}_\odot$). Similarly, the SSFR only significantly decreases in the top-right corner of the mass–density plane.

Taken together, these results suggest that stellar mass and environmental density might correlate with the star-formation properties of galaxies all the way until redshift $z \sim 3$. However, we find that the nature of this correlation changes significantly. At $z < 1.0$ we find the same as Peng et al. (2010), with evidence suggesting that galaxies with high stellar masses or inhabiting high-density environments are more likely to be quenched. At $1.0 < z < 2.0$ these trends weaken but still point in the same direction. In contrast, at $2.0 < z < 3.0$ only galaxies with the highest stellar masses and in the highest-density environments present a significant enhancement of the passive fraction or reduction in the mean SSFR. However, we cannot disentangle whether this is driven by massive galaxies being quenched in dense environments at these early times, or if massive galaxies in dense environments are intrinsically older due to an earlier assembly.

In order to investigate the effect of environment in more detail, we study the dependence of the passive fraction and star formation activity (SFR and SSFR) on the local density at fixed stellar mass and redshift. We decrease our mass resolution in order to increase the density resolution, so that we maintain a reasonable galaxy number count per bin. We split the total galaxy sample in four redshift bins, with edges at $z = (0.5, 1.0, 1.5, 2.0, 3.0)$. Additionally, we divide the sample into two stellar mass bins, we choose the division at $10^{10.3}{\rm M}_\odot$, which allows us to study the stellar mass dependence even in the highest redshift interval ($z > 2$). Then we study how the passive fraction and median SFR and SSFR change as a function of local density (see Figures 6.4, 6.5 and 6.6).

In Figure 6.4 we show the dependence of the passive fraction on environment and redshift. Interestingly, we find no evidence for environmental effects beyond $z = 2.0$. The passive fraction and median SSFR show no signs of any dependence with local density, in both stellar mass ranges studied. This lack of environmental trend could imply that galaxies at this epoch have not had the time to feel the effects of the environment, or those overdensities have not had time to grow enough to have an impact on the properties of galaxies. After all, the Universe was only about ~ 3.3 Gyrs old in this epoch.

In contrast, at $z < 2.0$ the passive fraction and star-formation properties of the galaxies in our sample show a clear correlation with environmental density. Figure 6.4 shows the build-up of a correlation between density and passive fraction with cosmic time. This correlation is the strongest in the lowest redshift bin (red line; $0.5 < z < 1.0$). We also observe that galaxies at the same redshift but with high/low stellar masses both reach a consistent maximum value for the passive fraction. However, we find that the slope of the relation is significantly different between our two stellar mass bins. The passive fraction of low-mass galaxies is flat, rising quickly at high overdensity [$\log(1+\rho) \gtrsim 0.5$]. In contrast, massive galaxies present a progressive increase of the passive fraction with density, over the full range of densities probed. With respect to the SSFR (see Figure 6.5), we also find results that are consistent with the trends observed in the passive fraction at $z < 2.0$. Similarly to the trend of passive fraction, low-mass galaxies have flat median SSFR until $\log(1+\rho) \sim 0.5$, after which the SSFR decreases with density. We also observe the same stellar mass dependence reported above, where massive galaxies show a

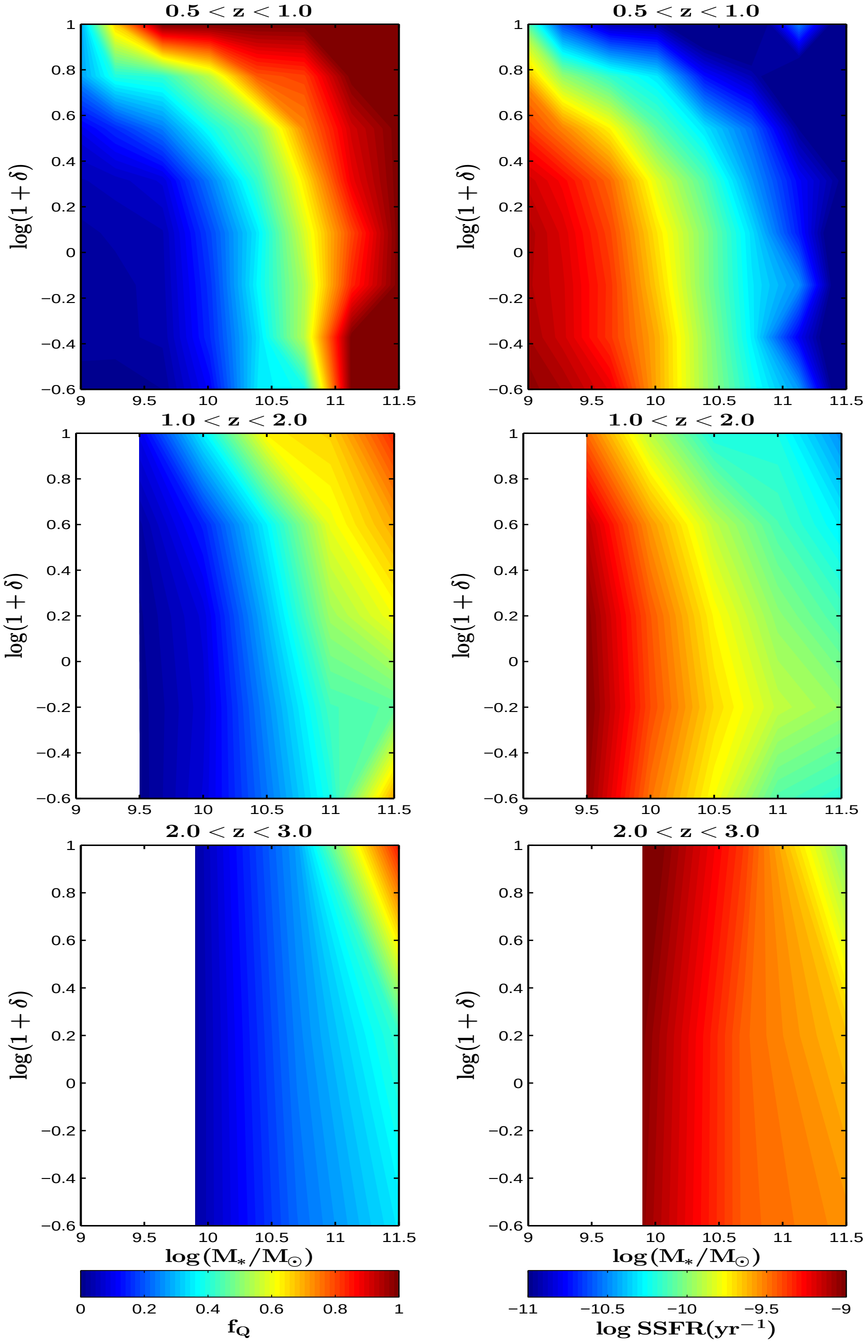

Figure 6.3. Passive fraction (left hand column) and average specific star formation rate (right hand column) as a function of stellar mass on the x-axis and environmental density on the y-axis in three different redshift bins spanning from $z = 0.5$ to $z = 3.0$. The mass–density plane is binned with bin sizes: $\Delta\log(1+\delta)\times\Delta\log(M_*/\mathrm{M}_\odot) = 0.38\times0.25$, 0.5×0.4 and 0.7×0.67; corresponding to the three redshift bins in increasing order. The white area in the second and third rows corresponds to the range of masses below the completeness limit.

more gradual decline of the median SSFR as a function of environment, with evidence for a downturn starting at $\log(1+\rho) \geq 0$. The median SSFR drops by almost two orders of magnitude from low densities to the densest environments at $z < 1.0$, while

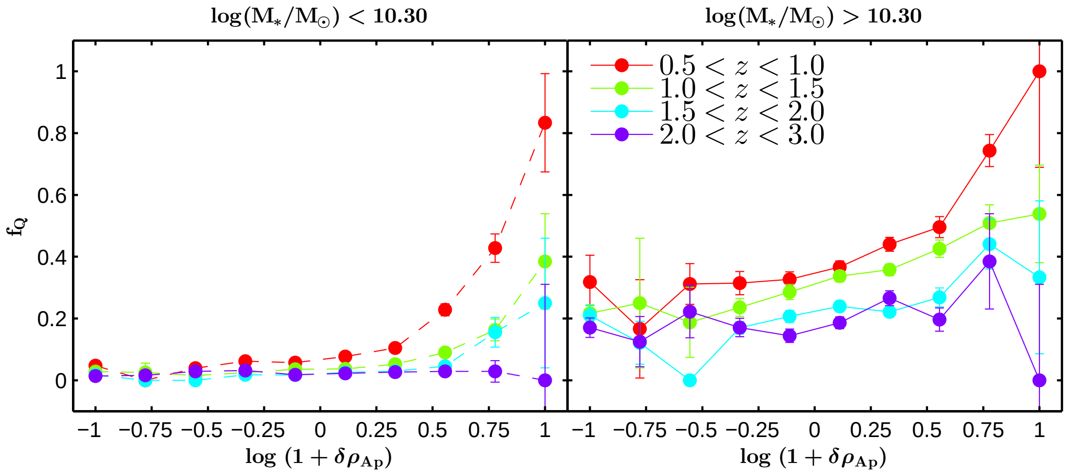

Figure 6.4. Galaxy passive fraction as a function of environmental density in different redshift intervals which span from $z = 0.5$ to $z = 3$. The left hand panel corresponds to all the galaxies in our sample with stellar masses $< 10^{10.3}\mathrm{M}_{\odot}$. The panel on the right corresponds to massive galaxies ($> 10^{10.3}\mathrm{M}_{\odot}$). Due to the density measures not being consistent across broad redshift ranges, we restrict the direct comparison to galaxies within the same redshift bin.

the dip in SSFR at $1.0 < z < 2.0$ is approximately of half an order of magnitude.

With respect to the stellar mass, we note that at all redshifts studied massive galaxies have systematically higher passive fractions and lower median SSFRs than low-mass galaxies at intermediate-low densities ($\log(1+\delta) \lesssim 0$). These higher passive fractions and lower SSFRs for massive galaxies are likely to be produced by the effect of mass quenching in the high-mass regime, already in action at $z > 2.0$. For high/low masses, we do observe that the median SSFR is systematically lower with decreasing redshift. For high-mass and low-mass at high density this can be explained by mass quenching and environmental quenching respectively. However, we also observe that the median SSFR of low-mass galaxies ($M_* < 10^{10.3}\mathrm{M}_{\odot}$) at $0.5 < z < 1.0$ is also systematically lower than in higher redshift bins. This environment-independent drop is probably due to the evolution of the galaxy star forming main sequence, which is believed to be driven by the decrease of available gas at lower redshifts (Elbaz et al. 2011). Alternatively, an additional quenching mechanism responsible for quenching low-mass galaxies in the field (for example tidal stripping in poor groups) could be contributing to this decrease of the median SSFR at low redshift.

To complement these results, we also study the star formation–density relation. Figure 6.6 shows that the median SFR evolves with redshift, regardless of environment and stellar mass. The median values of SFR decrease with cosmic time at all values of $\log(1+\delta)$ and in both stellar mass bins. This is consistent with the steady decline in the SFR density of the Universe since the peak of star formation at $z \sim 2$–3, which has been measured on numerous occasions (e.g. Sobral et al. 2013; Madau & Dickinson 2014). Interestingly, we see that the amount of decrease is dependent on environment. The general trend consists of SFR decreasing with local density and, although this trend weakens with redshift, it remains observable up to $z \sim 2$. For example, below $z = 1$ the median SFR falls by more than an order of magnitude, while at $1.0 < z < 2.0$ the drop is approximately only half an order

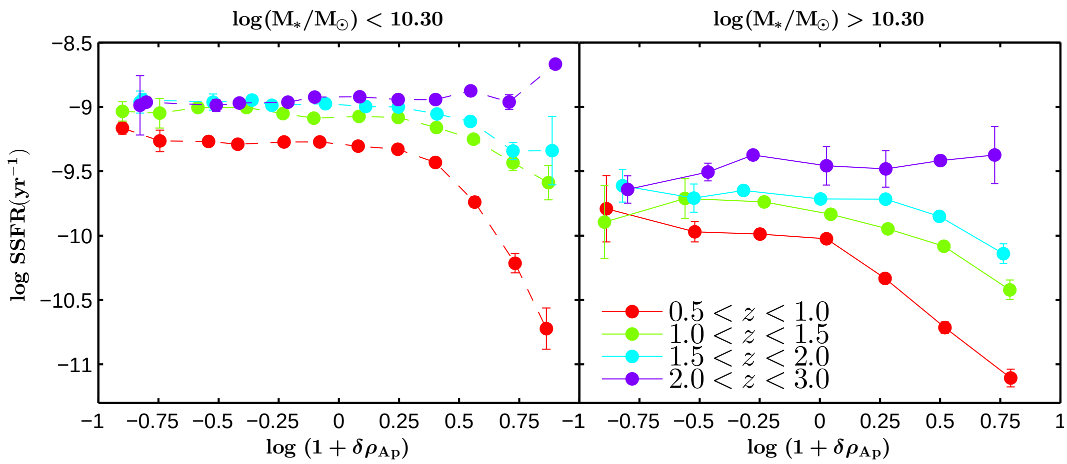

Figure 6.5. SSFR as a function of environmental density in different redshift intervals which span from $z = 0.5$ to $z = 3$. The left hand panel corresponds to all the galaxies in our sample with stellar masses $< 10^{10.3}\mathrm{M}_\odot$. The panel on the right corresponds to massive galaxies ($> 10^{10.3}\mathrm{M}_\odot$).

of magnitude, in both stellar mass bins. Once more, low-mass galaxies seem to only feel the effect of environment at high densities, where the median SFR plummets, whilst the massive galaxies experience a progressive decay in their SFR.

At higher redshifts ($2.0 < z < 3.0$), we find evidence for a reversal of the SFR–density relation of low-mass galaxies. Figure 6.6 suggests that the median SFR is enhanced by almost 0.5 dex at the highest densities, the same regime where the SFR is depleted in lower redshift bins. Given that we did not see the same trend with median SSFR at this epoch, we may infer that galaxies at high overdensity values and $z > 2.0$ are more massive. However, we use a KS test to compare the mass distributions of galaxies with $\log(1 + \delta) < 0.0$ and $\log(1 + \delta) > 0.5$, which fulfil the conditions $10.0 < \log(M_*/\mathrm{M}_\odot) < 10.3$ and $2.0 < z < 3.0$. The probability of rejecting the null hypothesis is $p_{\mathrm{KS}} = 0.11$, which indicates that the stellar mass distributions are not significantly dissimilar. Nevertheless, this may constitute evidence that there is a reversal of the SFR–density relation at high redshift. However, our results place this reversal at $z \gtrsim 2.0$, while most studies that report a reversal of the SFR–density relation find it at $z \sim 1.0$ (e.g. Elbaz et al. 2007; Cooper et al. 2008; Welikala et al. 2016).

Finally, we note that although the redshift evolution described in Figures 6.4, 6.5 and 6.6 is mostly dominated by the increase in the number of passive galaxies in dense environments with cosmic time, the trends persist if we only look at the star-forming population. Implying that environmental density truly anticorrelates with the average SSFR and SSFR of galaxies at $z < 2.0$. Additionally, due to the known correlation between stellar mass and density for massive galaxies (centrals), we need to be careful when interpreting the right-hand panels ($\log(M_*/\mathrm{M}_\odot) > 10.3$). However, this effect is not likely to be dominant since the stellar mass range considered is not too broad.

In summary, we find a strong correlation between the passive fraction and environment, and an anticorrelation between the star-formation activity (SFR and SSFR) and environmental density (Scoville et al. 2013; Darvish et al. 2016). Both weaken with redshift and virtually disappear beyond $z = 2.0$. Additionally, we find

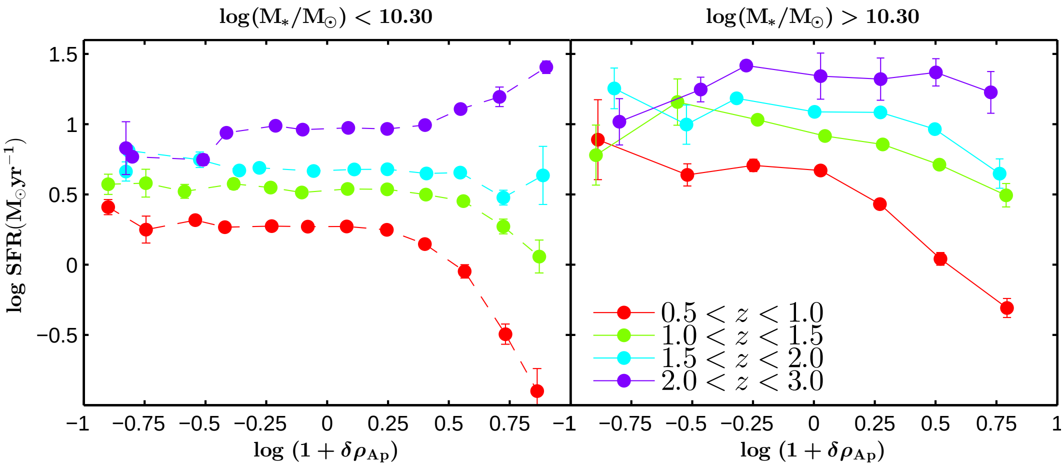

Figure 6.6. SFR as a function of environmental density in different redshift intervals which span from $z = 0.5$ to $z = 3$. The left hand panel corresponds to all the galaxies in our sample with stellar masses $< 10^{10.3}\mathrm{M}_\odot$. The panel on the right corresponds to massive galaxies ($> 10^{10.3}\mathrm{M}_\odot$).

that these trends differ between high and low-mass galaxies. For the $M_* < 10^{10.3}\mathrm{M}_\odot$ galaxy population we observe that all mentioned studied properties are independent on environment below a $\log(1+\delta) \sim 0.5$. Beyond this limit the environmental dependence becomes clear due to an abrupt change in the passive fraction, median SSFR and median SFR, simultaneously. In contrast, galaxies with $M_* > 10^{10.3}\mathrm{M}_\odot$ present a much smoother environmental dependence, with star formation properties being visibly affected by environment from lower overdensity levels, and experiencing a more gradual increase. Finally, we find that low-mass galaxies at $z \sim 2.5$ in high-density environments might have their SFR enhanced (possible reversal of the SFR–density relation).

6.4.3 The redshift evolution of the fraction of star-forming, passive and PSB galaxies

In this section, we study the evolution of the fraction of star-forming, quiescent and PSB galaxies from redshift $z = 3.0$ to $z = 0.5$ as a function of environment. In order to efficiently compare across environments, we bin our densities in two subsets that account for almost 90% of our galaxy sample. The high-density bin corresponds to all galaxies with local densities above the 90th density percentile [$\log(1+\delta) = 0.41$], while the low-density or field sample is defined as those galaxies within $\pm 1\sigma_\delta$ from the median value of the number density distribution [$\log(1+\tilde{\delta}) = 0.06$]. Note that, as mentioned above, we cannot strictly compare environments at different redshifts, nonetheless, the comparison between different galaxy types at the same epoch is valid. Furthermore, binning our data in two broad density intervals reduces the effect of the arbitrariness of the density measure, since we are just comparing the densest and typical environments at each redshift.

In Figure 6.7 we show the redshift evolution of the fraction of each galaxy population, while in Figure 6.8 we show the fraction of the star-forming sub-populations: SF1, SF2 and SF3 galaxies. The normalisation is such that the star-forming, passive and PSB fractions add to unity, and the sum of the SF1, SF2 and SF3 fractions is equal to the total star-forming fraction. We also separate the sample by environment: filled symbols correspond to high-density environments while open symbols represent low-density environments. The redshift intervals are the same used in Section 6.4.1, which are used throughout this section. In each redshift interval, the galaxy fraction is calculated using the stellar mass limit of the passive population (which is the highest of the three populations studied) evaluated at the upper limit of the redshift bin, and errorbars are estimated using a bootstrapping technique. Finally, we also separate between massive and low-mass galaxies, using the same criteria described above (i.e. stellar masses above and below $10^{10.3}\mathrm{M}_{\odot}$). As a result of this analysis, the stellar mass limit changes with redshift in the low-mass regime. This may result in some bias due to the lack of very low-mass galaxies toward increasing redshift. Furthermore, this issue also translates into lower number of galaxies at higher redshifts, leading to less robust trends at $z > 2.0$. Nonetheless, our main results tend to reside within the range $0.5 < z < 2.0$, so that these biases are not a major issue for the conclusions we draw from this study.

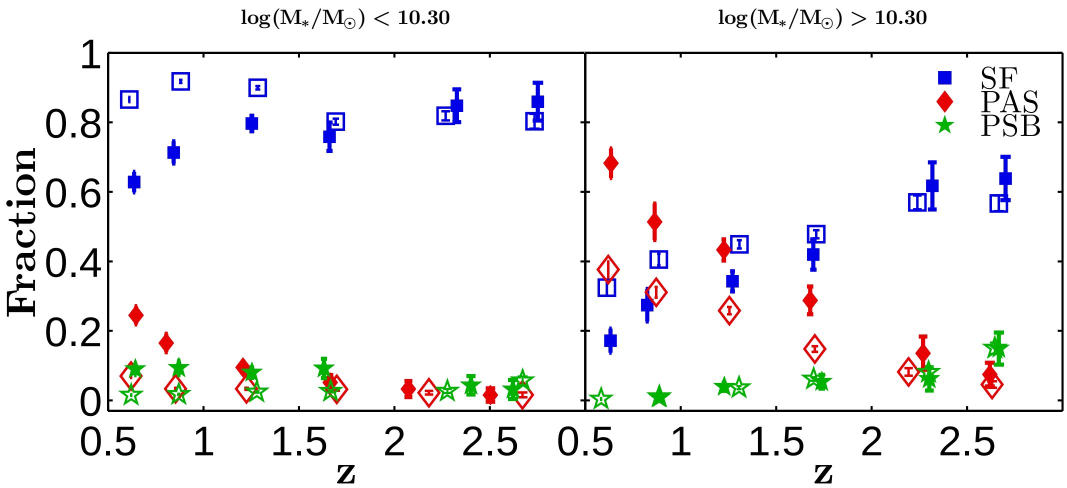

Figure 6.7. Redshift evolution of the fraction of SF (blue squares), PAS (red diamonds) and PSB (green stars) galaxies as a function of environment. Filled symbols correspond to dense environments, while open symbols represent the field environment.

Let us start by describing our results for low-mass galaxies, in the left-hand panel of Figure 6.7. We observe that the fraction of star-forming galaxies does not change significantly with redshift, and stays close to a constant $f_{\mathrm{SF}} \sim 0.8$. However, below $z \sim 1.75$ the fractions in high and low-density environments start to diverge so that at $z \sim 0.5$ the fraction in dense environments is about 20% lower than in the control or field sample. In contrast, the fraction of low-mass passive and PSB galaxies, which is very low at $z > 1.5$, rises in dense environments towards lower redshifts, while the fraction in the field remains flat. The fractions of passive and PSB galaxies reach values of 20% and 10% in high-density environments by $z = 0.5$, respectively. Within the star-forming population (SF1, SF2 and SF3 galaxies; of decreasing SSFR), Figure 6.8 shows that at $M_* < 10^{10.3}\mathrm{M}_{\odot}$, the fraction of SF1 galaxies falls rapidly, while the fraction of older SF3 galaxies increases with cosmic time. SF2 is the only population that shows no environmental trend at all at these stellar masses. These results are consistent with our findings on the mass functions from Chapter 4, where we focused on the environmental dependence of the mass

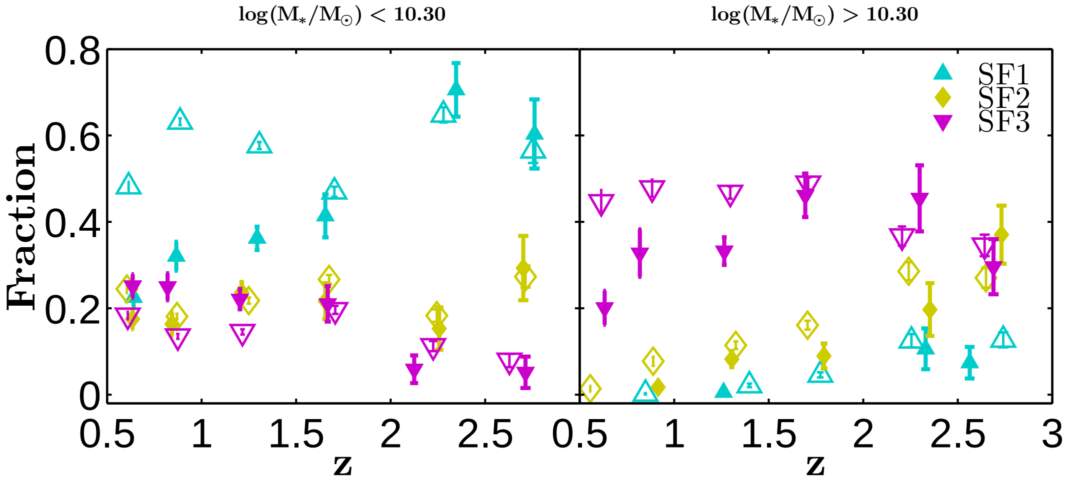

Figure 6.8. Redshift evolution of the fraction of SF1 (cyan triangles), SF2 (yellow diamonds) and SF3 (magenta inverted triangles) galaxies as a function of environment. Filled symbols correspond to dense environments, while open symbols represent the field environment.

function at $z < 1.0$. In that chapter, we found an enhancement of low-mass galaxies belonging to the passive, PSB and SF3 galaxy populations in clusters with respect to the field, whilst SF1 galaxies are strongly depleted.

Let us now consider the results for massive galaxies. The right-hand panel of Figure 6.7 reveals much stronger trends with both redshift and environment than observed for low-mass galaxies. The fraction of passive galaxies, which is nearly zero at $z > 2.5$, rises steadily with cosmic time. However, from the onset, the increase rate in dense environments is higher than in the field, so that by $z \sim 0.5$ the fraction of massive passive galaxies in dense environments is approximately 0.7, while it is only 0.4 in the field. In contrast, the overall number of massive star-forming galaxies declines with cosmic time, from about 60% at $z = 2, 5$ to 20% at $z = 0.5$. The effects of environment, however, become significant only at $z \lesssim 1.5$, giving rise to an almost 20% deficit of the fraction of star-forming galaxies in dense environments with respect to the field sample. With respect to PSB galaxies, we observe no environmental dependence of the massive PSB fraction. Nevertheless, its fraction declines steadily with evolving redshift, which mimics the general trends of the star-forming population. The fraction of massive PSB galaxies decreases from 10% of the total population at $z \sim 2.5$ to being practically negligible at low redshift. For the star-forming sub-populations, the right-hand panel of Figure 6.8 reveals that the fraction of massive SF3 galaxies in the field remains roughly constant through redshift. In contrast, the SF3 fraction in dense environments appears to be strongly depleted since $z = 1.5$, leading to a 20% discrepancy between the two environments. For the SF1 and SF2 populations, we find no evident environmental trends, their fractions are monotonically decreasing as a function of redshift. Therefore, the deficit of massive star-forming galaxies in clusters at $z < 1.5$ (see Figure 6.7), seems to be entirely driven by SF3 galaxies (star-forming galaxies with low SSFR). Finally, we note that the decay rate of SF1, SF2 and PSB galaxies is similar, this may suggest that high redshift PSB galaxies are descendants of massive SF1 and SF2 galaxies.

In summary, we find that environmental quenching becomes important at $z \leq 1.5$, and observe a notable shift in the preferentially-quenched population in dense environments as a function of stellar mass. At $z < 1.5$ we find that for galaxies with $M_* < 10^{10.3}\mathrm{M}_\odot$, it is galaxies with high SSFRs (SF1) which are strongly depleted in dense environments. In contrast, for more massive galaxies ($M_* > 10^{10.3}\mathrm{M}_\odot$) it is the SF3 population (low SSFR but high SFR) which are more strongly depleted in high-density regimes. Finally, we find that the fraction of low-mass PSB galaxies correlates with environment at $z < 1.5$, whilst the massive PSB population does not seem to depend on environment. This suggests that environmental quenching is important for rapid quenching at low masses at $z < 1.5$, but at higher mass an alternative mechanism is responsible for producing PSB galaxies.

6.4.4 The evolution of the low-mass end of the mass function as a function of redshift

In the previous section, we demonstrated that environmental quenching was particularly important in the low-mass regime. To build on these results, in this section, we study the evolution of the Schechter parameter α, also known as the faint-end slope parameter, as a function of galaxy population, redshift and environment. Being one of the parameters used to characterise the stellar mass function, the value of α contains fundamental information intrinsic to the galaxy population. In particular, the faint-end slope tells us about how much a galaxy population is dominated by low-mass galaxies. For example, for a population with $\alpha < 0$, most galaxies have stellar masses below the typical mass parameter M^*, whilst a population with $\alpha > 0$ is dominated by massive galaxies with masses above M^*. However, a drawback of using the low-mass end slope is its strong dependence on the mass limit of the sample. As mentioned previously, our stellar mass limit is redshift dependent. This means that as redshift increases the constraint on the α value weakens. Nevertheless, thanks to the careful fitting method employed (described below), we expect to be able to include this uncertainty in the errorbars presented in Figure 6.9.

For each population and environment, we construct mass functions at different redshifts using a similar procedure to that described in Section 6.4.1. Figure 6.9 shows the resultant values of α, where blue, red and green colours represent the star-forming, passive and PSB population respectively. Additionally, open symbols represent low-density environments while filled ones represent overdense environments. The errors are derived from the MCMC fitting method used to fit Schechter functions.

For the passive and star-forming populations, we observe that the typical α values do not change significantly with redshift. Field star-forming galaxies have a constant $\alpha = -1.5$ throughout the redshift range studied. The star-forming population in dense environments is also constant at $\alpha \sim -1,5$ but presents systematically higher α values than in the field at $z < 2.0$. Similarly, the passive population has $\alpha \sim 1$ at $z > 1$ regardless of density; however, the value of α drops at lower redshifts. This drop is more significant in dense environments, where the slope decreases to $\alpha = 0$. Finally, PSB galaxies present a strongly decreasing α value as a function of cosmic time. At high redshift ($z > 2.0$) the PSB population has high α values which are consistent with those of the passive population at the same redshift. However, α drops quickly with cosmic time and becomes consistent with the star-forming population by $z \sim 1.0$. This indicates that the nature of galaxies within the PSB population changes between $1.0 < z < 2.0$. From looking like the passive population at $z > 1.5$, to looking like the star-forming one (at $z < 1.5$), according to the α values. We find consistent results looking at the mass function as a whole (Figure 6.1).

Figure 6.9 also suggests that the change occurs first in dense environments ($z > 1.5$) and then in the field at later times. However, this result is uncertain due to it being drawn from just one redshift bin.

In summary, we find evidence suggesting that PSB galaxies originate through different processes at high and low redshifts, with the $z > 1.5$ population having typical α values similar to those of the passive population, while $z < 1.5$ PSB galaxies have α values as low, or lower, as the star-forming population. These results are consistent with previous work on PSB galaxies (e.g. Wild et al. 2016; Maltby et al. 2018).

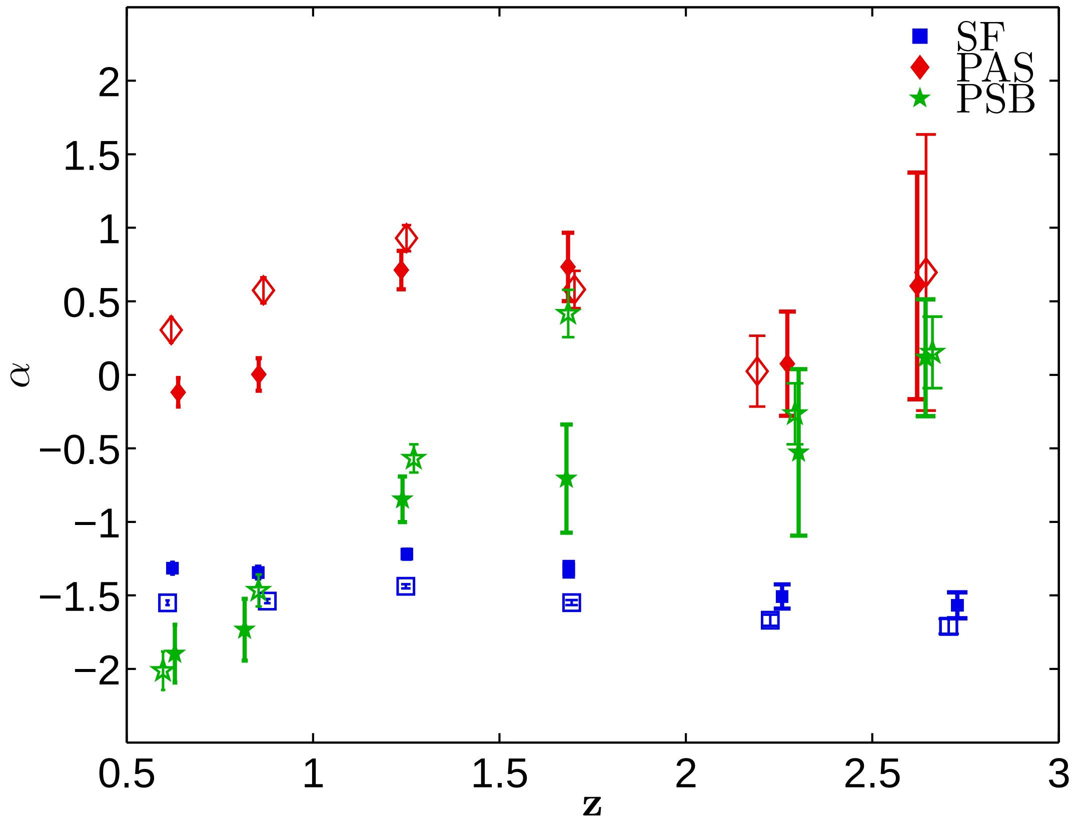

Figure 6.9. Redshift evolution of the low-mass slope (α) of the mass function. Each population, SF (blue), PAS (red) and PSB (green) is separated by environment into high-density (filled symbols) and low-density (open symbols).

6.5 Discussion

6.5.1 The mass dependence of environmental quenching

At $z < 1.0$, Peng et al. (2010) showed that the star formation activity of a galaxy is a function of both stellar mass and environment, a result which we also confirm in this chapter. However, in their paper they propose that these two processes are independent from each other, but we find some evidence suggesting that they probably are interconnected. To first order, mass and environmental quenching seem to be independent from each other. This is because the environmental trends for massive galaxies are approximately identical to the low-mass ones with an offset along the y-axis (see Figures 6.4, 6.5 and 6.6). However, in Section 6.4.3 we described how more massive galaxies seem to feel the effect of environment at lower overdensity levels (i.e. SSFR, SFR drop and quenched fraction rises). In contrast, low-mass galaxies seemed to require higher densities in order to have their star formation properties affected. Furthermore, we find that this difference between high- and low-mass galaxies is present since redshift $z = 2.0$.

Now let us discuss the potential reasons for these observed trends. We note though that while we try to explore the many different scenarios that could lead to the observed results, there might be alternative explanations that we have missed. The first scenario we consider is the existence of several environmental processes acting simultaneously in dense environments. Given that low-mass galaxies are only affected at high overdensity levels, we hypothesise that these galaxies are being quenched through processes associated with ram-pressure stripping. This is the obvious candidate given that ram-pressure is expected to quench low-mass galaxies more efficiently and has to occur in an environment that is dense enough to have developed a hot and dense ICM/IGrM. Some candidate mechanisms include ram-pressure stripping of the cold gas disc (Gunn & Gott 1972) or strangulation (Larson 1974). On the other hand, massive galaxies in very high density environments will also experience these same processes. However, on top of this, massive galaxies may be experiencing an enhanced amount of merging as mergers are more frequent in dense environments (Papovich et al. 2012; Rudnick et al. 2012; Lotz et al. 2013), given the close proximity of many galaxies. Furthermore, the merger probability is mass-dependent (Patton & Atfield 2008; Xu et al. 2012) being higher for massive galaxies. Consequently, if mergers are responsible for part of the environmental quenching we observe, stellar mass may also play a role. Furthermore, mergers prefer moderate overdensities as they are known to be rare in very dense cluster core environments where the high galaxy velocity dispersion make mergers very improbable. Nevertheless, cluster outskirts, galaxy groups and most overdensities at $z > 1$ are ideal environments for merging, given the combination of a high concentration of galaxies with low velocity dispersions.

Another plausible scenario consists of some secular processes being stronger in massive galaxies, which may assist the quenching of a galaxy that is simultaneously experiencing the effect of its environment. These two processes may be too weak or slow to quench a galaxy on their own, nonetheless, acting together they might join forces and have a more dramatic impact. For example, ram-pressure stripping on its own may only succeed in quenching low-mass galaxies in the densest environments. However, a small amount of ram-pressure would be enough to deprive any galaxy of its hot gas reservoir. Massive galaxies tend to have higher SFRs and stronger AGN feedback than low-mass galaxies, this could cause them to run out of gas prematurely (similar scenario to the one we put forward in Chapter 5 to explain the rapid quenching of low-mass PSB galaxies at $z < 1.0$).

Finally, we acknowledge the possibility that massive galaxies formed earlier on in denser environments, which means they have been there longer and, therefore, had more time to evolve and quench. In contrast, the low-mass population mostly consists of satellites that quench as they are accreted into the densest environments.

We conclude that the most likely explanation to our results is that mass and environmental quenching are not completely independent from each other. Higher environmental quenching efficiencies for massive galaxies, as well as more efficient mass quenching in dense environments, have been reported in previous published work (e.g. Darvish et al. 2016; Kawinwanichakij et al. 2017). This mass dependence of environmental quenching may be driven by galaxy mergers (Darvish et al. 2016) or secular processes coupled with environment (similar to 'overconsumption'; McGee et al. 2014).

6.5.2 The evolution of environmental quenching

In this chapter, one of our goals was to investigate the evolution of environmental quenching and try to identify the epoch at which it becomes established. Throughout Sections 6.4.2–6.4.4, we have found various correlations with environment at all redshifts studied, although most of them weaken or disappear towards high redshifts ($z > 2.0$). We found that the passive fraction, median SSFR and median SFR correlate with environmental density up to $z = 2.0$.

We have also studied the evolution in the fraction of various galaxy types (star-forming, passive and PSB) with redshift for different environments. From these analyses, we report that at $z < 1.5$ star-forming galaxies are depleted in dense environments, while passive galaxies are enhanced (see Figure 6.7). The overall trends for star-forming and passive populations do not seem to be significantly dependent on stellar mass. Nevertheless, the redshift at which environment starts showing an effect is significantly higher for more massive galaxies. This could suggest a stellar mass downsizing effect with redshift, i.e. the same environmental mechanism acts consistently through cosmic time; however, as a result massive galaxies quench earlier on, followed by low-mass galaxies at lower redshift. Furthermore, if we analyse the star-forming population in more detail (i.e. the SF1/SF2/SF3 sub-populations), we observe that the galaxies experiencing quenching have different star-formation properties depending on their mass. This suggests that there might be more than one quenching mechanism which depends on stellar mass. For galaxies with $\log(M_*/\mathrm{M}_\odot) < 10.3$, we find a strong depletion of galaxies with high SSFR (SF1 galaxies) in dense environments, while star-forming galaxies with low SSFR (SF3 galaxies) are enhanced. This result was partly presented in Chapter 4, but here we use the new data to show that the result holds to higher redshifts and see that this trend is already in place at least by $z = 1.5$. In contrast, in the case of galaxies with $\log(M_*/\mathrm{M}_\odot) > 10.3$ we see that SF3 galaxies are strongly depleted in dense environments since $z \sim 1.75$, while the rest of the star-forming population shows no significant environmental trends.

To understand these results, we need to consider that the SF3 population corresponds to the star-forming population with the lowest SSFR. However, they also tend to be the most massive of the star-forming galaxies as well, hence, they have the highest median SFRs ($\mathrm{SFR_{SF3}} = 4.7\ \mathrm{M_\odot yr^{-1}}$ compared to $\mathrm{SFR_{SF1}} = 2.5\ \mathrm{M_\odot yr^{-1}}$ and $\mathrm{SFR_{SF2}} = 2.9\ \mathrm{M_\odot yr^{-1}}$). Taking this into consideration, it is possible that these high-mass SF3 galaxies consume their gas in shorter timescales via star formation, once they stop accreting gas from the surrounding due to the effect of environment. Alternatively, we cannot reject the hypothesis that this population of massive SF3 galaxies might be quenched through major mergers or AGN feedback.

6.5.3 The changing face of post-starburst galaxies

In this chapter, most of our results point towards PSB galaxies being fundamentally different in nature above and below $z \sim 1.5$. Figures 6.1 and 6.9 show how much the PSB stellar mass function changes across redshift, with high-redshift PSB galaxies being typically massive ($M_* > 10^{10.3}\mathrm{M}_\odot$), whilst the low-redshift counterparts being predominantly of low-mass. We therefore confirm the results from Wild et al. (2016), extending the study to $z > 2.0$ and lower stellar masses.

Considering the fraction of PSB galaxies as a function of redshift (Figure 6.7), we found that low-mass PSB galaxies present a strong environmental dependence at $z < 1.5$, being ubiquitous in dense environments. This is consistent with the rapid environmental quenching process we describe in Chapters 4 and 5. In contrast, high-mass PSB galaxies show no environmental dependence across redshifts and their fraction simply drops with cosmic time, in a trend similar to those followed by massive SF1 and SF2 galaxies. This might imply that high-mass PSB galaxies are the descendants of star-forming galaxies with moderate to high SSFRs. Nevertheless, we lack the ability to constrain the exact mechanisms in action.

Finally, from a study of their mass functions, Figure 6.9 demonstrates that the high-redshift PSB galaxies have α values that are consistent with those of the passive population, in contrast, low-redshift PSB galaxies are consistent with the star-forming population. The role of environment also seems to be key in the transformation of low-mass PSB galaxies with cosmic time. However, Figure 6.9 suggests that the field PSB population also experiences the downsizing effect we attribute to environmental quenching. We think this could be produced by an increasing amount of pre-processing towards low redshift. The increasing number of smaller galaxy groups may be causing the fraction of low-mass PSB galaxies to rise in intermediate-density environments, which might decrease the corresponding value of α.

Taken together, these results suggest that PSB galaxies have different formation mechanisms as a function of stellar mass. The observed redshift evolution is driven by the change in the relative abundance of low and high-mass PSB galaxies as a function of cosmic time; given the stellar mass, one can infer the formation scenario regardless of redshift. Massive PSB galaxies, more abundant at high redshifts, do not depend on the environment. In contrast, low-mass PSB galaxies appear at lower redshifts and present strong trends with environment.

Analysing our result in the context of previous studies will provide a more complete view on the origins of PSB galaxies across redshift. For example, some studies on the structure of these galaxies have revealed that massive PSB galaxies are compact (at $z > 1.0$; Almaini et al. 2017) and have higher Sérsic index values ($0.5 < z < 2.0$; Maltby et al. 2018), therefore, they might have undergone a compaction event. These studies suggest that an external process, such as gas-rich major mergers, or a secular one, like disc instability, may lead to the observed compact remnants.

In contrast, low-mass PSB galaxies present more disc-dominated morphologies (Maltby et al. 2018 and Chapter 5), consistent with a faded disc. This implies that their formation mechanism does not destroy the galaxy disc. We also know that PSB galaxies need to be rapidly and recently quenched. These constraints point towards more gentle gas removal processes such as ram-pressure stripping or overconsumption, although minor mergers may also be considered.

Our results place the transition in the dominant PSB type at $1.0 < z < 2.0$. Above this redshift the PSB population is dominated by massive galaxies with properties rather similar to the passive population and below PSB galaxies are predominantly low-mass. However, during this transition period both types of PSB galaxies probably coexisted with similar contributions.

6.5.4 The reversal of the SF–density relation at $z > 2.0$

At low redshifts ($z < 1.0$), the star formation–density relation is well established, where galaxies in high-density environments are generally found to have lower SFRs and SSFRs than their counterparts in the field (Balogh et al. 2004; Kauffmann et al. 2004; Baldry et al. 2006). However, at $z \gtrsim 1$ there are currently conflicting results on the nature of this relation. Some studies find that at $z \sim 1$ galaxies follow the local trends (Patel et al. 2009; Muzzin et al. 2012), while others report that the local trends weaken or disappear (Grützbauch et al. 2011; Scoville et al. 2013). In complete contrast, some studies have even reported a reversal of the star formation–density relation from that observed locally (Elbaz et al. 2007; Cooper et al. 2008; Welikala et al. 2016). We note, however, that some of the latter are based on optically-selected samples, which may lead to a bias against passive galaxies at high redshift.

In this thesis, we find no evidence for a reversal of the star formation–density relation at $z = 1.0$, in fact we find that the same trend found at low redshift persists out until $z = 2.0$ (see Section 6.4.2). This is consistent with the work by Chuter et al. (2011), where they confirmed there is no reversal to at least $z \sim 1.5$. However, we do find a hint of a reversal in the star formation–density relation for galaxies with stellar masses $< 10^{10.3}\mathrm{M}_{\odot}$ at $z > 2.0$. The average SFR appears slightly enhanced, by almost 0.5 dex at the highest densities [$\log(1 + \delta) > 0.75$], with respect to the value measured at low densities. This would place the reversal of the star formation–density relation at higher redshift than the typical value reported by those who find a reversal ($z \sim 1$; Elbaz et al. 2007; Cooper et al. 2008). However, note that the result presented in this chapter is only tentative, and therefore worthy of further exploration in future studies.

6.6 Conclusions

In this chapter we have presented a preliminary study of galaxy evolution as a function of galaxy type, stellar mass and environment across a broad redshift range ($0.5 < z < 3.0$) using the extremely deep data from the UDS DR11. First, we showed the redshift evolution of the stellar mass function of star-forming, quiescent and PSB galaxies. This allowed us to visualise the rapid build up of the red sequence with cosmic time, as well as the mass downsizing that the passive population experiences since $z \sim 1.5$. Moreover, we also observe the complete transformation of the PSB mass function. At $z > 1.5$ PSB galaxies are dominated by massive galaxies, while at lower redshifts low-mass PSB galaxies vastly outnumber the massive ones.

We then explored various environmental correlations, and the dependency of our mass functions on environment at $0.5 < z < 3.0$, using an environmental density measure based on galaxy number density. We list our main findings below:

1. The star formation properties of galaxies (including passive fraction, median SSFR and SFR) are strongly correlated with local density until $z = 2.0$. The passive fraction increases with density, whilst both SSFR and SFR decrease. All these trends weaken towards higher redshifts and potentially disappear by $z > 2.0$. Furthermore, we also find that these environmental trends depend on stellar mass. We find that the star formation properties of galaxies with $M_{*} < 10^{10.3}\mathrm{M}_{\odot}$ are only affected at relatively high overdensity values. In contrast, more massive galaxies seem to be more sensitive to the effect of

environment, with a progressive decline in their SSFRs/SFRs beginning from low densities. Finally, we find some evidence for a reversal of the SFR–density relation at $z > 2.0$. A marginal enhancement of the median SFR of galaxies with $M_* < 10^{10.3}\mathrm{M}_\odot$ in the densest environments is detected in this particular redshift bin.

2. We find evidence suggesting environmental quenching begins to become important at $z \lesssim 1.75$ and also acts differently on galaxies depending on their stellar mass. We see that at low stellar masses environment preferentially quenches star-forming galaxies with high SSFRs but not so high SFR (the SF1 population), while at high stellar masses, environment strongly depletes the numbers of galaxies with high SFRs but low SSFRs (the SF3 galaxies). Furthermore, we also see that the fraction of low-mass SF3 galaxies is enhanced in dense environments, an effect we attribute to the 'slow environmental quenching' introduced in Chapter 4.

3. The deep DR11 catalogue used in this chapter, allows us to probe the environmental quenching of low-mass galaxies (studied in Chapter 4 at $z \leq 1.0$) to higher redshifts. This reveals that the effect of the environment on these galaxies persists until $z \sim 1.5$, which is potentially the redshift at which this kind of environmental quenching first appears.

4. The PSB population shows a distinctive redshift evolution. However, it appears this evolution is mainly driven by stellar mass, which dictates the evolutionary pathway that led them to the PSB phase. Massive PSB galaxies are common at higher redshifts and show no environmental dependence. In contrast, low-mass PSB galaxies are much more abundant at intermediate redshifts $0.5 < z < 1.5$ and are ubiquitous in dense environments, such as galaxy clusters. The redshift evolution observed is driven by the change in the ratio of high-mass to low-mass PSB galaxies as a function of redshift, which also means that both types can coexist, perhaps at intermediate redshifts.

In summary, we report strong correlations between galaxy properties and environment up to redshift $z = 2.0$. Moreover, we show evidence that these correlations with local density are also dependent on stellar mass. This may imply that the effects of mass and environment are entangled to some extent.

Chapter 7

Conclusions and future work

The primary aim of this thesis is to investigate the effect of environment on galaxy evolution within the redshift range $0.5 < z < 3.0$, using the photometric data from the two most recent UDS data releases (DR8 and DR11). In order to accomplish this we have studied the effect of galaxy environment on different galaxy populations (passive, star-forming and post-starburst) using mainly the stellar mass function and galaxy structure. In Chapter 1, we set the scene for our work by discussing our current knowledge on the topic of galaxy evolution and environmental correlations based on the previous work in this field. We then described the UDS survey and the catalogues we use throughout this thesis in Chapter 2. In Chapter 3 we reviewed the most frequently used methods for measuring galaxy environment in photometric surveys, after which we described our adopted cluster finder, which is based on a friends-of-friends algorithm, together with the corresponding tests and optimisation we carried out. Using our environmental measures, we then studied the stellar mass functions and galaxy structure, and how they correlate with environment (in Chapters 4 and 5) using the DR8 data. Finally, we extended the analysis of the stellar mass function and various correlations with environment (passive fraction, SFR and SSFR) to higher redshift ($z < 3.0$) and lower stellar mass thanks to the deeper DR11 data. In this chapter we summarise our work and discuss the main conclusions of this thesis, as well as explore some directions in which this work could be taken in the future.

7.1 The role of environmental quenching

In Chapter 4 we studied the stellar mass functions of star-forming, passive and PSB galaxies as a function of whether they inhabit a cluster or field environment at $0.5 < z < 1.0$. This revealed an enhancement of low-mass evolved galaxies within cluster environments, including quiescent and PSB galaxies but also low-SSFR star-forming galaxies (SF3). Simultaneously, we also observed a strong depletion of the star-forming populations with high SSFRs in dense environments with respect to the field. These strong environmental correlations suggest that environment is responsible for lowering the SSFR of low-mass star-forming galaxies as they are accreted into a cluster/group. Furthermore, we observe that the characteristic shape of the cluster PSB mass function, with a sharp up-turn at the low-mass end (see Figure 4.3), can only be reproduced by a rapid quenching of a significant fraction of the galaxy population with the highest SSFRs (SF1). However, another scenario is required to explain the observed excess of SF3 galaxies in clusters. In this case, such an excess is more likely to be driven by the slower environmental quenching of a population of galaxies with intermediate SSFRs (SF2). Consequently, we conclude that these trends are produced by two different types of environmental quenching acting simultaneously at $0.5 < z < 1.0$.

The first environmental quenching pathway corresponds to what we call 'rapid' environmental quenching, which causes the quenching of galaxies with high SSFRs (SF1) as they enter a cluster, triggering a PSB phase. This quenching must be rapid given that the fraction of SF1 galaxies shows a strong radial gradient, decreasing rapidly towards the central region of clusters. Such a radial trend implies that these SF1 galaxies are rapidly quenched in the initial infall towards the centre of the cluster, and therefore do not reach very small radii. Hence, the quenching must take place in less than the dynamical time of the cluster ($<$ 1 Gyr). In Chapter 5 we explored further this rapid environmental quenching mode by studying the structure of PSB galaxies and their progenitors, SF1 galaxies. We found that those SF1 galaxies that survive the initial cluster infall and remain for a longer time in the cluster environment have on average larger effective radii than those found in the field. This suggests that rapid quenching preferentially affects compact SF1 galaxies, i.e. those with smaller sizes for a given stellar mass, transforming them into PSB galaxies. In addition, the size and Sérsic indices of these compact SF1 galaxies matches those of the cluster PSB population, implying that rapid environmental quenching does not trigger significant structural changes during the transition from SF1 to PSB. Based on these results we put forward a model in which compact SF1 galaxies host stronger star-formation driven galactic-scale outflows, due to their higher star formation rate surface density. Upon cluster infall, we propose that these compact SF1 galaxies have their circumgalactic medium (CGM) removed via the ram-pressure exerted by the hot intra-cluster/group medium (ICM/IGrM). When this happens, the intense outflows may cause these galaxies to run out of fuel on shorter timescales than their more extended counterparts. We test this scenario towards the end of Chapter 5 using the stacked spectra of SF1 galaxies below (compact) and above (extended) the SF1 stellar mass–size relation. This yields evidence supporting stronger outflows for the compact population, which were measured using the blueshift of the MgII absorption feature.

The second environmental quenching pathway corresponds to 'slow' environmental quenching. We have seen that this mode is responsible for accelerating the drop in SSFR some star-forming galaxies experience in dense environments, triggering the transition of the SF2 population to SF3. We call it 'slow' because the affected population, SF2, shows a flat cluster-centric radial profile, suggesting that the quenching takes place on a longer timescale than the cluster dynamical time. Therefore, galaxies have time to orbit about the centre of the cluster before quenching, erasing any radial trend. This process, thought to affect galaxies with more moderate SSFRs or even the extended SF1 population, is consistent with environmental mechanisms such as galaxy strangulation, harassment or minor mergers; which are believed to quench star-formation in galaxies on timescales of several Gyrs.

In Chapter 6 we extended the study of environmental quenching to higher redshifts ($1.0 < z < 3.0$). This reveals that the star-formation properties (such as passive fraction or median SFR and SSFR) of low-mass galaxies ($M_* < 10^{10.3}\mathrm{M}_\odot$) are correlated with environment until $z \sim 1.5$, the redshift at which the environmental trends no longer persist in our data. That being said, we also find some evidence for a reversal of the SFR–density relation at $z \geq 2.0$, where the median

SFR of low-mass galaxies increases towards the highest density regime. Although tentative, this is an exciting result worthy of further exploration in future work.

In Chapters 4 and 5 we focused on the effects of environment on the build-up of the low-mass end of the red sequence at $z < 1.0$. However, in Chapter 6 we do not only extend the redshift range studied but also study the environmental dependence of galaxy properties across the full stellar mass range, and extend our analysis to higher mass galaxies. This leads to some observed differences between the properties of environmental quenching at high and low stellar masses (with the demarkation between the two chosen to be $M_* = 10^{10.3}\mathrm{M}_\odot$).

Regarding the massive end of the galaxy population, we find that properties such as the passive fraction, the median SFR and the median SSFR correlate with environmental density until $z \sim 2.0$. In contrast with what we found for low-mass galaxies, which are relatively unaffected by their environment until a 'critical' density value beyond which their SFR and SSFR quickly drop, for massive galaxies the dependence on environment is smoother, and presents a gradual decline of the median SFR and SSFR from lower overdensity values. This seems to suggest that massive galaxies are more sensitive to their environment than their low-mass counterparts at the same epoch. Finally, even though the trends of low-mass galaxies with environment in Chapter 6 are consistent with those found in Chapter 4, i.e. enhanced PSB and SF3 population and depleted SF1 population in dense environments; we find that this is not true at the high-mass end. Using the deeper DR11 data, we find that the population of massive SF3 galaxies is depleted in dense environments with respect to the field. In contrast, the SF1, SF2 and PSB populations show no correlation with environment at high stellar masses. It is important to note that most massive star-forming galaxies belong to the SF3 population, and that they have, on average, the highest SFR. We therefore propose that this trend is driven by the combined effect of secular and environmental processes, which may join forces to quench galaxies more efficiently. This model poses a likely scenario because massive galaxies are known to have stronger internal processes, such as AGN feedback or higher SFRs, which could lead to newly infalling galaxies running out of fuel relatively quickly after the cosmic accretion of new gas has been halted by the presence of a hot ICM/IGrM.

7.2 The connection between environmental and mass quenching

At present, the idea that mass is the main parameter determining the evolution of galaxies at all redshifts, with environmental quenching only kicking in at lower redshifts as a completely independent process, is quite established. Our results fit well into this paradigm, as we find correlations with environment since $z \sim 2.0$ but not at earlier times. Additionally, we also find that these environmental trends build up with cosmic time. At earlier epochs ($z > 2.0$) the existence of quenched galaxies is most likely linked to mass quenching or merging, as the dense environments required for environmental quenching would probably not have had time to develop and in turn affect their galaxy populations.

However, despite this, one key result of this thesis is the apparent connection between environmental and mass quenching processes at $z < 2.0$. In Chapter 5, we found evidence for this phenomenon at low stellar masses: compact star-forming galaxies being preferentially quenched in dense environments potentially due to the combined effect of ram-pressure stripping and strong stellar feedback. We also found evidence of this phenomenon at the high-mass end in Chapter 6: star-forming galaxies with $M_* > 10^{10.3}\mathrm{M}_\odot$ being more sensitive to their environment than their low-mass counterparts. We conclude that even though the mechanisms responsible for environmental and mass quenching are independent from each other, their effects can overlap, interfere and enhance each other. Based on our findings, we suggest that when both environmental and secular processes occur in conjunction (i.e. at the same time), their potential to quench a galaxy is much larger than if they were acting separately. This implies that environmental and mass quenching are interconnected and provides an explanation as to why galaxies with potentially stronger internal processes (e.g. compact or massive galaxies) seem to quench faster or be more affected by their environment.

Finally, we note that the potential connection between environmental and mass quenching is not a new discovery, as some external processes are known to depend on internal properties, e.g. mergers are more common between massive galaxies (Patton & Atfield 2008). Additionally, an increasing number of studies are finding enhanced mass quenching efficiencies in dense environments or the converse, higher environmental quenching efficiencies for massive galaxies (see Darvish et al. 2015, 2016; Kawinwanichakij et al. 2017, for some examples). Therefore, it seems clear that the '*nature*' vs '*nurture*' formalism often portrayed is a gross oversimplification of reality, with the two contenders coexisting and interacting with each other. It has also been proven by numerous studies that both processes are important, especially at low redshifts. However, the critical question to be answered is what is the exact interplay between environmental and secular processes, and how do these influence galaxy evolution as a whole.

7.3 The evolving nature of post-starburst galaxies

Throughout this thesis we have used PSB galaxies as a tool to study environmental quenching. In the process, we have also gained significant insight into this elusive galaxy population. In this work, we use a sample of photometrically selected PSB galaxies adopting a PCA classification applied to the UDS broadband photometry (see Chapter 2 for details). As we discussed in Section 2.2.2, the nature of this sample is slightly different from the classic definition of post-starburst galaxies. In the PCA method, PSB galaxies are selected as galaxies that have undergone a rapid and recent truncation of their star formation, which produces the strong Balmer absorption features in their spectra. Therefore, our PSB sample is more consistent with 'k+a' galaxies, which of course include the subset of classic post-starburst galaxies which quenched after a starburst.

Regarding the general properties of the PSB population across the redshift range $0.5 < z < 3.0$, we observe a strong apparent evolution with redshift (see Figure 6.1). At $0.5 < z < 1.5$, PSB galaxies represent about 2.5% of the total galaxy population, while at $1.5 < z < 3.0$ this fraction rises to 7% (evaluated above the corresponding mass limits). However, rather than one population evolving with cosmic time, we find evidence suggesting that there are two types of PSB galaxy (high and low-mass), which originate through different processes. Even though these two types of PSB galaxy are selected in the same way, meaning that they have similar spectral features, we identify at least two distinct populations for which other properties (e.g. stellar mass, environment, structure) differ. One or other of these two populations dominate the overall PSB population at different epochs, therefore, the redshift evolution is partly due to the shift in the prevailing PSB type.

Let us start by describing the properties of low-mass PSB galaxies, the predominant PSB population at $z < 1.5$ (see Figures 6.1 or 7.1). In Chapter 4, we also found that these galaxies tend to reside in galaxy clusters, in contrast with their massive counterparts, which are more abundant in the field. This suggests that low-mass PSB galaxies are produced in clusters, probably through environmental quenching processes. Based on our results in Chapter 4, we conclude that low-mass PSB galaxies originate through the rapid quenching mode (Section 7.1), which takes place in dense environments. In Chapter 5, we also concluded that PSB galaxies are the descendants of compact and low-mass star-forming galaxies with high SSFRs, which underwent a rapid truncation of their star formation as they entered the dense environment regime. In Chapter 5 we also found that these PSB galaxies tend to have disky morphologies, with typical Sérsic indices of $n \sim 1.5$, indicating that they might be fading discs rather than the remnants of a violent event (such as a major merger). In Chapter 4, we also use the stellar mass function in order to estimate the total fraction of low-mass passive galaxies that have gone through the PSB phase during the cosmic time interval corresponding to $0.5 < z < 1.0$ (2.7 Gyrs). This analysis indicates that the duration (or visibility) of the PSB phase is about 800 Myrs, which is consistent with the expected $\lesssim 1$ Gyr that it takes for the dominant A-star population to die out. Finally, we find that between the two main scenarios that lead to a PSB phase, i.e. rapid truncation or starburst-then-quenching, the first is more likely to be the one that applies to our sample of low-mass PSB galaxies. From stellar population synthesis models (presented in Chapter 4) we know that when a galaxy undergoes a significant starburst, the amplitude of the second principal component (SC2) increases significantly. In contrast, if a galaxy is star forming for an extended period of time, and then has its star formation suddenly truncated, the SC2 value does not increase as much. In this work, we find that all our cluster PSB galaxies at $0.5 < z < 1.0$ have relatively low SC2 values, while PSBs with higher SC2 values exist in the field. As a consequence we conclude that they probably did not experience a major starburst prior to quenching, and were simply quenched on a rapid timescale.

In contrast to low-mass PSB galaxies, their massive counterparts are far more abundant at high redshift ($z > 1.5$), and show no environmental dependence at any epoch. Consequently, we infer that these galaxies might have their star-formation truncated via internal processes, such as AGN or stellar feedback. Additionally, some studies have found that massive PSB galaxies at $z > 1.0$ are very compact, with high Sérsic index values, which might indicate that the strong feedback was initially triggered through major mergers or disc collapse.

7.4 Future work

In this final section, we consider a number of potential directions in which this work could be extended in the future.

One avenue that could be explored in the short term would be to test our current fast-quenching model. This would involve looking for outflow signatures in field compact SF1 galaxies, and comparing them to more extended ones. We could do this with the current generation of integral field spectrographs, such as the Multi Unit Spectroscopic Explorer (MUSE) instrument, mounted on the ESO VLT. High quality

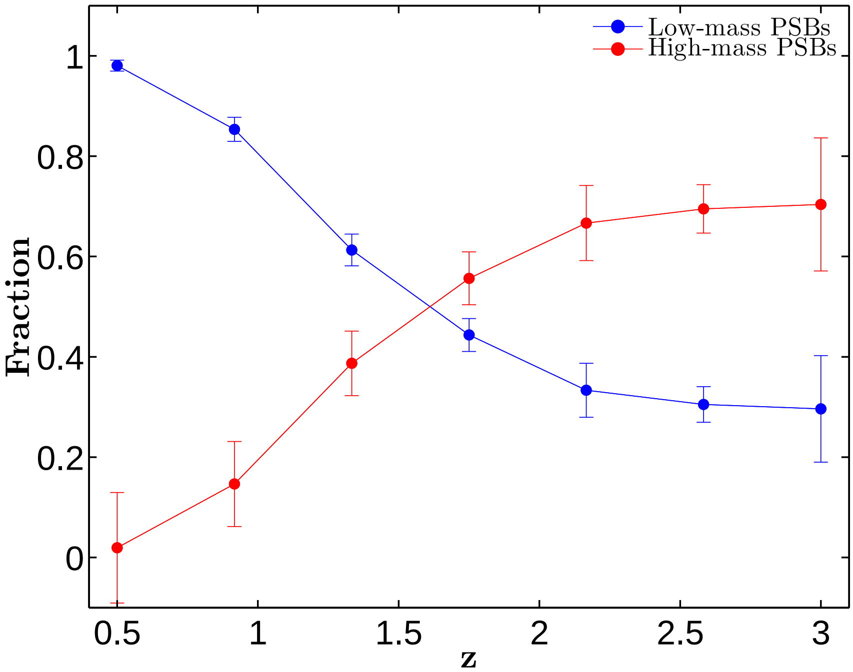

Figure 7.1. The redshift evolution of the fraction of PSB galaxies that exhibit high mass ($M_* > 10^{10.3}\mathrm{M}_\odot$; in red) and low mass ($M_* < 10^{10.3}\mathrm{M}_\odot$; in blue). This diagram shows how the fraction of massive PSB galaxies decreases with cosmic time, while the fraction of low-mass PSB galaxies increases. The crossover takes place at roughly $z = 1.5$.

Integral Field Unit (IFU) data would allow us to search for blue-shifted absorption features (e.g. [MgII]) marking the presence of galactic outflows. Furthermore, the use of MUSE in narrow field mode (NFM; with a field of view of 7.5×7.5 arcsec^2) would provide exquisite spatial resolution, which would be extremely beneficial, potentially allowing us to see which part of the galaxy the outflows are originating from. Acquiring IFU data would be still extremely useful even if the presence of outflows in compact SF1 galaxies turns out to be negative. For example, it would let us see whether the star formation is occurring globally or if it is localised in a certain region of the galaxy. If the star formation is localised in the core, it would suggest that the galaxy has undergone some process that has induced the collapse of the gas towards the central region. If, in contrast, star formation appears enhanced in the outskirts of the galaxy, it could imply that some process like ram-pressure is compressing the gas. Similarly, IFU spectroscopy would also allow us to look for signs of quenching, potentially showing whether quenching proceeds inside-out, outside-in or if it is a global process. This would be an exciting but challenging prospect for future work, considering the target galaxies are extremely faint and small galaxies at high redshifts $z \sim 1.0$.

Another option to test our ‘overconsumption’ scenario is to map the distribution of molecular gas around PSB or SF1 galaxies. The small size of these galaxies and the resolution needed in order to extract useful information requires observations with the Atacama Large Millimetre/submillimetre Array (ALMA). In the short-term, there are a number of galaxies with ALMA observations in the UDS field. Initially, we would like to go over these data and see how many of our target low-mass PSB and SF1 galaxies there are. This is a good starting point, however, it is unlikely that there will be many. Therefore, further observations targeting this particular population may be needed.

Our aim with ALMA is to analyse the presence of neutral gas within these galaxies. Our model suggests that the gas might be expelled from the disc plane through galactic-scale outflows. Therefore, we would look for H_2 tracers (e.g. CO) several arcseconds around the SF1 galaxies and compare between cluster and field galaxies as well as between compact and extended ones. Also investigating the presence of gas in our photometrically-selected low-mass PSB galaxies would be interesting. In principle we do not expect to find it, since we tend to think of our PSB galaxies as a quenched population, however, this has not been done before with the PCA sample. Nonetheless, some studies at low-redshift have found that local PSBs host large molecular gas reservoirs and yet have low SFRs (e.g. Rowlands et al. 2015; French et al. 2015, 2018). Consequently, it would be interesting to see if this is also true for high-redshift PSB galaxies.

In the long-term, obtaining deep spectra of high-redshift PSB galaxies is probably the obvious way to advance the work presented in this thesis. The only way to sample the photometrically selected PSB population to the lowest stellar masses is using the James Webb Space Telescope (JWST), whose launch is currently planned for 2021. JWST will be the first facility to enable obtaining good quality spectra of the low-mass PSB population at $z > 0.5$, key in the understanding of environmental quenching at this epoch, as the work presented here revealed. It will also allow for the reliable detection of PSB galaxies until higher redshifts than ever before.

In summary, there are a number of exciting prospects for the continuation of the work in this field. Despite the significant progress we have made, many more questions remain to be answered. There can be no doubt that this field will remain active for many years to come.

Bibliography

Abadi M. G., Moore B., Bower R. G., 1999, MNRAS, 308, 947

Abbott B. P., Abbott R., Abbott T. D., Abernathy M. R., Acernese F., Ackley K., Adams C., Adams T., Addesso P., Adhikari R. X., et al. 2016, Physical Review Letters, 116, 061102

Abell G. O., 1965, ARA&A, 3, 1

Aceves H., Velázquez H., Cruz F., 2006, MNRAS, 373, 632

Acquaviva V., Gawiser E., Guaita L., 2011, ApJ, 737, 47

Ade P. A. R., Aghanim N., Arnaud M., Ashdown M., Aumont J., Baccigalupi C., Banday A. J., Barreiro R. B., Bartlett J. G., et al. 2016, A&A, 594, A13

Akiyama M., et al., 2015, PASJ, 67, 82

Alatalo K., et al., 2011, ApJ, 735, 88

Alatalo K., et al., 2016, ApJ, 827, 106

Almaini O., Wild V., Maltby D. T., Hartley W. G., Simpson C., Hatch N. A., McLure R. J., Dunlop J. S., Rowlands K., 2017, MNRAS, 472, 1401

Andreon S., 1998, ApJ, 501, 533

Athanassoula E., Rodionov S. A., Peschken N., Lambert J. C., 2016, ApJ, 821, 90

Baldry I. K., Balogh M. L., Bower R. G., Glazebrook K., Nichol R. C., Bamford S. P., Budavari T., 2006, MNRAS, 373, 469

Baldry I. K., et al., 2012, MNRAS, 421, 621

Baldry I. K., Glazebrook K., Brinkmann J., Ivezić Ž., Lupton R. H., Nichol R. C., Szalay A. S., 2004, ApJ, 600, 681

Balogh M., et al., 2004, MNRAS, 348, 1355

Balogh M. L., McGee S. L., Mok A., Muzzin A., van der Burg R. F. J., Bower R. G., Finoguenov A., Hoekstra H., Lidman C., Mulchaey J. S., Noble A., Parker L. C., Tanaka M., Wilman D. J., Webb T., Wilson G., Yee H. K. C., 2016, MNRAS, 456, 4364

Bamford S. P., Milvang-Jensen B., Aragón-Salamanca A., 2007, MNRAS, 378, L6

Bamford S. P., Nichol R. C., Baldry I. K., Land K., Lintott C. J., Schawinski K., Slosar A., Szalay A. S., Thomas D., Torki M., Andreescu D., Edmondson E. M., Miller C. J., Murray P., Raddick M. J., Vandenberg J., 2009, MNRAS, 393, 1324

Barden M., Häußler B., Peng C. Y., McIntosh D. H., Guo Y., 2012, MNRAS, 422, 449

Barton E. J., Geller M. J., Kenyon S. J., 2000, ApJ, 530, 660

Bauer A. E., Conselice C. J., Pérez-González P. G., Grützbauch R., Bluck A. F. L., Buitrago F., Mortlock A., 2011, MNRAS, 417, 289

Bayliss M. B., et al., 2014, ApJ, 794, 12

Bekki K., 1998, ApJ, 502, L133

Bekki K., Couch W. J., Shioya Y., 2002, ApJ, 577, 651

Bell E. F., et al., 2004, ApJ, 608, 752

Bell E. F., et al., 2006, ApJ, 640, 241

Benson A. J., Bower R. G., Frenk C. S., Lacey C. G., Baugh C. M., Cole S., 2003, ApJ, 599, 38

Best P. N., Kaiser C. R., Heckman T. M., Kauffmann G., 2006, MNRAS, 368, L67

Best P. N., Kauffmann G., Heckman T. M., Brinchmann J., Charlot S., Ivezić Ž., White S. D. M., 2005, MNRAS, 362, 25

Birnboim Y., Dekel A., 2003, MNRAS, 345, 349

Blake C., et al., 2004, MNRAS, 355, 713

Blanton M. R., Eisenstein D., Hogg D. W., Schlegel D. J., Brinkmann J., 2005, ApJ, 629, 143

Blanton M. R., et al., 2003, ApJ, 594, 186

Bluck A. F. L., Mendel J. T., Ellison S. L., Patton D. R., Simard L., Henriques B. M. B., Torrey P., Teimoorinia H., Moreno J., Starkenburg E., 2016, MNRAS, 462, 2559

Bolzonella M., et al., 2010, A&A, 524, A76

Bonaventura N. R., Webb T. M. A., Muzzin A., Noble A., Lidman C., Wilson G., Yee H. K. C., Geach J., Hezaveh Y., Shupe D., Surace J., 2017, MNRAS, 469, 1259

Boselli A., Gavazzi G., 2006, PASP, 118, 517

Bothun G. D., Schombert J. M., Impey C. D., Sprayberry D., McGaugh S. S., 1993, AJ, 106, 530

Botzler C. S., Snigula J., Bender R., Hopp U., 2004, MNRAS, 349, 425

Bouché N., Dekel A., Genzel R., Genel S., Cresci G., Förster Schreiber N. M., Shapiro K. L., Davies R. I., Tacconi L., 2010, ApJ, 718, 1001

Bower R. G., Benson A. J., Malbon R., Helly J. C., Frenk C. S., Baugh C. M., Cole S., Lacey C. G., 2006, MNRAS, 370, 645

Bradshaw E. J., Almaini O., Hartley W. G., Chuter R. W., Simpson C., Conselice C. J., Dunlop J. S., McLure R. J., Cirasuolo M., 2011, MNRAS, 415, 2626

Bradshaw E. J., Almaini O., Hartley W. G., Smith K. T., Conselice C. J., Dunlop J. S., Simpson C., Chuter R. W., Cirasuolo M., Foucaud S., McLure R. J., Mortlock A., Pearce H., 2013, MNRAS, 433, 194

Brammer G. B., et al., 2009, ApJ, 706, L173

Brammer G. B., van Dokkum P. G., Coppi P., 2008, ApJ, 686, 1503

Brinchmann J., Charlot S., White S. D. M., Tremonti C., Kauffmann G., Heckman T., Brinkmann J., 2004, MNRAS, 351, 1151

Brodwin M., et al., 2013, ApJ, 779, 138

Brooks A. M., Governato F., Quinn T., Brook C. B., Wadsley J., 2009, ApJ, 694, 396

Bruzual G., Charlot S., 2003, MNRAS, 344, 1000

Buitrago F., Trujillo I., Conselice C. J., Häußler B., 2013, MNRAS, 428, 1460

Byrd G., Valtonen M., 1990, ApJ, 350, 89

Cales S. L., Brotherton M. S., 2015, MNRAS, 449, 2374

Cales S. L., et al., 2011, ApJ, 741, 106

Cappellari M., 2017, MNRAS, 466, 798

Cappellari M., Emsellem E., 2004, PASP, 116, 138

Carollo C. M., et al., 2013, ApJ, 773, 112

Casali M., et al., 2007, A&A, 467, 777

Cassata P., Cimatti A., Kurk J., Rodighiero G., Pozzetti L., Bolzonella M., Daddi E., Mignoli M., Berta S., Dickinson M., Franceschini A., Halliday C., Renzini A., Rosati P., Zamorani G., 2008, A&A, 483, L39

Cebrián M., Trujillo I., 2014, MNRAS, 444, 682

Chabrier G., 2003, PASP, 115, 763

Charlot S., Fall S. M., 2000, ApJ, 539, 718

Chevalier R. A., Clegg A. W., 1985, Nature, 317, 44

Chuter R. W., Almaini O., Hartley W. G., McLure R. J., Dunlop J. S., Foucaud S., Conselice C. J., Simpson C., Cirasuolo M., Bradshaw E. J., 2011, MNRAS, 413, 1678

Cicone C., et al., 2014, A&A, 562, A21

Cirasuolo M., et al., 2007, MNRAS, 380, 585

Cole S., et al., 2001, MNRAS, 326, 255

Conselice C. J., Blackburne J. A., Papovich C., 2005, ApJ, 620, 564

Cooke K. C., O'Dea C. P., Baum S. A., Tremblay G. R., Cox I. G., Gladders M., 2016, ApJ, 833, 224

Cooper M. C., Griffith R. L., Newman J. A., Coil A. L., Davis M., Dutton A. A., Faber S. M., Guhathakurta P., Koo D. C., Lotz J. M., Weiner B. J., Willmer C. N. A., Yan R., 2012, MNRAS, 419, 3018

Cooper M. C., Newman J. A., Coil A. L., Croton D. J., Gerke B. F., Yan R., Davis M., Faber S. M., Guhathakurta P., Koo D. C., Weiner B. J., Willmer C. N. A., 2007, MNRAS, 376, 1445

Cooper M. C., Newman J. A., Madgwick D. S., Gerke B. F., Yan R., Davis M., 2005, ApJ, 634, 833

Cooper M. C., Newman J. A., Weiner B. J., Yan R., Willmer C. N. A., Bundy K., Coil A. L., Conselice C. J., Davis M., Faber S. M., Gerke B. F., Guhathakurta P., Koo D. C., Noeske K. G., 2008, MNRAS, 383, 1058

Couch W. J., Barger A. J., Smail I., Ellis R. S., Sharples R. M., 1998, ApJ, 497, 188

Cowie L. L., Songaila A., 1977, Nature, 266, 501

Croton D. J., et al., 2005, MNRAS, 356, 1155

Croton D. J., et al., 2006, MNRAS, 365, 11

Cucciati O., et al., 2006, A&A, 458, 39

da Cunha E., Charlot S., Elbaz D., 2008, MNRAS, 388, 1595

Daddi E., Dickinson M., Morrison G., Chary R., Cimatti A., Elbaz D., Frayer D., Renzini A., Pope A., Alexander D. M., Bauer F. E., Giavalisco M., Huynh M., Kurk J., Mignoli M., 2007, ApJ, 670, 156

Darvish B., Mobasher B., Sobral D., Rettura A., Scoville N., Faisst A., Capak P., 2016, ApJ, 825, 113

Darvish B., Mobasher B., Sobral D., Scoville N., Aragon-Calvo M., 2015, ApJ, 805, 121

De Lucia G., Springel V., White S. D. M., Croton D., Kauffmann G., 2006, MNRAS, 366, 499

De Lucia G., Weinmann S., Poggianti B. M., Aragón-Salamanca A., Zaritsky D., 2012, MNRAS, 423, 1277

de Vaucouleurs G., 1959, Handbuch der Physik, 53, 275

Dekel A., Birnboim Y., 2006, MNRAS, 368, 2

Dekel A., Burkert A., 2014, MNRAS, 438, 1870

Dekel A., Sari R., Ceverino D., 2009, ApJ, 703, 785

Diamond-Stanic A. M., Moustakas J., Tremonti C. A., Coil A. L., Hickox R. C., Robaina A. R., Rudnick G. H., Sell P. H., 2012, ApJ, 755, L26

Dressler A., 1980, ApJ, 236, 351

Dressler A., Gunn J. E., 1983, ApJ, 270, 7

Dressler A., Oemler Jr. A., Couch W. J., Smail I., Ellis R. S., Barger A., Butcher H., Poggianti B. M., Sharples R. M., 1997, ApJ, 490, 577

Dressler A., Thompson I. B., Shectman S. A., 1985, ApJ, 288, 481

Drory N., Bundy K., Leauthaud A., Scoville N., Capak P., Ilbert O., Kartaltepe J. S., Kneib J. P., McCracken H. J., Salvato M., Sanders D. B., Thompson D., Willott C. J., 2009, ApJ, 707, 1595

Eggen O. J., Lynden-Bell D., Sandage A. R., 1962, ApJ, 136, 748

Eisenhardt P. R. M., Brodwin M., Gonzalez A. H., Stanford S. A., Stern D., Barmby P., Brown M. J. I., Dawson K., Dey A., Doi M., Galametz A., Jannuzi B. T., Kochanek C. S., Meyers J., Morokuma T., Moustakas L. A., 2008, ApJ, 684, 905

Elbaz D., Daddi E., Le Borgne D., Dickinson M., Alexander D. M., Chary R.-R., Starck J.-L., Brandt W. N., Kitzbichler M., MacDonald E., Nonino M., Popesso P., Stern D., Vanzella E., 2007, A&A, 468, 33

Elbaz D., et al., 2011, A&A, 533, A119

Evrard A. E., 1991, MNRAS, 248, 8P

Fabello S., Kauffmann G., Catinella B., Giovanelli R., Haynes M. P., Heckman T. M., Schiminovich D., 2011, MNRAS, 416, 1739

Faber S. M., 1973, ApJ, 179, 423

Faber S. M., et al., 2007, ApJ, 665, 265

Fabricant D., Franx M., van Dokkum P., 2000, ApJ, 539, 577

Farouki R., Shapiro S. L., 1981, ApJ, 243, 32

Fasano G., Poggianti B. M., Couch W. J., Bettoni D., Kjærgaard P., Moles M., 2000, ApJ, 542, 673

Fassbender R., et al., 2014, A&A, 568, A5

Finoguenov A., et al., 2010, MNRAS, 403, 2063

Foltz R., Rettura A., Wilson G., van der Burg R. F. J., Muzzin A., Lidman C., Demarco R., Nantais J., DeGroot A., Yee H., 2015, ApJ, 812, 138

Font A. S., Bower R. G., McCarthy I. G., Benson A. J., Frenk C. S., Helly J. C., Lacey C. G., Baugh C. M., Cole S., 2008, MNRAS, 389, 1619

French K. D., Yang Y., Zabludoff A., Narayanan D., Shirley Y., Walter F., Smith J.-D., Tremonti C. A., 2015, ApJ, 801, 1

French K. D., Zabludoff A. I., Yoon I., Shirley Y., Yang Y., Smercina A., Smith J. D., Narayanan D., 2018, ApJ, 861, 123

Furusawa H., et al., 2008, ApJS, 176, 1

Gaibler V., Khochfar S., Krause M., 2011, MNRAS, 411, 155

Galametz A., Pentericci L., Castellano M., Mendel T., Hartley W. G., Fossati M., Finoguenov A., Almaini O., Beifiori A., Fontana A., Grazian A., Scodeggio M., Kocevski D. D., 2018, MNRAS, 475, 4148

Galametz A., Vernet J., De Breuck C., Hatch N. A., Miley G. K., Kodama T., Kurk J., Overzier R. A., Rettura A., Röttgering H. J. A., Seymour N., Venemans B. P., Zirm A. W., 2010, A&A, 522, A58

Gallazzi A., et al., 2009, ApJ, 690, 1883

Geach J. E., Simpson C., Rawlings S., Read A. M., Watson M., 2007, MNRAS, 381, 1369

Geller M. J., Huchra J. P., 1983, ApJS, 52, 61

Geréb K., Morganti R., Oosterloo T. A., Hoppmann L., Staveley-Smith L., 2015, A&A, 580, A43

Gerke B. F., Newman J. A., Faber S. M., Cooper M. C., Croton D. J., Davis M., Willmer C. N. A., Yan R., Coil A. L., Guhathakurta P., Koo D. C., Weiner B. J., 2007, MNRAS, 376, 1425

Gladders M. D., Yee H. K. C., 2000, AJ, 120, 2148

Gómez P. L., et al., 2003, ApJ, 584, 210

Gonçalves T. S., Martin D. C., Menéndez-Delmestre K., Wyder T. K., Koekemoer A., 2012, ApJ, 759, 67

González-García A. C., Balcells M., 2005, MNRAS, 357, 753

Goto T., 2007, MNRAS, 381, 187

Goto T., et al., 2003, PASJ, 55, 771

Goto T., Yagi M., Tanaka M., Okamura S., 2004, MNRAS, 348, 515

Grazian A., Fontana A., Moscardini L., Salimbeni S., Menci N., Giallongo E., de Santis C., Gallozzi S., Nonino M., Cristiani S., Vanzella E., 2006, A&A, 453, 507

Grützbauch R., Conselice C. J., Bauer A. E., Bluck A. F. L., Chuter R. W., Buitrago F., Mortlock A., Weinzirl T., Jogee S., 2011, MNRAS, 418, 938

Gunn J. E., Gott III J. R., 1972, ApJ, 176, 1

Haines C. P., Pereira M. J., Smith G. P., Egami E., Babul A., Finoguenov A., Ziparo F., McGee S. L., Rawle T. D., Okabe N., Moran S. M., 2015, ApJ, 806, 101

Hartley W. G., Almaini O., Mortlock A., Conselice C. J., Grützbauch R., Simpson C., Bradshaw E. J., Chuter R. W., Foucaud S., Cirasuolo M., Dunlop J. S., McLure R. J., Pearce H. J., 2013, MNRAS, 431, 3045

Hartley W. G., et al., 2010, MNRAS, 407, 1212

Hatch N. A., De Breuck C., Galametz A., Miley G. K., Overzier R. A., Röttgering H. J. A., Doherty M., Kodama T., Kurk J. D., Seymour N., Venemans B. P., Vernet J., Zirm A. W., 2011, MNRAS, 410, 1537

Heckman T. M., Armus L., Miley G. K., 1990, ApJS, 74, 833

Henriksen M., Byrd G., 1996, ApJ, 459, 82

Hogg D. W., Blanton M., Strateva I., Bahcall N. A., Brinkmann J., Csabai I., Doi M., Fukugita M., Hennessy G., Ivezić Ž., Knapp G. R., Lamb D. Q., Lupton R., Munn J. A., Nichol R., Schlegel D. J., Schneider D. P., York D. G., 2002, AJ, 124, 646

Hopkins P. F., Hernquist L., Cox T. J., Di Matteo T., Martini P., Robertson B., Springel V., 2005, ApJ, 630, 705

Huang J.-S., Glazebrook K., Cowie L. L., Tinney C., 2003, ApJ, 584, 203

Hubble E., Humason M. L., 1931, ApJ, 74, 43

Hubble E. P., 1925, ApJ, 62

Hubble E. P., 1936, Realm of the Nebulae. Yale Univ. Press, New Haven

Huchra J. P., Geller M. J., 1982, ApJ, 257, 423

Huertas-Company M., et al., 2016, MNRAS, 462, 4495

Icke V., 1985, A&A, 144, 115

Ilbert O., et al., 2010, ApJ, 709, 644

Ilbert O., et al., 2013, A&A, 556, A55

Jarvis M. J., et al., 2013, MNRAS, 428, 1281

Kang X., van den Bosch F. C., 2008, ApJ, 676, L101

Kauffmann G., et al., 2003, MNRAS, 341, 33

Kauffmann G., White S. D. M., Heckman T. M., Ménard B., Brinchmann J., Charlot S., Tremonti C., Brinkmann J., 2004, MNRAS, 353, 713

Kaviraj S., Kirkby L. A., Silk J., Sarzi M., 2007, MNRAS, 382, 960

Kawata D., Mulchaey J. S., 2008, ApJ, 672, L103

Kawinwanichakij L., et al., 2016, ApJ, 817, 9

Kawinwanichakij L., et al., 2017, ApJ, 847, 134

Kelkar K., Aragón-Salamanca A., Gray M. E., Maltby D., Vulcani B., De Lucia G., Poggianti B. M., Zaritsky D., 2015, MNRAS, 450, 1246

Kelvin L. S., et al., 2012, MNRAS, 421, 1007

Kereš D., Katz N., Fardal M., Davé R., Weinberg D. H., 2009, MNRAS, 395, 160

Kereš D., Katz N., Weinberg D. H., Davé R., 2005, MNRAS, 363, 2

Kocevski D. D., et al., 2018, ApJS, 236, 48

Kocevski D. D., Lubin L. M., Gal R., Lemaux B. C., Fassnacht C. D., Squires G. K., 2009, ApJ, 690, 295

Kochanek C. S., Pahre M. A., Falco E. E., Huchra J. P., Mader J., Jarrett T. H., Chester T., Cutri R., Schneider S. E., 2001, ApJ, 560, 566

Kodama T., Smail I., Nakata F., Okamura S., Bower R. G., 2001, ApJ, 562, L9

Kodama T., Tanaka I., Kajisawa M., Kurk J., Venemans B., De Breuck C., Vernet J., Lidman C., 2007, MNRAS, 377, 1717

Kovač K., et al., 2014, MNRAS, 438, 717

Kriek M., van der Wel A., van Dokkum P. G., Franx M., Illingworth G. D., 2008, ApJ, 682, 896

Krishnan C., Hatch N. A., Almaini O., Kocevski D., Cooke E. A., Hartley W. G., Hasinger G., Maltby D. T., Muldrew S. I., Simpson C., 2017, MNRAS, 470, 2170

Kuchner U., Ziegler B., Verdugo M., Bamford S., Häußler B., 2017, A&A, 604, A54

Lacey C., Cole S., 1993, MNRAS, 262, 627

Lani C., Almaini O., Hartley W. G., Mortlock A., Häußler B., Chuter R. W., Simpson C., van der Wel A., Grützbauch R., Conselice C. J., Bradshaw E. J., Cooper M. C., Faber S. M., Grogin N. A., Kocevski D. D., Koekemoer A. M., Lai K., 2013, MNRAS, 435, 207

Larson R. B., 1974, MNRAS, 169, 229

Larson R. B., Tinsley B. M., Caldwell C. N., 1980, ApJ, 237, 692

Lawrence A., et al., 2007, MNRAS, 379, 1599

Lee S.-K., Im M., Kim J.-W., Lotz J., McPartland C., Peth M., Koekemoer A., 2015, ApJ, 810, 90

Leitherer C., Robert C., Drissen L., 1992, ApJ, 401, 596

Lewis I., et al., 2002, MNRAS, 334, 673

Licitra R., Mei S., Raichoor A., Erben T., Hildebrandt H., 2016, MNRAS, 455, 3020

Lintott C. J., et al., 2008, MNRAS, 389, 1179

Lotz J. M., Papovich C., Faber S. M., Ferguson H. C., Grogin N., Guo Y., Kocevski D., Koekemoer A. M., Lee K.-S., McIntosh D., Momcheva I., Rudnick G., Saintonge A., Tran K.-V., van der Wel A., Willmer C., 2013, ApJ, 773, 154

Lubin L. M., Oke J. B., Postman M., 2002, AJ, 124, 1905

Madau P., Dickinson M., 2014, ARA&A, 52, 415

Makino J., Hut P., 1997, ApJ, 481, 83

Maltby D. T., Almaini O., Wild V., Hatch N. A., Hartley W. G., Simpson C., McLure R. J., Dunlop J., Rowlands K., Cirasuolo M., 2016, MNRAS, 459, L114

Maltby D. T., Almaini O., Wild V., Hatch N. A., Hartley W. G., Simpson C., Rowlands K., Socolovsky M., 2018, MNRAS, 480, 381

Maltby D. T., Aragón-Salamanca A., Gray M. E., Barden M., Häußler B., Wolf C., Peng C. Y., Jahnke K., McIntosh D. H., Böhm A., van Kampen E., 2010, MNRAS, 402, 282

Marinoni C., Davis M., Newman J. A., Coil A. L., 2002, ApJ, 580, 122

Marshall H. L., Tananbaum H., Avni Y., Zamorani G., 1983, ApJ, 269, 35

Martin D. C., et al., 2007, ApJS, 173, 342

Martini P., Sivakoff G. R., Mulchaey J. S., 2009, ApJ, 701, 66

McCarthy P. J., et al., 2007, ApJ, 664, L17

McGee S. L., Balogh M. L., Wilman D. J., Bower R. G., Mulchaey J. S., Parker L. C., Oemler A., 2011, MNRAS, 413, 996

McGee S. L., Bower R. G., Balogh M. L., 2014, MNRAS, 442, L105

McLure R. J., et al., 2013, MNRAS, 428, 1088

McNamara B. R., Nulsen P. E. J., 2007, ARA&A, 45, 117

Mendez A. J., Coil A. L., Lotz J., Salim S., Moustakas J., Simard L., 2011, ApJ, 736, 110

Merchán M. E., Zandivarez A., 2005, ApJ, 630, 759

Merritt D., 1983, ApJ, 264, 24

Merritt D., 1984, ApJ, 276, 26

Mihos J. C., Hernquist L., 1996, ApJ, 464, 641

Miyaji T., Zamorani G., Cappelluti N., Gilli R., Griffiths R. E., Comastri A., Hasinger G., Brusa M., Fiore F., Puccetti S., Guzzo L., Finoguenov A., 2007, ApJS, 172, 396

Mok A., Balogh M. L., McGee S. L., Wilman D. J., Finoguenov A., Tanaka M., Giodini S., Bower R. G., Connelly J. L., Hou A., Mulchaey J. S., Parker L. C., 2013, MNRAS, 431, 1090

Moore B., Katz N., Lake G., Dressler A., Oemler A., 1996, Nature, 379, 613

Moore B., Lake G., Quinn T., Stadel J., 1999, MNRAS, 304, 465

Mortlock A., Conselice C. J., Hartley W. G., Duncan K., Lani C., Ownsworth J. R., Almaini O., Wel A. v. d., Huang K.-H., Ashby M. L. N., Willner S. P., Fontana A., Dekel A., Koekemoer A. M., Ferguson H. C., Faber S. M., Grogin N. A., Kocevski D. D., 2015, MNRAS, 447, 2

Mortlock A., et al., 2013, MNRAS, 433, 1185

Moutard T., Arnouts S., Ilbert O., Coupon J., Davidzon I., Guzzo L., Hudelot P., McCracken H. J., Van Werbaeke L., Morrison G. E., Le Fèvre O., Comte V., Bolzonella M., Fritz A., Garilli B., Scodeggio M., 2016, A&A, 590, A103

Moutard T., Sawicki M., Arnouts S., Golob A., Malavasi N., Adami C., Coupon J., Ilbert O., 2018, MNRAS, 479, 2147

Muldrew S. I., et al., 2012, MNRAS, 419, 2670

Muzzin A., Marchesini D., Stefanon M., Franx M., McCracken H. J., Milvang-Jensen B., Dunlop J. S., Fynbo J. P. U., Brammer G., Labbé I., van Dokkum P. G., 2013, ApJ, 777, 18

Muzzin A., van der Burg R. F. J., McGee S. L., Balogh M., Franx M., Hoekstra H., Hudson M. J., Noble A., Taranu D. S., Webb T., Wilson G., Yee H. K. C., 2014, ApJ, 796, 65

Muzzin A., Wilson G., Yee H. K. C., Gilbank D., Hoekstra H., Demarco R., Balogh M., van Dokkum P., Franx M., Ellingson E., Hicks A., Nantais J., Noble A., Lacy M., Lidman C., Rettura A., Surace J., Webb T., 2012, ApJ, 746, 188

Naab T., Johansson P. H., Ostriker J. P., 2009, ApJ, 699, L178

Nair P. B., Abraham R. G., 2010, ApJS, 186, 427

Narayanan D., et al., 2008, ApJS, 176, 331

Noll S., Burgarella D., Giovannoli E., Buat V., Marcillac D., Muñoz-Mateos J. C., 2009, A&A, 507, 1793

Norton S. A., Gebhardt K., Zabludoff A. I., Zaritsky D., 2001, ApJ, 557, 150

Oemler Jr. A., 1974, ApJ, 194, 1

Oogi T., Habe A., 2013, MNRAS, 428, 641

Ostriker J. P., 1980, Comments on Astrophysics, 8, 177

Overzier R. A., Heckman T. M., Kauffmann G., Seibert M., Rich R. M., Basu-Zych A., Lotz J., Aloisi A., Charlot S., Hoopes C., Martin D. C., Schiminovich D., Madore B., 2008, ApJ, 677, 37

Papovich C., et al., 2012, ApJ, 750, 93

Patel S. G., Holden B. P., Kelson D. D., Illingworth G. D., Franx M., 2009, ApJ, 705, L67

Patton D. R., Atfield J. E., 2008, ApJ, 685, 235

Pawlik M. M., Taj Aldeen L., Wild V., Mendez-Abreu J., Lahén N., Johansson P. H., Jimenez N., Lucas W., Zheng Y., Walcher C. J., Rowlands K., 2018, MNRAS, 477, 1708

Peng C. Y., Ho L. C., Impey C. D., Rix H.-W., 2002, AJ, 124, 266

Peng Y.-j., et al., 2010, ApJ, 721, 193

Pentericci L., Kurk J. D., Röttgering H. J. A., Miley G. K., van Breugel W., Carilli C. L., Ford H., Heckman T., McCarthy P., Moorwood A., 2000, A&A, 361, L25

Perlmutter S., et al., 1999, ApJ, 517, 565

Piffaretti R., Arnaud M., Pratt G. W., Pointecouteau E., Melin J.-B., 2011, A&A, 534, A109

Planck Collaboration Ade P. A. R., Aghanim N., Arnaud M., Ashdown M., Aumont J., Baccigalupi C., Balbi A., Banday A. J., Barreiro R. B., et al. 2011, A&A, 536, A8

Poggianti B. M., 2006, in Del Toro Iniesta J. C., Alfaro E. J., Gorgas J. G., Salvador-Sole E., Butcher H., eds, The Many Scales in the Universe: JENAM 2004 Astrophysics Reviews p. 71

Poggianti B. M., et al., 2009, ApJ, 693, 112

Poggianti B. M., et al., 2013, ApJ, 762, 77

Poggianti B. M., Smail I., Dressler A., Couch W. J., Barger A. J., Butcher H., Ellis R. S., Oemler Jr. A., 1999, ApJ, 518, 576

Pozzetti L., et al., 2010, A&A, 523, A13

Quadri R., van Dokkum P., Gawiser E., Franx M., Marchesini D., Lira P., Rudnick G., Herrera D., Maza J., Kriek M., Labbé I., Francke H., 2007, ApJ, 654, 138

Quadri R. F., Williams R. J., Franx M., Hildebrandt H., 2012, ApJ, 744, 88

Quintero A. D., et al., 2004, ApJ, 602, 190

Rasmussen J., Ponman T. J., Mulchaey J. S., 2006, MNRAS, 370, 453

Ravindranath S., et al., 2004, ApJ, 604, L9

Riess A. G., et al., 1998, AJ, 116, 1009

Rowlands K., Wild V., Nesvadba N., Sibthorpe B., Mortier A., Lehnert M., da Cunha E., 2015, MNRAS, 448, 258

Rubin V. C., Ford Jr. W. K., Thonnard N., 1978, ApJ, 225, L107

Rudnick G. H., Tran K.-V., Papovich C., Momcheva I., Willmer C., 2012, ApJ, 755, 14

Rykoff E. S., et al., 2016, ApJS, 224, 1

Rykoff E. S., Rozo E., Busha M. T., Cunha C. E., Finoguenov A., Evrard A., Hao J., Koester B. P., Leauthaud A., Nord B., Pierre M., Reddick R., Sadibekova T., Sheldon E. S., Wechsler R. H., 2014, ApJ, 785, 104

Salim S., et al., 2007, ApJS, 173, 267

Schawinski K., et al., 2009, MNRAS, 396, 818

Schawinski K., Urry C. M., Simmons B. D., Fortson L., Kaviraj S., Keel W. C., Lintott C. J., Masters K. L., Nichol R. C., Sarzi M., Skibba R., Treister E., Willett K. W., Wong O. I., Yi S. K., 2014, MNRAS, 440, 889

Schaye J., et al., 2015, MNRAS, 446, 521

Schechter P., 1976, ApJ, 203, 297

Scodeggio M., et al., 2016, ArXiv e-prints

Scoville N., et al., 2013, ApJS, 206, 3

Sérsic J. L., 1968, Atlas de Galaxias Australes

Shankar F., Marulli F., Bernardi M., Mei S., Meert A., Vikram V., 2013, MNRAS, 428, 109

Shen S., Mo H. J., White S. D. M., Blanton M. R., Kauffmann G., Voges W., Brinkmann J., Csabai I., 2003, MNRAS, 343, 978

Shimakawa R., Kodama T., Tadaki K.-i., Tanaka I., Hayashi M., Koyama Y., 2014, MNRAS, 441, L1

Sil'Chenko O. K., Chilingarian I. V., Sotnikova N. Y., Afanasiev V. L., 2011, MNRAS, 414, 3645

Silk J., Rees M. J., 1998, A&A, 331, L1

Simpson C., Rawlings S., Ivison R., Akiyama M., Almaini O., Bradshaw E., Chapman S., Chuter R., Croom S., Dunlop J., Foucaud S., Hartley W., 2012, MNRAS, 421, 3060

Simpson C., Westoby P., Arumugam V., Ivison R., Hartley W., Almaini O., 2013, MNRAS, 433, 2647

Smail I., Ellis R. S., Dressler A., Couch W. J., Oemler A., Sharples R. M., Butcher H., 1997, ApJ, 479, 70

Smail I., Sharp R., Swinbank A. M., Akiyama M., Ueda Y., Foucaud S., Almaini O., Croom S., 2008, MNRAS, 389, 407

Smith G. P., Treu T., Ellis R. S., Moran S. M., Dressler A., 2005, ApJ, 620, 78

Sobral D., Smail I., Best P. N., Geach J. E., Matsuda Y., Stott J. P., Cirasuolo M., Kurk J., 2013, MNRAS, 428, 1128

Socolovsky M., Almaini O., Hatch N. A., Wild V., Maltby D. T., Hartley W. G., Simpson C., 2018, MNRAS, 476, 1242

Socolovsky M., Maltby D. T., Hatch N. A., Almaini O., Wild V., Hartley W. G., Simpson C., Rowlands K., 2019, MNRAS, 482, 1640

Spitzer Jr. L., Baade W., 1951, ApJ, 113, 413

Springel V., White S. D. M., Jenkins A., Frenk C. S., Yoshida N., Gao L., Navarro J., Thacker R., Croton D., Helly J., Peacock J. A., Cole S., Thomas P., Couchman H., Evrard A., Colberg J., Pearce F., 2005, Nature, 435, 629

Steinhauser D., Schindler S., Springel V., 2016, A&A, 591, A51

Strateva I., et al., 2001, AJ, 122, 1861

Strazzullo V., et al., 2010, A&A, 524, A17

Strazzullo V., Gobat R., Daddi E., Onodera M., Carollo M., Dickinson M., Renzini A., Arimoto N., Cimatti A., Finoguenov A., Chary R.-R., 2013, ApJ, 772, 118

Tomczak A. R., et al., 2014, ApJ, 783, 85

Toomre A., Toomre J., 1972, ApJ, 178, 623

Tran K.-V. H., Franx M., Illingworth G., Kelson D. D., van Dokkum P., 2003, ApJ, 599, 865

Tran K.-V. H., Franx M., Illingworth G. D., van Dokkum P., Kelson D. D., Magee D., 2004, ApJ, 609, 683

Treu T., Ellis R. S., Kneib J.-P., Dressler A., Smail I., Czoske O., Oemler A., Natarajan P., 2003, ApJ, 591, 53

Trevese D., Castellano M., Fontana A., Giallongo E., 2007, A&A, 463, 853

Ueda Y., Watson M. G., Stewart I. M., Akiyama M., Schwope A. D., Lamer G., Ebrero J., Carrera F. J., Sekiguchi K., Yamada T., Simpson C., Hasinger G., Mateos S., 2008, ApJS, 179, 124

van Breukelen C., et al., 2006, MNRAS, 373, L26

van den Bosch F. C., Aquino D., Yang X., Mo H. J., Pasquali A., McIntosh D. H., Weinmann S. M., Kang X., 2008, MNRAS, 387, 79

van der Wel A., et al., 2012, ApJS, 203, 24

van der Wel A., et al., 2014, ApJ, 788, 28

van der Wel A., Holden B. P., Zirm A. W., Franx M., Rettura A., Illingworth G. D., Ford H. C., 2008, ApJ, 688, 48

van Dokkum P. G., 2005, AJ, 130, 2647

van Dokkum P. G., Franx M., Fabricant D., Illingworth G. D., Kelson D. D., 2000, ApJ, 541, 95

van Dokkum P. G., Stanford S. A., Holden B. P., Eisenhardt P. R., Dickinson M., Elston R., 2001, ApJ, 552, L101

Vanderlinde K., et al., 2010, ApJ, 722, 1180

Vazdekis A., Sánchez-Blázquez P., Falcón-Barroso J., Cenarro A. J., Beasley M. A., Cardiel N., Gorgas J., Peletier R. F., 2010, MNRAS, 404, 1639

Venemans B. P., Röttgering H. J. A., Miley G. K., van Breugel W. J. M., de Breuck C., Kurk J. D., Pentericci L., Stanford S. A., Overzier R. A., Croft S., Ford H., 2007, A&A, 461, 823

Vergani D., et al., 2010, A&A, 509, A42

Vogelsberger M., Genel S., Springel V., Torrey P., Sijacki D., Xu D., Snyder G., Nelson D., Hernquist L., 2014, MNRAS, 444, 1518

von der Linden A., Wild V., Kauffmann G., White S. D. M., Weinmann S., 2010, MNRAS, 404, 1231

Webb T. M. A., Muzzin A., Noble A., Bonaventura N., Geach J., Hezevah Y., Lidman C., Wilson G., Yee H. K. C., Surace J., Shupe D., 2015, ApJ, 814, 96

Weinmann S. M., Kauffmann G., von der Linden A., De Lucia G., 2010, MNRAS, 406, 2249

Welikala N., et al., 2016, MNRAS, 455, 1629

Wen Z. L., Han J. L., Liu F. S., 2012, ApJS, 199, 34

Wetzel A. R., Tinker J. L., Conroy C., 2012, MNRAS, 424, 232

Wetzel A. R., Tinker J. L., Conroy C., van den Bosch F. C., 2013, MNRAS, 432, 336

Wheeler C., Phillips J. I., Cooper M. C., Boylan-Kolchin M., Bullock J. S., 2014, MNRAS, 442, 1396

Whitaker K. E., Kriek M., van Dokkum P. G., Bezanson R., Brammer G., Franx M., Labbé I., 2012, ApJ, 745, 179

White S. D. M., Frenk C. S., 1991, ApJ, 379, 52

White S. D. M., Rees M. J., 1978, MNRAS, 183, 341

Wild V., Almaini O., Cirasuolo M., Dunlop J., McLure R., Bowler R., Ferreira J., Bradshaw E., Chuter R., Hartley W., 2014, MNRAS, 440, 1880

Wild V., Almaini O., Dunlop J., Simpson C., Rowlands K., Bowler R., Maltby D., McLure R., 2016, MNRAS, 463, 832

Wild V., Walcher C. J., Johansson P. H., Tresse L., Charlot S., Pollo A., Le Fèvre O., de Ravel L., 2009, MNRAS, 395, 144

Williams R. J., Quadri R. F., Franx M., van Dokkum P., Labbé I., 2009, ApJ, 691, 1879

Willis J. P., Clerc N., Bremer M. N., Pierre M., Adami C., Ilbert O., Maughan B., Maurogordato S., Pacaud F., Valtchanov I., Chiappetti L., Thanjavur K., Gwyn S., Stanway E. R., Winkworth C., 2013, MNRAS, 430, 134

Willmer C. N. A., et al., 2006, ApJ, 647, 853

Wilman D. J., Zibetti S., Budavári T., 2010, MNRAS, 406, 1701

Wilson G., Muzzin A., Yee H. K. C., Lacy M., Surace J., Gilbank D., Blindert K., Hoekstra H., Majumdar S., Demarco R., Gardner J. P., Gladders M. D., Lonsdale C., 2009, ApJ, 698, 1943

Xu C. K., Zhao Y., Scoville N., Capak P., Drory N., Gao Y., 2012, ApJ, 747, 85

Yan R., Newman J. A., Faber S. M., Konidaris N., Koo D., Davis M., 2006, ApJ, 648, 281

Yang Y., Zabludoff A. I., Zaritsky D., Lauer T. R., Mihos J. C., 2004, ApJ, 607, 258

York D. G. e. a., 2000, AJ, 120, 1579

Young J. S., 1999, ApJ, 514, L87

Younger J. D., Cox T. J., Seth A. C., Hernquist L., 2007, ApJ, 670, 269

Zabludoff A. I., Zaritsky D., Lin H., Tucker D., Hashimoto Y., Shectman S. A., Oemler A., Kirshner R. P., 1996, ApJ, 466, 104

Zolotov A., Dekel A., Mandelker N., Tweed D., Inoue S., DeGraf C., Ceverino D., Primack J. R., Barro G., Faber S. M., 2015, MNRAS, 450, 2327

Zubovas K., Nayakshin S., King A., Wilkinson M., 2013, MNRAS, 433, 3079

Zwaan M. A., Kuntschner H., Pracy M. B., Couch W. J., 2013, MNRAS, 432, 492

Zwicky F., 1933, Helvetica Physica Acta, 6, 110